

Ion Beam Treatment of Functional Layers in Thin-Film Silicon Solar Cells

Wendi Zhang



Forschungszentrum Jülich GmbH Institute for Energy and Climate Research (IEK) Photovoltaics (IEK-5)

Ion Beam Treatment of Functional Layers in Thin-Film Silicon Solar Cells

Wendi Zhang

Schriften des Forschungszentrums Jülich Reihe Energie & Umwelt / Energy & Environment Bibliographic information published by the Deutsche Nationalbibliothek. The Deutsche Nationalbibliothek lists this publication in the Deutsche Nationalbibliografie; detailed bibliographic data are available in the Internet at http://dnb.d-nb.de.

Publisher and Forschungszentrum Jülich GmbH

Distributor: Zentralbibliothek

52425 Jülich

Phone +49 (0) 24 61 61-53 68 · Fax +49 (0) 24 61 61-61 03

e-mail: zb-publikation@fz-juelich.de Internet: http://www.fz-juelich.de/zb

Cover Design: Grafische Medien, Forschungszentrum Jülich GmbH

Printer: Grafische Medien, Forschungszentrum Jülich GmbH

Copyright: Forschungszentrum Jülich 2013

Schriften des Forschungszentrums Jülich

Reihe Energie & Umwelt / Energy & Environment Band / Volume 170

D 82 (Diss., RWTH Aachen University, 2012)

ISSN 1866-1793 ISBN 978-3-89336-864-8

The complete volume is freely available on the Internet on the Jülicher Open Access Server (JUWEL) at http://www.fz-juelich.de/zb/juwel

Neither this book nor any part of it may be reproduced or transmitted in any form or by any means, electronic or mechanical, including photocopying, microfilming, and recording, or by any information storage and retrieval system, without permission in writing from the publisher.

Contents

Αŀ	ostrac	:t		1
Zι	ısamı	nenfass	sung	2
1	Intro	oductio	n	5
2	Fund	dament	tals	9
	2.1	Ion bea	am treatment	9
		2.1.1	Ion source	9
		2.1.2	Ion-sample interaction	15
			2.1.2.1 Sputtering yield	16
			2.1.2.2 Reactive or molecular ions and compound substrates	18
	2.2	Transp	parent conducting oxide	19
		2.2.1	ZnO structure	20
		2.2.2	Electrical properties	20
		2.2.3	Optical properties	24
		2.2.4	Deposition of ZnO:Al films	27
			2.2.4.1 Magnetron sputtering	27
			2.2.4.2 Preferred orientation	29
			2.2.4.3 Thin-film growth mechanism	30
			2.2.4.4 As-grown rough ZnO films	33
			2.2.4.5 Surface evolution	34
	2.3	Silicon	Thin-film Solar cells	39
		2.3.1	Hydrogenated amorphous silicon	39
		2.3.2	Hydrogenated microcrystalline silicon	40
		2.3.3	Operating principle	41
		2.3.4	Characterization parameters	41
3	Exp	eriment	tal	45
-	3.1		ition techniques	45
		3.1.1	ZnO:Al films - Magnetron sputtering	45
			3.1.1.1 Standard ZnO:Al films - Planar ceramic target	45
			3.1.1.2 High rate ZnO:Al films - tube target	-
			3.1.1.3 Small area deposition system	47
		3.1.2	Silicon - PECVD	47
	3.2		am treatment	
	- · -		Competry of the ion source	17

Contents

		3.2.2	Parameters	48
	3.3	Chara	cterization methods	49
		3.3.1	Electrical properties	49
			3.3.1.1 4-point probe measurement	50
			3.3.1.2 Hall effect measurement	50
		3.3.2	Optical Properties	51
			3.3.2.1 Total and diffuse transmission, Haze, reflection	51
			3.3.2.2 Angular resolved scattering (ARS)	52
		3.3.3	Surface topography	53
			3.3.3.1 Scanning Electron Microscopy (SEM)	53
			3.3.3.2 Atomic Force Microscopy (AFM)	54
		3.3.4	Structural properties	55
			3.3.4.1 X-ray diffraction (XRD)	56
			3.3.4.2 Transmission electron microscopy (TEM)	57
		3.3.5	Surface composition - X-ray photoelectron spectroscopy (XPS)	59
		3.3.6	Solar cells characterization	61
			3.3.6.1 Current-voltage measurement	61
			3.3.6.2 Quantum efficiency	61
4	Cha	racteri	zation of the ion beam treatment	63
	4.1	Optica	al emission spectroscopy of the ion beam	63
	4.2		etching	65
		4.2.1	Different source gas	65
		4.2.2	Tilted ion source	67
	4.3	Dynar	mic etching	68
		4.3.1	Different power and tilt angle	68
		4.3.2	Different source gas and substrate	69
	4.4	Discus	ssion	70
	4.5	Summ	ary	73
5	lon	beam 1	treatment of the glass surface	75
	5.1		own rough ZnO:Al films	75
		5.1.1	Different glass pretreatment	75
		5.1.2	Electrical properties	79
			5.1.2.1 Annealing without Si capping layer	80
			5.1.2.2 Annealing with Si capping layer	81
			5.1.2.3 Discussions	82
		5.1.3	Optical properties	83
		5.1.4	Solar cells	85
			5.1.4.1 Amorphous Si thin-film solar cells	85
			5.1.4.2 Microcrystalline Si thin-film solar cells	86
			5.1.4.3 Tandem Si thin-film solar cells	88
		5.1.5	Summary	90

Contents

Bi	bliog	raphy		177
7	Sum	nmary a	and Outlook	175
	6.6	Summ	ary	. 172
			6.5.5.2 Influence of HCl etching time on textured glass \dots	
			6.5.5.1 Influence of the treatment on textured glass	
		6.5.5	Solar cells	. 165
			6.5.4.4 Summary	. 164
			6.5.4.3 ZnO:Al films on cleaned textured glass	
			6.5.4.2 ZnO:Al films on Ar/O_2 treated textured glass	
			6.5.4.1 ZnO:Al films on Ar treated textured glass	
		6.5.4	ZnO:Al films on textured glass	
		6.5.3	Different etching mask	
		6.5.2	Preparation of textured glass	
		6.5.1	Motivation	
	6.5		red glass	
	6.4		grown on ion beam treated ZnO:Al films	
	6.3		ication of the TCO surface by ion beam etching	
	6.2		Al films grown on ion beam treated ZnO:Al films	
J	6.1		ffect of ion beam treatment on HCl etching behavior of ZnO:Al fil	
6	lon	haam t	treatment of the TCO surface	137
	5.7	Summ	ary	. 135
	5.6		h model	
	5.5		h of ZnO:Al on ZnO crystal	
		5.4.4	Summary	
		5.4.3	Different ion beam system	
		5.4.2	XPS core level spectra scan	
			5.4.1.2 Static ion beam treatment	
			5.4.1.1 Dynamic ion beam treatment	
		5.4.1	X-Ray photoelectron spectroscopy survey scan	
	5.4	X-Ray	photoelectron spectroscopy of the glass substrate	
		5.3.3	X-ray diffraction measurements	
		5.3.2	Transmission electron microscopy measurements	
	0.0	5.3.1	Film evolution	
	5.3		e evolution and structural properties	
		5.2.4 $5.2.5$	Different ion beam system	
		5.2.4	Sputter ZnO:Al film with different temperature	
		5.2.3	Sputter ZnO:Al film in different system	
		5.2.1 $5.2.2$	Different substrates	
	5.2	5.2.1	n of rough growth	
	F 9	D	or of normal manually	00

List of Figures

2.1	Schematic diagrams of the discharge zone in close drift ion sources/thrusters.	10
2.2	Magnetic and electric field in the discharge zone of anode layer ion source.	11
2.3	Configuration of linear anode layer ion source used in this work	13
2.4	Energy distribution of oxygen ions at 5 sccm oxygen gas flow into a linear	
	anode layer ion source	15
2.5	Wurtzite structure of ZnO crystal	21
2.6	Optical transmission, reflection and absorption of a typical ZnO:Al film	25
2.7	Burstein-Moss broadening of the optical band gap of degenerate semicon-	
	ductors.	26
2.8	The schematic drawing of magnetron sputtering	28
2.9	Schematic drawing of randomly textured, out-of-plane textured, and bi-	
	axial textured thin films	29
2.10	Modified Thornton-model for RF-sputtered ZnO:Al films	31
2.11	SEM micrographs of a series of ZnO:Al films deposited under different	
	conditions	32
2.12	Comparison of the local surface morphology for surface with similar	
	roughness σ , but different values of α	34
2.13	Representative height-height correlation function obtained from a self-	
	affine surface	35
2.14	Representative power spectrum density function obtained from a self-	
	affine surface	36
2.15	Diagram of growth effects including diffusion, reemission and shadowing	
	that may effect the surface morphology during thin-film growth. [87]	37
2.16	Monte Carlo simulated β value as a function of sticking coefficient s_0 for	
	sputter deposition. It is assumed that the sticking coefficient of the second	
~ - -	strike at the surface for the re-emitted atom is 1 [95]	38
2.17	Absorption coefficient of a-Si:H, μ c-Si:H and crystalline Si (c-Si) as a	40
0.10	function of photon energy.	40
	Schematic diagram of a single junction Si thin-film solar cell	42
2.19	Typical curve for current density as a function of voltage in dark and	40
	illuminated	42
3.1	Sketch of the vertical in-line deposition system	46
3.2	Photo and Geometry of the linear anode layer ion source	48
3.3	Schematic diagram of the ion beam treatments with non-tilted ion source	
-	and tilted ion source.	49

List of Figures

3.4	Schematic diagram of the principle of 4-point probe measurement	50
3.5	Schematic diagram of measurement setup of angular resolved scattering.	53
3.6	Schematic of the working principle of atomic force microscopy	54
3.7	Schematic of Bragg's law and a typical diffraction peak versus 2θ of	
	ZnO:Al films.	56
3.8	Schematic of the objective lens and imaging system of a typical TEM setup.	58
3.9	Schematic of the emission of electrons by excitation of x-ray and a typical	
	XPS spectrum of Corning glass	59
4.1	Optical emission spectra of ion beams generated from Ar, Ar/O ₂ and O ₂	
	gas	64
4.2	Removed thickness and static etch rate of glass substrates by Ar, O ₂ , and	
	Ar/O_2 ions	66
4.3	Removed thicknesses of glass substrates at different ion source tilt angle.	67
4.4	Dynamic etch rate (DER) of glass substrates by Ar ions versus discharge	
	power of the ion source at different tilt angle	69
4.5	Dynamic etch rate of glass and ZnO:Al films	70
4.6	Sputtering yields versus incident angle simulated by TRIM program. $$	72
5.1	Experiment procedure of ion beam pretreatment	76
5.2	ZnO:Al films grown on different ion beam pretreated glass substrates	76
5.3	Haze of ZnO:Al films grown on different ion beam pretreated glass sub-	
0.0	strates	77
5.4	Cross-sectional SEM images of reference and as-grown rough ZnO:Al films.	78
5.5	Electrical properties of as-grown rough ZnO:Al films	80
5.6	Electrical properties after annealing in vacuum.	81
5.7	Haze and ARS of reference, as-grown rough ZnO:Al and SnO ₂ :F films	84
5.8	Quantum efficiency of amorphous Si solar cells on HCl etched reference	
	ZnO:Al and as-grown rough ZnO:Al films.	86
5.9	External quantum efficiency (EQE) and 1- cell reflection R of microcrys-	
	talline silicon cells grown on as-grown rough and HCl etched reference	
	ZnO:Al films.	88
5.10	External quantum efficiency of tandem Si solar cells on HCl etched refer-	
	ence ZnO:Al and as-grown rough ZnO:Al films.	89
5.11	ZnO:Al films grown on ion beam treated substrates, including Borofloat	
	glass, Diamond glass and Si wafer	91
	Experimental process of post-cleaning process	92
5.13	The effect of post HCl and NaCl etching of ion beam treated glass sub-	
	strates on the growth of ZnO:Al films	93
5.14	The effect of post HCl etching and re-cleaning of ion beam treated glass	
	substrates on the growth of ZnO:Al films	94
	ZnO:Al films deposited in different sputtering system	96
5.16	ZnO:Al films sputtered at different temperatures	97

5.17	The experimental process of ion beam pretreatment in the sputter etcher	
	system	98
5.18	ZnO:Al films grown on the glass substrates which were treated by ions	
	from sputter-etcher	99
	Evolutions of reference ZnO:Al films	100
	Evolutions of as-grown rough ZnO:Al films	101
	SEM micrograph of as-grown rough ZnO:Al film at 57 min	102
5.22	Statistics on the large conical grains of the ZnO:Al films grown on ${\rm Ar/O_2}$ treated glass	103
5 93	Height-height correlation function $H(r,t)$ and power spectral density func-	100
0.20	tion $PSD(k,t)$ of the reference and as-grown rough ZnO:Al films with	
		104
5.24		105
	Coarsening exponent of reference and as-grown rough ZnO:Al films	105
	TEM bright field images of reference ZnO:Al films	107
	TEM SADP of reference ZnO:Al films	108
5.28	Cross-section TEM of as-grown rough ZnO:Al films	109
5.29	Plan view TEM of as-grown rough ZnO:Al films	110
5.30	Radial profile plot of ring SADP from the large conical grains	111
5.31	$\theta-2\theta$ XRD scans of the two thickness series of reference and as-grown	
	rough ZnO:Al films	113
	Comparison of XRD peaks for reference and as-grown rough ZnO: Al films.	114
5.33	Comparison of additional XRD peaks of as-grown rough ZnO:Al films and	
	powder ZnO	115
5.34	Detail analysis of (0002) peaks of reference and as-grown rough ZnO:Al	
	films.	116
5.35	Schematic experimental process of XPS overview scans on statically ion	110
T 0.0	beam pretreated glass substrates	119
5.30	Rms roughness of ZnO:Al films grown on statically Ar and Ar/O_2 beam treated glass substrates	120
5 27	The dependence of ZnO:Al film roughnesses on the removed thicknesses	120
0.07		121
5 38	Comparison of O 1s peaks detected from Ar and Ar/O_2 treated glass to	121
0.00	reference Corning glass surfaces	123
5.39	The roughness of ZnO:Al films versus the number of O dangling bonds	
	on the static ion beam treated samples	126
5.40	Detail scan of O 1s of the pretreated glass by sputter-etcher	128
	Top SEM micrographies of ZnO:Al films grown on ZnO crystal with dif-	
	1 V	130
5.42	Cross-sectional SEM micrographies of ZnO:Al films grown on ZnO crystal	
	with different polarity	130
5.43	Growth model of ZnO: Al films on different substrates	134

List of Figures

6.1	$2\mathrm{s}$ HCl etching of untreated ZnO:Al film and $\mathrm{Ar/O_2}$ treated ion beam	
	treated ZnO film	138
6.2	2 s HCl etching of untreated ZnO:Al film and Ar treated ion beam treated	
	ZnO film.	139
6.3	2 s, 10 s and 40 s HCl etching of untreated, soft and strong Ar/O ₂ ion	
	beam treated ZnO:Al films	140
6.4	SEM micrographs of ZnO:Al on Ar/O ₂ treated as-deposited and HCl tex-	
	tured ZnO:Al films	142
6.5	rms roughness and crater depth of the Ar etching series of the ZnO films	144
6.6	The topographies of Ar ion beam treated HCl textured ZnO:Al films	145
6.7	External quantum efficiency (EQE) of the μ c-Si solar cells prepared on	
	untreated and Ar treated ZnO:Al films	147
6.8	Crystallinities of μ c-Si p-layer deposited on Ar ion beam treated as-	
	deposited and HCl etched ZnO films	148
6.9	Crystallinities of μ c-Si deposited on a variety ion beam treated ZnO:Al	
	films	149
6.10	The schematic diagram of the solar cells based on traditional flat and	
	textured glass	150
6.11	Motivation of using textured glass in Si thin-film solar cells	151
6.12	Preparation process of textured glass	152
6.13	AFM images of textured glass prepared by ion beam etching of 60s HCl	
	etched ZnO films	153
6.14	Crater depth, roughness, and lateral correlation length of a series of tex-	
	tured glass prepared by normal ion beam etching of different time HCl	
	etched ZnO films with initial thickness of 800 nm	154
6.15	Haze of a series of textured glass prepared by normal ion beam etching of	
	different time HCl etched ZnO films with initial thickness of 800 nm	155
6.16	Crater depth, roughness and lateral correlation length of two series of	
	textured glass by tilted ion beam etching of different time HCl etched	
	ZnO films with initial thickness of 800 nm and 1500 nm	156
6.17	Textured glass prepared by ion beam etching of Asahi U SnO2:F film. $$	157
6.18	Textured glass prepared by ion beam etching of ZnO micro-particles	158
6.19	AFM measurements of ZnO:Al films grown on Ar treated textured glass.	159
6.20	Height-height correlation function of Ar treated textured glass and	
	ZnO:Al film grown on the textured glass	159
6.21	Haze and ARS of Ar treated textured glass and ZnO:Al film grown on	
	the textured glass	160
6.22	AFM measurements of ZnO:Al films grown on Ar/O_2 treated textured	
	glass	161
6.23	Height-height correlation function of Ar/O ₂ treated textured glass and	
	ZnO: Al film grown on the textured glass	161
6.24	Haze and ARS of ${\rm Ar/O_2}$ treated textured glass and ZnO:Al film grown	
	on the textured glass	162
6.25	AFM measurements of ZnO: Al films grown on cleaned textured glass	163

6.26	Height-height correlation function of cleaned textured glass and ZnO:Al	
	film grown on the textured glass	163
6.27	Haze and ARS of ${\rm Ar/O_2}$ treated textured glass and ZnO:Al film grown	
	on the textured glass	164
6.28	SEM micrographs of three ZnO: Al films on cleaned, Ar treated and ${\rm Ar/O_2}$	
	treated textured glass	165
6.29	Haze and ARS of the ZnO:Al substrates grown on different treated tex-	
	tured glass	166
6.30	Quantum efficiency of μ c-Si single junction solar cells based on cleaned,	
	Ar and Ar/O_2 treated textured glass	167
6.31	Haze of a series of textured glass which were prepared from different HCl	
	etched ZnO:Al films.	169
6.32	Haze and ARS of ZnO: Al films grown on the series of textured glass. $$	169
6.33	The results of μ c-Si single junction solar cells deposited on textured glass	
	prepared from different HCl etching time of ZnO:Al films	170
6.34	Quantum efficiency of μ c-Si single junction solar cells deposited on tex-	
	tured glass prepared from different HCl etching time of ZnO:Al films. $$. $$.	173

List of Tables

4.1	icated sputtering yield of atomic Ar and O ions bombardment of O, Si
4.2	and Zn atoms
5.1	The thickness, sheet resistance, lateral feature size and rms roughness of as-sputtered ZnO:Al films on different glass substrates
5.2	Electrical properties pf as-grown rough ZnO:Al films after annealing with Si capping layer
5.3	Photovoltaic parameters of a-Si:H solar cells grown on as-grown rough ZnO:Al films and HCl etched reference ZnO:Al films
5.4	Photovoltaic parameters of microcrystalline solar cells on as-grown rough
5.5	and HCl etched reference ZnO:Al films
5.6	rough and HCl etched reference ZnO:Al films
	treated Corning glass
5.7	XPS compound measurement results on the glass substrates
5.8 5.9	XPS survey scan results on the glass substrates treated by round ion source. 127 XPS core level scans on the glass substrates treated by round ion source. 127
5.10	Growth parameters of polycrystalline ZnO:Al thin film deposited on a
	Zn-terminated ZnO crystal, O-terminated ZnO crystal and Corning glass. 129
6.1	J-V measurement results of the μ c-Si solar cells prepared on untreated
6.2	and Ar treated ZnO:Al films
0.2	and Ar/O_2 treated textured glass

Abstract

In silicon thin-film solar cells, transparent conductive layers have to fulfill the following requirements: high conductivity as effective contact, high transparency to transmit the light into the cell, and a textured surface which provides light scattering. Magnetron sputtered and wet-chemically textured aluminum doped zinc oxide (ZnO:Al) films are widely used as the transparent conductor. The technological goal of this dissertation is to develop an alternative to the wet etching process for light trapping in the thin silicon absorber layers through modification of the glass/ZnO:Al or ZnO:Al/Si interfaces by ion beam treatment. The study focuses on the textured growth of ZnO:Al films on ion beam pretreated glass substrates, and the preparation and application of textured glass for light trapping.

The technological aspects such as the etch rates of the glass substrate and ZnO:Al films with different ion beam configurations were studied. The experimental etch rates are compared with simulated and theoretically predicted values. With regard to the ion beam treatment of glass substrate, the influence of the ion pretreated glass on the growth of ZnO:Al films was investigated. The ZnO:Al films grown on ion beam pretreated glass substrates exhibit self-textured morphology with surface roughness of 40 nm while remaining highly conductive. Silicon thin-film solar cells prepared on the as-grown rough ZnO:Al films show that this front contact can provide excellent light trapping effect. The highest initial efficiencies for amorphous single junction solar cells on as-grown rough ZnO:Al films was 9.4 %. The as-grown rough morphology was attributed to large conical ZnO:Al grains initiated from the ion pretreated glass surface. It was found that the roughness of the as-grown rough ZnO:Al film is proportional to the number of O dangling bonds created by ion beam treatment on the glass substrate. A growth model was proposed to explain the growth mechanism of ZnO:Al films on Zn- and O-polar ZnO single crystals, as well as on untreated and ion beam treated glass substrates.

With regard to the ion beam treatment of ZnO:Al films, the influence of the ion treatment on the surface morphology, HCl etching, silicon growth, and additional ZnO:Al growth was investigated. Ion beam etching has a smoothening effect on the textured ZnO:Al films. Using sputtered and wet chemically etched ZnO:Al as ion beam etching mask, textured glass with features similar to the ZnO:Al films were obtained. Textured glass with a wide range of morphologies was prepared by varying the etching mask and the ion beam treatment conditions. Finally, as-grown textured ZnO:Al films prepared on ion beam treated textured glass, which exhibit 'double textured' features, were produced and applied in solar cells.

The ion beam treatment enabled the preparation of light scattering surfaces by textured glass and as-grown rough ZnO:Al films without the need of wet etching between TCO preparation and absorber deposition. Further, new 'double textured' surface structures could be created by the combination of both techniques. Solar cells with efficiency of 11.9 % proved the applicability as-grown textured ZnO:Al for light trapping. The growth studies provided deeper insights and a new understanding of ZnO structure formation and will govern optimization of ZnO:Al film properties.

Zusammenfassung

In Dünnschichtsolarzellen aus Silizium müssen transparente, leitfhige Schichten folgende Anforderungen erfüllen: Hohe Leitfähigkeit als guter Kontakt; hohe Transparenz an der Frontseite der Solarzelle; und eine strukturierte Oberfläche, die das einfallende Licht effektiv streut. Durch Magnetronsputtern erzeugte und nasschemisch texturierte, mit Aluminium dotierte Zinkoxid (ZnO:Al) Schichten werden häufig als transparente Leiter eingesetzt. Das technologische Ziel dieser Dissertation ist es, durch Modifikation der Glas/ZnO:Al- oder ZnO:Al/Si-Grenzfläche mittels Ionenstrahl eine Alternative zur nasschemischen Ätzung zu finden, um das Licht in den dünnen Absorberschichten aus Silizium einzufangen. Die Studie konzentriert sich auf das texturierte Wachstum von ZnO:Al-Schichten auf Glassubstraten, die mit Ionenstrahlen vorbehandelt wurden, sowie auf die Herstellung von texturiertem Glas und deren Anwendung in Solarzellen.

Zunächst wurden technologische Aspekte, wie Ätzraten der Glassubstrate und ZnO:Al-Schichten mit verschiedenen Ionenstrahlkonfigurationen, untersucht und die experimentellen Daten mit theoretisch berechneten Werten verglichen. Mittels Ionenstrahl vorbehandeltes Glas führte zu texturiertem Wachstum der ZnO:Al-Schicht während des Sputterprozesses. Solche ZnO:Al-Schichten weisen eine texturierte Oberfläche mit einer Rauheit von 40 nm auf, wobei die hohe Leitfähigkeit erhalten bleibt. Dünnschichtsolarzellen aus Silizium, die auf der rau gewachsenen ("as-grown") ZnO:Al-Schicht angefertigt wurden, zeigen, dass dieser vordere Kontakt einen ausgezeichneten Lighttrapping-Effekt bieten kann. Die höchste anfängliche Effizienz für amorphe Einzel Solarzellen aus Silizium auf as-grown rauen ZnO:Al-Schichten erreichte 9,4 %. Die raue as-grown Morphologie konnte auf große konische ZnO:Al-Körner zurückgeführt werden, deren Nukleation durch das mit Ionen vorbehandelte Glas hervorgerufen wurde. Es wurde ein linearer Zusammenhang zwischen der Rauheit der as-grown ZnO:Al-Schicht und dem Anteil der offenen Sauerstoff-Bindungen ("dangling bonds") gefunden, die durch die Ionenstrahlbehandlung auf dem Glassubstrat erzeugt wurden. Basierend auf den experimentellen Beobachtungen wurde ein Modell entwickelt, das den Mechanismus der Nukleation und des Wachstums von ZnO:Al-Schichten auf Zn- und O-polaren ZnO-Einkristallen, sowie auf unbehandelten und mit Ionenstrahl vorbehandelten Glassubstraten qualitativ erklärt.

Der Einfluss der Ionenbehandlung von ZnO:Al-Oberflächen auf die Oberflächenbeschaffenheit, HCl-Ätzung, Siliziumwachstum und auf erneutes ZnO:Al-Wachstum wurde systematisch untersucht. Die Ionenstrahlätzung hat eine leicht glättende Wirkung auf die strukturierten ZnO:Al-Schichten. Durch längere Ionenstrahlätzung von nasschemisch geätztem ZnO:Al konnte die Oberflächentextur in das Glassubstrat übertragen und so strukturiertes Glas mit ähnlicher Oberfläche wie die der ZnO:Al-Schicht hergestellt werden. Strukturiertes Glas mit einer großen Bandbreite an Morphologien ist durch Variation der Ätzmaske der Bedingungen der Ionenstrahlbehandlung verfügbar. Die Kombination von as-grown texturierten ZnO:Al-Schichten und texturiertem Glas führte zu "doppelt strukturierten"Oberflächen, deren auswirkungen ebenfalls in Solarzellen getestet wurden.

Die Ionenstrahlbehandlung ermöglichte die Herstellung von lichtstreuenden Oberflächen durch strukturiertes Glas und as-grown raue ZnO:Al-Schichten ohne nasschemisches Ätzen zwischen TCO-Präparation und Absorberdeposition. Weiterhin konnten neuartige "doppelt texturierte"Oberflächenstrukturen durch die Kombination beider Techniken erzeugt werden. Solarzellen mit einem Wirkungsgrad von bis zu 11,9 % beweisen die exzellenten Eigenschaften der hergestellten Frontkontakte. Die Wachstumsuntersuchungen liefern weitere Einsichten in und ein neues Verständnis von ZnO-Strukturenbildung und werden die künftige Optimierung der Eigenschaften von ZnO:Al-Schichten begünstigen.

1 Introduction

Presently, the increasing consumption and combustion of fossil energy resources are causing severe economic and environmental problems. To meet the quickly increasing demand for energy, photovoltaics, which directly convert sunlight into electricity, is regarded as a promising technique for a future energy supply, due to its almost infinite source and environmentally friendly nature. In the past decades, several types of solar cells have been developed. Among them, silicon wafer based monocrystalline and multicrystalline silicon solar cells were classified as the first generation solar cells. The efficiency of monocrystalline silicon solar cells has been improved significantly from 6% to 25% [1]. The material cost and high energy consumption during production of the silicon wafer, however, makes it a challenge to compete with traditional energy sources.

The second generation solar cells, including thin-film silicon solar cells and copper indium gallium selenide (CIGS) solar cells have received increased interest in the photovoltaic market over the past decade. The thickness of the absorber layer in thin-film solar cells is only one percent of that of crystalline silicon solar cells [2]. Additionally, thin-film solar cells are usually deposited at low temperatures, which allows for the use of large area and low cost substrates such as glass and plastics. A drawback of thin-film solar cells is their lower efficiency as compared to that of wafer based solar cells. Stabilized efficiency for thin-film silicon solar cells of 13% has been reported [3]. In industrial production, presently available amorphous solar modules usually have efficiency in the range of 4.5-8.5% [4]. A lot of effort has been made and is still ongoing with the aim of increasing the stable efficiency of thin-film silicon solar cells while keeping the manufacturing cost low in large scale production. This is also the aim of this work.

Thin-film silicon solar cells usually consist of hydrogenated amorphous and/or microcrystalline silicon absorber layers, sandwiched between a transparent conducting oxide (TCO) front contact and a conductive back reflector. The low absorption of the very thin silicon layers requires a textured TCO/silicon interface in order to achieve light scattering and a subsequent light trapping effect. The short circuit current density of a single junction microcrystalline silicon solar cell can be increased by about 40% with the help of a textured TCO/silicon interface as compared with that of a same solar cell with flat TCO/silicon interface. The textured interface can be introduced by the TCO surface or by the glass substrate. The former has been widely investigated and has already been applied in industrial applications. The latter concept of textured glass on the photovoltaic scale has become popular in recent years.

For a TCO layer on flat glass the material prerequisites are, low resistance, high transmission in the visible and near infrared region, and a surface texture that leads to effective light trapping in the silicon absorber layers. Aluminum doped zinc oxide

1 Introduction

(ZnO:Al) films have proved to be such material. The wide band gap of ZnO (3.4 eV) makes it transparent in the visible range. By degenerate doping, it can be made nearly as conductive as a metal. The electrical and optical properties of doped ZnO films have to be balanced carefully, as the high doping level which is required for high conductivity decreases the transparency of ZnO films due to high free-carrier absorption. Highly transparent and conductive ZnO:Al films have been deposited by magnetron sputtering with both low and high growth rates [5, 6]. To achieve the textured interface, the ZnO:Al films are typically textured in wet chemicals, as sputtered ZnO:Al films are usually flat. Ideally, the ZnO:Al film sputtering and silicon, as well as the back contact deposition, would be performed in an in-line process system. However, currently the vacuum has to be broken for wet chemical etching. This leads to further energy demand for cooling and heating cycles, as well as, additional vacuum equipment usage. The solution for solving the above problem in order to further decrease the production cost is as-grown textured ZnO films. A few methods have already shown this capability, including, asgrown textured ZnO by low pressure or metal-organic chemical vapor deposition [7, 8] or as-grown textured by sputtering at high pressure or with water vapor [9–14]. However, none of these yet has taken the way to full vacuum in-line production systems. In this work, it is found that ZnO: Al films grown on ion beam pretreated glass substrates exhibit self-textured morphology while still keeping high conductivity. The nucleation of ZnO thin film is very sensitive to the underlying substrate. Thus, by modifying the substrate by ion beam treatment, the ZnO:Al films can be tuned in such a way that the surface is dominated by large pyramids.

Additionally, textured glass on millimeter scale are very common in decorative glass. However, to be used in photovoltaics, the patterns in the textured glass should be in the wavelength range of visible and near infrared light. Textured glass with periodical or random patterns in this range has been developed by glass casting operation [15], aluminum induced texture (AIT) process [16], sandblasting, lithography, and wet chemical etching by hydrofluoric acid [17]. However, textured glass is difficult or expensive to prepare and optimized solar cells have only previously been prepared only on textured TCO films. In this work, another promising method for transferring structures of three dimensional masks to glass is presented. The dry etching masks can be prepared by self-organizing patterned films or nano-particles. If the wet chemically etched ZnO:Al films are used as the etching mask, textured glass with features similar to sputtered and wet chemically etched ZnO films can be prepared.

The afore-mentioned methods have a common aspect: the ion beam processing is utilized during production to improve solar cells. The ion beam technologies have been developed rapidly since the middle of the last century. The energetic ions can be used to remove and modify the film surface or influence the growth of thin film [18]. Parameters of an ion beam, species, energy, flux, charge state, and divergence are all easily quantified and controlled [18]. However, application of ion beam technologies is rare in the field of thin-film photovoltaics. In this work, the ion beam processing technology will be applied on glass substrate and ZnO:Al films during the preparation of thin-film solar cells. The influences of the ion beam treatment on the glass substrate and ZnO:Al films on solar cells will be thoroughly discussed. The main focus of this work will be on the

study and understanding of as-grown textured ZnO:Al films on ion beam pretreated glass substrates and the preparation and application of textured glass.

The following chapter reviews the relevant physics upon which this work is based. A short discussion of ion beam generation and ion-solid interactions will first be given, followed by the basic properties of ZnO thin films and Si thin-film solar cells. In Chapter 3, the ion beam treatment and film deposition systems will be briefly introduced. The underlying principles and experimental process of various characterization techniques used in this work will be presented.

The results of new experiments begin in Chapter 4. First, the ion beam treatments are characterized by static and dynamic etch rates on glass substrates and ZnO thin films. The experimental etch rates are compared with simulated and theoretically predicted values. Chapter 5 examines the effects of ion beam treatment of glass substrate on the growth of ZnO:Al films. The electrical and optical properties of ZnO:Al films on ion beam pretreated glass are investigated. Single junction amorphous Si thin-film solar cells deposited on these ZnO:Al films exhibit efficiency of 9.4%. To better understand the influence of ion beam pretreatment on ZnO:Al growth, the crystallographic structure of ZnO:Al films is studied, and the chemical bond structures of ion beam treated glass surface are investigated. Finally, a comprehensive growth model is developed. Chapter 6 shows that the ZnO:Al surfaces can be modified by ion beam treatment, leading to different HCl etching, or growth of ZnO:Al or Si. Chapter 6 further presents the fabrication and application of textured glass in solar cells. The textured glass can be obtained by ion beam etching of wet chemical etched ZnO:Al films. A short summary and outlook for further work are provided in Chapter 7.

2 Fundamentals

This chapter is intended to introduce and explain the theory and background upon which this work is based on. First, the fundamentals of ion beam treatment are introduced. The configuration of ion source, as well as, the mechanism of ion generation and the ion-solid interaction are discussed. Then, a short overview of current understanding of the physics and technologies of transparent conducting oxide (TCO) are given. With many types of TCO films, the motivation of using ZnO:Al films in thin-film silicon solar cells are discussed. The electrical, optical and growth properties of ZnO:Al films are then introduced. At the end of this chapter, the basics of silicon thin-film solar cells with ZnO:Al films as front contacts are discussed. The operating principle and characterization methods of solar cells are presented.

2.1 Ion beam treatment

Ion beam is a directed flux of ions with certain energies in vacuum. Ion beams have been widely used in various fields and for numerous applications, including implantation, etching and ion beam assisted deposition. In this work, ion beams are used for etching and surface modification. The generation and applications for ions beams are briefly introduced in the section.

2.1.1 Ion source

An ion source is a type of plasma source from which one can extract ions in order to form a beam. The source gas will define the type of ions, while the plasma generation and extraction system will determine the parameters of the ion beam. A typical ion source system consist of three parts, ions generation, acceleration, and extraction system. Typically, the ions are generated in the following way: first, a filament is heated by alternating or direct current. The electrons emitted by the hot filament are then accelerated towards a wall by applying high voltage. Supposing the volume is filled with an appropriate gas, then the gas atoms are ionized by the collisions with electrons. Thus, a plasma containing ions and electrons is ignited. The electrons are then separated from the ions by applying negative voltage on a grid [19]. The drawback of this traditional structure is that the hot filament and sensitive grid increases the maintenance difficulty. In the middle of last century, most ion sources were based on the filament heated principle. Then in the 60ies, inductively coupled ion sources were introduced, identified by the coil with a small number of windings driven by radio frequency and an isolating (quartz) vessel. Later on microwaves were used for ionization, providing

2 Fundamentals

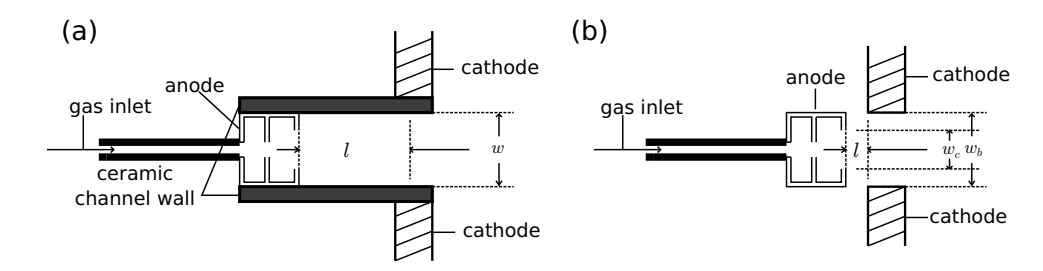


Figure 2.1: Schematic diagrams of the discharge zone in close drift ion sources/thrusters, in which (a) is the magnetic layer type and (b) is the anode layer type.

high ionization density and low electron temperature [19]. In the nineties, more simple and robust ion sources without filament and grid appeared in the thin-film industry, for example end-hall or close-drift ion sources. The concepts come from the ion thrusters used in the spacecraft, which have attracted more interest and obtained pronounced progress [20]. The ion source used in this work belongs to the type of close-drift. The word 'close-drift' relates to the circular movement of electrons. Generally there are two types of ion source in the category of close-drift ion thrusters [21]: (1) ion sources with extended acceleration zone, which are also called magnetic layer ion sources, and (2) ion sources with short acceleration zone, which are also called anode layer ion sources. The former is characterized by a ceramic discharge channel wall, while the latter is identified by a conductive channel wall. The schematic diagram of the two ion sources are shown in Fig. 2.1 and their working principles are discussed in the following paragraphs.

Both types of the ion sources have a gas inlet, an anode, and two cathodes. Voltages up to several kV are applied to the anodes while their outer and inner cathodes are grounded. Thus, an electric field is formed between anode and cathode, and electrons are accelerated from cathode to anode. The volume between cathode and anode is the discharge zone, where the positive ions flow from anode to cathode. The differences between the two types of ion source are also drawn in the Fig. 2.1. Magnetic layer ion sources have ceramic discharge channel walls in addition to the anode and cathode. When the electrons and ions are moving in the channel, a fraction of them collide with the ceramic walls, generating low energy secondary electrons. These secondary electrons tend to keep the temperature of electrons low in the plasma. Thus, the discharge zone is extended further by the lower temperature of electrons, resulting in a longer discharge length l than width w [20]. In the anode layer type ion sources, there is no ceramic channel wall to lower the temperature of electrons. The electrons flowing from the cathode to the anode increase in temperature which results in a sharp increase in plasma potential as the anode is approached, so a large fraction of the ion generation and acceleration take place in a thin layer near the anode, which is the origin of the name 'anode layer' [20]. The walls of the discharge channel might be considered the inner and outer cathodes, so that the channel width, w_b , is the width between these cathodes. The discharge length l between the cathode and anode is short, as compared with its width

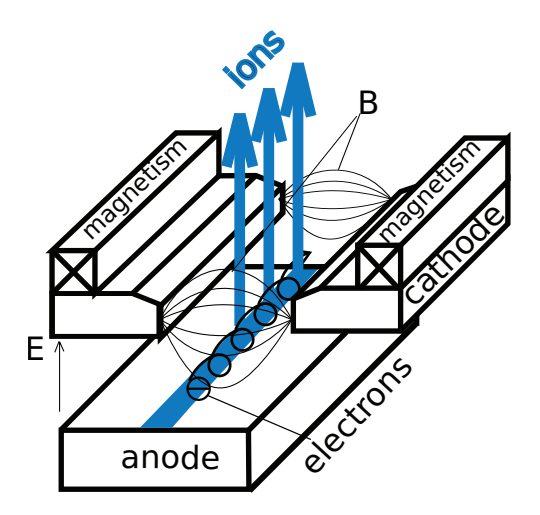


Figure 2.2: Magnetic and electric field in the discharge zone of anode layer ion source.

The electrons gyrate around the magnetic line, while the ions are accelerated and shot from the slit between the cathodes.

 w_b . The erosion of these cathodes is minimized by confining most of the accelerated beam of ions to a narrower beam width, as shown by the width, w_c , in Fig. 2.1(b) [20].

The principle of an anode layer ion source is shown in Fig. 2.2. A radial magnetic field (B) which is perpendicular to the electric field (E) is induced by magnetic windings or permanent magnets. The magnetic field induces a Lorentz force on the electrons, forcing the electrons onto a circular path perpendicular to the magnetic field lines, i.e. the electrons gyrate around the magnetic field lines. With the confined mobility, the electrons often collide with the gas atoms or molecules which flow into the discharge zone through a gas inlet pipe. Ions and more electrons are then generated. The discharge channel is self contained because of magnetically enhanced electron density, so the filament is not required for this function. Part of the newly generated electrons provide neutralization to the ions in the plasma. The huge mass of ions are primarily influenced by the electric field, hence they do not drift like electrons, but are accelerated from the source and then shot from the slit between the inner and outer cathodes. After the ion beam has left the ion source, the electrons leaked from the cathodes and secondary electrons from the environment provide neutralization to the ion beam, thus the ion source does not need additional compensations. In the anode layer ion source, the generation and acceleration of ions are simultaneous. The magnetic layer type of close drift ion sources with extended acceleration zone is favorable in space due to their higher energy efficiency. However, the anode layer sources are preferred in the industry application due to its simper design. Moreover, as compared with magnetic layer ion sources, the anode layer sources suffer less from cathode erosion, and therefore have a longer lifetime. Several companies have applied the anode layer ion source in the field of thin-film and nano-technologies.

2 Fundamentals

When pure Ar is used as source gas, depending on the energy of electrons, the following collisions may occur between the electrons and Ar gas atoms:

- electron impact ionization: Ar + e⁻ → Ar⁺ + 2e⁻, E_{th} = 15.8 eV
 Electrons with sufficient energy can remove one electron of Ar atom and produce one extra electron and ion. The extra electron can again be accelerated to gain enough energy and ionize another atom. Through this mechanism, it is possible to maintain a continuous plasma. The threshold energy E_{th} to remove one electron from Ar is 15.8 eV.
- electron impact exitation: $Ar + e^- \rightarrow Ar^* + e^-$ Electrons with sufficient energy can also excite the electrons of Ar atoms from low energy level to a high energy level. This process produce excited neutral atoms whose chemical reactivity towards the surface could be quite different from the ground state atoms [22]. The excited Ar* atoms are called metastables [22].
- electron metastable ionization: $Ar^* + e^- \rightarrow Ar^+ + 2e^-$ Electrons with sufficient energy can remove the excited electrons in metastables and produce one extra electron and ion. Since the metastable is already excited, less energy is required for this ionization process.

When pure O_2 is used as source gas, the processes between electrons and O_2 molecules are more complex than Ar, since the dissociation of diatomic oxygen molecules occurs as well as ionization.

- electron impact dissociation: $O_2 + e^- \rightarrow O + O + e^-$, $E_{th} = 5.1 \text{ eV}$ Electrons with sufficient energy can break the chemical bond of an O_2 molecule and produce atoms.
- electron impact exitation: O₂ + e⁻ → O₂* + e⁻
 Similar as the process as Ar*, electrons with sufficient energy can excite the electrons of O₂ molecule from ground state to excited state. Depending on the excited state, the threshold energy of the excitations varies in the range of 0 − 10 eV.
- electron impact ionization: $O_2 + e^- \rightarrow O_2^+ + 2e^-$, $E_{th} = 12.2 \text{ eV}$ [22] This is very similar to the process produce Ar^+ ions. The threshold energy to remove one electron of O_2 is 12.2 eV.

Beside the above basic processes, following reactions also exist in oxygen plasma The channels to generate ions are listed in the following with their threshold energies, respectively.

•
$$O_2 + e^- \rightarrow O^+ + O + 2e^-$$
, $E_{th} = 18 \text{ eV} [23]$

•
$$O_2 + e^- \rightarrow O_2^{2+} + 3e^-$$
, $E_{th} = 24.1 \text{ eV} [24]$

•
$$O_2 + e^- \rightarrow O_2^{2+} + 3e^- \rightarrow O + O^{2+} + 3e^-$$
, $E_{th} = 52.7 \text{ eV}$ [24]

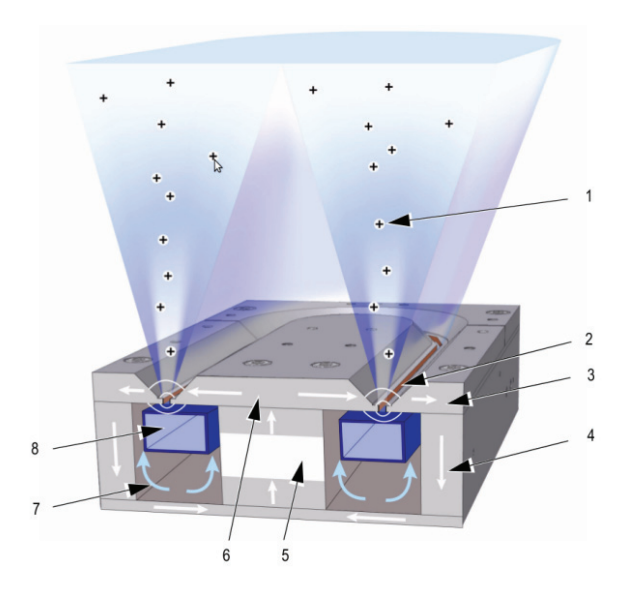


Figure 2.3: Configuration of linear anode layer ion source (Type LION 420, VON AR-DENNE Anlagentechnik GmbH [30]). 1. ionized gas, 2. racetrack, 3. Outer cathode, 4. Water-cooled magnetic package, 5. Magnetic system from permanent magnetism, 6. Inner cathode, 7. Gas, 8. Water-cooled anode.

•
$$O_2 + e^- \rightarrow O_2^{3+} + 4e^- \rightarrow O^+ + O^{2+} + 4e^-, E_{th} = 63 \text{ eV} [23]$$

When mixed Ar/O₂ is used as source gas, additional processes between Ar atoms and O₂ molecule, for example $Ar^* + O_2 \rightarrow Ar + O + O$, may occur. Therefore, the fraction of O atoms with respect to O₂ molecules might be enhanced [25].

To summarize, the majority of particles in Ar ion beams are neutral Ar* and Ar⁺ ions, but excited Ar^{+*} and double ionized Ar²⁺ ions might also exist. The O_2 ion beams are composed of mixture of neutral and ionized particles O_2^* , O^* , O_2^+ , O^+ , O_2^{2+} and O^{2+} . The electron impact ionization cross sections of the above mentioned ions were measured experimentally or calculated in detail by many groups [26–29]. The results reveal that the cross sections have the relationship $\sigma_{O_2^+} > \sigma_{O^+,O_2^{2+}} > \sigma_{O^{2+}}$. Therefore, the fraction of O_2^+ should be highest among the various of ions.

The shape of the permanent magnet has to be specially constructed in order to provide the appropriate distribution of magnetic field. The paths of electrons have to be without obstacles, as well as with high uniformity. Usually, they are maintained with an axis-symmetric construction such as circular ion source. Non-circular sources, for example, the elongated racetrack structure which is also called linear ion source is also possible with careful design. Moreover, the linear anode layer ion source has nearly unlimited scalability for industrial purposes [31], therefore it has become a popular source in recent years for large area thin-film or glass treatment. The linear anode layer ion source used

in this work was supplied by VON ARDENNE Anlagentechnik GmbH (Type LION 420). The configuration of this ion source is shown in Fig. 2.3. It consists of a water-cooled anode and permanent magnet, inner and outer cathodes, and gas inlet system. The inner and outer cathodes are made of iron and are grounded, thus the discharge wall is conducting. The gases flow into the ion source near the anode and leave as ions through the slit between the inner and outer cathode. With the essentially perpendicular magnetic field and electric field, electrons move along the racetrack and produce a strong drift current along the way.

The physical parameters for characterizing an ion beam mainly include ion energy, ion energy distribution, ion current, charge number, beam diameter, and lateral current density distribution. All of the above parameters depend on the configuration of the ion source, as well as the working parameters. Depending on the pressure and gas flow rate, the ion source can work in collimated or diffused beam modes. The collimated beam is characterized by high energy and low density, while the diffused beam is characterized by low energy and high density having a plasma-cloud shape. The two types of beams can be distinguished by the naked eye. In the collimated beam, the ion current density J_i is limited by the space charge law (Child-Langmuir Law):

$$J_i = K \frac{V_d^{3/2}}{d^2},\tag{2.1}$$

where K is a constant related to charge to mass ratio of the particle, V_d is the plasma potential which is the discharge voltage applied to the anode, and d is length of the plasma. Thus, the ion current increases with the discharge voltage. By increasing the gas flow or working pressure, the ion source can be switched to diffuse-beam mode. The high pressure increases the impact between the ion and gas collision, leading to a loss of ion energy. At some point, the energy of ions is so low that they do not come out between the slit at the cathode, but form a pseudo-neutral plasma together with the neutralized electrons. Therefore, the ion current is no longer limited by the space charge law. The discharge current of the ion source in diffuse mode can be much higher than in collimated mode. However, in the diffuse mode, the ions are not well confined to a particular width and thus the erosion of cathode is increased, resulting in higher contamination of the treated samples.

For a linear anode layer ion source, the average energy of ions in electronvolt (eV) is approximately half that of the discharge voltage in volts (V) [32]. A typical energy distribution of an oxygen ion beam from a linear anode layer ion source is shown in Fig. 2.4. In general, ion beam current is proportional to ion density and the temperature of the electrons [19]. In collimated mode, the ion beam current is approximately equal to 80-90% of discharge current [33].

On the way from ion source to the substrate, the ions collide with the background gas and lose energy. The mean free path of collision which is defined as the average distance an ion travels before a collision, is inversely proportional to the charge exchange cross-section and density of background atoms. Therefore, high vacuum conditions ($< 2 \times 10^{-3}$ mbar) are required to minimize the energy loss of ions.

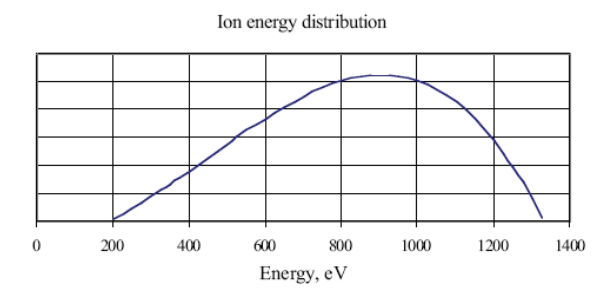


Figure 2.4: Energy distribution of oxygen ions at 5 sccm oxygen gas flow into a linear anode layer ion source (type: LIS-65, Advanced Energy Industries) at discharge voltage of 1500 V, and gas pressure in vacuum chamber is 0.21 mTorr [32].

2.1.2 Ion-sample interaction

In the last century, the interaction between ions and sample has been investigated thoroughly. More detailed theoretical overviews of the topic can be found in the recent monographs [34, 35]. This section briefly discusses physical backgrounds of the interactions between ions and treated samples. The kinetic energy of moving ions is dissipated via elastic (nuclear excitation) and inelastic collisions (electronic excitation). In electronic collisions, the energy of incident ions or knock-on atoms are transferred to 'bound' electrons, leading to emission of Auger electrons, X-rays, or photons. The electronic excitations can cause the trapping of charge at defects, as well as local changes in bonding and free energy; these can lead to permanent bond breakage and the formation of defects in the atomic structure.

In nuclear collisions, an incident ion collides with a sample nucleus, and the energy is exchanged via momentum transfer. The energy might dissipate as heat if it is lower than displacement energy of the atom on the sample. If the energy exceeds the displacement energy of the atom on the sample, the primary knock-on atom is created, leaving a vacancy behind. The primary knock-on atom might receive enough energy to displace other atoms in the sample. The result is a collision cascade, which is also called an atomic displacement cascade. Eventually, a large number of atoms within the sample can be set in motion. This can lead to a distribution of vacancies, interstitial atoms, mixing of layers in the vicinity of interfaces, or lattice disorder in the region around the ion bombardment position. It seems that the defects are not desired in the sample material. However, in recent years, the re-organization of surface atoms by ion beam incident can be used to modify surface structures in a controllable way. For example, off-normal ion bombardment of amorphous substrate often produces periodic ripples structures [36, 37]. Ion beams were also used to tailor the properties of carbon nanotubes [38]. If the incident ions are incorporated into the sample, the process is considered as ion implantation. If materials from the treated sample are emitted from its surface due to ion bombardment,

the process is then called sputtering, which is a main focus of this work. Sputtering is an important mechanism for the use of ion beam in nano-technology. The sputtering of the sample materials by ion bombardment is often called as ion beam milling or etching, which is a typical dry etching method and often used to remove layers or build 2- or 3-dimensional structures with the help of etching masks. The sputtering yield is defined as the average number of total sputtered atoms per incident ion. In the following, the sputtering yields are analyzed based on a number of collision theories.

2.1.2.1 Sputtering yield

A number of moved recoils in the collision cascade are produced during the nuclear collisions. Recoils that reach the surface with energy exceeding the surface binding energy will leave the sample surface. It is conceivable that the sputtering yield is dependent on the properties of both the incident ions and the treated samples, however quantitative theories are required to describe the direct relationships between the yield and the ion beam etching parameters. The sputtering yield was predicted by linear cascade theory developed by Sigmund *et al.* [39, 40]. With this approach, sputtering yield is proportional to the energy deposited in elastic collisions at the surface, $F_D(E_i, \theta, x = 0)$

$$Y = \wedge F_D(E_i, \theta, 0). \tag{2.2}$$

In the equation, \wedge is a material dependent parameter, which depends on the angle, depth, and energy averaged probability of a target atom escaping from the surface [41]. \wedge is inversely proportional to the surface binding energy, U_s (usually taken as the sublimation energy). $F_D(E_i, \theta, x)$ is the energy transferred by the bombarding ion with energy E_i and incident angle θ relative to surface normal in low-energy recoils in the depth interval (x, x + dx). $F_D(E_i, \theta, 0)$ is linearly proportional to the nuclear stopping cross section $S_n(E_i)$ and equation 2.2 can be written as

$$Y = \frac{3}{4\pi^2 C_0} \frac{\alpha S_n(E_i)}{U_s} f(\theta) = 0.042 \frac{\alpha S_n(E_i)}{U_s} f(\theta).$$
 (2.3)

Here, C_0 is a constant appearing in the power approximation of the scatting cross-section. α is a dimensionless function of the incident angle θ , the atomic mass of incident ion (M_1) and sample atom (M_2) . With normal incidence, absolute values of α at different mass ratios were given by Sigmund et~al. and can also be fitted from experimental sputtering yields. For $M_2/M_1 \leq 0.5$, α is nearly constant (\sim 0.2), but rises strongly with an increase of M_2/M_1 above 0.5. Approximation for α in the range of $0.5 \leq M_2/M_1 \leq 10$ can be written as

$$\alpha = 0.3(M_2/M_1)^{2/3}. (2.4)$$

The stopping cross section $S_n(E_i)$ of nuclear collision has often been expressed by simple analytical expressions as a function of reduced energy $\varepsilon = \frac{E_i}{E_{it}}$, where E_{it} is a scaling constant depending only on the ion and substrate masses M_1, M_2 and atomic

numbers Z_1, Z_2 , given by

$$E_{it} = \frac{1}{32.5} \left(1 + \frac{M_1}{M_2}\right) Z_1 Z_2 (Z_1^{2/3} + Z_2^{2/3})^{1/2} [keV]. \tag{2.5}$$

 $S_n(\varepsilon)$ was reliably estimated by Wilson et al. as [42]

$$S_n(\varepsilon) = \frac{1}{2} \frac{ln(1+\varepsilon)}{\varepsilon + 0.107\varepsilon^{0.375}}.$$
 (2.6)

Finally, $f(\theta)$ in equation 2.3 describes the sputtering yield dependence of incident angle. The yield increases with larger incident angle because of the higher energy transfer in the vicinity of the surface. For not too oblique incidence, $f(\theta)$ is approximated as

$$f(\theta) = (\cos\theta)^{-b},\tag{2.7}$$

where b is a function of M_2/M_1 . For $M_2/M_1 > 5$, $b \sim 1$, thus the dependence is roughly $1/\cos\theta$. For $M_2/M_1 < 3$, $b \sim 5/3$. At large values of θ (approaching 90°), the scattering and reflection of incident beams increases, leading to rapidly decrease of sputtering yield. The linear cascade theory is valid for many regularly sputtering behavior of amorphous or polycrystalline elemental targets bombarded with atomic ions.

Note that the linear cascade theory as well as angle dependence of sputtering yield discussed above is only applicable for ion energies in the keV range. For ions with lower energies ($E_i < 1 {\rm keV}$) and/or very light ions (e.g. H, D, He), the sputtering is predominately due to primary recoils. The collisions may only involve a small number of atoms and a collision cascade does not develop. The number of collisions between the first ion-sample interaction and the final ejection collisions should be small, indicating that reflective scattering collisions near the sample surface contribute predominately to sputtering. The process in this regime is often called as direct knock-on collisions and does not fulfill the linear cascade theory. In this regime, the sputtering yield is expressed as

$$Y \cong \frac{3}{4\pi^2} \alpha \frac{\gamma E_i}{U_s} \quad \text{for} \quad E_i > E_{th}, \tag{2.8}$$

where γ is the maximum energy transfer between ions and sample atoms in a knock-on collision and is written as

$$\gamma = 4M_1 M_2 / (M_1 + M_2)^2. \tag{2.9}$$

The threshold energy for sputtering E_{th} can be estimated as

$$E_{th} = \frac{U_s}{\gamma(1-\gamma)}. (2.10)$$

Zalm et al. [43] derived a sputtering yield from the simplified expression of stopping power in equation 2.6 for the region $0.2 < Z_2/Z_1 < 5$:

$$Y = \frac{1.9}{U_0} \left(\frac{Z_2}{f}\right)^{1/2} \left(E_p^{1/2} - 0.09U_0^{1/2}\right),\tag{2.11}$$

where $f = \frac{1}{2}[(Z_1/Z_2)^{2/3} + (Z_2/Z_1)^{2/3}]$ is a slowly varying function of Z_2/Z_1 . The sputtering yield is almost independent of the choice of the projectile and the accuracy is within 10 %.

The angle dependence of sputtering yield given in equation 2.7 cannot describe the direct knock-on collisions [44], because of a strong influence of the target material by the difference in threshold energies. Oechsner *et al.* fitted *b* by etching of a series of elemental targets with 1.05 keV Ar⁺ [45]. The results show a large deviation between experimentally fitted *b* and theoretical predications. The incremental sputtering yield $\Delta Y(\theta)$ between the yield $Y(\theta)$ at incident angle θ and Y(0) at normal incidence is found to be inversely proportional to the surface binding energy U_s [46], as

$$\triangle Y(\theta) = Y(\theta) - Y(0) = c \frac{\sigma_1 \gamma}{d^2 U_s} F(\theta/\theta_{max}), \qquad (2.12)$$

where σ_1 is the atomic hard sphere collision cross sections for the first interaction between an ion and a sample atom, d is the average distance between atoms in the sample, and $F(\theta/\theta_{max})$ is a uniform function of the reduced angle θ/θ_{max} , where θ_{max} is the bombarding angle for maximum sputtering yield. It was reported that $F(\theta/\theta_{max})$ varies approximately as $(\theta/\theta_{max})^2$ for bombarding angle up to 50°. Additionally, Bay et al. reported that the light ions in low keV range often lead to yield increase more pronounced than $cos(\theta)^{-1}$ [44].

On the other hand, if the incident ions have very high energy and large mass, the density of recoil atoms within the cascade is so high that collisions between moving atoms become frequent, and then the linear collision cascade assumption breaks down and a non-linear cascade regime is reached. Since the ions in this work do not reach such high energies, the sputtering yield in this regime is not discussed.

2.1.2.2 Reactive or molecular ions and compound substrates

The situation becomes more complicated when the incoming ion can react chemically with the treated sample surface. The formation of a volatile compound can enhance the removal of treated sample and hence the sputtering yield. For example, bombardment of Si with F or Cl ions can remove the materials much more rapidly, than similar mass noble gas ions like Ar. Conversely, if an involatile compound forms, such as O and Si leading to SiO or O and Zn leading to ZnO, the sputtering yield is generally reduced. As a rough approximation, the total sputtering yield is reduced to -b/(a+b) of physical sputtering yield if involatile compound T_aI_b is produced by ions I on substrate T [18].

For molecular ions, at energies above a few hundred eV, the total sputtering yields are generally higher than those for comparable mass noble gas ion sputtering, which results from the probably overlapping of collision cascade initialed simultaneously by individual atoms [18]. It was reported that a molecular enhancement factor Y_{mol}/nY_{atom} , where n is the number of atoms of the bombarding molecule is 10 for 90 keV Sb₃ incident on Ag [47, 48].

If the substrates are composed of more than one element, for example metal alloys and oxides, the sputtering yield of the elements in the compound might be different,

depending on the stopping power of each element. Thus, preferential sputtering is generally observed for ion beam etching of multi-component compound and alloys, resulting in compositional changes at surface [34]. Simultaneously, the region far beyond the topmost surface layer is influenced by preferential sputtering. The linear cascade theory can be extended and detail analysis on sputtering of multi-component substrate can be found in [34]. Preferential sputtering of metal oxides by bombardment with 1-5 keVinert and reactive ions have been widely studied both experimentally and theoretically [49–53]. Preferred sputtering of O was observed clearly on some oxides, for example, Ta_2O_5 and MoO_3 . According to Sigmund's linear collision theory, the loss of O is related to the mass and surface binding energy ratio of the metal atoms [50]. Specifically for Al₂O₃ and ZnO, which are interested in this work, it was reported that no obvious changes in the surface composition were observed by Ar⁺ etching [49–51]. Recent report showed that ZnO (0001) surface was not influenced, while ZnO (000-1) surface exhibited some O deficiency for low energy Ar⁺ bombardment [54]. As for SiO₂, which is the main component in a glass substrate, the experimental observations were not the same due to different analysis techniques and methods. Most reports show that no or only slightly O loss happened by Ar^+ etching [50, 53].

2.2 Transparent conducting oxide

Transparent conducting oxides (TCOs) are doped metal oxides used in many optoelectronic devices such as flat panel displays and photovoltaics. TCOs play important roles in Si thin-film solar cells as a source of light scattering and current conduction. The requirements of TCOs in Si thin-film solar cells are the following: high conductivity to avoid ohmic losses, high transmission in the active range of the absorber layer, and morphologies favorable for light scattering and Si deposition. To date, typical candidates to be applied in Si thin-film solar cells are tin doped indium oxide (In₂O₃:Sn), fluorine doped tin oxide (SnO₂:F) and aluminum or boron doped zinc oxide (ZnO:Al or ZnO:B) films. In₂O₃:Sn films have been widely applied as transparent electrodes over the past decades. In₂O₃:Sn films with high transparency and conductivity are commercially available, however, it is difficult to achieve rough morphology for light scattering. Moreover, the scarcity of In in nature yields a high price, which is not favorable for thin-film solar cells. SnO₂:F films have been successfully applied in amorphous Si solar cells. However, due to the chemical reduction of SnO₂:F to metallic Sn in hydrogen containing plasmas present during the chemical vapor deposition of microcrystalline Si, the transmission of SnO₂:F films decreases. This effect makes uncoated SnO₂:F unsuited as substrate for single junction microcrystalline Si solar cells.

Doped ZnO films have been considered as a promising material of front contacts in solar cells. As compared with In, Zn has 400 times higher abundance in earth crust. ZnO films offer excellent transparency in the visible range and are highly resistant to hydrogen plasmas. With sufficient doping, the films show low sheet resistance and can be used to transport current generated in the Si absorber layer. Magnetron sputtering is widely used to deposit thin-films due to its high deposition rate and the possibility of adaption to

large area. One of the focuses of this work is improving the magnetron sputtered ZnO:Al films through ion beam treatments of the glass substrates. The physical properties and growth of ZnO:Al films by magnetron sputtering are summarized in the following sections.

2.2.1 ZnO structure

ZnO belongs to II-VI binary compound semiconductors with hexagonal wurtzite structure as shown in Fig. 2.5. Each zinc atom is surrounded by four oxygen at the corners of a tetrahedron, and vice versa. As shown by the left figure, the structure is composed of two interpenetrating hexagonal-close-packed (hcp) sublattices, each of which consists of one type of atom displaced with respect to each other along the c-axis. Thus the stacking sequence of (0001) plane is $AaBbAaBb\cdots$. Due to the absence of inversion symmetry, the ZnO crystal exhibits polarity. This means that there is a direction of the c-axis and the (0001) and (000-1) planes are different. When the bonds along the c-axis are from Zn to O, the polarity is referred to as Zn termination. On the other side, when the bonds along the c-axis are from O to Zn, the polarity is referred to as O termination. Zn and O terminated surfaces are marked by (0001) and (000-1) planes which are perpendicular to c-axis. Many properties of the ZnO material depend on the polarity, for example, growth, etching, and piezoelectricity. Besides the primary basal (0001) plane and associated direction (0001), which are the most commonly used surface and direction for growth, many other planes and growth directions exist. At room temperature the lattice parameters in the wurtzite are a = 0.325 nm, c = 0.52066 nm [55]. Besides the wurtzite structure, rocksalt structure has also been observed. The wurtzite is thermodynamically stable at ambient conditions, while the rocksalt structure is obtained only under relatively high pressure [56].

The melting points of Zn metal and ZnO compound are 419.6 °C and 1975 °C, respectively. Above 200 °C, Zn is no longer stable anymore, and tends to absorb O_2 to form ZnO. The thermal expansion along the a and c directions (see Fig. 2.5) are linearly dependent on temperature, as long as T is above 300 K [57]. The density of ZnO is 5.6 g/cm^3 [58].

2.2.2 Electrical properties

Low resistivity is required for ZnO films used in TCO applications. In order to understand the meaning of resistivity, the transport of electrons is first introduced. Suppose a group of electrons with density of n_s flows in a electrical field E. The drift current density is

$$\overrightarrow{J} = n_s q \overrightarrow{v}, \tag{2.13}$$

where \overrightarrow{v} is the drift velocity of the electrons and q is the electrical charge.

The drift velocity of electrons is proportional to the applied electrical field, i.e.

$$\overrightarrow{v} = \mu \overrightarrow{E}. \tag{2.14}$$

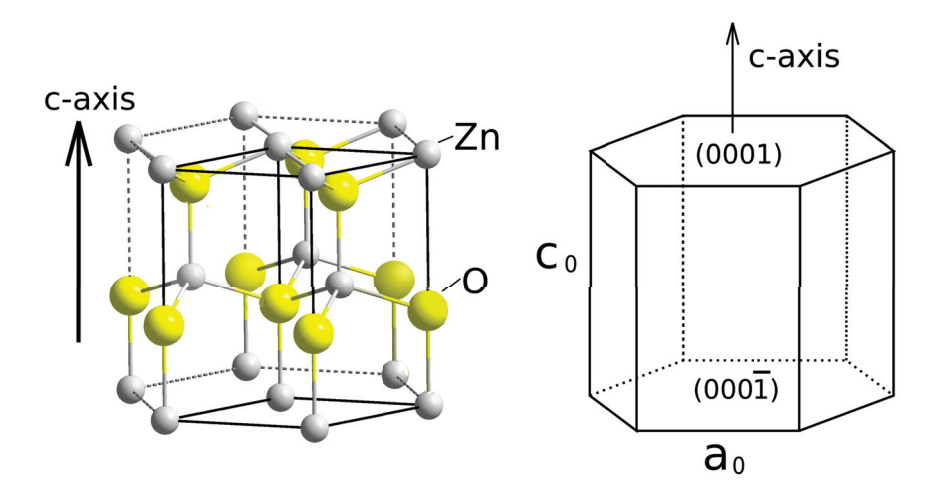


Figure 2.5: Wurtzite structure of ZnO crystal.

In this equation, mobility μ is defined as the ratio between the electrical field and the electron drift velocity.

A common approximation for the current density assumes that the current density is simply proportional to the electrical field, as expressed by:

$$\overrightarrow{J} = \sigma \overrightarrow{E}. \tag{2.15}$$

For intrinsic semiconductors, the conductivity is expressed as

$$\sigma = n_s q \mu_n + p_s q \mu_n, \tag{2.16}$$

where n_s and μ_n , and p_s and μ_n are the carrier density and mobility for electrons and holes, respectively.

For materials with electrons as primary carriers for electrical transport, for example metals and n-type semiconductors, the above equation is written as

$$\sigma = n_s q\mu. \tag{2.17}$$

The resistivity of the material is defined as the reciprocal of conductivity

$$\rho = \frac{1}{\sigma} = \frac{1}{n_s q \mu}.\tag{2.18}$$

The mobility of transport carriers in semiconductors can also be written as

$$\mu = \frac{q\tau_c}{m^*},\tag{2.19}$$

where m^* is the effective mass of the particle and τ_c is the time between scattering events. Therefore, if the mass of a particle is small and the time between scattering is large, the mobility of the carrier will be higher. Greater effective mass of holes is the reason why they have lower mobility than electrons. The mobilities of transport carriers are mainly limited by scattering events in the lattice or defects.

Generally, for an intrinsic semiconductor, the Fermi level is in the middle of valence band and conduction band. By n- or p-type doping, the Fermi level shifts toward the conduction or valence band, respectively. ZnO is a II-VI semiconductor with direct band gap of $3.2-3.4~\rm eV$. Photoelectron microscopy showed that the Fermi level position is approximately 2.8 eV higher on the valence band maximum for an undoped ZnO thin film [57]. Thus, the Fermi level in undoped ZnO is close to conduction band, indicating that the non-intentionally doped ZnO is an n-type semiconductor.

Non-intentionally doped ZnO films are conducting because of deviations from stoichiometry. Zinc interstitial and oxygen vacancy are generally considered to be the intrinsic shallow donors that cause n-type conductivity [59, 60]. Annealing of ZnO crystals in an oxygen atmosphere produce crystals with higher resistivity. On the other hand, annealing in a hydrogen atmosphere or zinc vapor produce more conductive crystals. The carrier concentration, Hall mobility, and resistivity for undoped ZnO crystals are around 10^{15} cm⁻³, 200 - 225 cm²/Vs and 1 - 10 Ω cm, respectively [61–64]. The shallow donors can be compensated by acceptors, for example, the resistivity of ZnO can be increased to 10^{12} Ω cm by annealing in a Li₂CO₃ melt [65]. For an undoped ZnO polycrystalline thin film, the resistivity is very high: on the order of 1500 Ω cm perpendicular to and > 10^{9} Ω cm parallel to the substrate [66]. Therefore, the conductivity of intrinsic ZnO thin film is not high enough for TCO applications. Extrinsic doping atoms have to be added in order to improve the conductivity.

Using extrinsic dopants, ZnO can easily be n-type doped, while p-type doping remains difficult. B, Al, In and Ga are the commonly used n-type dopants for ZnO, improving the conductivity of ZnO by orders of magnitude. It is assumed that the dopant atoms are built into the Zn lattice sites, providing additional electrons. The carrier concentration increases with the doping level. Equation 2.18 shows that increasing the mobility or carrier concentration decreases the resistivity. However, when the carrier concentration is above 10¹⁷ cm⁻³, the Hall mobility start to decreases continuously. This is caused by ionized impurity scattering. The highest reported carrier concentration for a doped ZnO crystal is 7×10^{19} cm⁻³ [67]. The Hall mobility is decreased to around 50 cm²/Vs [67]. For polycrystalline ZnO thin films, the highest reported carrier concentration is 1.5×10^{21} cm⁻³. Higher carrier concentrations are not possible due to a limited solubility of the donor substance in ZnO. The Fermi level of heavily doped ZnO thin films shifts into the conduction band, resulting in so called degenerate semiconductors. The shift of Fermi level has been predicted by many theories and also been measured experimentally. Heavily doped ZnO thin film behave more like a metal than like a semiconductor. The scattering of electrons in the material is the main limit for the high mobility. Various scattering mechanisms are listed in the following for doped ZnO polycrystalline thin films.

- Phonon scattering: Phonon scattering refers to the scattering of transport carriers by vibrations in the crystal lattice. The electrons interact with the electrical field induced by optical phonons. As compared with the mobility of other semi-conductors, such as $\mu_n[Si] = 1415 \text{ cm}^2/\text{Vs}$ and $\mu_n[GaAs] = 8500 \text{ cm}^2/\text{Vs}$, the lower electron mobility of ZnO is mainly caused by the strong scattering by optical phonons. Acoustic phonons from lattice vibration lead to a local energy shift of the band edges. Acoustic mode scattering is less dominate than the optic mode scattering. At room temperature, the mobility of undoped ZnO crystal is mainly limited by the optic phonon scattering.
- Piezoelectric scattering: Piezoelectric scattering is caused by the electric fields induced by acoustic phonons. It is only significant at low temperatures around 100 K.
- Ionized impurity scattering: This scattering is caused by ionized dopant atoms and dominates at carrier concentration above 10¹⁹ cm⁻³. Several theoretical models were proposed to simulate the mobility of ZnO with different carrier concentration. In order to match the experimental results, the non-parabolicity of the conduction band of degenerate semiconductors has to be considered in the model. Moreover, clusters of impurities act as scattering centers with higher discharge state, leading to greater scattering effects. The dependence of the electron mobility on the carrier concentration was fit by a empirical curve with certain fit parameters. The fit revealed that clusters of charge can have a maximum value up to 6. For a detailed review of ionized impurity scattering, readers are referred to [58].
- Neutral impurity scattering: This scattering is caused by the unionized dopant atoms in ZnO. The mobility is inversely proportional to the density of neutral scattering centers in the material. The ionization energy of shallow donors in TCO materials is around about 50 meV. In degenerate semiconductors, this energy is further reduced. Therefore, the density of neutral impurities in doped ZnO thin films at room temperature is very low.
- Dislocation scattering: Dislocation scattering is relatively low in ZnO single crystals, but in polycrystalline materials, it seems to be a common scattering process. However, this process is rarely used to explain experimental carrier transport in ZnO, since it is difficult to estimate the defect density in ZnO thin films.
- Grain barrier limitation: This is an important carrier scattering mechanism for polycrystalline ZnO materials, due to the crystallographically disturbed regions. Defects at grain boundaries trap electrons, resulting in a depletion zone on both sides of the grain boundary leading to an energetic barrier of height ϕ_B for electrons. The mobility of the whole material is expressed as

$$\mu_{eff} = \mu_0 exp(-\frac{\phi_B}{kT}), \qquad (2.20)$$

where k and T are the Boltzmann constant and sample temperature, respectively. μ_0 is the mobility in the grains given by

$$\mu_0 = \frac{eL}{\sqrt{2\pi m^* kT}}. (2.21)$$

The barrier height ϕ_B depends on the doping concentration N, the grain size L, and the carrier trap density N_t at the boundary

$$\phi_B = \frac{e^2 L^2 N^2}{8\varepsilon\varepsilon_0} \quad \text{for} \quad LN < N_t, \tag{2.22}$$

$$\phi_B = \frac{e^2 N_t^2}{8\varepsilon\varepsilon_0 N} \quad \text{for} \quad LN > N_t.$$
 (2.23)

Suppose that the grain size L and carrier trap density N_t are fixed, and then the doping concentration N is increased from a low to a high value. Equation 2.22 indicates that the barrier height ϕ_B is proportional to the doping concentration N as long as $N < N_t/L$. When $N > N_t/L$, equation 2.23 reveals that ϕ_B is inversely proportional to N. The barrier height reaches the maximum value as $N = N_t/L$. Therefore, for very high doping concentrations, additional tunneling through barrier takes place, which increases the current flow between grains. The carrier trap density N_t at grain boundaries can be obtained by fitting the experimental data with the above equations. Many results show that the trap density changes significantly depending on the deposition conditions [57]. Generally, ZnO films grown by pulsed laser deposition (PLD) or RF magnetron sputtering have lower trap densities than films deposited by DC or pulsed-DC magnetron sputtering. It is assumed that the reduction of particle bombardment on the growing film decreases the carrier trap densities at grain boundaries, resulting in better crystal quality.

2.2.3 Optical properties

ZnO films are characterized by high transparency in the visible (VIS) and near infrared (NIR) region, due to its large band gap ($E_g=3.2-3.4\,\mathrm{eV}$). When a light beam incident on ZnO, the light is either reflected, transmitted, or absorbed. Thus, optical properties of a material are described by reflectance (R), transmission (T), and absorption (A). The absorption is calculated by A=1-R-T. In the long wavelength region, the transmission is limited by the free carrier absorption. Typical optical properties of ZnO:Al films are shown in Fig. 2.6 as a function of light wavelength. The figure can be divided into three regions.

• Urtraviolet region (300-400 nm): The energy of photons (E) in any monochromatic light is related to its wavelength λ by

$$E = \frac{hc}{\lambda},\tag{2.24}$$

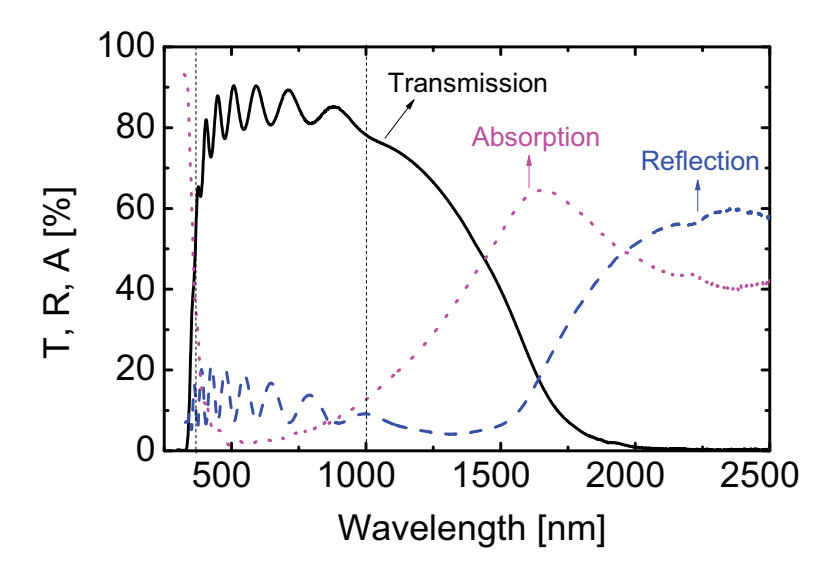


Figure 2.6: Optical transmission (T), reflection (R), and absorption (A) of a typical ZnO:Al film.

where h and c are plank constant and the speed of light, respectively. When the energy of the photon exceeds that of the band gap E_g , electrons in valence band can be excited to conduction band. Photons with lower energy tend to be transmitted through the material. For ZnO materials with a band gap of $E_{g0}=3.4~\rm eV$, the absorption peak is around 365 nm according to equation 2.24. Fig. 2.6 however shows that the absorption peak in the ultraviolet region is around at 300 nm. The reason is directly related to the electrical properties of highly doped ZnO materials. For degenerate semiconductors, the Fermi level is located in the conduction band, resulting in a population of electrons in lowest states of conduction band. The electrons in valence band require more energy to be excited into free states within the conduction band. Therefore, the optical band gap is increased, leading to a shift of absorption peak to higher photon energy, i.e. smaller wavelength. This is the so called Burstein-Moss Effect (blue shift). Illustration of this effect is shown in Fig. 2.7. The shift of optical band gap ΔE_{BM} is given by

$$\Delta E_{BM} = \frac{h^2}{2} (3n\pi^2)^{2/3} (\frac{1}{m^*} + \frac{1}{m_h^*}), \qquad (2.25)$$

where m_h^* is the effective mass of holes in valence band, and n is the electron concentration. A second effect resulting from electron-electron and electron-dopant interactions counteracts the Burstein-Moss effect, resulting in a band gap slightly smaller than $E_{g0} + \Delta E_{BM}$. Theoretical and experimental evaluations have shown that the Burstein-Moss effect is dominant for ZnO materials.

2 Fundamentals

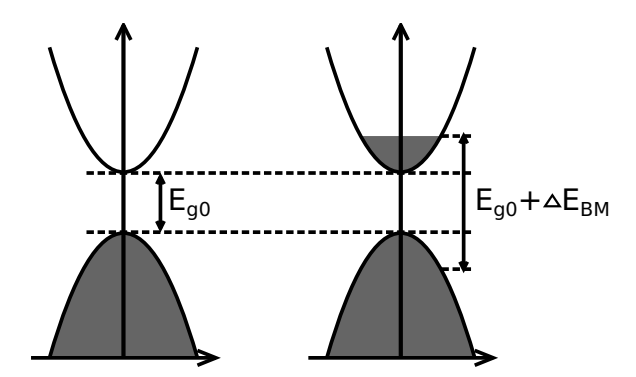


Figure 2.7: Burstein-Moss broadening of the optical band gap of degenerate semiconductors.

- VIS and NIR region (400-1000 nm): The photon energy in this region is too low for electron excitation, and therefore, there is significant increase of transmission. The transmission is as high as 80% from 450 nm until near 1000 nm. The pronounced interference is caused by the reflections at the front and back side of the sample. The limitations to transmission in this region are mainly caused by reflection and absorption as a result of impurities and non-stoichiometry. Free carrier absorption which is discussed in inferred region, has tiny effect in this region.
- infrared region (1000-2500 nm): The optical properties of ZnO in this region is related to the plasma frequency of free-charge-carriers. In degenerate semiconductors, the material behaves similar to a metal, and the electrons can be described as free electron gas. The material can be viewed as an aggregate of a negatively charged plasma of free electrons and a positively charged background of atomic cores. The resonance oscillation frequency of electrons ω is expressed as

$$\omega_p = \sqrt{\frac{n_s q^2}{\varepsilon_\infty \varepsilon_0 m^*}},\tag{2.26}$$

where q is the elemental charge, and ε_{∞} and ε_{0} are the high-frequency and static dielectric constants of ZnO, respectively. The equation shows that plasma frequency ω_{p} depends only on the free carrier density n_{s} . When the incident light has the same angular frequency as the plasma frequency of the free electron gas, the highest absorption occurs. The wavelength of the absorption peak is calculated by

$$\lambda_p = \frac{2\pi c}{\omega_p} = 2\pi c \sqrt{\frac{\varepsilon_\infty \varepsilon_0 m^*}{n_s q^2}}.$$
 (2.27)

With decreasing free carrier density, the absorption peak shifts to longer wavelength, and therefore grater transparency in the near infrared region is expected.

When the wavelength of incident light approaches λ_p , the reflection is still low, while the absorption increases continuously. Thus, the transmission of ZnO:Al film decreases. When the wavelength of incident light is larger than λ_p ($\omega < \omega_p$), most of the light is reflected, resulting in very low transmission.

As mentioned earlier, high transmission through TCO material is required. The optical properties of ZnO at near infrared region depend mainly on the carrier density. Optimized TCO materials typically have low carrier density and high mobility. The latter ensures that the films still have good conductivity while maintaining high transmission at near infrared region.

2.2.4 Deposition of ZnO:Al films

ZnO thin films can be deposited by a various of techniques, including chemical vapor deposition (CVD), magnetron sputtering, pulsed laser deposition (PLD), and electrical chemical deposition. The structural properties of ZnO thin films depend strongly on the deposition methods and conditions. To reach the requirements of front contacts in Si thin-film solar cells, i.e. good conductivity and high transparency, while keeping the deposition methods economically applicable, CVD and sputtering were commonly used in the lab and industry over the past decade. The roughness of ZnO:Al films deposited by the two methods can be varied from 3 nm to over 100 nm. The morphology of the ZnO surface can also be varied over a wide range, such as pyramids, round shape, hillock, and so on. The low pressure CVD deposited ZnO:B films exhibit large pyramid topographies, while magnetron sputtered ZnO:Al films tend to show small crater-like structures. This section will first introduce the principles behind the magnetron sputtering of ZnO:Al films used within this work, and then many aspects related to the growth of ZnO thin films are presented.

2.2.4.1 Magnetron sputtering

Sputtering refers to the ejection of particles from a condensed-matter target due to the impingement of energetic particles. A schematic drawing of magnetron sputtering is shown in Fig. 2.8. Sputtered deposition is performed within a vacuum chamber. The source of coating material, termed as 'target', is mounted opposite to the substrate in a vacuum chamber which has a base pressure approximately in the range of $10^{-6} - 10^{-8}$ mbar. Normally, the chamber is filled with a background gas, for example Ar, in order to generate positive charged gas ions. Applying an electrical potential between cathode and anode accelerates the positive charged gas ions towards the target, leading to sputtering of target materials. The sputtered atoms are then deposited on the substrate. The sputtering of target materials is a result of collisional cascade as discussed in Section 2.1.2. The energy and angular distribution of sputtered atoms which are important to the property of growing film are mainly determined by the energy of ions, target materials, temperature, and pressure.

Historically, one of the challenges of sputter deposition was a very low deposition rate. The pressures required to achieve discharge were high, leading to a relatively small mean

2 Fundamentals

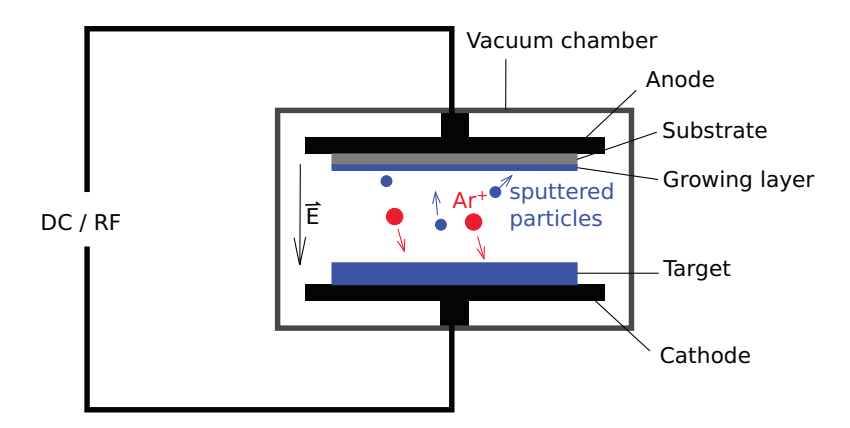


Figure 2.8: The schematic drawing of magnetron sputtering.

free path for the ejected target material, and thus a low deposition rate. To achieve high sputtering yield, a magnetic field is generally incorporated in sputtering system. The applied magnetic field B is parallel to the target, therefore perpendicular to the electrical field E. Similarly as discussed in Section 2.1.1, the electrons are trapped in the $E \times B$ field, flowing along the circuit of a cylindrical target or racetrack of a planar target. The density of electrons are highly enhanced by the magnetic field. Thus, the probability of collisions between electrons and background gas are increased, and then the plasma can be retained at low pressure. The ions are accelerated to the target by the E - field. The sputtered atoms are not trapped in the $E \times B$ field due to their relatively large mass as compared to that of the electrons. Therefore, the integrating of magnetic field dramatically improves the sputtering yield, resulting in high deposition rates.

Depending on the target materials, direct current (DC) and radio frequency (RF) excitations can be applied on the electrodes. DC discharge is generally used to deposit metals or conducting films. The positive charge deposited by ions on the target can be neutralized by the electrons from cathode, as long as the target is conducting. However, if the target is not conductive, the accumulated positive charges on the target build an electrical field opposite the external applied field. These charges can cause arcs to disturb the sputtering or even damage the target. RF magnetron sputtering is used to solve this problem for sputtering of non-conductive or semiconductor films. When the target is negatively biased, the materials from target are sputtered as in DC sputtering. On the other half circle, when the target is positively biased, the electrons flow toward target to neutralize the built-in positive charges, while ions don't follow the switching due to their heavy mass. Generally, frequencies in the low MHz range are required. RF magnetron sputtering can be used to deposit both conductive or insulating films. The ZnO:Al films used in this work were deposited by RF magnetron sputtering.

An alternative technique to deposit insulating compound films with DC power discharge is reactive sputtering. The target is usually composed of a pure metal. A reactive gas for example O_2 or N_2 is injected into the system together with a background gas.

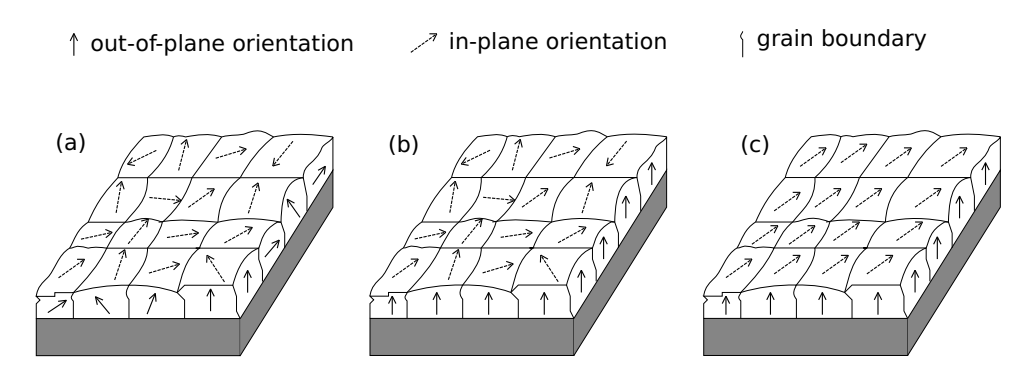


Figure 2.9: Schematic drawing of randomly textured (a), out-of-plane textured (b), and a biaxial textured (c) thin films. The solid arrows indicate the crystallographic out-of-plane orientation, while the dashed arrows indicate the inplane orientation.

Chemical reactions occur on the sample or target surface. More information about the reactive sputtering of ZnO:Al films can be found in [68].

2.2.4.2 Preferred orientation

The polycrystalline thin-films are composed of a collections of grains or columns. Each crystalline grain is characterized by its crystallographic texture with respect to the substrate. The direction perpendicular to the substrate is called out-of-plane orientation. In-plain orientation is defined as perpendicular to the out-of-plane orientation [69, 70]. Three situations may exist in polycrystalline thin films as shown in Fig. 2.9. The grains in a thin film might have different out-of-plane and in-plane orientations (a). The film is then regarded as having no preferred orientation (random texture). Fig. 2.9(b) shows a film with preferred out-of-plane orientation and random in-plane orientation; and (c) shows a film with preferred out-of-plane and in-plane orientations (biaxial aligned) [69].

It is easy to achieve c-axis textured ZnO films by magnetron sputtering even at room temperature, i.e. the c-axes of the grains are perpendicular to substrate. The preferred orientation of ZnO films has been discussed thoroughly by Kajikawa et al. [71]. The growth of polycrystalline ZnO films is divided into two stages: initial nucleation stage and bulk growth stage. It is debatable that whether the preferred orientation is already induced in the initial nucleation stage or determined by the evolutionary selection in the bulk growth stage. The evidence for nucleation stage is the minimization of surface energy which results in preferred nucleation. Fujimura et al. calculated that the surface energy by counting the dangling bond density of each plane, and the results show that (0001) plane has the smallest surface energy as compared with (11-20) and (10-10) planes [72]. It was also recently reported that bombardment with low energy Xe ions during magnetron sputtering can promote c-axis preferred orientation in nucleation stage, while bombardment with high energy oxygen ions lead to a-axis texture in nucle-

ation stage [70]. However Wander et al. calculated the cleavage energy using ab initio density functional theory (DFT). The results show that the (0001) plane does not have the smallest energy [73, 74]. Moreover, high magnification TEM image of ZnO/glass interface reported by Yoshino et al. shows that there is about a 5 nm thick amorphous layer and a 10 nm thick random oriented layer [75, 76]. The paper also showed that for ZnO films sputtered on crystallized substrate, for example Au and sapphire, ZnO grows with preferred orientation from the initial nucleation stage.

2.2.4.3 Thin-film growth mechanism

When the particles sputtered from target reach a bare substrate, these particles can touch-down, diffuse, adsorb, or desorb on it. Depending on the energy transfer between the particles and between the particle and substrate, the particles may eventually stick together and form a stable nucleus (island formation) or form a complete monolayer on the surface. The former is called island or Vollmer-Weber growth, while the latter is called layer-by-layer or Frank-van der Merwe growth. More information about the nucleation and growth of thin-films can be found in [77]. In the following, the relationship between the sputter parameters and growth ZnO:Al film is briefly introduced.

Magnetron sputtered ZnO films on amorphous glass substrate generally belongs to 3D island growth, due to the large lattice mismatch between the substrate and film. The mobility of the impinged particles is mainly determined by substrate temperature and pressure in the chamber. Based on this, many structure zone models were proposed. A review of different growth models can be found in [69]. Among them, Thornton model was developed to describe the growth of sputtered metals in dependence of two parameters, substrate temperature and sputter pressure [78, 79]. Kluth et al. has proposed a modified Thornton model to describe the growth and etching behavior of sputtered ZnO films [80]. The model is shown in Fig. 2.10. In the figure, SEM micrographs of different ZnO:Al films, denoted by type A, B and C, before (left) and after (right) HCl etching are given, as well as a sketch of structural properties as function of deposition pressure and substrate temperature.

The crystallites can be easily distinguished in type A film by high resolution cross-sectional SEM. However, this is more difficult for type B and C film. It indicates the increasing compact and dense structures of the materials from type A to C. After etching in HCl solution, more obvious morphology differences can be observed (see Fig. 2.10 right). Since type A ZnO:Al films can be easily etched, very small features are observed after etching. In contrast, compact type B and C films develop craters on the surface after etching. The opening angle of these craters is between 120° and 135° as measured by AFM. Type B films consist of homogeneous craters which was shown to provide best light trapping effect in solar cells, while type C film surface is composed of few large craters and many small craters.

Similarly, Jost *et al.* has shown a series of ZnO:Al films change from compact to porous structures, by adjusting the deposition parameters [82]. The SEM micrographs before and after HCl etching are listed in the left and right column of Fig. 2.11. From film A to H, the surface changes from crater type to pyramid type. Accordingly, the

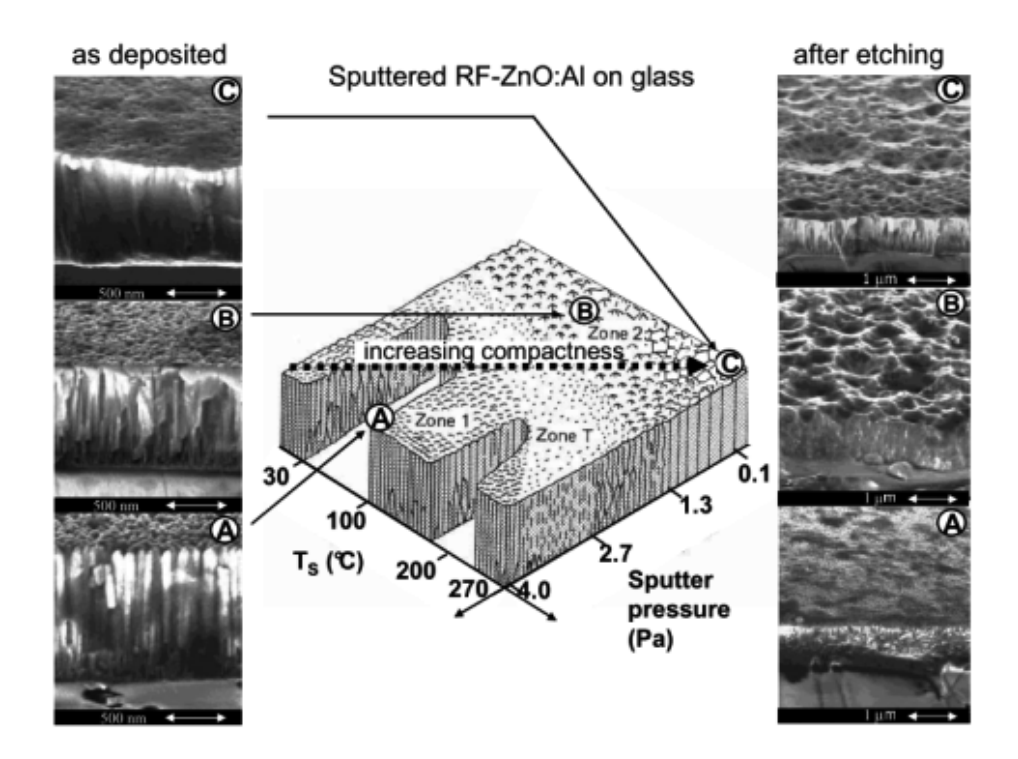


Figure 2.10: Modified Thornton-model for RF-sputtered ZnO:Al films according to Kluth et al. [80]: Structural properties and etching behavior as function of deposition pressure and substrate temperature T_s . The SEM micrographs show cross sections and the surface in the as-deposited state (left) and after etching in HCl (right). The matrix of the substrate temperature and deposition pressure contains structure zones according to the Thornton model [78, 79, 81].

feature size increases from around 50 nm to approximately 100 nm. After etching, film A to D develop round craters on the surface, while the other films exhibit small hillock structures

To summarize, the morphology and properties of as-deposited ZnO:Al film are strongly dependent on the sputtering parameters. Low temperature and high sputter pressure tend to develop porous ZnO films with relatively large lateral features, while high temperature and low sputter pressure tend to lead to compact films with small lateral features. Consequently, the morphologies of HCl etched ZnO:Al films are related to the compactness of ZnO:Al films. Compact ZnO:Al films tend to develop craters with HCl etching. The size of the craters are much larger than those on the as-deposited surface. On the other hand, HCl etching of porous films tends to develop hillock structures. Porous

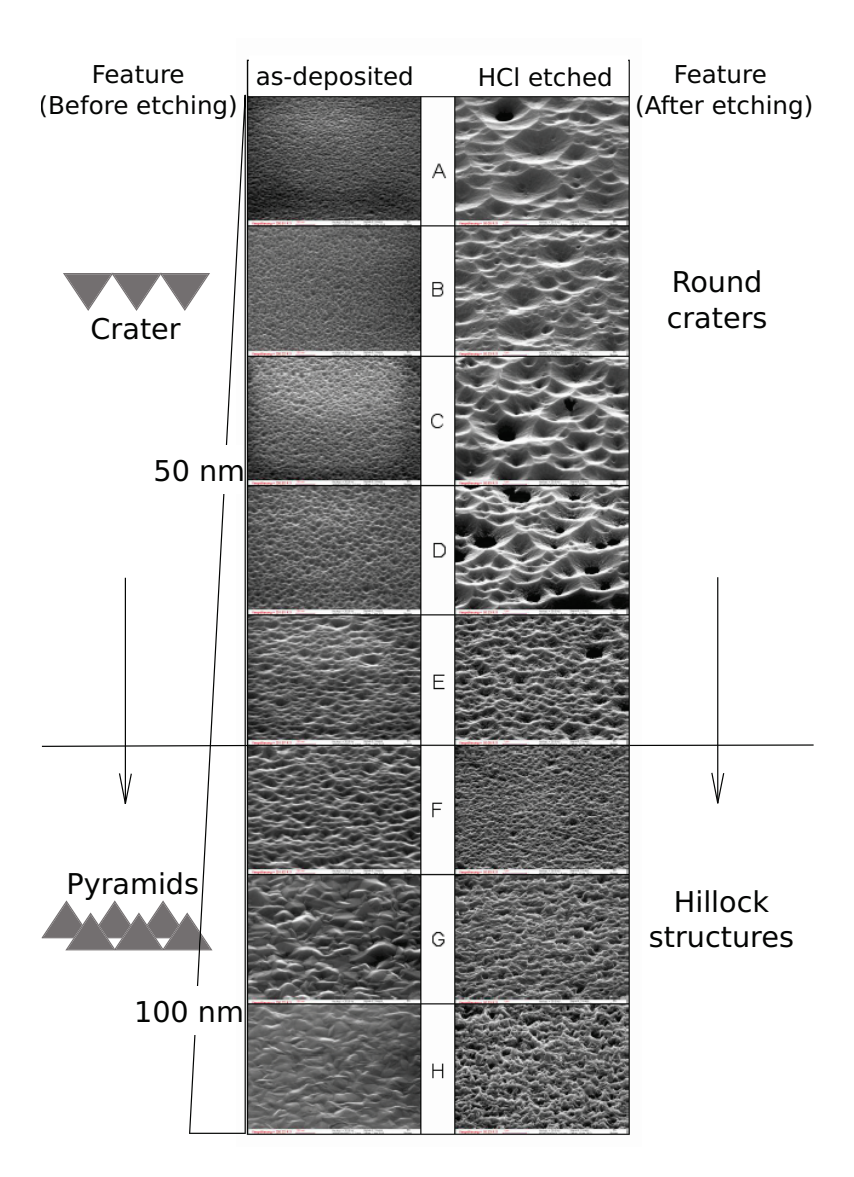


Figure 2.11: A series of ZnO:Al films deposited at different conditions. The left column shows the SEM micrographs of ZnO:Al films before HCl etching and the right column show the films after HCl etching [82].

ZnO:Al films are also characterized by low material density, relatively high resistivity and high HCl etch rate.

2.2.4.4 As-grown rough ZnO films

As-grown rough ZnO:B films have been prepared by several deposition techniques such as low pressure chemical vapor deposition (LPCVD) [83, 84] and expanding thermal plasma CVD [85]. As already discussed, magnetron sputtered ZnO films tend to exhibit c-axis preferred orientation. Compared with those CVD prepared films, sputter deposited ZnO films generally exhibit smaller lateral features. Thus, the flat sputtered ZnO:Al films have to be etched in wet chemicals in order to provide a light scattering effect at the ZnO/Si interface. The replacement of wet chemical etching by dry etching or as-grown rough ZnO seems very attractive for industry process, because the vacuum break can be avoided. There have been many attempts to sputter as-grown rough ZnO films by magnetron sputtering [9–13]. In the following, the literature related to as-grown rough ZnO films by magnetron sputtering are briefly reviewed.

Generally, as-grown rough ZnO surfaces were sputtered at very high pressures or with water vapor. It was reported by Minami et al. and Sato et al. that wedge-like surface features were sputtered on undoped ZnO and ZnO: Al films with gas pressure between 3 and 10 Pa and substrate temperature of about 300 °C. The sheet resistance of these films is approximately 1.8 Ω at thickness of 3 μ m [9, 11, 12]. Nakada et al. added H₂O together with Ar gas in the sputtering chamber. With increasing H₂O partial pressure, the columnar structure which can be seen in ZnO films deposited in pure Ar disappeared. The maximum lateral feature size for ZnO films grown in pure H₂O was approximately 1 μm. With Al doping, the change of surface morphology was not significant. The mobility of the ZnO:Al film sputtered in mixed water vapor and Ar, however, is quite low 3 cm²/Vs. After annealing in vacuum, the mobility can be improved to 9 cm²/Vs. As a result, the electrical properties of these ZnO:Al films are not sufficient for the front contact in solar cells. Similar results were found by Kluth et al. [14]. As-grown rough ZnO:Al films were obtained as long as the fraction of water vapor in the Ar gas is larger than 1% and the film thickness is larger than 500 nm. However, these films also suffered high resistivity. It was also noted by the above authors that gas mixtures such as Ar/O_2 and Ar/H₂ do not lead to as-grown rough ZnO:Al films.

Additionally, it was found by Krantz et al. that adding N_2 into the sputter chamber, as-grown rough ZnO:Al films were obtained by reactive sputtering [86]. The surface lateral size was increased from 50 nm to 500 nm as the flow rate of N_2 was increased from 0 to 10 sccm. The sheet resistance of the film, however, was increased from 4 to 4277 Ω cm due to the large decreasing mobility.

To summarize, as-grown rough ZnO:Al films have been deposited by magnetron sputtering at very high pressure or by adding water vapor or N_2 to the sputter process. The as-grown rough ZnO:Al films, however, tend to exhibit low mobility as well as high resistivity, making them unlikely to be applied in solar cells. One important focus of this work is the sputtering of as-grown rough ZnO:Al films without strongly deteriorated electrical properties.

2.2.4.5 Surface evolution

The evolution of thin-film surfaces has been characterized through the concept of dynamic scaling theory for many years. Under this theory, the roughness is assumed to evolve with a time- and scale-invariant structure, characterized by a set of scaling parameters, namely global roughness exponent α , growth exponent β , and coarsening exponent 1/z, respectively [87]. The last one is also called dynamic exponent in some books [88]. The above exponents can be obtained by either experimental observations or simulations with certain growth models. The scaling theory was first analyzed based on self-affine surfaces, and then it can be generalized to more complex surfaces. The self-affine surface is defined similar to fractals in that the vertical and horizontal directions of the surface can be rescaled to yield a new surface that is statistically identical to the original surface. Systematical discussions about the thin-film evolution can be found in [87, 88]. In this section, the parameters used to describe a rough surface are briefly introduced, and then the evolution of the rough surface is discussed with regard to some growth models used in this work.

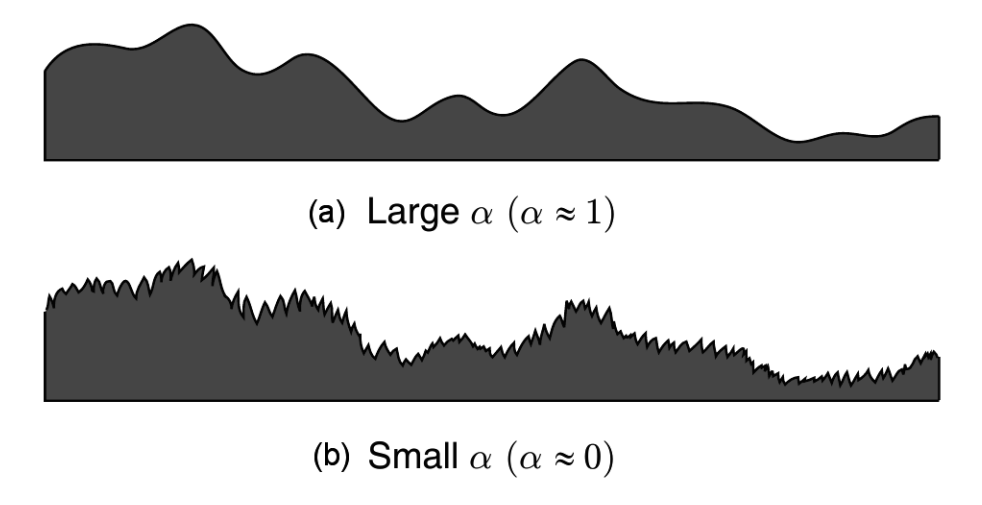


Figure 2.12: Comparison of the local surface morphology for surface with similar roughness σ , but different values of α . A smaller α implies a rougher local surface, where α lies between 0 and 1 [87].

Generally, rough surfaces are characterized by three parameters: roughness σ , lateral correlation length ξ , and roughness exponent α . Roughness σ is the most widely used measure of roughness. It characterizes the spatial variation of a rough surface along the vertical direction. Lateral correlation length ξ is the distance within which the surface variations are correlated but beyond which the surface fluctuations spread. Roughness exponent α describes a measure of surface in the short range ($< \xi$). A larger value of α indicates a smooth surface in short range (see Fig. 2.12(a))while a smaller value of α

corresponds to a more jagged local surface morphology as shown in Fig. 2.12(b).

The three surface parameters can be obtained from height-height correlation function (HHCF) [87], which is defined as following:

$$H(r,t) = \langle [h(r,t) - h(0,t)]^2 \rangle,$$
 (2.28)

where $\langle \rangle$ is the spatial average over the measured area and h(r,t) is the surface height at position r and time t. For a self-affine rough surface, the height-height correlation function can be expressed in a scaling form

$$H(r,t) = 2\sigma(t)^2 f(r/\xi(t))$$
 (2.29)

where the function $f(r/\xi(t))$ behaves as,

$$f(r/\xi(t)) = \begin{cases} r^{2\alpha} & \text{for } r \ll \xi \\ 2\sigma^2(t) & \text{for } r \gg \xi. \end{cases}$$
 (2.30)

An example of H(r) is shown in Fig. 2.13. It is seen that H(r) scales as $H(r) \sim r^{2\alpha}$ for $r \ll \xi$ and becomes constant for $r \gg \xi$. Thus, the roughness exponent α is derived from the slope of the H(r,t) curve at short r range. The value of σ is obtained directly from the saturating value of H(r) when $r > \xi$. The average value of ξ is obtained from the crossovers of the H(r).

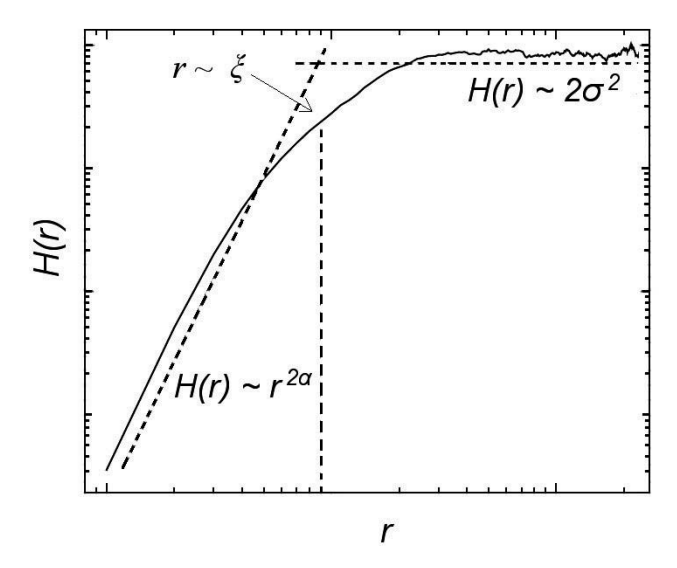


Figure 2.13: Representative height-height correlation function obtained from a self-affine surface. The plot is on log-log scale, which gives the H(r) a linear behavior for small r with slope 2α [87].

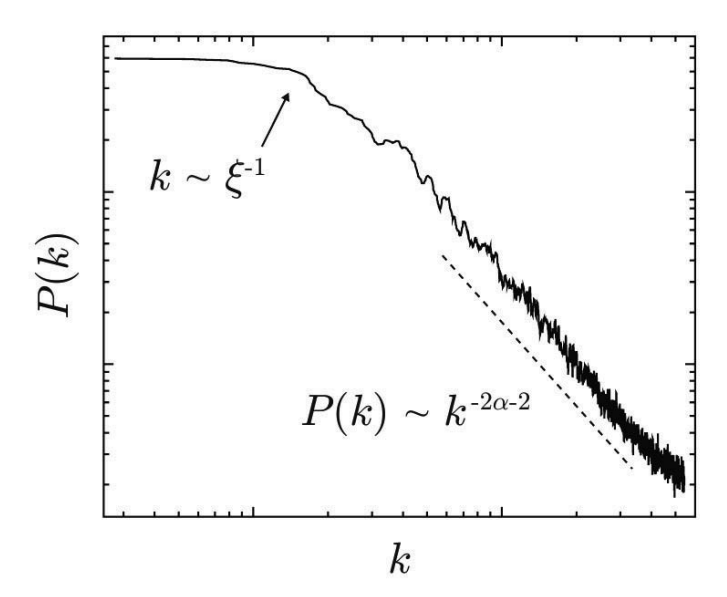


Figure 2.14: Representative power spectrum density function obtained from a self-affine surface. The plot is on log-log scale, which gives the PSD(k) a linear behavior for large k with slope $-2\alpha - 2$ [87].

The surface fluctuation in reciprocal space is characterized by the power spectrum density (PSD) function

$$PSD(k,t) = \langle H(k,t)H(-k,t)\rangle, \tag{2.31}$$

where H(k,t) is the Fourier transform of surface height and k is the spatial frequency. An example of PSD(k) is shown in Fig. 2.14. In a similar fashion, the PSD shows a power-law behavior as $PSD(k,t) \sim k^{-2\alpha-2}$ for $k > \xi^{-1}$ and becomes k-independent for small frequencies.

The parameters are not only characterized for films at a time, but also invariant with time. It is common to observe a power law behavior for the roughness in deposition time

$$\sigma \sim t^{\beta},$$
 (2.32)

where β is referred as growth exponent. Similarly, the power law behavior of ξ is characterized by coarsening exponent 1/z as

$$\xi \sim t^{1/z}.\tag{2.33}$$

For self-affine surfaces, the relation $\beta/\alpha = 1/z$ is fulfilled [88]. This relation has been reported by many experimental investigations, including sputter-deposited ZnO, TiN, and AlN thin-films [89–92]. However, during the thin-film growth, many factors such

as shadowing, step-edge barrier lead to break-down of dynamic scaling, i.e. the relation $\beta/\alpha = 1/z$ is not fulfilled [87, 88, 93].

A simple model to describe thin-film growth is random deposition which means that no growth effects are present. This model serves as an analytically solvable model with exact prediction of $\beta = 1/2$. This β is often reported at very early points in the growth process from a flat substrate when noise is the most dominant growth mechanism.

In realistic thin-film deposition processes, shadowing, reemission, and surface diffusion are the main growth effects on the growing surface, as shown in Fig. 2.15. Among these three effects, diffusion is generally defined as local effect since atoms can diffuse to nearby locations depending on deposition conditions such as activation energy and temperature [87]. By definition, nonlocal growth effects are of much longer range than local effects. The primary nonlocal effect is the shadowing effect, where taller surface features block incoming flux from reaching lower-lying areas of the surface. Shadowing is an inherently nonlocal process because the shadowing of a surface feature depends on the heights of all other surface features, not just close, or local, ones [93]. Reemission effect is also inherently nonlocal because an event that occurs at one place on the surface can affect the surface profile a far distance away [87]. Thin film growth models can be separated into two main categories: models that are based on continuum mathematics, and models that are based on discrete mathematics. In the past few decades, a number of models of both types have been proposed and have been shown to successfully predict properties of certain types of thin film growth, each with their own advantages and disadvantages. Both types of models were first built based on only local effect. Models that include nonlocal effects build off the results of local models.

First, the continuous and discrete local models are introduced in this paragraph. If only the diffusion effect is considered in the discrete model, β is decreased from 0.5 to approximately 0.24 ± 0.03 when the surface diffusion is increased from zero to infinity [87]. The results are consistent with $\beta = 0.25$ predicted by continuous Mullins diffusion model. To conclude, diffusion tends to smoothen the local surface during film growth process.

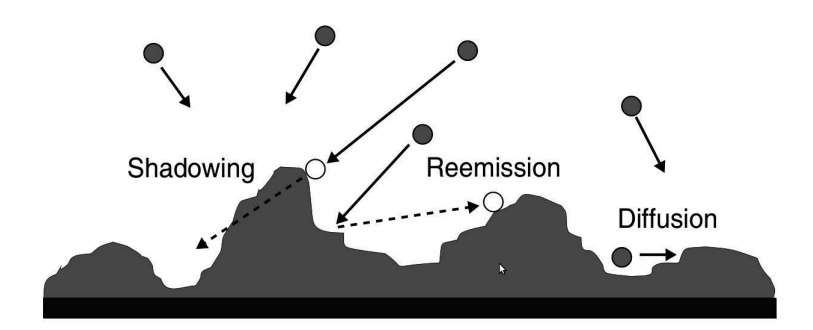


Figure 2.15: Diagram of growth effects including diffusion, reemission and shadowing that may effect the surface morphology during thin-film growth. [87]

2 Fundamentals

This paragraph expands the model to non-local area. Shadowing and reemission are competitive mechanisms in this range, where shadowing leads to rough surface and reemission leads to smooth surfaces. The shadowing effect is a result of the tilted incident angle. For normal incident atoms, the shadowing effect is zero. Yao and Guo have calculated that with the shadowing effect, films grow with $\beta=1$ and 1/z=1/3 in three dimensions [94]. However, this calculation was performed with a uniform angular distribution of incoming atoms, which is not experimentally realistic. Experimentally, depending on target geometry and substrate movement, different angular distributions are present. Generally cosine angular distributions are considered. On the other hand, the reemission effect hinders roughness development. Reemission is related to sticking coefficient s_0 such that when the sticking coefficient s_0 is high, the probability of reemission of the incident atom is low.

There were many models calculating the competition of shadowing and reemission, and similarly results were obtained. With the shadowing effect, when the sticking coefficient s_0 is high, i.e. low reemission effects are present, $\beta \approx 1$ is obtained as shown in Fig. 2.16. When the sticking coefficient s_0 is low, i.e. with high reemission effects, $\beta \ll 1$ are commonly observed [87, 93, 95]. In both cases, the diffusion effect D/F seems to be negligible for β . However, 1/z is still very sensitive to both of the diffusion and reemission. The value of 1/z is in the range of $0.12 \pm 0.05 \sim 0.61 \pm 0.01$ [87]. Note that when the shadowing is dominant, the growing surface is no longer self-affine, and therefore, $\beta/\alpha \neq 1/z$.

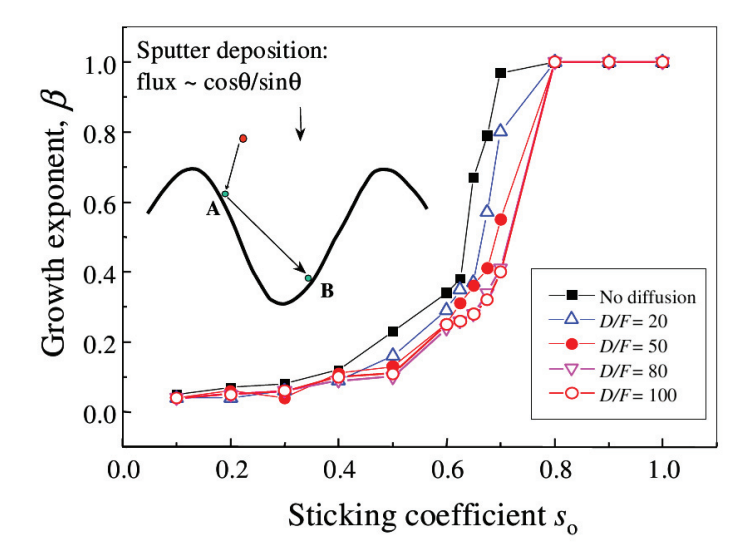


Figure 2.16: Monte Carlo simulated β value as a function of sticking coefficient s_0 for sputter deposition. It is assumed that the sticking coefficient of the second strike at the surface for the re-emitted atom is 1 [95].

The discussions above have not considered the effect of grains crystallinity and orientation during the film growth which are not present in amorphous semiconductor thin-film growth. However, during the MBE process, step-edge barrier effect also gives significant influences to the surface roughening process [87]. This effect does not allow atoms to diffuse over the edge of a step on the surface, which creates an overall uphill current of diffusive particle flux. This effect is a characteristically local growth effect because it involves the diffusion of particles on the surface. For sputtered polycrystalline thin-films, the models to describe the crystallinity and step-edge barrier effect on the growth behavior is lacking on the theoretical level. From an experimental point of view, the role of step-edge barrier effects in the polycrystalline thin-film is debated. It was assumed that in a polycrystalline film step-edge barriers will be improbable if growth starts out with randomly orientated grains and grain sizes much smaller than film thickness [96, 97]. However, recently step-edge barrier effects have been proved to be key parameter for the growth of 1 µm thick polycrystalline Cu films by sputtering, when the grains have a size close to 200 nm [98] and 1.5 µm thick ZnO films by pulsed laser ablation, when the grain size is close to 500 nm [99]. During sputter depositions, there are other effects such as damage to the film by impinging high energy oxygen ions or Ar neutral atoms [100].

2.3 Silicon Thin-film Solar cells

One of the goals in performing ion beam treatment is to improve the efficient of solar cells. This section introduces the basic physical concepts and the materials related to Si thin-film solar cells. Solar cells are a opto-electrical device that convert the energy of light directly into electricity by the photovoltaic effect. There are many types of absorber materials, for example, solar cells based on element or compound semiconductors with heterojunctions or based on organic electrochemical photovoltaic materials. Within this work, only Si based materials are used. Among the different kinds of Si solar cells, thin-films solar cells based on amorphous and microcrystalline silicon have the advantage of low-cost and large area deposition as compared with crystalline Si solar cells. Hydrogenated amorphous silicon (a-Si:H) and hydrogenated microcrystalline silicon (μ c-Si:H) are used as absorber layers in Si thin-film solar cells. In this section, the physical properties of the two materials are briefly introduced, and then the operating principle and characterization methods of thin-film Si solar cells will be summarized.

2.3.1 Hydrogenated amorphous silicon

Amorphous Si is characterized by the absence of long range order, which is caused by the deviations in the bond lengths and bond angles in the Si-Si bonds. Amorphous Si consists of a covalently bonded random network of Si-H and Si-Si bonds. H atoms are used to terminate the dangling bonds, in order to reduce the defect density. The amorphous Si behaves like a direct band gap semiconductor with a band gap between 1.7 and 1.8 eV, resulting in a very high absorption coefficient in short wavelength region.

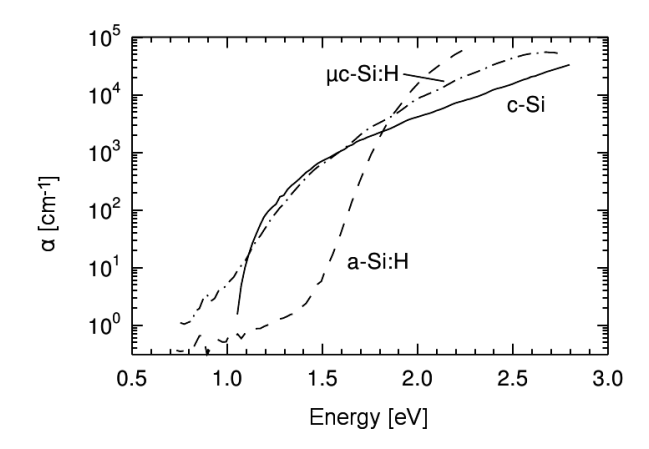


Figure 2.17: Absorption coefficient of a-Si:H, μ c-Si:H and crystalline Si (c-Si) as a function of photon energy.

Therefore, the a-Si:H solar cells can be made much thinner than μ c-Si:H solar cells. The drawback of a-Si:H solar cells is the deterioration in the cell performance after long term illumination. The degradation is caused by increased defect density after light soaking, which increases the carrier recombination rate, this effect is called 'Staebler-Wronski effect' [101]. More information on amorphous Si can be found in [102].

2.3.2 Hydrogenated microcrystalline silicon

Opposite to the homogeneous nature of a-Si:H, μ c-Si:H can be considered as a mixture of crystallites, amorphous regions, grain boundaries, and voids. Depending on the deposition conditions, the volume fraction and spatial distribution of crystallites and amorphous regions can be adjusted. During the plasma enhanced chemical vapor deposition (PECVD), process parameters such as silane concentration, power, and pressure can be used to tune the structure from highly microcrystalline to fully amorphous growth.

 μ c-Si:H is an in-direct semiconductor with band gap of 1.1 eV. The optical absorption coefficient α of a typical μ c-Si:H film is shown in Fig. 2.17 together with that of a-Si:H and crystalline Si (c-Si) as a function of photo energy [103]. The absorption of μ c-Si:H and c-Si are almost the same over a wide range. Only at high photon energies, α of μ c-Si:H is higher than c-Si. This is mostly caused by the presence of an amorphous phase and the internal scattering at grain boundaries. Compared to a-Si:H, μ c-Si:H show higher absorption in the red and infrared region. Accordingly, μ c-Si:H solar cells have higher spectra response in the wavelength range of 700 to 1100 nm as compared to a-Si:H solar cells.

2.3.3 Operating principle

Due to the high defect density in the doped a-Si:H and μ c-Si:H films, the diffusion length of charge carries is relatively short. Thus, the p-n structure used in crystalline Si solar cells does not work in Si thin-film solar cells. A 1 μ m intrinsic layer (i-layer) is usually used as light absorption layer, where electron-hole pairs are generated. The electron-hole pairs are separated by the electrical field provided by the p- and n- type doped Si layers which are deposited on both sides of i-layer. The electrons are electrostatically driven to n-layer and the holes are driven to p-layer. Thus, a photovoltage is built up by the separation of electron-hole pairs. Finally, front and back contacts are required to transport the current if the solar cell is connected into a circuit.

Due to the smaller mobility of holes in Si thin film, the solar cells are usually illuminated from p-layer side. As a result, most of charge carries are generated close to p-layer, leading to a shorter avearge distance for the holes travel to reach the p-layer. Therefore, the TCO front contact coated glass substrates are adjacent to the p-layer. The configuration of the single junction Si thin-film solar cells used in this work is shown in Fig. 2.18. Textured ZnO films are deposited on a glass substrate, providing a light scattering effect. Subsequently a very thin p-doped layer (15 – 20 nm), a thin intrinsic (\sim 300 nm for a-Si:H and \sim 1 µm for μ c-Si:H), and a very thin n-doped layer (15 – 20 nm) are deposited on top of the ZnO films. Finally, a back reflector consisting of Ag or ZnO/Ag layer is deposited on the Si layers. This configuration is the so called p-i-n superstrate structure.

A simplified band diagram is shown on the bottom of Fig. 2.18. Light with sufficient photon energy excite the electrons from the valence band to conduction band, leaving a positively charged hole in valence band. The electrons and holes are driven and separated by the internal electrical field. More information about the amorphous and microcrystalline silicon thin-film solar cells can be found in [104].

2.3.4 Characterization parameters

In solar cells, generally current density J is used instead of current I. Fig. 2.19 gives a typical dark and illuminated J-V curve for a Si thin-film solar cell. The dark J-V curve is measured without illumination and the solar cell behaves simply as a diode. The illuminated J-V curve of a solar cell is the superposition of the J-V curve of the solar cell diode in the dark and the light-generated current density. The important parameters for a solar cell are denoted in the figure, including open circuit voltage (V_{oc}) , short circuit current density (J_{sc}) , and maximum power point (MPP). MPP is defined as the working point where the solar cell can deliver maximum power. The maximum output power P_{max} is marked by the gray area in the figure. The fill factor (FF) of a solar cell is defined as the ratio between the maximum power and the product of V_{oc} and J_{sc}

$$FF = \frac{P_{max}}{V_{oc} \times J_{sc}}. (2.34)$$

2 Fundamentals

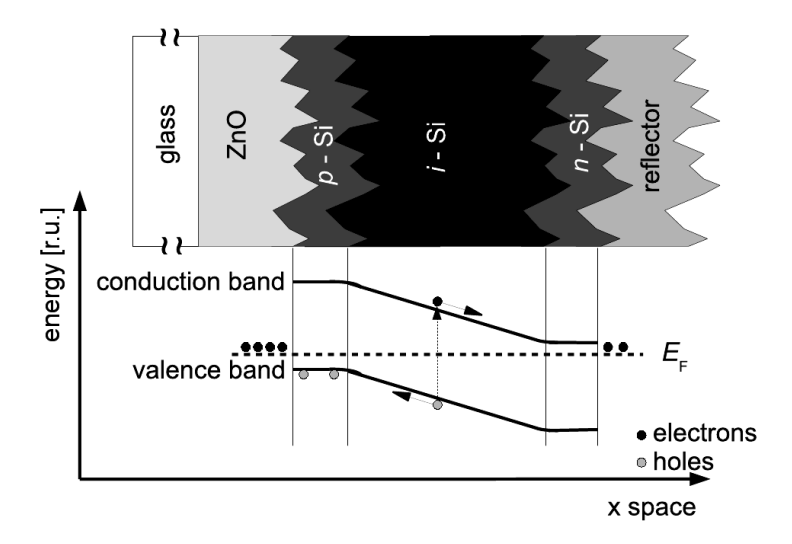


Figure 2.18: Schematic diagram of a single junction Si thin-film solar cell. The bottom of this figure represents a simplified band diagram resulting from p- and n-doped layers and shows the electron hole pair generation as well as charge collection.

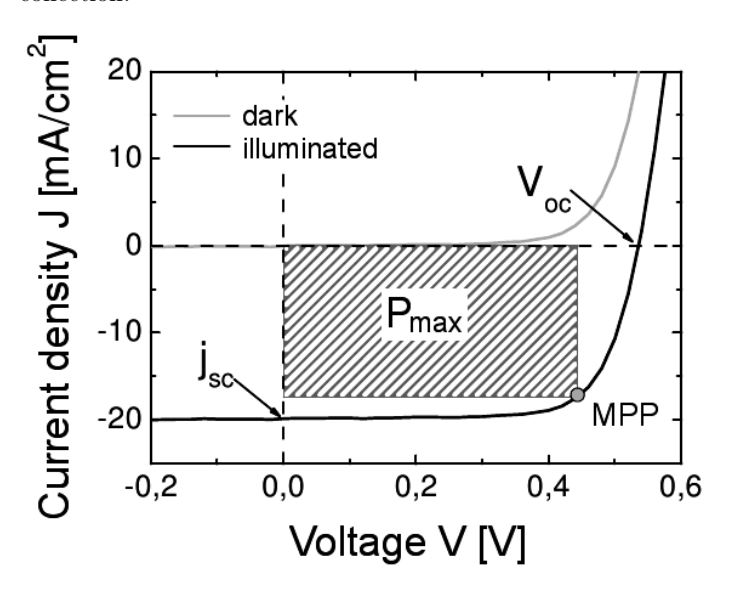


Figure 2.19: Typical curve for current density as a function of voltage in dark and illuminated.

The efficiency η of solar cells is defined as the ratio between the maximum output power and the energy input of light,

$$\eta = \frac{P_{max}}{P_{light}} = \frac{V_{oc} \times J_{sc} \times FF}{P_{light}}.$$
 (2.35)

The spectrally resolved response of a solar cell provides important information on light incoupling and light trapping. The spectra response is defined as the ratio of the number of carriers collected by the solar cell $N_e(\lambda)$ to the number of photons of a given energy incident on the solar cell $N_{\gamma}(\lambda)$. The quantum efficiency of a solar cell for a given wavelength λ can be expressed as

$$\frac{N_e(\lambda)}{N_{\gamma}(\lambda)} = QE(\lambda) = \frac{J_{ph}(\lambda)}{q \times \Phi(\lambda)},\tag{2.36}$$

where $J_{ph}(\lambda)$ is the photo current density at wavelength λ , q is the elemental charge and $\Phi(\lambda)$ is the photo flux. This form is also referred to as the external quantum efficiency (EQE). The so-called internal quantum efficiency (IQE) only takes photons which are actually absorbed in the solar cell device into account. Thus, the reflection of the solar cell R_{cell} is removed when calculating IQE

$$IQE = \frac{QE}{1 - R_{rell}}. (2.37)$$

The short current density (J_{sc}) can be calculated by integrating the product of the electron charge, the quantum efficiency, and the photo flux over the wavelengths of any given spectrum

$$J_{sc} = q \int QE(\lambda)\Phi(\lambda)d\lambda. \tag{2.38}$$

3 Experimental

This chapter describes the experimental processes related to this work, including the deposition techniques for ZnO:Al and Si thin-films, the surface treatments by ion beam, and the methods used to characterize the materials and devices. To begin, the deposition of ZnO:Al films by magnetron sputtering and Si films by plasma enhanced chemical vapor deposition (PECVD) are presented. Then, the geometry of the ion source and the experimental process of ion beam treatment are introduced. Next, the various characterization techniques of glass and ZnO thin-films are introduced, as sorted by their functionality, including electrical properties, optical properties, surface topographies, and structural properties. Finally, the characterization methods of solar cells are presented.

3.1 Deposition techniques

Within this work, ZnO:Al films and Si absorber layers were deposited by magnetron sputtering and PECVD process, respectively. The following sections describe the experimental details during the preparation of different samples.

3.1.1 ZnO:Al films - Magnetron sputtering

ZnO:Al layers were sputtered from different types of targets, including planar ceramic target, tube ceramic target, tube metallic target, and small area round ceramic target. Most of the ZnO:Al films were prepared in a vertical in-line deposition system (VIS 300) provided by Von Ardenne Anlagentechnik GmbH. Fig. 3.1 shows a sketch of the sputtering system. The system contains two load chambers and two process chambers. All chambers are equipped with heaters. The left process chamber contains a linear ion source (LION) for various surface ion beam treatment (See Section 3.2) and a rotatable dual magnetron (See Section 3.1.1.2). The other process chamber includes several planar cathodes RF, DC, or AC (See Section 3.1.1.1). Ceramic or metallic, rectangular or tube targets are mounted on the double cathodes. Unless otherwise specified, depositions were made onto $10 \times 10 \text{ cm}^2$ glass (Eagle XG, Corning) substrates. Prior to deposition, substrates were cleaned in deionized water and weak acidic decantate at 68 °C. The following sections give the specific deposition details for different ZnO:Al films.

3.1.1.1 Standard ZnO:Al films - Planar ceramic target

Within this work, the so-called 'Standard' ZnO:Al films are sputtered from a planar ceramic target in the VIS 300 system. The target is a linear planer ceramic ZnO:Al₂O₃ (1

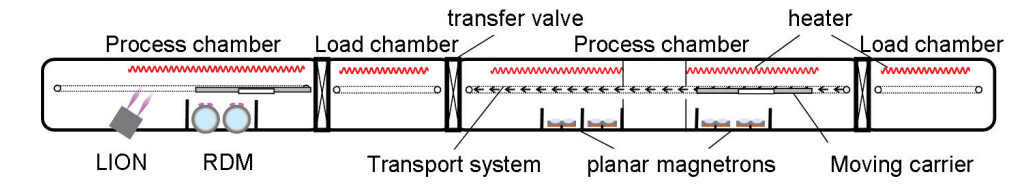


Figure 3.1: Sketch of the vertical in-line deposition system with two load chambers, and two process chambers including ion source (Lion), tube targets (RDM) and different cathodes.

wt%) with length of 75 cm and width of 10 cm. Substrates with size up to $30 \times 30 \text{ cm}^2$ can be deposited homogeneously in this system. For standard ZnO:Al films, the excitation frequency and power of the generator are 13.56 MHz and 1.5 kW, respectively. The substrates are heated to 300 °C for one hour prior to sputtering. A background gas flow of 100 sccm provides Ar ions which bombard the target. The process pressure is kept at 1 µbar during sputtering. Depositions are made in dynamic mode with the substrates oscillating in front of the target for several passes until the desired thickness is achieved. For the standard ZnO:Al films, a thickness of 800 nm are obtained when the substrates are oscillated 32 times. The dynamic deposition rate as calculated from the film thickness is around 6 nm·m/min.

3.1.1.2 High rate ZnO:Al films - tube target

ZnO:Al films are also sputtered from tube targets in the VIS 300 system. The principle of the sputtering is similar as the one above, except the target rotates during the sputtering process. As compared with the planar target, the benefit of the tube target is the improved utilization of the target material. The tube target is also mounted in the large area in-line magnetron sputtering system, and it is composed of ZnO:Al₂O₃ (0.5 wt%). The system is operated in mid-frequency mode having a excitation frequency of 40 kHz. The power of generator is 14 kW. A background Ar gas flow of 200 sccm is used as source gas and the working pressure is 20 μ bar during the sputtering process. The substrates are heated to 350 °C. With these parameters, the films are deposited with dynamic mode. The dynamic deposition rate is 110 nm·m/min. For more information about sputtering from ceramic tube targets, the readers are referred to [105, 106].

Additionally, deposition of ZnO:Al films by reactive magnetron sputtering from metallic tube targets was performed. The metallic target is composed of Zn:Al (0.5 wt%). 200 sccm Ar is used as source gas. The $\rm O_2$ gas flow is controlled by plasma emission monitoring. The frequency, power of the generator, working pressure, and substrate temperature are 40 kHz, 10 kW, 9.5 μ bar, and 350 °C, respectively. Under these conditions, the dynamic deposition rate is around 100 nm·m/min. For more information about magnetron sputtering from metallic tube targets, the readers are referred to [6].

3.1.1.3 Small area deposition system

ZnO:Al films are also deposited in a small area magnetron sputtering system provided by Kurt J. Lesker Company. The so called 'small area' refers to the smaller maximum size of substrate $10 \times 10~\rm cm^2$ used in the system. The target in this system is round with a diameter of 15.24 cm (6 inches) and is composed of ZnO:Al₂O₃ (0.5 wt%). The power of the generator, substrate temperature, Ar gas flow, and working pressure during the sputtering process are 225 W, 400 °C, 8 sccm, and 2.7 µbar, respectively. The substrate is static during the deposition. Therefore, only the center of the substrate is relatively uniformly sputtered. More information about this system can be found in [14, 107].

3.1.2 Silicon - PECVD

This section briefly introduces PECVD, which was used in this work to deposit Si layers. The Si depositions are made in an in-house modified PECVD system (Materials Research Group). This system has two process chambers, one is used for developing p- and n-type doped Si, while the other is only used for depositing intrinsic Si. The plasma excitation frequency is in the RF range at 13.56 MHz. Substrate temperature is kept at 250 °C. Hydrogen (H₂) and silane (SiH₄) are used as precursor gases during silicon deposition. Trimethylborane (B(CH₃)₃) and phosphine (PH₃) are introduced for p- and n-type doping of the Si, respectively. The doped layers are around 20 nm thick. A showerhead is used to homogeneously introduce all the gases. Further details about the PECVD system can be found in [108].

3.2 Ion beam treatment

Within this work, the glass substrates and ZnO:Al films were treated by Ar and O_2 ion beam. The ion beam treatments were performed in the VIS 300 system as shown in Fig. 3.1. The following sections give the geometry of the ion source and system, and the main parameters during the treatments.

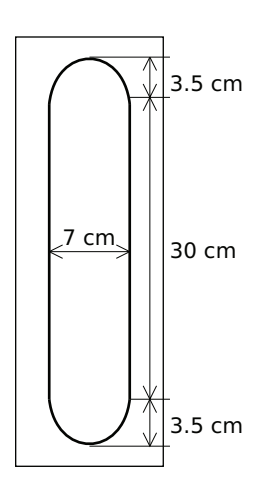
3.2.1 Geometry of the ion source

Among many types of ion sources as referred in Section 2.1.1, a linear anode layer ion source was chosen for our system, because of its simplified gridless design, possibility to scale-up, and excellent performance such as long, uninterrupted ion beams. This section describes the geometry of the ion source, including the active beam length, the width of the racetrack, and the angle of the incident beams.

A photograph of the ion source is shown in Fig. 3.2(a). As discussed in 2.1, the ions are shot from the racetrack, which is a slit between the inner and outer iron cathodes. The size of the racetrack is shown in Fig. 3.2(b). The width and height of the racetrack are 7 cm and 30 cm, respectively. The semicircles on the top and bottom of the racetrack have radius of 3.5 cm. The intensity of the ion beams in the vertical direction is similar. Thus, the height of maximum homogeneous treated area is approximately 30 cm.

3 Experimental





- (b) Geometry of the racetrack

Figure 3.2: (a) Photograph of the linear anode layer ion source. (b) the geometry of the racetrack.

As already said, the ion source is installed in an in-line process vacuum chamber, next to the ZnO:Al₂O₃ tube target. Fig. 3.3 gives a schematic diagram of the process chamber during the ion beam treatment. The chamber wall on the left side is the end of the in-line system. The substrate is placed in a vertical carrier, which is located on the back chamber wall and can move along the x-direction. Optical emission spectroscopy (OES) is used to measure the ions through a window on the back chamber wall. The ion source in Fig. 3.3(a) is not tilted, and the ion beam is directed in y-direction. In Fig. 3.3(b), the ion source is tilted to an angle of θ with respect to x-direction, this means that the substrate receives ion beam with angle of θ around the y-axis. For this system, the ion source can only be tilted to the right direction, The maximum tilt angle is 40°. When the ion source is not tilted, the distance between the racetrack and the substrate is 16 cm; if the ion source is tilted by 40°, the distance is increased to approximately 21 cm. The size of the substrate holder is $30 \times 30 \text{ cm}^2$.

3.2.2 Parameters

As mentioned in Section 2.1.1, the ion source has two operating modes, diffuse and collimated modes. Due to the severe Fe contamination in the diffuse mode [109], in this work all films were treated in collimated mode. In collimated mode, discharge voltage,

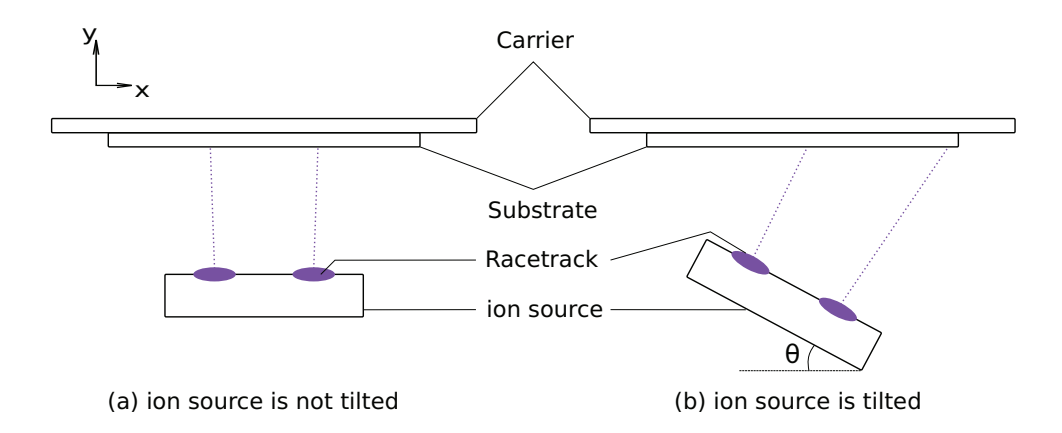


Figure 3.3: Schematic drawing of the ion beam treatments with non-tilted ion source (a) and tilted ion source (b).

source gas flow, and working pressure are adjustable parameters. The discharge current, however, depends on the above three parameters. The discharge voltage can be adjusted in the range of $0-3~\rm kV$ on the generator. All the treatments were performed at room temperature. Ar or O_2 were used as source gas.

Dynamic carrier is required for homogeneous treatment. The dynamical etch rate (DER) is defined as the following

$$DER = \frac{T \times v}{n},\tag{3.1}$$

where T is the removed thickness of the substrate, v is the speed of the carrier, and n is the number of passes the carrier made through the ion beam. For example, $DER = 5 \text{ nm} \cdot \text{m/min}$ means that the removed thickness would be 5 nm if the carrier was moved through the ion beam once with a speed of 1 m/min.

3.3 Characterization methods

3.3.1 Electrical properties

Two methods are available for measuring the electrical properties of ZnO:Al films in air and at room temperature. One is 4-point probe measurement, which is an easy and quick method to measure the sheet resistance of ZnO:Al films. It takes less than 1 min to obtain the results. The other one is Hall effect measurement, which can measure the resistivity, carrier concentration, and carrier mobility of ZnO:Al films.

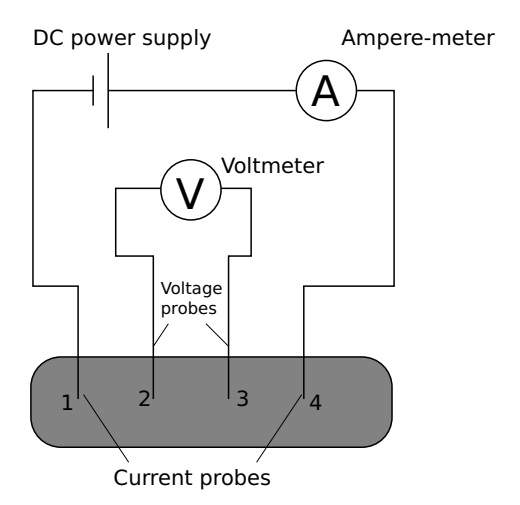


Figure 3.4: Schematic diagram of the principle of 4-point probe measurement.

3.3.1.1 4-point probe measurement

Four-point probe measurements are widely used to measure the sheet resistance of thinfilm semiconductors. Fig. 3.4 shows a schematic diagram of 4-point probe measurements. A current I which flows through the thin-film is measured by the outer probes with an ampere-meter, while the voltage drop over the sample V is measured by the inner probes with a voltage meter. If the film is infinitely large and the distance between the four probes are the same, the sheet resistance is calculated by

$$\rho_{\square} = \frac{\pi}{\ln(2)} \cdot \frac{V}{I}.\tag{3.2}$$

For the standard ZnO:Al film, the sheet resistance is approximately $3.2~\Omega$. If the sample does not have infinite size as compared with the space between the probes, correction factors in the range of 0.5 - 1 need to be considered.

3.3.1.2 Hall effect measurement

In Hall effect measurements, there are also 4-points contacts, but the 4-contacts are not in a line but in the corners of a square sample. Like the 4-point probe measurement, two contacts are used to measure current and the other two contacts are used to measure Hall voltage. Unlike the 4-point probe, during the measurement, the sample is located in a magnetic field. When an electrical current (I) flows through a sample in x-direction and a the magnetic field (B) is applied perpendicularly along z-axis, the electrons are subjected to a Lorentz force and drifted away from the current direction, resulting in an excess negative electrical charge on one side of the sample. The Lorentz force (F_L) from the magnetic field is perpendicular to the direction of current flow and magnetic field.

The value is given by

$$\overrightarrow{F_L} = e \overrightarrow{v} \times \overrightarrow{B}, \tag{3.3}$$

where v is the velocity of the electrons. The deflected electrons accumulate on one side of the sample until this transverse electrical field balances the Lorentz force, resulting the Hall voltage (V_H) , a potential drop across the two sides of the sample. For metals or semiconductors with primarily one type of carriers, the Hall voltage depends on the number of electrons n_s in the films

$$V_H = \frac{-IB}{qdn_s},\tag{3.4}$$

where d is the thickness of the sample. The carrier type is determined by the sign of the Hall voltage. During the measurement, the current (I) and magnetic field (B) are known, and the sheet resistance (R_{sh}) and Hall voltage (V_H) are directly measured. Thus, the carrier density (n_s) can be calculated by using equation 3.4. If the thickness of the film is known, the resistivity (ρ) can be calculated by

$$\rho = R_{sh}d. \tag{3.5}$$

Finally, the carrier mobility (μ) is calculated by using equation 2.18.

In this work, the Hall effect measurements are performed using a commercial Hall setup Keithley 926. The sample is square with size of 0.8×0.8 cm². Silver paste is used to make the four contacts on the corners of the square sample. The errors of this measurements depend on the area of the silver contact as compared to the sample area. To address this sample-particular error, at least two measurements were made on each sample generally at a current of 1 and 10 mA.

3.3.2 Optical Properties

The optical properties of the glass and ZnO:Al films are measured with spectrometers, where the total and diffuse transmissions, and reflections are measured. Using the above parameters, the absorption and Haze of ZnO:Al films can be calculated. Haze is defined as the percentage of light scattered in the total transmitted light. The distribution of the scattered light is determined by angular resolved scattering (ARS) measurements.

3.3.2.1 Total and diffuse transmission, Haze, reflection

To measure the optical properties, a LAMBDA 950 spectrometer from Perkin Elmer is used. The spectrometer contains two light sources in order to provide light with wavelength in the range of 250-2500 nm. During measurement, a monochromatic light beam is generated using a monochromator in the optical system. The light beam is divided into two beams by a mirror in the system. One of the beam is used as measurement beam, and the other is used as reference beam. While the measurement beam travels through a sample and is measured by a detector, the reference beam is

measured by the detector without traveling through the sample. By comparing the two measured intensities, the influence of the variation of light intensity can be excluded.

The light intensity is measured by the detectors located in the inner wall of an integrating sphere. The inner wall is coated with a highly reflective layer, so that all light in the sphere can be reflected to the detector. The measurement light beam comes into the sphere through a slit at one side of the sphere. When the total or diffused transmission measurements are made, the sample is put in front of the slit. The glass side of the sample faces the beam direction, like the situation in solar cells. On the other side of the sphere there is another slit, which can be covered either by a white reflector or a black absorber. With the white reflector, the directly transmitted beam is reflected back into the sphere, so that the total transmission (T_{total}) is measured. With a black absorber, the direct beam is absorbed, and only diffuse transmission $(T_{diffuse})$ is measured. Then, Haze is calculated as

$$Haze = \frac{T_{diffuse}}{T_{total}}. (3.6)$$

When the reflection is measured, the sample is put on the back slit of the sphere. The glass side of the sample still face the beam direction. The total reflected light (R) is measured by the detector. Then, the absorption (A) of ZnO:Al films is calculated by

$$A = 1 - T_{Total} - R. (3.7)$$

In this work, total transmission, diffuse transmission, and reflection measurements are made on textured glass, ZnO:Al films in the wavelength range of 300-1300 nm, with a resolution of 2 nm. The error of the spectrometer is approximately in the range of \pm 2 %. In near inferred region, the error increased to approximately \pm 4 % due to the variation in the sensitivity of the detector and intensity of the Halogen lamp. At wavelength near 860 nm, the error is much larger due to the change of detector.

3.3.2.2 Angular resolved scattering (ARS)

The angular distribution of the scattered light is measured using an in-house made system. A schematic diagram of the setup is shown in Fig. 3.5. A green laser with a wavelength of 550 nm is used as light source. After passing through a filter, a chopper, and an aperture plate, the light beam is scattered by the sample. The scattered light intensity is measured by a photo diode that rotates around the sample in a plane with a step of 1°. The scattered light intensity is first measured from 0° to + 170° in one direction. The measurement is then repeated once in the other direction 0° to - 170°. If the rough features on the sample are statistically symmetric, the measured intensity in the two directions should be the same; otherwise, the asymmetric structures yield different distributions in the two directions. In order to ensure that the detector and the sample are in the same plane, the height and position need to be adjusted carefully before every measurement. The voltage measured by the photo diode is assumed to be proportional to the light intensity, *i.e.* the light intensity can be represented by the diode voltage V_s . Because the measuring is performed in in-plane geometry, the diode

measured data has to be integrated over all azimuthal scattering angle to include the whole light scattering cone at a certain polar angle θ . Thus, in this work, the angular distribution function $S(\theta)$ of scattered light is calculated by

$$S(\theta) = 2\pi \times \frac{r^2[\cos(|\theta - 0.5|) - \cos(|\theta + 0.5|)]}{a_{detector}} \times \frac{V_s(\theta)}{V_0},$$
(3.8)

where r is the distance between the detector and sample, $a_{detector}$ is the area of the detector, and V_0 is the reference diode voltage measured without sample. This calculation is correct if the sample is isotropic, which leads the same measured intensity in the two directions.

3.3.3 Surface topography

Within this work, the surface topography of glass and ZnO:Al films are characterized by Scanning Electron Microscopy (SEM) and Atomic Force Microscopy (AFM). SEM can give clear topographies with very high magnifications at different angles, while AFM yields three dimensional images which can be statistically analyzed.

3.3.3.1 Scanning Electron Microscopy (SEM)

During the SEM measurement, the sample is scanned by a focused electron beam of specific energy. The electron beam, which typically has an energy ranging from 0.5 keV to 40 keV, is focused by one or two condenser lenses to a spot about 0.4 nm to 5 nm in diameter. The beam passes through pairs of scanning coils or pairs of deflector plates in the electron column, typically in the final lens, which deflect the beam along the x and y axes such that it scans in a raster fashion over a rectangular area of the sample surface. The primary electrons interact and exchange energy with the sample surface. High energy electrons are reflected back from the surface through elastic scattering and secondary lower energy electrons are emitted by the inelastic scattering. Both of

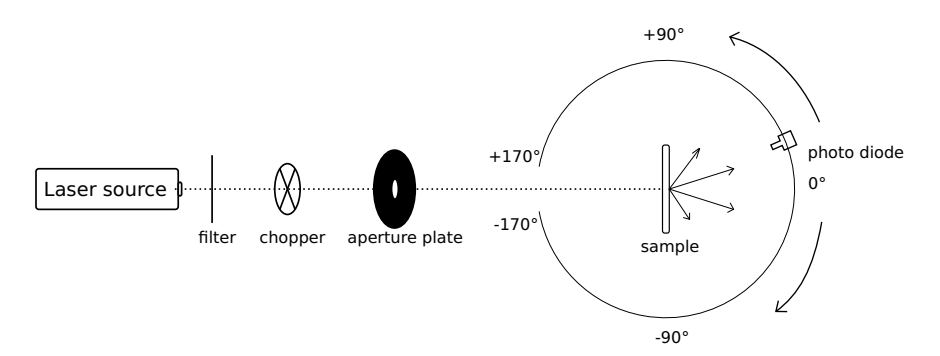


Figure 3.5: Schematic diagram of measurement setup of angular resolved scattering (ARS).

3 Experimental

them can be detected by specific detectors and used as information for the topography and internal structures of the samples. Electronic amplifiers of various types are used to amplify the above signals are displayed as variations in brightness. Therefore, the topography of the scanned area is recorded. The magnification the microscopy can be adjusted, by changing the size of the primary electrons raster. Since an electron beam is used to image, the sample can be cut and cross-sectional images are possible.

In this work, the measurements are performed with a Gemini field-emission SEM by LEO. Typically the electrons used for bombarding the samples have energy of 20 kV and incident angle of 60° with respect to the surface normal. The samples used for SEM measurements have size of $1\times 1~\rm cm^2$. To prepare cross-sectional SEM samples, the samples are broken manually with the help of a glass cutting machine. Cautions are required in order to protect the cross-section of sample. The maximum resolution of the SEM measurements is in the range of $1-10~\rm nm$. If the samples are not conductive, a thin gold or iridium layer must first be sputtered onto the sample surface.

3.3.3.2 Atomic Force Microscopy (AFM)

Unlike SEM measurements, conducting films are not required for AFM measurements. During an AFM measurement a $\rm Si/SiO_2$ tip, fabricated by lithography and having a height of $10-15~\mu m$, is used to scan the sample surface. The operating principle of the AFM is shown in Fig. 3.6. A monochromatic light beam from a laser strikes

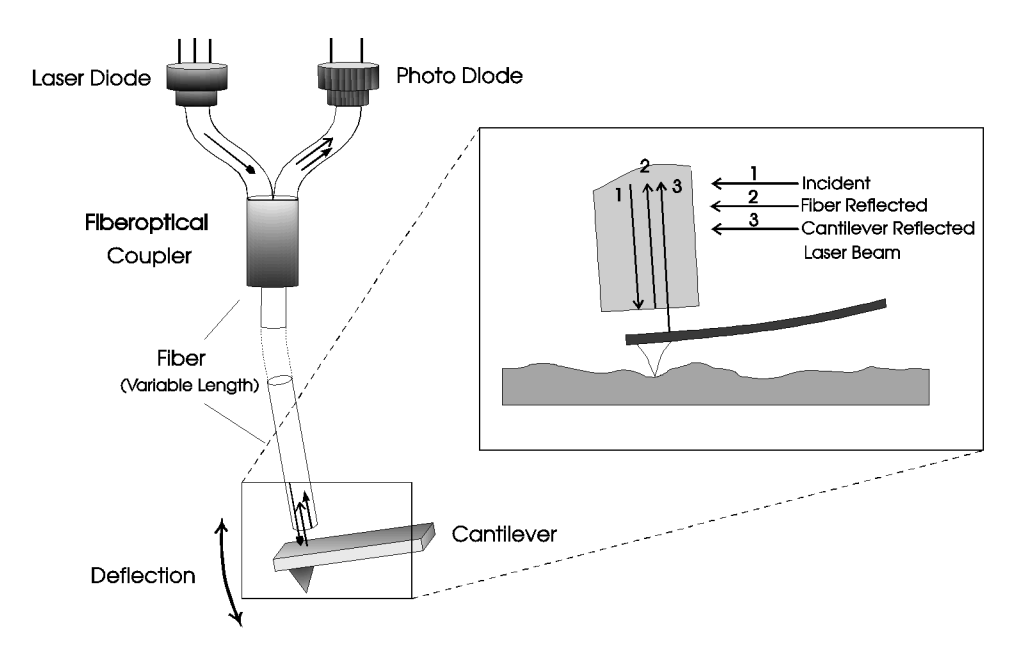


Figure 3.6: Schematic of the working principle of atomic force microscopy (AFM) [110].

the cantilever. Two reflected light signals are detected by a photo diode. One is the reflection of the fiber, which serves as reference signal. The other is the reflection from the cantilever. By analyzing the superposition of the two reflected signals, the distance between the fiber and cantilever is determined. When the tip is scanning over a sample, laser light incident on the back of the cantilever is deflected differently as the surface features change.

In general, there are two operation modes for AFM measurements: contact and noncontact (or tapping) mode. In contact mode, the tip presses on the sample while scanning and the topography of sample is measured directly by the deflection of the cantilever. The load force between the tip and sample is held constant by adjusting the potential across the piezoelectric z-axis control. The deviation of z-feedback determines the topography of surfaces. In the non-contact mode, the cantilever is externally oscillated at or close to its fundamental resonance frequency by a small piezoelectric element. The distance between tip and sample can be controlled by the amplitude and set point of the cantilever. When the tip is within $1-10~\rm nm$ of the sample surface, the van der Waals forces tend to change the amplitude and frequency of the cantilever. The target value of z-feedback is a constant amplitude. Thus, the frequency of the piezoelectric element has to be modulated. The modulation values correspond to the surface topography. In the non-contact mode the tip does not interact with the sample directly, therefore wears down the tips more slowly as compared to contact mode.

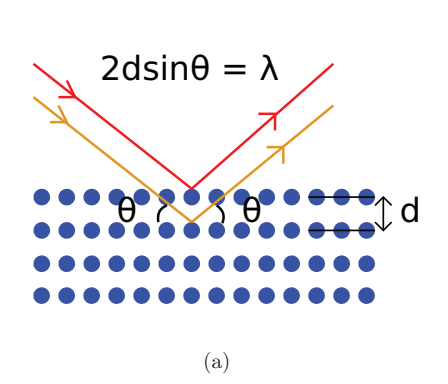
In this work, the AFM measurements are performed in non-contact mode using a Nano 300 (SIS). It takes around 15 - 40 min to get one image depending on the scanning speed, size, and resolution. To get a good image, the tip has to be clean and sharp, and has a good shape before the measurement. After scanning, the AFM images have to be leveled by plane correction. Typically the obtained images have a data size of 512×512 pixels, which corresponds to the surface height h(x,y) in x- and y- directions. Therefore, it is possible to characterize a surface by many statistical parameters. The most common statistic parameter used to describe the roughness of a surface is standard deviation σ of the surface heights, also called root-mean-square (rms) roughness. The rms roughness is calculated by

$$\sigma = \sqrt{\langle [h(\overrightarrow{r}) - \overline{h(r)}]^2 \rangle}, \tag{3.9}$$

where $\overline{h(r)}$ is the average height of the surface. The roughness σ characterizes the spatial variation of a rough surface along the vertical direction. Larger values of σ indicates a rougher surface. Two other parameters, lateral correlation length ξ and roughness exponent α characterize the spatial variation in lateral direction and can be determined from the height-height correlation function H(r) as described in Section 2.2.4.5.

3.3.4 Structural properties

Within this work, the structural properties of the ZnO:Al films are characterized by x-ray diffraction (XRD) and transmission electron microscopy (TEM). Though TEM can also determine the topography of thin-films, the role of TEM in analyzing the structural properties is emphasized, as the topographies are more easily available from SEM



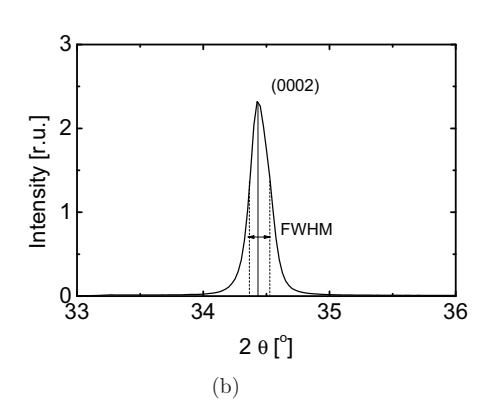


Figure 3.7: (a) - Schematic of Bragg's law; (b) - a typical diffraction peak versus 2θ of ZnO:Al films.

and AFM measurements. In the following, the sample preparation and measurement principles of XRD and TEM are briefly introduced.

3.3.4.1 X-ray diffraction (XRD)

XRD is a non-destructive technique for determine the crystallographic structures in crystals and polycrystalline thin-films. The energetic x-rays can penetrate deep into the samples and providing information about the bulk material. The wavelength of the x-rays used is comparable to the size of atoms (in the range of a few angstroms to 0.1 angstroms). Thus, x-rays are suited to probe the arrangement of atoms or lattices in a wide range of materials. a common XRD measurement is the so-called $\theta-2\theta$ scan. In the $\theta-2\theta$ geometry, the x-ray tube is stationary, the sample is moved by the angle θ and the detector is simultaneously moved by the angle 2θ . To achieve this configuration, the sample holder and the detector are driven in a 1:2 relationship.

In $\theta-2\theta$ measurement, if the sample has crystalline portions parallel to the surface with a periodic lattice plane spacing (d) larger than that of the incoming x-rays, the x-rays will constructively interfere when the Bragg condition is meet. The Bragg condition is expressed as

$$2d\sin(\theta) = n\lambda,\tag{3.10}$$

where d is the inter-plane distance, θ is the incident angle of x-ray beam, n is an integer representing the order of the diffraction peak, and λ is the wavelength of the x-rays. A schematic of Bragg's law is shown in Fig. 3.7(a). By scanning through different angles (but keeping the $\theta-2\theta$ geometry), peaks in the reflected signal appear when Equation 3.10 is satisfied. The positions of the diffracted peaks correspond to a given lattice spacing that can be correlated to a particular crystal orientation, assuming the composition of the sample is know. The different crystallographic orientations are denoted by Miller indices (hkl). With hexagonal and rhombohedral lattice systems, it is possible to use

the Miller indices which have 4 numbers (hkil), where i=-h-k. In the $\theta-2\theta$ measurement, since the sample is fixed, thus only the planes parallel to the substrate are measured. Therefore, it is important to note that other orientations may exist, but are not observed.

A typical XRD diffractogram of sputtered ZnO:Al films is shown in Fig. 3.7(b). The dominate peak position is normally locate at an angle of 34.4°, which corresponds to (0002) out of plane orientation. The positions, widths, intensities, and shape of the peaks provide important information about the structure of the measured materials. The position of peaks shift to smaller or larger angles if the lattice constant is larger or smaller, respectively. The shifts of the peak in ZnO:Al films can be caused by stress in the films and the impurities such as dopants in the films.

In this work, the XRD measurements were performed by Xpert-pro (PANalytical) in $\theta-2\theta$ mode. The x-ray source was copper- K_{α} with a wavelength of 0.154 nm. The incident angle of x-ray beam θ was changed from 10° to 40° in small steps. The widths of the peaks are characterized by the full width at half maximum (FWHM) which is denoted Fig. 3.7(b). The vertical grain size τ of a grain can be calculated from the FWHM of the peak using the Scherrer formula

$$\tau = \frac{K\lambda}{\beta(2\theta)\cos(\theta)},\tag{3.11}$$

where K is the shape factor and β is the FWHM of a particular peak in radians. The dimensionless shape factor has a typical value of about 0.9. Note that lattice distortions such as defects and strain reduce the estimated grain size, since the estimated grains corresponds to the thickness of the coherently scattering layers in the vertical direction. Note that the relative error of FWHM has been estimated to be between +20 and -3 % [68], since FWHM is sensitive to the sample alignment.

3.3.4.2 Transmission electron microscopy (TEM)

TEM is a microscopy technique whereby a beam of electrons is transmitted through an ultra thin specimen, interacting with the specimen as it passes through. TEMs are capable of imaging at a significantly higher resolution than light microscopes, owing to the small de Broglie wavelength of high energy electrons. Unlike the SEM, where back scattered and secondary electrons are utilized, forward scattering electrons include a direct beam of mostly elastically scattered electrons, and a diffraction and inelastic scattered electrons through the thin specimen are seen on a screen as diffraction patterns or images. From top to bottom, TEM measurement set up normally consist of three components: illumination system, objective lens/stage, and the imaging system. The illumination system contains the electrons gun and the condenser lenses. Its role is to take the electrons from the source and transfer them to the specimen. Parallel electron beams were used in this work. The stage is used to clamp the specimen holder in a correct position such that the objective lens can produce reproducible diffraction patterns and images. The distance between the sample and intermediate lens has to be fixed. The imaging system uses several lenses to magnify the image or the diffraction patterns

3 Experimental

produced by the objective lens and focus these on the viewing screen. The center part of a TEM is the objective lens. A schematic drawing of objective lens and imaging system is shown in Fig. 3.8. Typically, there are two operation modes in TEM measurement: diffraction mode and image mode. The working principle of the two operation modes are shown separately in the figure. The objective lens disperses the electrons emerging from the back surface of the specimen, to create a diffraction pattern in the back-focal plane. The intermediate lens and project lens then take the diffraction pattern as object, and project them on the viewing screen. If an aperture is inserted on a plane conjugate with the specimen, then it creates a real aperture on the specimen. The resulting diffraction pattern is called selected area diffraction pattern (SADP).

To view the images of the specimen, an aperture is inserted on the back-focal plane of the objective lens to block out most of the diffraction pattern, except that small area which is visible through the aperture. If the aperture is adjusted such that only electrons in the direct beam can pass through, then the bright-field (BF) images are obtained. If instead the scattered electrons (e.g., a specific diffracted beam (usually) or a portion of a diffraction ring) are selected, dark-field (DF) images are obtained.

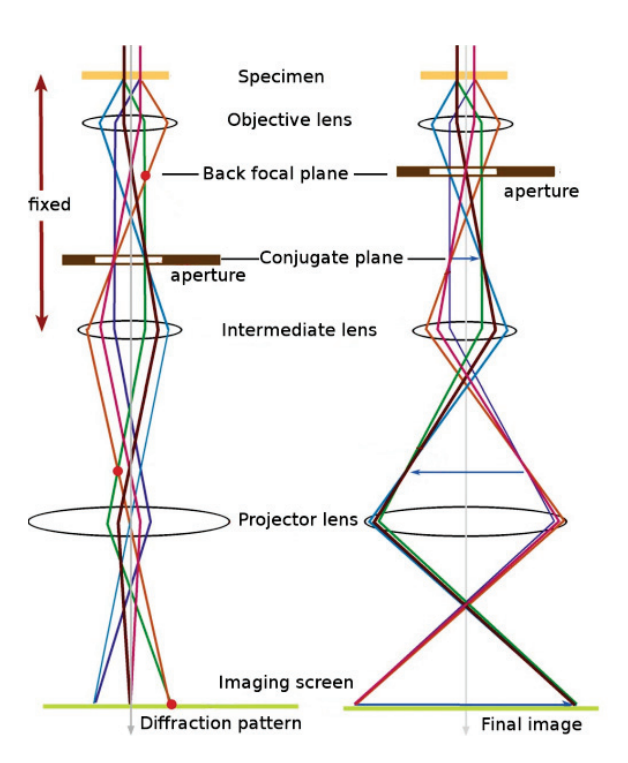


Figure 3.8: Schematic of the objective lens and imaging system of a typical TEM setup. The left figure shows the diffraction operation mode while the right one shows the image working mode. [111]

One challenge of making TEM measurement is that thin specimens are required (generally less than 100 nm). Cross-sectional and plan view ZnO:Al films were investigated. To prepare the specimen for cross-sectional image, focused ion beam (FEI co., Helios nanolab 400S) was used to cut the ZnO:Al films on glass substrates twice to get a thin lamella. Pt was deposited on the ZnO:Al film surface in order to protect the surface of the film during ion beam bombardment. Planar view specimens were prepared by mechanical grinding, dimpling, and Ar ion milling employing the back thinning technique.

The SADP depends on the nature of the specimen. The positions of the spots in the SADP corresponds to the reciprocal distances of the planes in the specimen. Only the planes parallel to the electron beam are detected by TEM measurements. Thus, in a planar view of c-axis oriented ZnO:Al sample, the diffraction spots from (0002), (10-10), (10-12) and (10-13) planes are absent, and only the spots from (10-10), (11-20) and (20-20) planes are observed [72]. Generally, a ring pattern indicates a random in-plane distribution of the crystallites within the selected area, while regular spots indicates the crystallites within the selected area have preferred in-plane orientation. By integrating over the rings of a diffraction pattern, the radius of the rings is the reciprocal of the lattice constant. A curve with many peaks similarly to XRD spectra is obtained. However, the integration of rings from a TEM SADP is different than an XRD pattern, since in XRD $\theta-2\theta$ measurements, the planes parallel to the substrate surface are detected. Moreover, the diffraction peaks of electrons from the atoms in TEM are broader than in XRD.

3.3.5 Surface composition - X-ray photoelectron spectroscopy (XPS)

Within this work, the surface chemical composition after ion beam treatment is characterized by x-ray photoelectron spectroscopy (XPS).

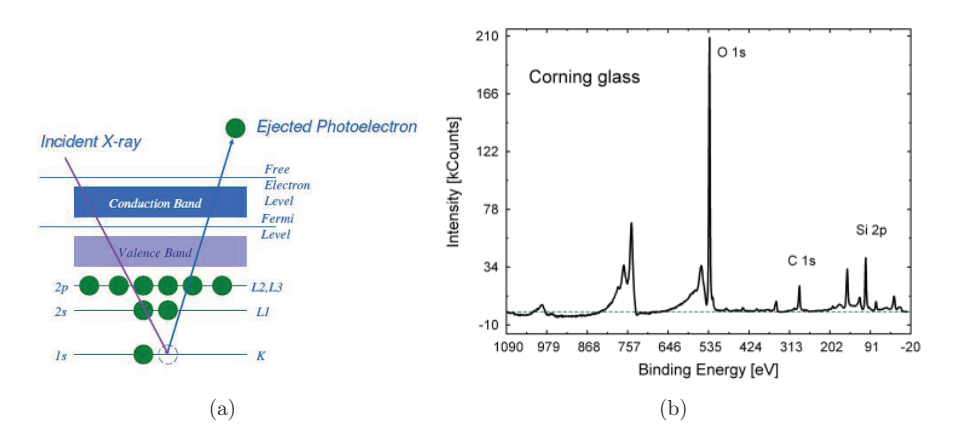


Figure 3.9: (a) Schematic of the emission of electrons by x-ray. (b) A typical XPS spectrum of Corning glass.

3 Experimental

Photoelectron spectroscopy utilizes photo-ionization and analysis of the kinetic energy distribution of the emitted photoelectrons to determine the composition and electronic state of the surface region of a sample. In the XPS, the photon energy of x-ray is usually in the range of 200 - 2000 eV. The energy of the photons E is expressed as

$$E = h\nu, \tag{3.12}$$

where h is the Planck constant and ν is the frequency of the photon. The photons with certain energies $h\nu$ are absorbed by material, leading to ionization and the emission of core (inner shell) electrons. The kinetic energy of the emitted photoelectrons KE must obey the energy conservation law

$$E(A) + h\nu = E(A^{+}) + KE,$$
 (3.13)

where E(A) and $E(A^{+})$ are the energy of atom before and after ionization, respectively. Thus

$$KE = h\nu - (E(A^{+}) - E(A)).$$
 (3.14)

The term $E(A^+) - E(A)$, representing the energy difference between ionized and neutral atoms, is the binding energy of the electron. Another simplified consideration about the binding energy of electrons is shown in Fig. 3.9(a). The binding energy may be regarded as the energy difference between the initial and the final state after the photoelectron has left the atom. Because there is a variety of possible final states of the ion from each type of atom, there is a corresponding variety of kinetic energies of the emitted electrons. Moreover, there is a different probability or cross-section for each final state. Therefore peak intensity indicates the relative probabilities of the various ionization processes.

Because each element has a unique set of binding energies, XPS can be used to identify and determine the concentrations of the elements in the surface. Variations in the elemental binding energies (the so called chemical shifts) arise from differences in the chemical potential and polarizability of compounds. These chemical shifts can be used to identify the chemical state of the material being analyzed.

In this work, XPS analysis were carried out with a Physical Electronics XPS 5600 spectrometer using monochromatized Al K α radiation (hv = 1486.6 eV). The analyzed area of the sample was 800 μ m². The pressure in the analysis chamber was around 5×10^{-9} mbar. Two different measurement modes were recorded. The survey scans were performed using a high pass energy of 187.8 eV and a step size of 1 eV, which correspond to an energy resolution of a few eV. This mode was used to detect the elemental composition of the surfaces. The binding energy scale was calibrated from the hydrocarbon contamination using the C 1s peak at 285.0 eV. The relative error of the estimated atomic percentage is $\pm 15\%$. Fig. 3.9(b) shows a typical XPS survey scan of a Corning glass surface. The O 1s, Si 2p and C 1s core levels are identified by the peaks at binding energy of 532 eV, 102 eV and 285 eV, respectively. The intensity of each peak is directly related to the quantity of each element within the measured area.

In addition core level spectra were recorded (pass energy $= 11.75 \, \text{eV}$, step size $= 0.05 \, \text{eV}$) with an energy resolution of about $0.5 \, \text{eV}$ in order to determine the different

compounds of each element. Core peaks were analyzed using a nonlinear Shirley-type background [112]. The peak positions and areas were optimized by a weighted least-squares fitting method using a convolution of Gaussian and Lorentzian line shapes. Quantification was performed on the basis of Scofield's relative sensitivity factors [113]. Thus, by making a detailed scan of several peaks, more information about the corresponding elements are extracted.

3.3.6 Solar cells characterization

3.3.6.1 Current-voltage measurement

As mentioned in Section 2.3.4, the performance of solar cells are characterized by cell efficiency η , fill factor FF, short circuit current density J_{sc} , and open circuit voltage V_{oc} . These parameters can be obtained from the characteristic of an illuminated J-Vcurve. Standardized measurement conditions of solar cells allows for the comparison of different cells. The standards for cell testing are Air Mass 1.5 spectrum (AM 1.5) for terrestrial cells and Air Mass 0 (AM 0) for space cells. The intensity of AM 1.5 solar irradiation is 1000 W/m² and cell temperature is 25 °C. The cells in this work were measured by a class A solar simulator (WXS-140S-Super, Wacom) under standard test conditions. The class of the sun simulator is defined according to the spectra match, irradiance inhomogeneity, and temporal instability. The light source in this setup comes from the combination of xenon and halogen lamps, which produce light with shorter and longer wavelengths, respectively. Several filters are then utilized to simulate the AM 1.5 spectrum. The challenges for maintaining stable results are the homogeneity of the light source and the temperature control of the solar cell. The homogeneity of the light is achieved by integrator and collimator lenses. The solar cells are fixed with vacuum to a copper plate equipped with water cooling and integrated electrical heating keeping its temperature constantly at 25 °C. Moreover, the intensity of the light source might also be influenced by the age of the lamps. Therefore, calibrations of the setup with photo diode are performed regularly before the cell measurement to ensure the accuracy of the results. The cell current densities are measured as a function of voltage by SMU 238 (Keithley) while the cells are illuminated. Short circuit current density J_{sc} , open circuit voltage V_{oc} , and fill factor FF were then determined from the J-V curve. Cell efficiency is calculated from the maximum output electrical power over the light, as introduced by equation 2.35. Additionally, blue (BG 7) and red filters (OG 590) were used to block part of the spectrum when cell performances under a special light spectrum are desired.

3.3.6.2 Quantum efficiency

Spectral response of solar cells in this work was measured with an in-house made setup. A xenon lamp was used as light source. Using a monochromator and chopper, a monochromatic light with wavelength between 200 and 1400 nm were generated. The source beam is then divided into two beams using a mirror. A reference beam is directed to a photodiode and the other is used to illuminate the solar cell. The generated current density

3 Experimental

of the solar cell sample is detected with a source measurement unit, normalized to the illumination density of the lamp, and is referred to as the differential spectral response (DSR). For QE measurement of microcrystalline Si thin-film solar cells, light with wavelengths from 300 to 1100 nm are used with a step of 10 nm. The quantum efficiency is calculated from the differential spectral response as shown in equation 2.36.

4 Characterization of the ion beam treatment

This chapter introduces the characterization of the ion beam treatment. The ion beam is generated from a linear anode layer ion source. First of all, the characterization of the ion beam by Optical emission spectroscopy (OES) is given. In order to modify the surfaces by ion beam treatments in a controllable way, the characteristics of the ion beam etching should be investigated. Therefore, as a foundation of this work, this chapter shows the etch rates of glass substrates and ZnO:Al films under different treatment conditions. The experimental etch rates are compared with simulation and theoretical predicted values.

4.1 Optical emission spectroscopy of the ion beam

Optical Emission Spectroscopy (OES) has been applied to detect Ar and O_2 ions in different ion beams. The optical fiber was fixed at the backside of the process chamber in order to watch the ion beams through a window. The detectable wavelengths of this optical fiber are in the region of 393-526 nm. Fig. 4.1(a) shows the emitted light spectra of Ar and O elements versus wavelength by black and blue lines, respectively [114]. The intensities of these lines represent quantitative estimates of relative line strengths that take account of varying detection sensitivity at different wavelengths. State I and II indicate neutral and single ionized elements, respectively. It is seen that both neutral and single ionized Ar^+ are detectable, while only single ionized O_2^+ and O^+ ions can be detected by this measurement setup, since the lines emitted by neutral oxygen are in the wavelength region of 616-778 nm.

The emission spectra of ion beams generated with different parameters were recorded. The discharge voltage was varied from 2 kV to 1 kV, while the pressure in the chamber was kept at 1 μ bar. 30 standard cubic centimeter per minute (sccm) Ar, 60 sccm O₂, and mixed 20/20 sccm Ar/O₂ were used as source gases for the ion source, respectively. The emission spectra of the six ion beams are shown in Fig. 4.1(b). Most peaks can be attributed to Ar and O elements, as compared with Fig. 4.1(a). Few peaks might be related to the impurities in the environment or caused by the artificial error of the spectrometer. In this work, the focuses are on the Ar and O peaks with highest intensities which are marked by arrows in Fig. 4.1(b) and enlarged in Fig. 4.1(c) and (d), respectively. The ion beams generated from discharge voltage of 2 kV are shown in bold lines, while the ion beams with smaller discharge voltage are shown in thin curves. The Ar, O₂, and mixed Ar/O₂ ions are shown by solid, dash-dotted, and dashed curves, respectively.

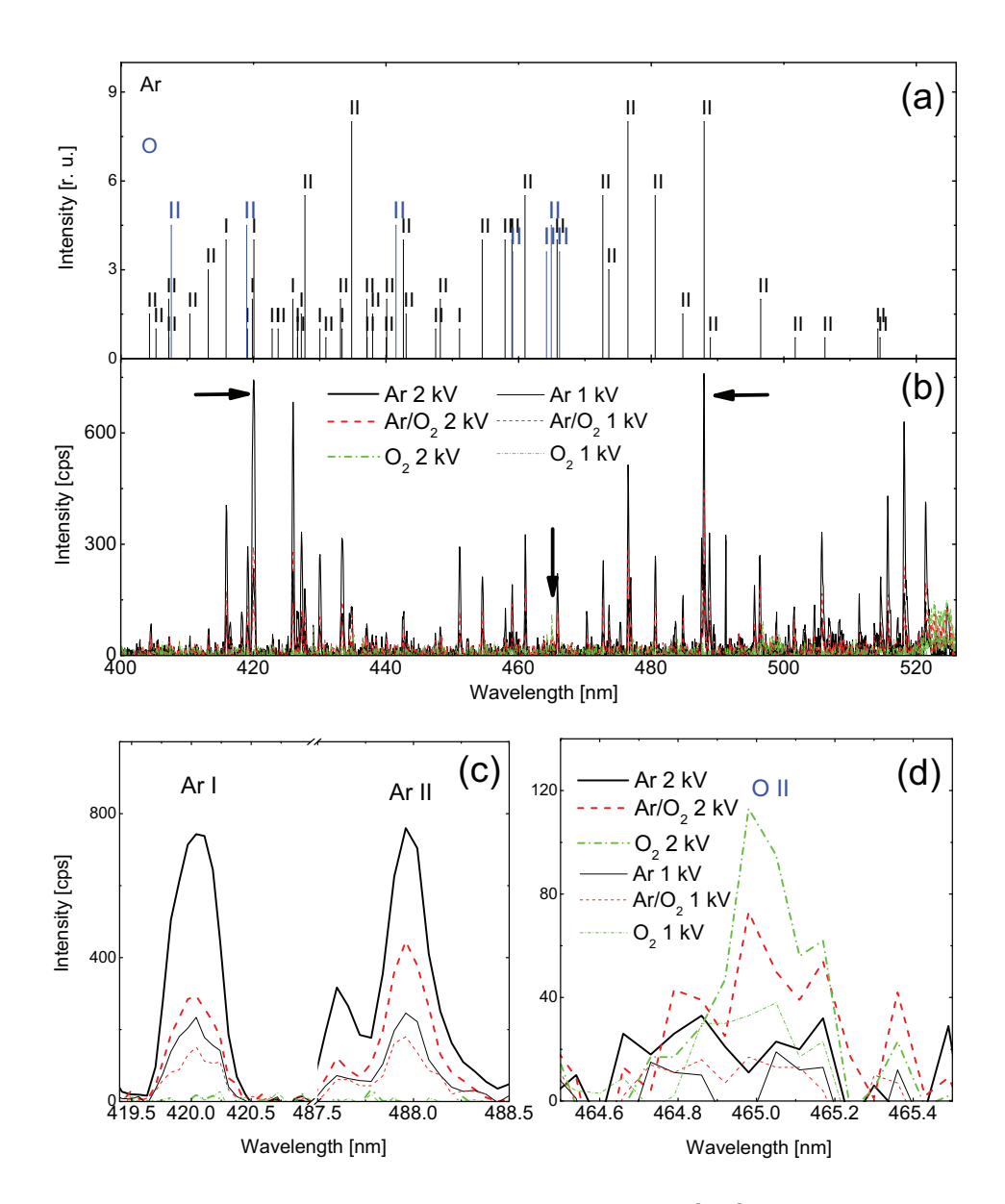


Figure 4.1: Optical emission spectra of Ar and O elements [114], in which I indicates neutral and II indicates singly ionized gas (a). OES signals of ion beams generated from Ar (solid curve), ${\rm Ar/O_2}$ (dashed curve) and ${\rm O_2}$ (dash-dotted curve) gas in the wavelength range of 393-526 nm (b). Two enlarged spectra are given in the range of 419.5-420.5 nm and 487.5-488.5 nm (c) and 464.5-465.5 nm (d).

For Ar ion beams with two different discharge voltages, the peaks at wavelength about 420 nm originated from neutral Ar has similar intensity to the peaks of singly ionized Ar at about 488 nm (see Fig. 4.1(c)). It indicates that in Ar ion beam, the ionization fraction of Ar gas atoms may be approximately 50%. With half discharge voltage, the Ar peak intensity decreases more than a factor of 3, indicating that much less ions were generated with smaller discharge voltage. For O_2 ion beam, because the neutral state of oxygen is not measurable with this setup, it is not possible to estimate the oxygen ionization fraction. However, the intensities of oxygen ions are so low that when the discharge voltage was 2 kV, only one peak at 465 nm was measured, and when the discharge voltage was 1 kV, almost no signals were detected (see Fig. 4.1(d)). The O peak at 465 nm represents first ionized state, i.e. O_2^+ or O^+ . Because the threshold energy for O^+ ions is higher than O_2^+ ions (see Section 2.1.1), it is assumed that O_2^+ ions contribute more to this peak.

When pure Ar or O_2 were used as source gases, only Ar or O peaks were detected, respectively. With source gas of mixed Ar/O_2 , both Ar and O peaks were observed, though with lower discharge voltage, the intensity of O peak was very low. In the mixed Ar/O_2 ion beams, the intensity of Ar ions peak is around 8 times higher than that of O peak, means that the concentration of Ar ions is much higher than O ions, indicating lower ionization fraction of O_2 ions.

4.2 Static etching

Static etching refers to static substrates in front of the ion source. The ions are shot from the narrow racetrack of the ion source, thus the intensities of the ions are not uniform along the x-direction (see Fig. 3.3). The removed thickness of ion bombarded substrates is proportional to the intensity of the ions, including ion energy and density. Assuming that the distribution of ion energies is not related to their positions in the beam, the etch rate is proportional to the ion density. The removed thickness profiles of statically treated substrates were measured, in order to obtain information on the ion beam density. Source gas and tilt angle were varied in this section. The etch rate of glass substrates with different parameters were estimated based on these removed thickness profiles.

4.2.1 Different source gas

It is known that the etch rate of certain material depends on the species of ions. The mass, velocity and chemistry of different ions influence the interactions between the ions and the substrates. Static ion beam etchings were performed with different source gases $(Ar, O_2 \text{ and mixed } Ar/O_2)$.

Three Corning glass substrates were etched statically by ions generated from different gas compositions. The source gas for the three treatments was 30 sccm Ar, 60 sccm O_2 , and mixed 20/20 sccm Ar/O_2 , respectively. The discharge voltage was 2 kV and the working pressure in the process chamber was 1 µbar. The treatment time was fixed

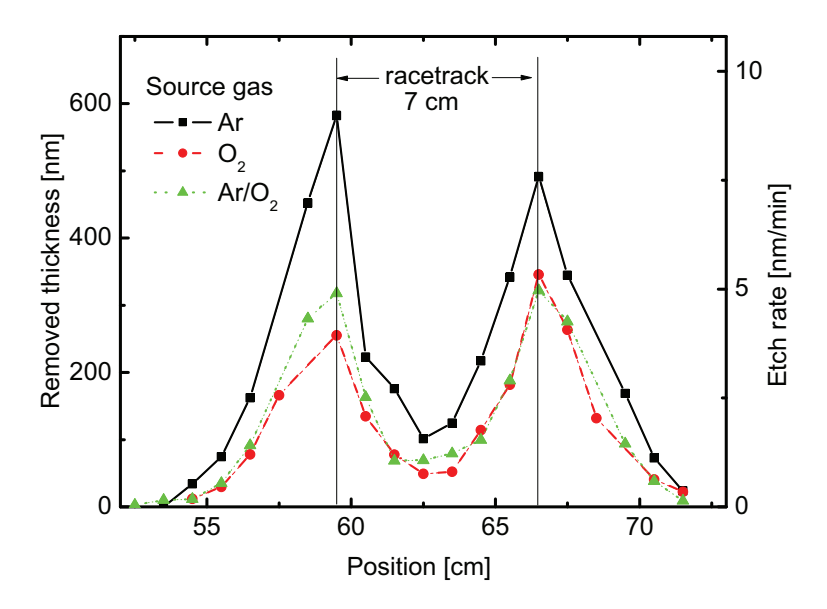


Figure 4.2: Removed thickness and static etch rate of glass substrates by Ar (squares), O_2 (circles), and Ar/O_2 (triangles) ions.

for 65 min. Discharge current was determined by the source gas, working pressure, and discharge voltage. Under the above conditions, the discharge currents were in the range of 0.14-0.19 A for the three treatments. The ion source was not tilted during these treatments. A line under a vacuum tape was protected from the ion beam etching, while the other areas were etched. Thus, after removing the vacuum tape, the thickness step at the edge of vacuum tape measured by Dektak provides the removed thickness.

The removed thickness and static etch rate of differently treated glass substrates are shown in Fig. 4.2 versus positions on the substrate. The x-axis represents the distance to the left chamber wall. For each treatment, the removed thickness profile has two peaks, indicating the fastest etched positions. The distances between the two peaks is 7 cm, the same as the width of the racetrack of ion source. Therefore, it is concluded that the removed thicknesses are the highest at the racetrack positions, and decreases at other positions. It means that the ion flux is higher in front of the racetrack, and decreases as getting far away from the racetrack.

The figure also shows that the removed thickness and etch rate of Ar ion etching are the highest among the three treatments, while the other two etchings lead to similar smaller removed thicknesses and etch rates. Removed thicknesses are directly corresponding to sputtering yield (atoms/ion) multiplied by ion flux (number of ions). The ion flux generated from O_2 gas is lower than from Ar gas, as shown by OES measurements in the last section. The comparison of sputtering yield by Ar and O ions on glass substrates

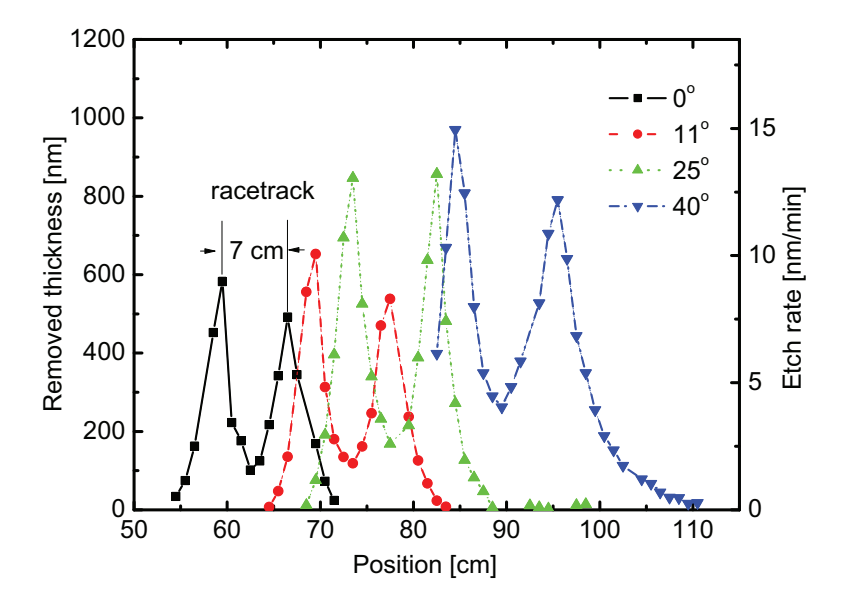


Figure 4.3: Removed thicknesses and etch rates of Corning glass substrates by Ar etching from non-tilted ion source (squares), 11° tilted (circles), 25° tilted (triangles) and 40° tilted (inverse triangles) ion source.

will be discussed in the final section of this chapter.

4.2.2 Tilted ion source

As shown in Fig. 3.3, the ion source can be tilted to change angle of incidence. The etch rates of the substrates are different for ion beams incident from different angles. The etch rates of Corning glass substrates by Ar ion beams were investigated at four different angles in terms of removed thickness.

Three $10 \times 10~\rm cm^2$ glass substrates were placed along x-direction and treated by Ar ion beams for 65 min. The experiments were performed when the ion beam was not tilted and tilted 11°, 25°, and 40° to surface normal. The discharge voltage for all the ion beam treatments was fixed at 2 kV. The source gas was 30 sccm Ar and the working pressure in the process chamber was 1 µbar. Vacuum tape was used to measure the removed thickness along x-direction.

Fig. 4.3 shows the removed thicknesses and static etch rates of glass substrates versus positions on the substrates. As the last figure, the x-axis represents the distance to the left chamber wall, and the peaks in each etching profile correspond to the racetrack. The distances between the two peaks for the etchings by non-tilted, 11° tilted, 25° tilted, and 40° tilted ion source are 7 cm, 8 cm, 9 cm, and 11 cm, respectively. The slightly increase

of the width of peak was caused by the tilt of ion source. Moreover, with tilted ion source, the etched area gets wider and shifts to larger x-position.

The figure also shows that the etch rate gets higher with increasing tilted angle, which is a common effect for ion beam etching as discussed in Section 2.1.2.1. The sputtering yield increases with increasing incident angle and reaches maximum at about $70-80^{\circ}$, because more sputtered recoils can move to sample surface with tilted ion incident angle. When the incident angle is approaching 90° , sputtering yield will dramatically decrease as a result of extended scattering and reflection. However, the maximum tilt angle of the ion source in this system is 40° . Thus, it is not possible to check the incident angle for maximum sputtering yield.

4.3 Dynamic etching

This section examines the etch rate of Corning glass and ZnO:Al films by dynamic ion beam etching. The substrate was moved through the ion beam in order to receive uniform treatment. The etch rate of ZnO:Al films and glass substrates by various ion beam treatments are presented in the following.

4.3.1 Different power and tilt angle

A series of glass substrates were etched by Ar ion beams with different discharge power and tilt angle of ion source. The pressure during the ion beam etching was fixed at 1 µbar and the source gas was kept at 30 sccm. The discharge voltage was varied from 500 V to 2000 V to achieve various discharge powers. The discharge power is the product of discharge voltage and discharge current. The dynamic etch rates (DER) defined according to equation 3.1 in Section 3.2.2 were calculated from the removed thickness. The etchings were performed by ion source with tilted angle of 25° and 40° to surface normal. Experimental obtained dynamic etch rates versus discharge power with different incident angles are shown in Fig. 4.4 by solid symbols. The dynamic etch rates estimated from static etching in Fig. 4.3 are also shown by empty symbols. These DERs were estimated by integrating the static etch rates over the etched area. It is shown that the estimated DERs from static etching are consistent with the experimental measured DERs.

As already experienced in static etching, the DER is higher at large tilted angle. If higher etch rates are required, the ion source needs to be tilted. DER increases linearly with increasing discharge power, reflecting the fact that ions with higher energy lead to higher sputtering yields than those of low energy. Note that when the discharge voltage is in low kV range, most of ions obtained energies also in low keV range, then the ion-sample collisions belong to knock-on regime, in which the sputtering yield is proportional to ion energy E_i , as described by equation 2.8. Thus, the DER increases linearly with the increasing discharge voltage. Maximum etch rate of 1.5 nm·m/min was achieved at 40° and discharge power of 313 W.

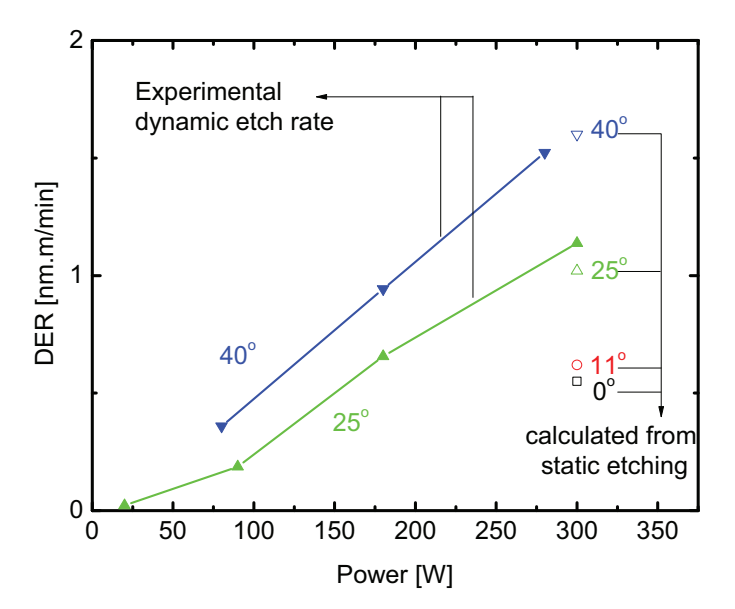


Figure 4.4: Dynamic etch rate (DER) of glass substrates by Ar ions versus discharge power of the ion source when the tilt angle of ion source is 25° (triangles) and 40° (inverse triangles). The calculated DER from static etching in Fig. 4.3 are shown with empty symbols.

4.3.2 Different source gas and substrate

The DER also depends on the ion species and etched materials. The static etching experiments of glass substrates with different ions have shown that the Ar ions have higher etch rate than the O_2 ions. This section presents the DER of Ar and O_2 ions on ZnO:Al films and glass substrates.

When the ion source was tilted 40° to substrate normal, $30 \, \text{sccm}$ Ar and $60 \, \text{sccm}$ O_2 were used as source gases to treat ZnO:Al films and glass substrates with different discharge power. Again, the pressure in the process chamber during the ion etching was fixed at 1 µbar and the discharge power was varied by using different discharge voltage. The DER results versus discharge power for different treatments are shown in Fig. 4.5. Similarly as last figure, DERs increase linearly with increasing discharge power. With the same source gas and discharge power, both Ar and O_2 ion beams have faster etch rates on ZnO:Al films than on glass substrates. For the same substrates, Ar ions have faster etch rates than O_2 ions with similar discharge power, which is the same as in static etching.

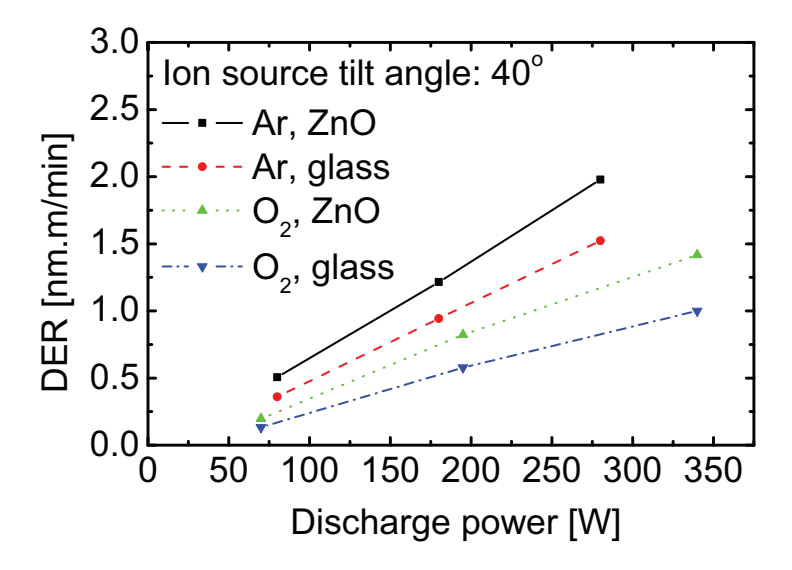


Figure 4.5: Dynamic etch rate of glass and ZnO:Al films.

4.4 Discussion

As mentioned, the collisions lie in the knock-on regime, indicating the sputtering yield is described by equation 2.8. The sputtering yields are proportional to the dimensionless function α and energy transfer coefficient γ between ions and substrate atoms during the collisions, which both are determined by the mass ratio M_2/M_1 for perpendicular incidence. The values of α and γ for Ar and O ions bombardments of O, Si and Zn atoms calculated from equation 2.4 and 2.9 are listed in Table 4.1. Here atomic ions and substrates are assumed. For Ar and O ions, the energy transfer coefficients γ to Zn are lower than to Si, seems that less energies are transferred to ZnO films than to glass substrates. However, Zn atoms have higher α than Si atoms, resulting in higher coefficient of $\gamma \times \alpha$. Moreover, the sputtering yields are inversely proportional to substrate surface binding energy U_s . The absolute sputtering yield Y calculated from equation 2.11 in Section 2.1.2.1 are also listed in the table. The surface binding energy U_s are taken from the sublimation energy of the atomic elements. The incident energy of the atomic ion for the calculation is 1000 eV. The results indicate that $Y_{Zn} > Y_O > Y_{Si}$.

However, in ZnO and glass substrates, the surface binding energy of the molecules differs from elemental substrates. Generally, the surface binding energy describes the amount of energy required to remove the atoms from sample surface. Several methods have been proposed to estimate surface binding energy for metal alloys and oxides [115–117]. This work follows the method introduced by May P.W. et al., which uses the heat of atomization to estimate U_s [117]. In this calculation, it was assumed that the average surface energy is relevant to all atoms equally. It was assumed that in Corning

Table 4.1: Energy transfer coefficient γ between ions and substrate atoms, dimensionless function α , and theoretical predicated sputtering yield Y of atomic Ar and O ions bombardment of O, Si and Zn atoms. M_1 and M_2 represent the mass of ions and substrate atoms, respectively. U_s represents the surface binding energy of substrate atoms.

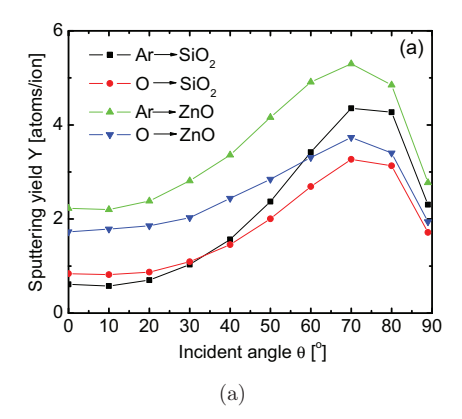
Su	bstrat	te		Ar ic	ons (M_1)	=40)	O ions $(M_1 = 16)$			=16)
Type	M_2	U_s	γ	α	$\gamma \times \alpha$	Y	γ	α	$\gamma \times \alpha$	Y
		eV				atoms/ion				atoms/ion
О	16	2	0.82	0.2	0.16	2.2	1	0.3	0.3	2.3
Si	28	1.35	0.97	0.24	0.23	1.2	0.92	0.44	0.40	1.2
Zn	65	4.7	0.94	0.42	0.39	6.7	0.63	0.76	0.48	5.8

Table 4.2: Estimation of surface binding energy by summarizing compound formation enthalpy $\triangle H_f$, sublimation energy $\triangle H_s$ and gas dissociation energy $\triangle H^{\dagger}$.

Substrate	Reactions	Energy kJ/mol	Total energy
ZnO	$ZnO(s) \rightarrow Zn(s) + 1/2 O_2(g)$	$\triangle H_f = 348 \text{ kJ/mol}$	725.5 kJ/mol
	$1/2 O_2 (g) \to O (g)$	$\triangle H^{\dagger} = 247 \text{ kJ/mol}$	=
	$Zn (s) \rightarrow Zn(g)$	$\triangle H_s = 130.5 \text{ kJ/mol}$	3.75 eV/atom
SiO_2	$\mathrm{SiO}_2\ (\mathrm{s}) o \mathrm{Si}\ (\mathrm{s}) + \mathrm{O}_2\ (\mathrm{g})$	$\triangle H_f = 908 \text{ kJ/mol}$	1607 kJ/mol
	$O_2 (g) \rightarrow 2 O (g)$	$\Delta H^{\dagger} = 247 \text{ kJ/mol}$	=
	$Si(s) \rightarrow Si(g)$	$\triangle H_s = 494 \text{ kJ/mol}$	5.55 eV/atom

glass substrate, the materials are composed of amorphous SiO_2 . Table 4.2 shows the estimations of the ZnO and SiO_2 compounds, in which $\triangle H_f$ denotes the formation enthalpy per molecule of compounds, $\triangle H^\dagger$ denotes the energy required for dissociation of molecular atoms, and $\triangle H_s$ represents the sublimation energy of the elements. The above energies were found in SI and JANAF chemical tables [118, 119]. As a result, the surface binding energies for ZnO and SiO_2 are 3.75 eV/atom and 5.55 eV/atom, respectively. Combined with the coefficient $\gamma \times \alpha$ as shown in Table 4.1, it is conceivable that ZnO can be etched faster than glass substrates.

The sputtering yield of atomic Ar and O ions bombardments of ZnO and SiO_2 films were calculated by TRIM, which is a Monte Carlo computer program that calculates the interactions of energetic ions with amorphous samples [120]. TRIM codes are also based on binary collisions as the linear collision theories. Therefore, the results from TRIM simulations shall be consistent to the above theoretical analysis. Sputtering yield in atoms/ion is one of many output results of TRIM program. The properties of ions, including ion type, energy, and incident angle are defined by input parameters. The properties of substrates are described by several parameters, for example film density, thickness, and compositions. Additionally, lattice binding energy, displacement energy, and surface binding energy of each element in the substrate are required. Calculated surface binding energy as shown in Table 4.2 were used in the TRIM program, while



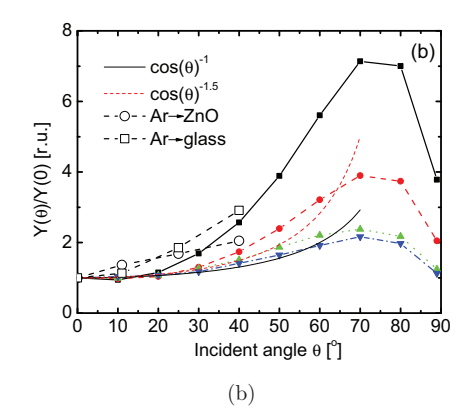


Figure 4.6: (a) - Sputtering yields versus incident angle simulated by TRIM program of four ion beam treatments: Ar bombardments of glass (squares), O bombardments of glass (circles), Ar bombardments of ZnO (triangles) and O bombardments of ZnO (inverse triangles). (b) - $Y(\theta)/Y(0)$ of the above TRIM simulated results, compared with $cos(\theta)^{-b}$ when b=1 and 1.5.

the other two parameters were taken from default values in the program. The total sputtering yields of glass substrates or ZnO films by atomic Ar and O ions are shown versus incident angle in Fig. 4.6(a), in which 0° indicates normal incidence. Energy of incident ion for the TRIM simulation is 1000 eV.

At normal incidence ($\theta=0$), sputtering yields from TRIM simulation of ZnO and SiO₂ by Ar ions are 2.23 and 0.61 atoms/ion, respectively. Similarly, by O ions, the sputtering yields of ZnO and SiO₂ are 1.73 and 0.84 atoms/ion, respectively. As discussed already, lower sputtering yield of SiO₂ as compared with ZnO is due to higher surface binding energy U_s and smaller product of energy transfer coefficient and dimensionless factor $\gamma \times \alpha$.

The TRIM simulation also shows that on ZnO substrate, sputtering yields of Ar ions are higher than O ions at all incident angles, while on glass substrate, Ar ions lead to lower sputtering yield than the O ions when the incident angle is below 30°. When the incident angle is larger than 40°, Ar ions again lead to higher sputtering yield than O ions. However, in experiments, Ar ions always show higher etch rate than O ions, even for perpendicular bombardments of glass substrates (see Fig. 4.2). The reason might be related to the reduced sputtering yield due to the formation of nonvolatile oxides by reactions between substrate atoms and O atoms. Therefore, the real etch rate of O ions shall be smaller than the prediction of TRIM simulation.

The angle dependence of experimental etch rate is considered together with the TRIM simulation in this paragraph. The simulation shows that the sputtering yield increases with increasing incident angle and to the highest at 70° , and then decreases with further larger tilted angle. The sputtering yields at incident angle θ are divided by the yield

at normal incidence. The results are shown in Fig. 4.6(b). As introduced in Section 2.1.2.1, angle dependence of sputtering yield often follows $cos(\theta)^{-b}$, where b is a constant related to mass ration M_2/M_1 . However, this relationship might break down for light or low energy ions. The solid and dashed lines represent curves of $cos(\theta)^{-b}$ with b=1and 1.5, respectively. It shows that the increase of sputtering yield of ion-ZnO system is fitted approximately close to b=1.5, while the sputtering yield of ion-glass etching increases with angle more pronounced than $cos(\theta)^{-1.5}$. The former is consistent with the theoretical predicted value and the latter seems more like in low energy knock-on regime. The experimental etch rates of ZnO and glass from $0-40^{\circ}$ are also shown in the figure by empty circles and squares, respectively. The experimental etch rate increases with increasing incident angle in a much more pronounced way than the TRIM simulations and theoretical predictions, which can be explained by several reasons. Firstly, the discharge voltage for these experimental data points was 2 kV, so the average ion energy is approximately 1000 eV with energy distribution similar to Fig. 2.4. Thus, a large fraction of ions in the ion beam have lower energy than 1000 eV, indicating that more collisions belong to low-energy regime. Secondly, the theory deals with totally flat surfaces, while in reality, the glass and ZnO are not ideally flat. The ZnO films used in this work have crater-like morphologies with lateral length in the range of 50 nm. The local slope on the surface increases the incident angle, leading to enhanced etch rate. Therefore, in the experiments, etch rates increase with increasing incident angle faster than the predictions of theories.

4.5 Summary

The compositions of ion beams have been investigated by OES in this chapter. It was concluded that both neutral and ionized ions exist in the ion beam. Static and dynamic etching of ZnO and glass substrates by ions generated from Ar and O_2 gas have been studied in the last sections. The removed thickness and etch rates were obtained under different treatment parameters and compared with theoretical values. It is important for the following experiments, since the treatment time for glass substrates or ZnO:Al films can be estimated as long as the required removed thickness and treatment parameters are known.

5 Ion beam treatment of the glass surface

p-i-n silicon thin-film solar cells are composed of many layers, including glass substrate, front contact, absorber silicon layer, and back contact. The surface condition of one layer is quite sensitive for the growth of the next layer. Therefore, an ion beam is used to treat film surfaces in the silicon thin-film solar cells, with the aim of improving the performance of solar cells. This chapter focuses on the ion beam treatment of the glass substrate. In the first section, it is shown that the ion beam pretreatment of glass substrate influences the growth of ZnO:Al films significantly, resulting in as-grown rough ZnO:Al film. The as-grown rough ZnO:Al films provide proper electrical and optical properties for solar cells. Further, amorphous and microcrystalline silicon thinfilm solar cells on these substrates show that as-grown rough ZnO:Al films can provide efficient light trapping effect. Then, a series of post treatment experiments and XPS measurements are investigated, in order to find out the reason of the rough growth. The surface evolution and structural properties of the as-grown rough ZnO:Al films are analyzed in the following section. Finally growth mechanisms of as-grown rough ZnO films are proposed, enlightened by the growth behaviors of ZnO:Al films sputtered on single ZnO crystal.

5.1 As-grown rough ZnO:Al films

The ZnO:Al films grown on ion beam treated glass substrates are introduced in this section. Different ion beam treatments were applied on bare, clean Corning glass (Eagle XG), then standard ZnO:Al films were sputtered on the ion beam pretreated glass substrates. On ion beam treated glass substrates, the ZnO:Al films show as-grown rough features. Firstly, electrical and optical properties of the ZnO:Al films developed on Ar/O_2 treated glass substrates are examined. Then, a-Si:H, μ c-Si:H and tandem solar cells prepared on the as-grown rough ZnO:Al films will be given.

5.1.1 Different glass pretreatment

In the following, the properties of the ZnO:Al films grown on ion beam treated glass are discussed. Different characterization methods such as SEM, haze measurements, thickness measurements, and hall measurements were taken on the ZnO:Al films.

The experimental procedure is shown in Fig. 5.1. Firstly, cleaned Corning glass substrates were treated by ion beams. 30 sccm Ar, 60 sccm O_2 , and mixed 20/20 sccm

(1) Ion beam pretreatment (2) Magnetron sputtering ZnO:Al Glass Glass

Figure 5.1: The experimental procedure of ion beam pretreatment of glass substrates before sputtering of ZnO:Al films.

 ${\rm Ar/O_2}$ were used as source gases, respectively. The discharge voltage of these ion beam treatments was kept at 2 kV and the working pressure was 1 µbar. The discharge currents determined by the above parameters were all in the range of 0.14-0.19 A for the three treatments. The substrates were oscillated 5 passes with carrier speed of 1 mm/s in front of the ion source in order to receive homogeneous treatment. The ion beam treatments time were approximately 16 min. Then the glass substrates were transferred from the ion source chamber to the sputtering chamber. Note that there is vacuum break during the transfer process. Standard ZnO:Al films were sputtered on the glass substrates by rf magnetron sputtering as introduced in Section 3.1.1.1. Additionally, an untreated glass substrate was added to the series as reference. The four ZnO:Al films were co-sputtered at the same time.

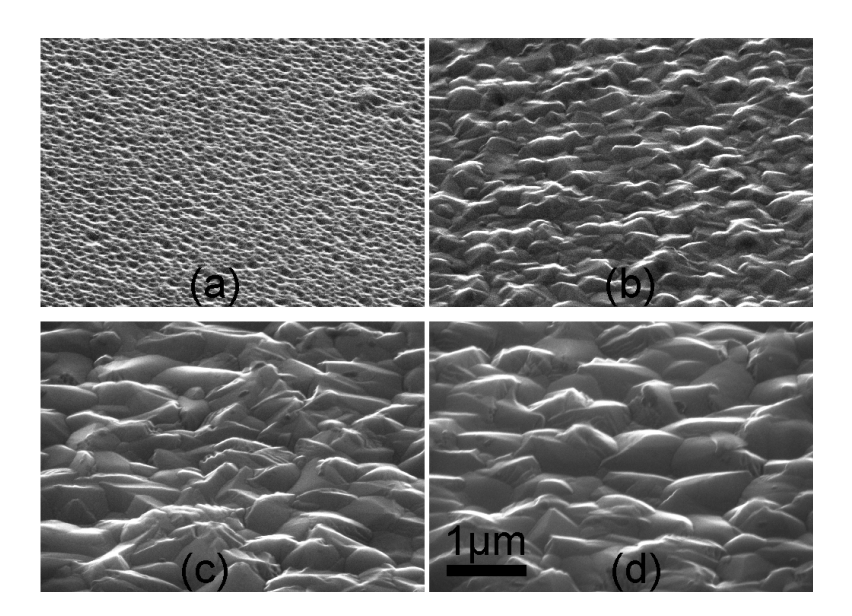


Figure 5.2: Top SEM micrographs of four as-grown ZnO:Al films on different glass substrates: (a) - untreated glass, (b) - Ar ion beam treated glass, (c) - O_2 ion beam treated glass, and (d) - Ar/O_2 ion beam treated glass.

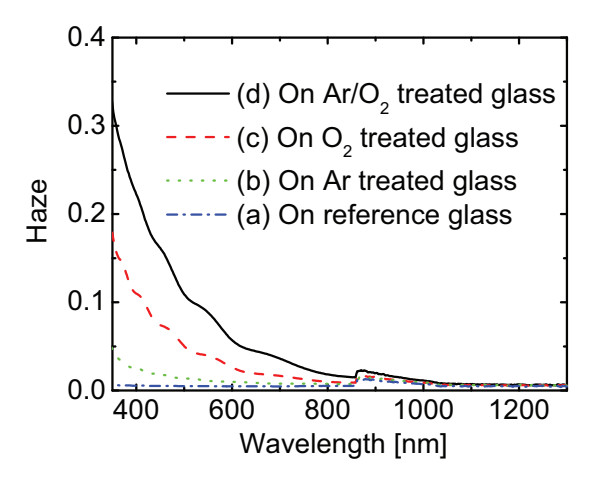


Figure 5.3: Haze of the different ZnO:Al films grown on different glass substrates: (a) dash-dotted curve - untreated glass, (b) dotted curve - Ar treated glass, (c) dash curve - O_2 treated glass and (d) solid curve - Ar/O_2 treated glass.

The topographies of the four ZnO:Al films are shown in Fig. 5.2. Fig. 5.2(a) shows the ZnO:Al film grown on the untreated glass substrate. This is the standard reference ZnO:Al films in this work. The standard ZnO:Al film exhibits small crater-like features which are around 50 nm in diameter. Fig. 5.2(b) shows the ZnO:Al film grown on the Ar treated glass substrate. The ZnO:Al film exhibits small pyramidal grains, and the surface features are larger than the ones of standard film. On the O_2 treated glass substrate (Fig. 5.2(c)), the feature size of the ZnO:Al film increases further to around 300 nm. On the Ar/ O_2 treated glass substrate (Fig. 5.2(d)), the ZnO:Al film shows largest feature size which is around 500 nm in diameter.

The Haze of the four different ZnO:Al films from 350 nm to 1300 nm wavelength are shown in Fig. 5.3. The dash-dotted curve is the haze of ZnO film on untreated glass. Since the surface feature of the ZnO film is only in the range of 50 nm, the haze is very low. The dotted and dashed curves are haze of ZnO films grown on Ar and O_2 treated glass, respectively. The haze increases with increased surface roughness. The solid curve presents the haze of ZnO film grown on Ar/O_2 treated glass substrate. It has highest value because the ZnO film has highest surface roughness.

Concerning Fig. 5.2 and Fig. 5.3 together, it is concluded that the haze value is related to the surface feature. This is in accordance with the scalar scattering theory [121–124]

$$H_{RT} = 1 - exp^{-(\frac{4\pi\sigma}{\lambda})^2},$$
 (5.1)

where, σ is the rms roughness of the ZnO:Al film, and λ is the wavelength of the light. The haze of the film is increased with increasing rms roughness.

The thickness and sheet resistance of ZnO:Al films grown on the different glass sub-

Table 5.1: The thickness, sheet resistance, lateral feature size and rms roughness of as	-
sputtered ZnO:Al films on different glass substrates.	

Glass		As-grown ZnO:Al films					
	thickness	sheet resis-	Lateral	Rms			
		tance	feature	roughness			
			size				
	nm	Ω	nm	nm			
(a) on reference glass	785	4.9	50	4			
(b) on Ar treated glass	746	8.1	100	12			
(c) on O ₂ treated glass	688	8.9	200-300	34			
(d) on Ar/O ₂ treated glass	690	11	500	44			

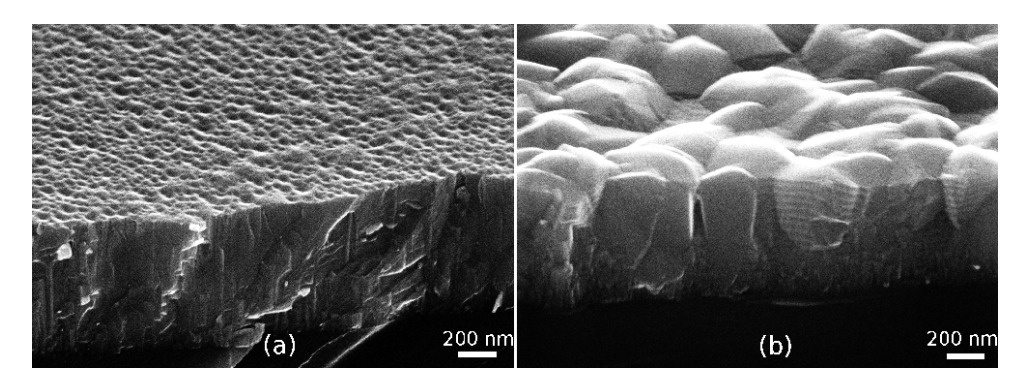


Figure 5.4: The cross-sectional SEM micrographs of ZnO:Al films on (a) untreated glass and (b) Ar/O_2 ion beam treated glass substrates.

strates are listed in Table 5.1. The first column shows the thickness of the four films. The standard ZnO:Al film has highest thickness, while the thicknesses of the other three films are reduced. The thickness difference indicates that the ZnO:Al film on untreated glass has a higher growth rate than the films on ion beam treated substrates. The second column is the sheet resistances of the four ZnO:Al films measured by 4-point probe setup. The sheet resistance of 4.9 Ω is lowest for standard ZnO:Al on untreated glass, and highest for the film grown on Ar/O₂ treated glass (11 Ω).

The lateral feature size estimated from SEM micrographs and rms roughness calculated from AFM measurements are also listed in Table 5.1. The film grown on $\rm Ar/O_2$ treated glass has the highest rms roughness of 44 nm, while the reference film is comparably flat with a rms roughness of only 4 nm. Note that with increasing rms roughness, the sheet resistance of a film also increases. Detailed studies on the electrical properties are provided in Section 5.1.2.

Cross-sectional SEM micrographs were taken on two ZnO:Al films: reference film and the film grown on Ar/O_2 treated glass. They are shown in Fig. 5.4 by (a) and (b),

respectively. Due to the break edge of the sample, the fringes on the cross-section are difficult to avoid. Besides of the fringes, the reference ZnO:Al film shows columnar grains, while the film on ${\rm Ar/O_2}$ treated glass exhibits two types of grains: columnar grains and conical grains. The surface of the film is dominated by the top of the conical grains. These conical grains seem to grow much faster than the columnar grains, thus they overtake the majority of the film's surface. Note that the as-grown rough ZnO:Al film has slower growth rate than the reference film. Therefore, the columnar grains in the as-grown rough ZnO:Al film has much slower growth rate than the columnar grains in the reference film. The columnar grains in the as-grown rough ZnO and the reference material must be different.

The topographies, haze, growth rate, and resistance differences show that the ion beam pretreatment has significant influence on the growth of ZnO films. Apparently the pretreatment of the glass substrates leads to as-grown rough ZnO:Al films. Among the three ion species, mixed ${\rm Ar/O_2}$ ions develop ZnO:Al films with largest lateral feature size and rms roughness, which are favorable in the Si thin-film solar cells. Thus in the following part of this chapter, the ${\rm Ar/O_2}$ ion beam pretreatment will be focused.

The effect of Ar/O₂ ion beam pretreatment on the ZnO:Al growth might be influenced by the ion beam treatment intensity and the duration of the ion beam treatment. Therefore, the ion beam treatment intensity was varied from 2 kV to 1 kV, as well as the ion beam treatment time from 5 min to more than 120 min. However, the rough growth behavior of ZnO:Al film was not changed so much. No obvious trends were concluded from these experiments. In the next experiments, the parameters of ion beam treatments will not be emphasized, but only the species of the ions will be pointed out.

To conclude, unlike the small crater features of standard ZnO:Al film, the ZnO:Al films grown on ion beam treated glass substrates show larger surface features with pyramidal shape. Among different gas composition of the ion beam, ${\rm Ar/O_2}$ ion beam pretreatment of glass substrate gives ZnO:Al film largest feature size and highest haze. When the ZnO:Al films features become larger, the growth rate of the magnetron sputtering is reduced. The sheet resistances of the as-grown rough ZnO:Al films are higher than the standard ZnO:Al film. The optical and electrical properties of as-grown rough ZnO:Al films will be examined in detail in the following parts of this section. Afterwards, the films are applied in thin-film Si solar cells.

5.1.2 Electrical properties

This section focuses on the electrical properties of the ZnO:Al films. Reference and as-grown rough ZnO:Al films on ${\rm Ar/O_2}$ pretreated glass were deposited with different duration, in order to prepare the thickness series.

Hall effect measurements were performed on those ZnO:Al films at room temperature. The resistivity, mobility, and carrier concentration were drawn versus film thicknesses in Fig. 5.5. The reference ZnO:Al films are shown by black squares while the as-grown rough films are shown by red circles. Though the two types of films were co-deposited, the as-grown rough films have slower growth rate than the reference films. Therefore, the data points of the as-grown rough films were shifted to small thickness.

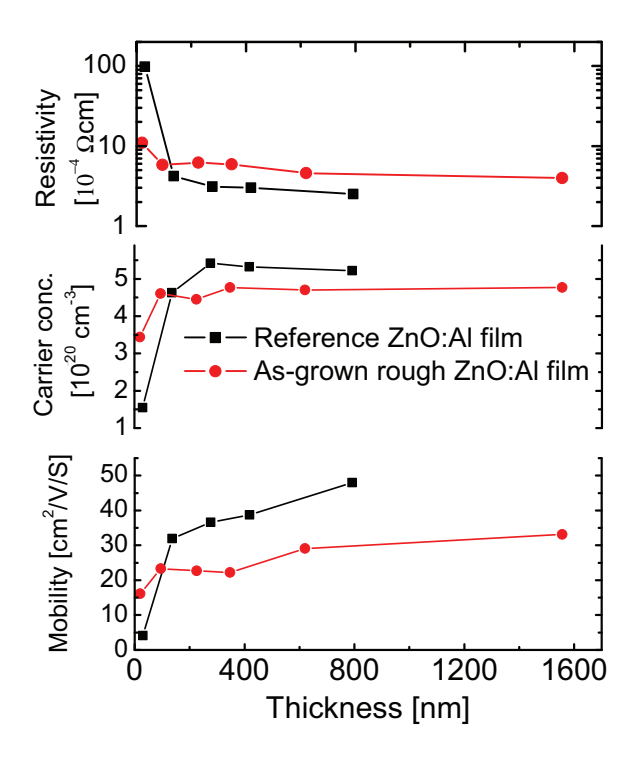


Figure 5.5: The electrical properties of the as-grown rough ZnO: Al films and reference ZnO: Al film.

For both series of films, the resistivity drops dramatically at the beginning of film growth, and then decreases slowly with increased film thickness. Carrier concentration increases significantly at the initial growth stage and then stays almost constant. Similarly the mobility of the two series of films rises fast when the films are thinner than 150 nm and then slow when the films are thicker. From the Fig. 5.5 it is also seen that the gradient in the resistivity, mobility and carrier concentration of the as-grown rough ZnO:Al films is much lower than the reference film. There is a crossover, i.e. thick as-grown rough films have higher resistivity and lower mobility, whereas for very thin films below 100 nm an opposite trend can be observed.

5.1.2.1 Annealing without Si capping layer

Annealing experiments for as-grown rough ZnO:Al films were performed with and without Si capping layer. As-grown rough ZnO:Al films with thickness of 1556 nm was annealed in vacuum for 1 to 3 hours. The heater temperature was 600 °C. The base pressure in the chamber was approximately 1×10^{-7} mbar. The electrical properties of the ZnO:Al films before and after annealing were measured by Hall effect measurements

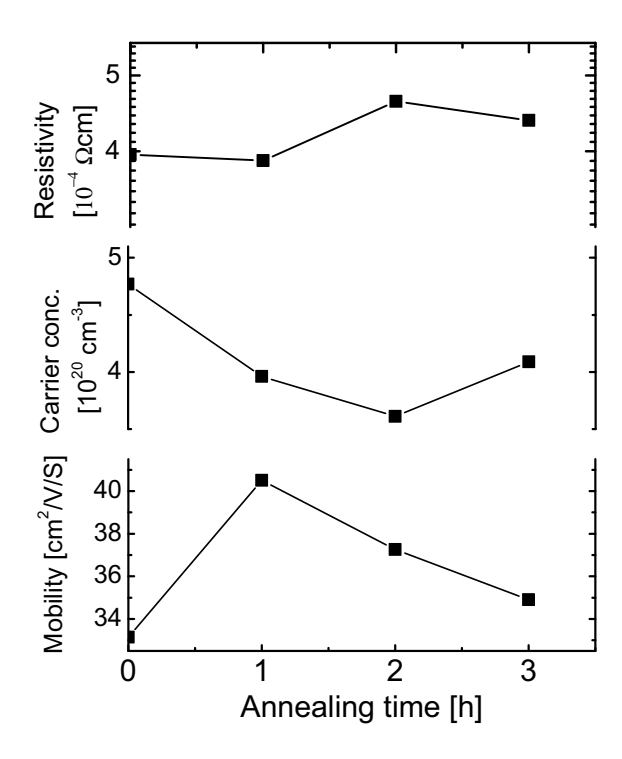


Figure 5.6: The electrical properties of the as-grown rough ZnO:Al film (1556 nm thick) after annealing in vacuum up to 3 hours. No Si capping layer was covered on the ZnO:Al film surface.

at room temperature.

The changes of the electrical properties are shown in Fig 5.6. Before annealing, film mobility is around $33 \, \mathrm{cm^2/Vs}$. The mobility of the annealed films increases at the first hour to around $40 \, \mathrm{cm^2/Vs}$. However, by further increasing of annealing time, the mobility decreases again to near $34 \, \mathrm{cm^2/Vs}$. The carrier concentration decreases from $4.7 \times 10^{20} \, \mathrm{cm^{-3}}$ to $3.6 \times 10^{20} \, \mathrm{cm^{-3}}$ at first two hours, and then increases a bit at the third annealing hour. The final carrier concentration is still lower than the as-deposited film. Annealing of reference ZnO:Al films at 450 °C and 500 °C were described by Ruske et al. in [125]. It was reported that the mobility and carrier concentration were reduced significantly by annealing without capping layer.

5.1.2.2 Annealing with Si capping layer

Annealing with Si capping layer has been applied on reference ZnO:Al films as an effective method to improve the electrical properties to a large extent [125]. Therefore, similar experiments were carried on the as-grown rough ZnO:Al films.

Annealing with capping layer experiment was done on as-grown rough ZnO:Al films with thickness of 620 nm. The ZnO film was thoroughly cleaned and then coated with n-type amorphous silicon films. Annealing was carried out under N_2 atmosphere at 600 °C for 24 h.

The electrical properties of the ZnO:Al films before and after capping-annealing are shown in Table 5.2. The carrier concentration keep constant, while mobility increases from $27~\rm cm^2/Vs$ to $37~\rm cm^2/Vs$. Accordingly, the sheet resistance and specific resistivity decreases.

Table 5.2: Electrical properties of as-grown rough ZnO:Al film (620 nm thick) before and after annealing for 24 hours in N_2 with Si capping layer.

	Capping-annealing	Sheet	Specific re-	Mobility	Carrier con-		
		resistance	sistivity		centration		
ľ		Ω/Square	$\Omega \mathrm{cm}$	${ m cm^2/Vs}$	cm^{-3}		
Ì	Before	7.4	4.6×10^{-4}	27	5.2×10^{20}		
	After	5.4	3.4×10^{-4}	37	5.2×10^{20}		

5.1.2.3 Discussions

In bulk polycrystalline ZnO:Al films, the electron mobility can be limited mainly by two mechanisms: the electron scattering within the grains (e.g. the scattering by the ionized impurities, lattice defects, or phonons) or the electron scattering that occurs at the grain boundaries, due to the potential barrier formed at these locations [84]. If the mobility is dominated by the latter, the mobility should increases with increased grain size, because the grain boundary density decreases, which is the case for the reference films, their mobility increases with increased thickness. However, for the bulk as-grown rough films, the mobility gradient is lower. For the films from 95 nm to 350 nm, i.e. before the large conical grains connect to each other, the mobility is constant at 23 cm²/Vs. This indicates that during the growth of as-grown rough films, two possible mechanisms exist. One is that the electron scattering in the grains contribute more to the mobility, means that there are more defects in the grains. The other one is that the grain boundary density keeps similar during the thin film growth, i.e. the average grain size doesn't increase accordingly with film thickness. However, from the AFM results, it is known that the large grains size increases during the film growth. The latter possible mechanism can be almost excluded. Thus, the conclusion would be that there are more defects in the large conical grains, which results in a lower mobility for as-grown rough film, $29 \text{ cm}^2/\text{Vs}$ at 620 nm, compared to $48 \text{ cm}^2/\text{Vs}$ for the reference film at 800 nm. The carrier concentration, which is 5×10^{20} cm⁻³, is roughly constant for the two films after nucleation stage. The resistivity has similar trends like the mobility. For the asgrown rough ZnO:Al film at 620 nm the resistivity is $4.6 \times 10^{-4} \Omega$ cm, even though it is not as low as the reference ZnO:Al films, it is as already low enough to be considered as the front contact for thin films solar cells.

The improvement of as-grown rough ZnO:Al films after annealing in vacuum without Si capping layer in the first hour may be related to the improved crystallographic quality in the grains. With continuous annealing in vacuum, the degradation of ZnO:Al films might be caused by the oxygen diffusion in the films, even though the oxygen content is low in the ambient. Similar results were reported by Berginski et al. [126] on ZnO:Al films deposited from low Al content target. The mobility of the ZnO films keep in a range of $\pm 16\%$. Annealing thermal treatments with Si capping layer can improve the conductivity even after 24 h's annealing. It was assumed that the amorphous silicon capping layer can prevent the degradation of the films during heat treatment, because amorphous silicon can protect the oxygen diffusion into the ZnO films. Similar results were also applied on other ZnO:Al films and successfully improved the film electrical properties [127–129].

5.1.3 Optical properties

Fig. 5.3 has shown that Ar/O_2 ion beam pretreatment of the glass substrate develops ZnO:Al film with highest haze. This section focuses on the optical properties of the as-grown rough ZnO:Al films compared with HCl etched reference ZnO:Al films and AsahiU SnO₂:F film. Not only total transmission and haze, but also angular resolved scattering (ARS) are investigated to characterize different TCO films. One as-grown rough ZnO:Al film was prepared on Ar/O_2 treated glass substrate with thickness of 650 nm. The rms roughness of the ZnO:Al film is around 35 nm. The total transmission, diffuse transmission were measured by optical spectrometer with light from 300 nm to 1300 nm. Angular resolved scattering was measured by the in-house made setup with rotated light detector as introduced in Section 3.3.2.2.

The total transmission (T_{total}), haze versus light wavelength, and ARS versus scattering angle are shown in Fig. 5.7. The as-grown rough ZnO:Al films are shown in dashed line. As mentioned, the HCl etched reference ZnO:Al film and the AsahiU SnO₂:F film were added for comparison. They are represented by solid and dotted curves, respectively. T_{total} of the ZnO:Al films are higher than 80% in the wavelength range of 600-1000 nm, while the T_{total} of Asahi U SnO₂ film is a bit lower in this wavelength range. However, the SnO₂:F film has higher T_{total} at smaller wavelength range due to higher band gap as compared with the ZnO:Al films. T_{total} of as-grown rough ZnO:Al film and Asahi U SnO₂:F film have pronounced interferences as compared with the T_{total} of HCl etched ZnO:Al film. HCl etched reference ZnO:Al film has the highest haze, while the other two films have much lower haze.

In Fig. 5.7(b), the data from 0° to 90° show the diffused transmitted light, while the data from 90° to 170° present the diffused reflected light. The ARS curves of the as-grown textured ZnO:Al film and AsahiU SnO₂:F film are lower according to the lower haze value at 550 nm, but have a more Lambertian-like distribution. The highest intensity of the scattered light for HCl etched reference ZnO:Al film occurs at 12° , while for the other two films, the highest intensities are shown around 40° .

HCl etched reference ZnO:Al film has highest Haze, which is in accordance to scalar scattering theory [123]. The lateral feature size of the HCl etched reference ZnO:Al

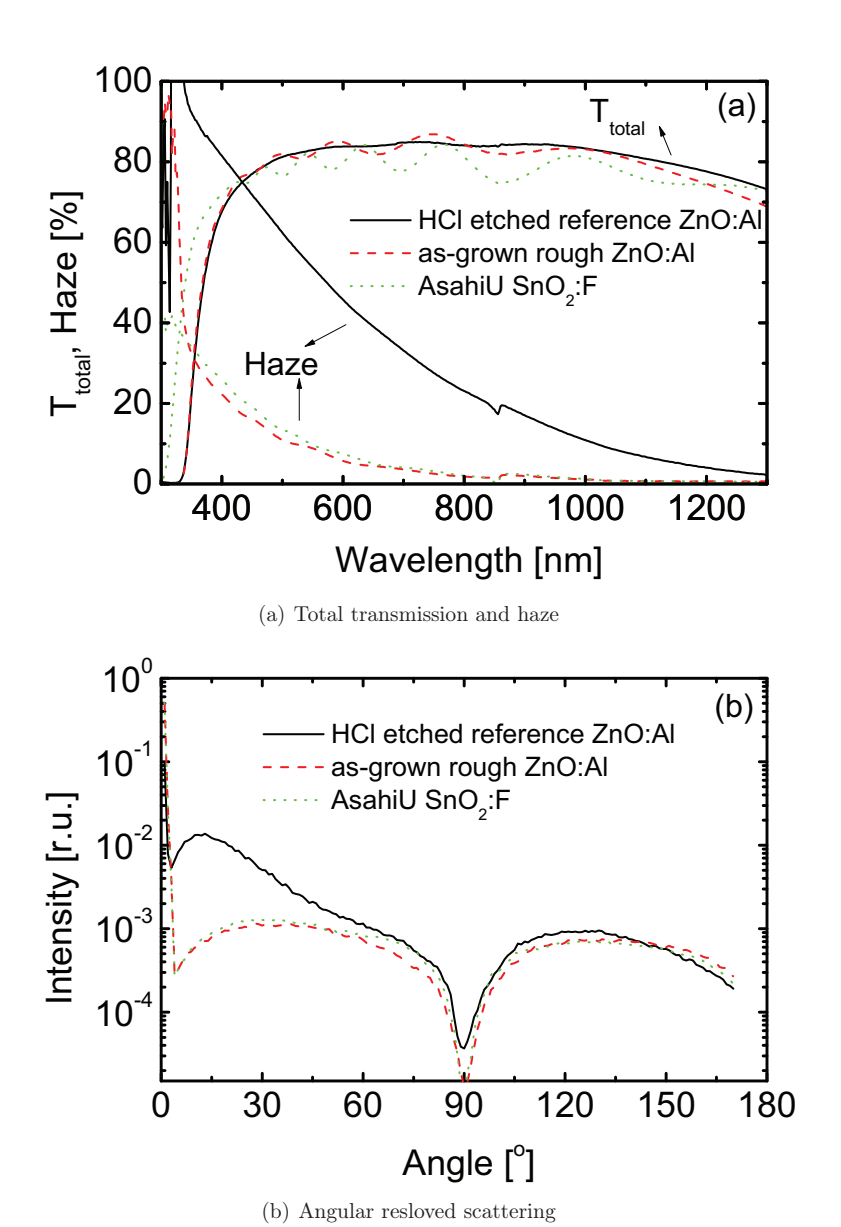


Figure 5.7: Optical properties of as-grown rough ZnO:Al films: (a) - Total transmission and haze; (b) - Angular resolved scattering at 550 nm. HCl etched reference ZnO:Al film and AsahiU SnO₂:F film are added for comparison.

film is around $1-2~\mu m$, which is much larger than those of as-grown rough ZnO:Al film and AsahiU SnO₂:F film. Pronounced interferences of as-grown rough ZnO:Al film indicate a low rms roughness as compared with the HCl etched reference film. SnO₂:F films have sharp pyramids, while the pyramids on the surface of as-grown rough ZnO:Al films have round top. Even the topography of the two films are slightly different, the Haze and ARS of the two film are very similar. The ARS of HCl etched ZnO:Al films and SnO₂:F films have been related to surface inclination angle by Schulte *et al.* [130]. Consistent results were found that the maximum scattering angle of SnO₂:F is larger than HCl etched ZnO:Al films. It means that for the as-grown textured ZnO:Al films and AsahiU SnO₂:F film, the transmitted light tends to be scattered to large angles, which is favorable for solar cells [82, 131, 132]. Though the total intensities of scattered light by as-grown rough ZnO:Al and SnO₂:F films are not as high as by the HCl etched reference film, the broader scattering angle can compensate the low haze.

5.1.4 Solar cells

In the previous sections, the electrical and optical properties of the as-grown rough ZnO:Al films have been examined. Based on these measurements, it was claimed that they are suitable for Si thin-film solar cells. Thus, this section presents the results of solar cells grown on these ZnO:Al films. ZnO:Al films prepared on Ar/O_2 pretreated glass substrates were used as front contacts for amorphous, microcrystalline, and tandem solar cells. The cell results are given in the following and compared with cells on HCl etched reference ZnO:Al films.

5.1.4.1 Amorphous Si thin-film solar cells

Amorphous Si thin-film solar cells were deposited on as-grown rough ZnO:Al front contacts. The roughness of the front contact is around 37 nm. The sheet resistance is around 7.1 Ω . For comparison, a standard ZnO:Al film which was etched in 0.5% HCl solution for 40 s was applied as reference. The amorphous Si absorber layers were codeposited in an industrial PECVD cluster at Applied Materials. Combined ZnO/Ag layers were used as back contacts. 18 small square cells with area of $1 \times 1 \text{ cm}^2$ were separated on each substrate by back contacts. The I-V measurements were performed by the sun simulator as introduced in Section 3.3.6 under standard condition. Three best solar cells were averaged and the results are shown in Table 5.3. The best cell on each substrate was used to measure quantum efficiency. Their results are shown in Fig. 5.8.

The solar cells prepared on the as-grown rough ZnO:Al films give higher cell efficiency η , fill factor FF, and open circuit voltage V_{oc} , which are 9.4 %, 71 %, and 932 mV, respectively. The short circuit current density J_{sc} of the two cells are the same 14.5 mA/cm², as can also be seen from the Fig. 5.8, indicating the as-grown rough ZnO:Al films can provide excellent light trapping as the reference ZnO:Al substrates. The higher FF and V_{oc} of the solar cells on as-grown rough ZnO:Al films show that the as-grown rough features are favorable for the growth of amorphous Si layers.

Table 5.3: Photovoltaic parameters of a-Si:H solar cells grown on as-grown rough ZnO:Al films and HCl etched reference ZnO:Al films.

Front contact	Back contact	White			;
		η	FF	V_{oc}	J_{sc}
		%	%	mV	$\mathrm{mA/cm^2}$
as-grown rough	$\mathrm{ZnO/Ag}$	9.4	71	925	14.5
HCl etched Ref.	ZnO/Ag	9.1	70	911	14.5

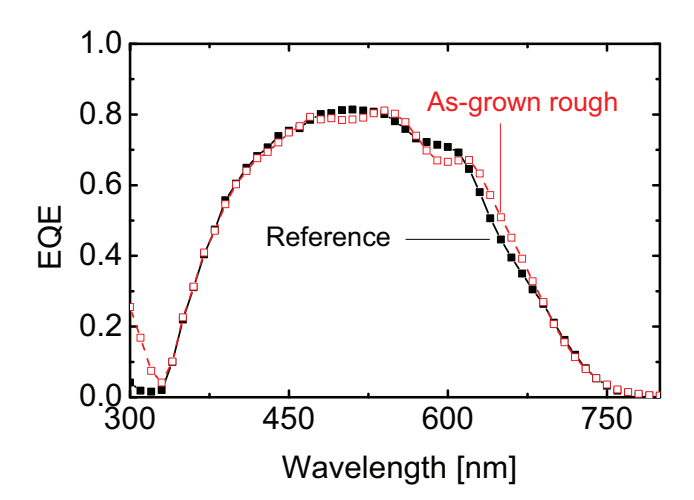


Figure 5.8: External quantum efficiency (EQE) of amorphous Si solar cells on HCl etched reference ZnO:Al (solid symbols) and as-grown rough ZnO:Al films (dashed symbols).

5.1.4.2 Microcrystalline Si thin-film solar cells

This section shows the μ c-Si thin-film solar cells deposited on the as-grown rough ZnO:Al films. For this experiment, as-grown rough ZnO:Al films were prepared on Ar/O₂ treated glass substrates. 40 s HCl etched standard ZnO:Al films were added for comparison. The absorber layers were deposited in the large area PECVD chamber in the lab of IEK-5 institute. The thickness of the absorber layer is around 1.1 μ m. Single Ag and combined ZnO/Ag layers were used as back contacts in this experiment. The cells were separated to $1\times1~cm^2$ small cells by the back contacts. After the Ag evaporation, the cells were annealed in oven at 160 °C for 30 min. The cell measurements were performed by the sun simulator as introduced in Section 3.3.6. The best three cells were selected to calculated the average value, and the best cell on each substrate was used to measure quantum efficiency.

The cell results are shown in Table 5.4. With single Ag as back contact, HCl etched reference ZnO:Al films provide effective light trapping effect with the J_{sc} of 18.1 mA/cm².

IIOI etcii	ITCI etched reference Zho. Ai minis.									
Front contact	Back contact		1	White	Blue	Red				
		η	η FF V_{oc} J_{sc}		J_{sc}	J_{sc}				
		%	%	mV	$\mathrm{mA/cm^2}$	$\mathrm{mA/cm^2}$	$\mathrm{mA/cm^2}$			
HCl etched Ref.	Ag	6.9	73.5	521	18.1	2.86	8.9			
as-grown rough	Ag	6.2	69.3	491	18.2	2.9	8.9			
HCl etched Ref.	ZnO/Ag	8.0	70.3	509	22.3	2.67	13.2			
as-grown rough	ZnO/Ag	6.6	69.4	508	18.7	2.29	10.8			

Table 5.4: Photovoltaic parameters of microcrystalline solar cells on as-grown rough and HCl etched reference ZnO:Al films.

The as-grown rough ZnO:Al films can also provide excellent light trapping, since they give comparable J_{sc} of 18.2 mA/cm². The solar cells grown on as-grown rough ZnO:Al film give lower FF and V_{oc} as compared with reference cells. Under blue and red illumination, comparable J_{sc} are also obtained. In all, the solar cells on as-grown rough ZnO:Al films show lower η than the reference cells because of the lower FF and V_{oc} .

With ZnO/Ag as back contacts, the performance of cells on HCl etched reference ZnO:Al films are significantly improved, J_{sc} is increased to 22.3 mA/cm² and η is increased to 8.0 %. However, for the cells deposited on as-grown rough ZnO:Al films, the J_{sc} increases only to 18.7 mA/cm². The quantum efficiency (QE) and 1-reflection (1-R) of the four solar cells are shown in Fig. 5.9. The solar cell prepared on as-grown rough ZnO:Al film is shown in solid curve while the reference cell is shown in dashed curve. For the two cells with only Ag as back contacts (Fig. 5.9(a)), the QE curves are almost the same while the 1-R curves have slight difference. 1-R represents the absorbed light of the cell. The cell prepared on as-grown rough ZnO:Al film has less absorbed light because of the pronounced interference originated from less rough TCO surface. For the two cells with ZnO/Ag as back contacts (Fig. 5.9(b)), reference solar cell shows higher QE than the solar cell on as-grown rough ZnO:Al film.

Generally, ZnO/Ag back contacts can provide higher current density as compared with the Ag back contacts. It is explained by that ZnO back contact can shift the back contact absorption peak from about 800 nm to 500 nm where is less relevant to μ c-Si cells [133]. However, for the as-grown rough ZnO:Al substrate, the improvement of current density by adding ZnO to the back contact is small. This might be due to the following two reasons. One reason is that the lateral feature size of this specific ZnO:Al film is too small to scatter light in the wavelength range of 600 – 1000 nm. Researchers have shown that features with lateral size at about 900 nm are favorable for μ c-Si:H solar cells [134]. The lateral feature size of as-grown rough ZnO:Al film (\sim 500 nm), is not optimal for μ c-Si:H solar cells. Another reason would be that the absorption peak of the ZnO/Ag back contacts is shifted to small wavelength [133]. The most effectively scattered light by the as-grown rough ZnO:Al films is in the range of its lateral length, i.e. also in the range of 500 nm. Therefore, a large fraction of the light traveled through the Si absorber layer after the first optical path is absorbed by ZnO/Ag back reflector, instead of reflecting back to the absorber layer.

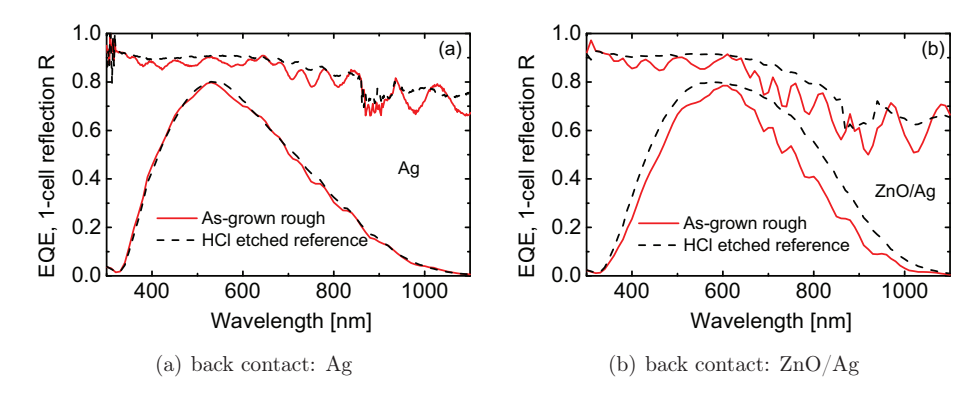


Figure 5.9: External quantum efficiency (EQE) and 1- cell reflection R of microcrystalline silicon cells grown on as-grown rough (dashed lines) and HCl etched reference ZnO:Al films (solid lines).

The differences in the FF and V_{oc} for cells with different back contacts is most probably given by the reproducibility of the PECVD system since the two series of solar cells were deposited during different runs. Lower FF and V_{oc} of cells on as-grown rough ZnO:Al films are obtained as compared with the cells on reference ZnO:Al films, which might be due to the topography. The morphology of the as-grown textured ZnO:Al films might be less suitable for the μ c-Si growth compared to the etched ZnO, even though the Raman measurements show that the crystallinity fraction of the silicon i-layer is very similar for both substrates. Dropped FF and V_{oc} also happened for cells grown on LPCVD deposited ZnO:B films and AsahiU SnO₂:F films [135, 136]. The reasons are generally considered to be more grain boundary defects or voids in Si layers grown on the v-shaped valleys of the substrates [137].

5.1.4.3 Tandem Si thin-film solar cells

This section presents tandem Si thin-film solar cells prepared on as-grown rough ZnO:Al films. Similar to the a-Si cells, the tandem absorber layers were deposited in PECVD system by Applied Materials. 40 s HCl etched standard ZnO:Al film was used as reference. Combined ZnO/Ag layers were used as back contacts. 18 small square cells with area of 1×1 cm² were separated by the back contacts on each substrate. The cell measurements were performed by the sun simulator as introduced in Section 3.3.6. Three best solar cells from the J-V measurement were averaged and shown in Table 5.5. The best cell was used to measure quantum efficiency.

As compared with the reference solar cells, the solar cells on as-grown rough ZnO:Al film exhibit higher V_{oc} and J_{sc} . In all, the η of the tandem solar cells on as-grown rough ZnO:Al film is 0.4% higher than that of the reference cells. The EQE of the solar cells on HCl etched reference and as-grown rough ZnO:Al films are shown by the solid and dashed curves in Fig. 5.10, respectively. For both substrates, the J_{sc} generated from

Table 5.5: Photovoltaic parameters of tandem Si thin-film solar cells on as-grown rough and HCl etched reference ZnO:Al films.

Front contact	Back contact	White			
		η	FF	V_{oc}	J_{sc}
		%	%	mV	$\mathrm{mA/cm^2}$
as-grown rough	ZnO/Ag	11.9	74	1393	11.6
HCl etched Ref.	ZnO/Ag	11.5	74	1378	11.4

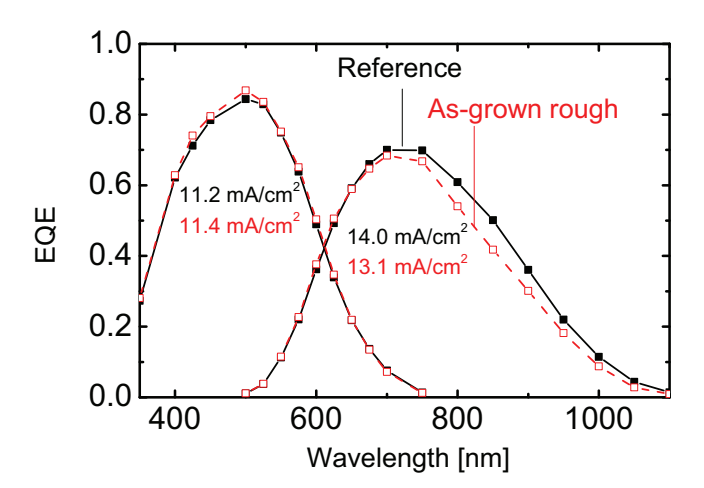


Figure 5.10: External quantum efficiency (EQE) of tandem Si solar cells on HCl etched reference ZnO:Al (solid lines) and as-grown rough ZnO:Al films (dashed lines).

top a-Si:H solar cells is lower than that of bottom μ c-Si:H solar cells, indicating that the solar cells are top limited and the J_{sc} are determined by the top a-Si:H solar cells. The solar cell on as-grown rough ZnO:Al films show higher EQE at wavelength region of 400 - 500 nm, however, lower EQE at wavelength region of 700 - 1100 nm, as compared with the reference solar cell. Therefore, the tandem solar cells prepared on as-grown rough ZnO:Al films give slightly higher J_{sc} than the reference solar cells. It is conceivable that if the thickness of the bottom cell is decreased till the tandem cell is bottom limited, the J_{sc} of the tandem solar cell on as-grown rough ZnO:Al film will be lower than the reference solar cell.

The as-grown rough ZnO:Al films show a good potential to be applied as front contacts in a-Si:H, μ c-Si:H, and tandem solar cells. Especially for a-Si:H solar cells, as-grown rough ZnO:Al films show excellent light trapping effect similar to the HCl etched reference ZnO:Al films. However it is difficult to achieve the same light trapping effect as the reference ZnO:Al films for μ c-Si:H cells. This is because the lateral length of the

as-grown rough ZnO:Al film is approximately 500 nm, which is sufficient for a-Si:H cells, but not optimal for μ c-Si:H cells. The solution would be to increase the lateral feature size of the as-grown rough films, which might be possible by adjusting the deposition conditions, e.g. deposition time for thicker film or lower deposition temperature for larger pyramids.

5.1.5 Summary

The effects of the ion beam pretreatment on the growth of ZnO:Al films were introduced in this section. The ZnO:Al films show as-grown rough features on ion beam treated glass substrates. Among pure Ar, pure O_2 , and mixed Ar/O_2 ion beam treatment, the last one leads to roughest ZnO surface, which has roughness approximately 40 nm and lateral length approximately 500 nm. The as-grown rough ZnO:Al films are composed of two types of grains, large conical grains and small columnar grains. The large grains exhibit faster growth rate and dominate the surface gradually due to the survival of the fastest grains. Finally a surface fully covered by pyramid grains is developed.

Though the as-grown rough ZnO:Al films exhibit higher resistivity and lower mobility as compared to the reference films sputtered on untreated glass substrate, the electrical properties of the films are sufficient for the application as front contact layers in solar cells. The haze and angular distribution of the as-grown rough film is similar to that of AsahiU SnO₂:F films. Excellent light trapping effects are confirmed by a-Si:H thin-film solar cells. The highest cell efficiency of the a-Si:H solar cells on as-grown rough ZnO:Al film is 9.4%.

5.2 Reason of rough growth

The first section of this chapter introduced the as-grown rough ZnO:Al films grown on ion beam pretreated glass substrates. This section focuses on the reason of the rough growth. Ion beam treatment and magnetron sputtering were tried with other deposition parameters and systems. Substrates were varied from Corning glass to other types. The ion beam treated glass was cleaned.

5.2.1 Different substrates

In this section, the Corning glass was replaced by other glass substrates and Si wafer. The aim of this experiment is to test that whether the substrate material or the surface treatment is responsible for the change in ZnO:Al growth.

Fig. 5.11 shows the AFM images of ZnO:Al films grown on different untreated (left column) and pretreated substrates (right column). The AFM measurement scan size for all the films is $4\times4~\mu\text{m}^2$. The Z range on top of each figure represents the height of color bar. From (a) to (d), the substrates are Borofloat glass, Borofloat glass with SiN coating, Diamond glass (Saint-Gobain), and Si wafer, respectively. The ion beam pretreatment and ZnO:Al films deposition were performed at the same condition. The

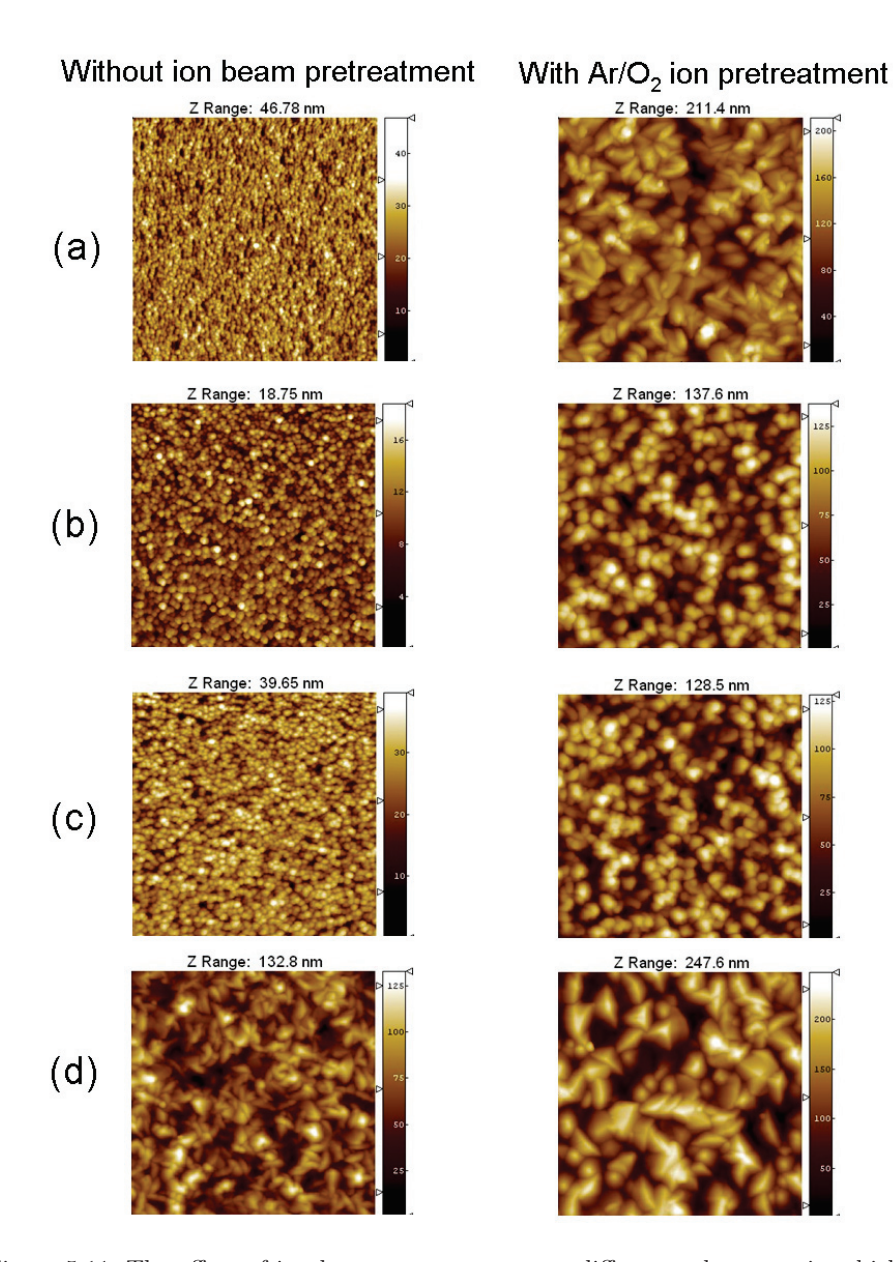


Figure 5.11: The effect of ion beam pretreatment on different substrates, in which (a): Borofloat glass, (b): Borofloat glass with SiN coating, (c): Diamond glass (Saint-Gobain) and (d): Silicon wafer. The images on the left column are the ZnO:Al films grown on untreated substrates, while on the right column are grown on ion beam pretreated substrates. The AFM measurement scan size for all the films is $4\times 4~\mu m^2.$ The Z range on top of each figure represents the height of color bar.

figure shows that the ZnO:Al films on untreated substrates show small surface features while the films on ion pretreated substrates exhibit large surface features. Additionally, small differences were observed for different substrates.

As a conclude, the rough growth is observed on different types of glass substrates, even on Si wafer. It means that the ion beam pretreatment has common effect on the treated surface. The method of developing as-grown rough ZnO:Al films can be applied to other cheap glass substrates.

5.2.2 Post-cleaning of ion treated glass

In this section, cleaning was applied on ion beam treated glass substrates. After the glass was treated by mixed ${\rm Ar/O_2}$ ion beam, the glass surface was treated by different process before the ZnO:Al film was deposited on the glass. The aim of the post-treatments is to understand more about the surface influence of the ion beam treatment on growth of ZnO:Al films.

Fig. 5.12 shows the experimental process in this experiment. The first step was ion beam treatment by ${\rm Ar/O_2}$ ion beam on Corning glass. Then, the treated glass substrate was cleaned by different methods, for example, dipping into HCl and NaCl solutions at room temperature. The ion beam treated glass substrate may also be processed by standard glass cleaning which contains two steps: first dip the glass in deionized water and weak acidic decantate at 68 °C. Then put the glass together with the decantate in an ultrasonic cleaner for 3 h. Afterwards, the glass substrate was rinsed by deionized water and dried by ${\rm N_2}$ gas. Finally, standard ZnO:Al films were sputtered on the glass substrates. The ion beam pretreated glass substrates without post-treatment were used as reference.

Firstly, the effect of HCl and NaCl cleaning was investigated. Two ion beam treated glass substrates were dipped into HCl and NaCl solution for 2 min, respectively. Fig. 5.13 shows the AFM images of ZnO:Al films grown on the different glass substrates. The AFM measurement scan size for all films are $4\times4~\mu\text{m}^2$. One ZnO:Al film grown on ion beam pretreated glass without post-treatment was added as reference and shown

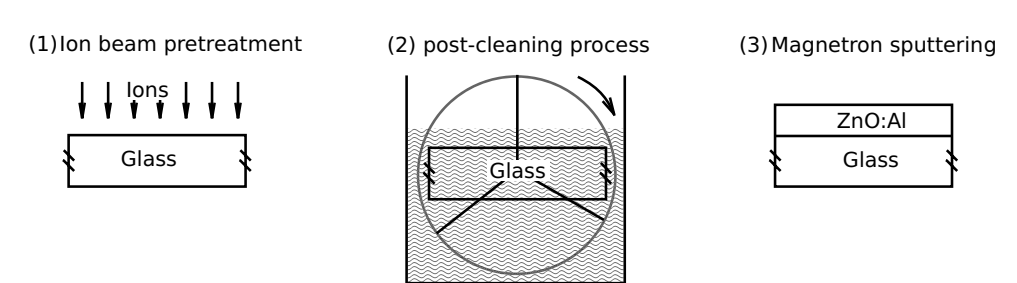


Figure 5.12: Experimental process of post-cleaning process. After the glass was treated by mixed Ar/O_2 ion beam, the glass substrate was cleaned by different methods before the ZnO:Al film was deposited on the glass.

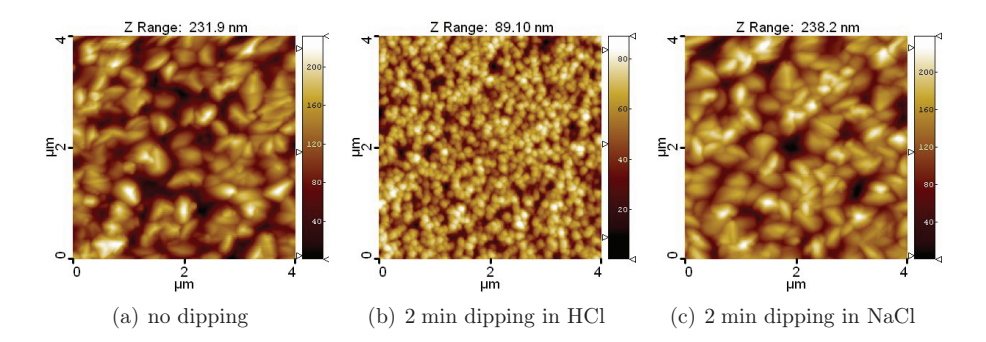


Figure 5.13: The effect of post HCl and NaCl etching of ion beam treated glass substrates on the growth of ZnO:Al films. The images show ZnO:Al films grown on Ar/O₂ beam pretreated glass substrates. After Ar/O₂ beam pretreatment, substrate (a) was not dipped in HCl or NaCl, (b)was dipped into HCl Solution for 2 min, (c)was dipped into NaCl Solution for 2 min. The AFM measurement scan size for all the films are $4\times4~\mu\mathrm{m}^2$. The Z range on top of the AFM images means the height of the color bar.

as film (a). As introduced before, the rough large grains were developed on the top surface. Film (b) was grown on ion beam pretreated glass substrate after 2 min dip in HCl solution. The rough growth was not developed. Film (c) was prepared on ion beam pretreatment glass substrate after 2 min dip in NaCl solution. The rough growth was not influenced by NaCl dip.

Next, the duration of post HCl etching was studied. 15 s and 1 min HCl etching were performed on the same $\rm Ar/O_2$ pretreated glass substrates. Then the ZnO:Al films were sputtered on the glass substrates. Fig. 5.14(a - c) present the AFM images of these surfaces. Note that the ZnO films in this series have smaller thickness than in the last figure. The thickness of the films is not important here, because the aim of this experiment is to observe whether the rough growth is changed. Film (a) was grown on pretreated glass without post-cleaning. Rough growth was observed on this substrate as usual. Film (b) and (c) show the film grown on pretreated glass substrates with 15 s and 1 min post HCl etching, respectively. The feature size of film (b) was slightly reduced compared with film (a), while film (c) exhibits much smaller surface feature. The rough growth of ZnO:Al films on ion beam pretreated glass with long time HCl etching is not observed any more.

Finally, the effect of standard glass cleaning process was investigated. Film (d) in Fig. 5.14 shows the ZnO:Al film grown on pretreated glass substrates with standard post-cleaning process. Standard small grains were developed instead of the large grains. It clearly shows that the rough growth effect is removed by the glass cleaning process.

ZnO:Al films grow differently on ion beam treated glass substrates. Either the physical or the chemical state of the glass surface or both must be changed by the ion beam

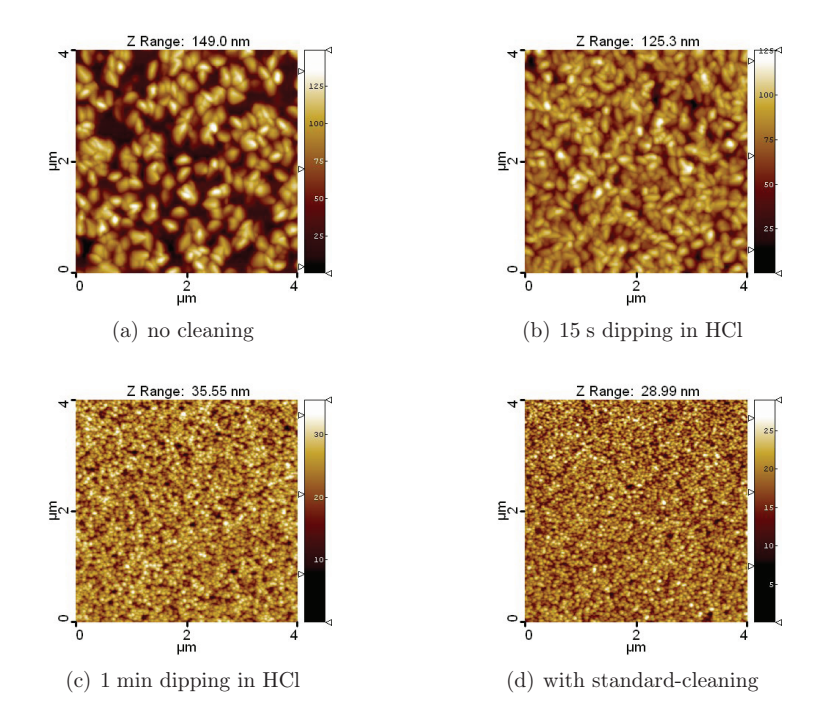


Figure 5.14: The effect of post HCl etching and re-cleaning of ion beam treated glass substrates on the growth of ZnO:Al films. The AFM images show ZnO:Al films grown on Ar/O₂ beam pretreated glass substrates without post-cleaning (a), with 15 s dipping in HCl solution (b), 1 min dipping in HCl solution (c) and with post-standard cleaning process (d). The AFM measurement scan size for all the films are $4\times4~\mu\mathrm{m}^2$. The Z range on top of the AFM images means the height of the color bar.

treatment. SEM and AFM were taken on the ion beam pretreated glass substrates, and no surface roughness was observed. Therefore, the chemical states of the glass surface must be altered by the ion beam treatments. Post HCl etching of the ion beam treated glass substrate lead the growth of ZnO:Al films back to standard, while the NaCl etching has no effect on the rough growth. This indicates that HCl etching can remove the chemical effects on the glass substrates which are needed for the rough growth of the next ZnO:Al films. Moreover, the etching effect of HCl is time dependent and can be changed gradually. Short time dip in the diluted HCl solution cannot fully remove the chemical effects.

As a conclusion for this section, the rough growth of ZnO:Al films was not observed if the ion beam pretreated glass was etched in HCl or re-cleaned by standard cleaning process. These facts indicate the chemical changes on the glass surface caused by the

ion beam treatment are not persistent with acidic solution. The observations give a hint to explore the reason of the rough growth.

5.2.3 Sputter ZnO:Al film in different system

In the previous sections the glass substrates were changed or modified by post-cleaning process. This section examines the growth of ZnO:Al film in other sputtering systems. In our institute, apart from the large area planar target, small area round target, tube ceramic target, and tube metallic target are available as introduced in Section 3.1.1. As for the large area planar target, a sputtering area of $30 \times 30 \text{ cm}^2$ is possible, while sputtering area of $10 \times 10 \text{ cm}^2$ is considered in small area sputtering system. The new installed tube target benefits from its high target material utilization and high sputtering rate. Sputtering process has been optimized at high rate sputtering for Si thin-film solar cells.

In this experiment, Corning glass substrates were pretreated by mixed ${\rm Ar/O_2}$ ion beam under the same condition. Then the glass substrates were transferred to different ZnO:Al sputtering system. ZnO:Al films around 800 nm were sputtered in all systems. In each sputtering system, an untreated glass substrate was added as reference. Finally, the ZnO:Al films were characterized by AFM and 4-point measurement.

The characterization of the ZnO:Al films grown in the four sputtering systems are listed in Fig. 5.15. The scan size of AFM measurement for all samples is $4\times4~\mu\text{m}^2$. The sheet resistance and rms roughness of each sample are marked on the right of the AFM images. For all the samples, with ion beam pretreatment, higher resistance and larger roughness of ZnO:Al films are observed, even though the topographies of ZnO:Al film grown in various system differ from each other.

The rough growth of ZnO:Al films on Ar/O_2 treated glass substrates is a universal effect in different sputtering system. Based on this results, the as-grown rough ZnO:Al films might be possible to transfer to other sputtering system, for instance for industrial process.

5.2.4 Sputter ZnO:Al film with different temperature

This section examines the rough growth of ZnO:Al films in the standard sputtering system with different sputtering parameters. As introduced by the modified Thornton-model in Section 2.2.4.3, the growth of ZnO:Al films depend on the substrate temperature and sputtering pressure. In this section, the deposition temperature was varied to increase the roughness further, while keeping the sheet resistance and total transmittance in a moderate range. Three different heater temperatures were applied during the ZnO:Al deposition. The topography and sheet resistance of the ZnO:Al films change with temperature. On an untreated glass substrate, the ZnO:Al films change from crater-like to pyramid-like feature with decreased compactness as shown in Fig. 2.11 when the temperature decreases. The influence of the rough growth by decreasing the temperature is interested since as-grown rough ZnO:Al films have already pyramide-like features and lower compactness.

Different system	Without ion pretreatment	With Ar/O ₂ pretreatment	
Large area sputtering Planar target ZnO:Al ₂ O ₃ (1wt%)	4 μm 4.5 Ω Rms: 3.4 nm	7 Ω Rms: 32 nm	
Small area sputtering Round target ZnO:Al (0.5 wt%)	20 Ω Rms: 6 nm	70 Ω Rms: 28 nm	
Tube ceramic target ZnO:Al ₂ O ₃ (0.5 wt%)	4.6 Ω Rms: 12 nm	6.7 Ω Rms: 22 nm	
Tube metallic target Zn:Al (0.5 wt%)	3.7 Ω Rms: 8 nm	6.8 Ω Rms: 20 nm	

Figure 5.15: ZnO:Al films deposited in different sputtering systems. The target in each system is described in the first column. The AFM topography of the ZnO:Al films grown on untreated and ${\rm Ar/O_2}$ treated glass are shown in the second and third column, respectively. The sheet resistance and rms roughness of each sample are displayed on the right of the AFM images.

The first step of the experiments is ion beam pretreatment by mixed ${\rm Ar/O_2}$ ions. Afterwards the glass substrates were transfered to standard sputtering chamber and heated in the chamber for at least 90 min. Finally, the ZnO:Al films were sputtered at the standard condition except the temperature is varied. For a reference ZnO:Al film, 430 °C is used as heater temperature. In this experiment, lower temperature of 350 °C and 250 °C were examined. The deposition time was adjusted to achieve ZnO:Al films with desired thickness.

The results are shown in Fig. 5.16. The scan size of AFM measurement for all samples is $4\times4~\mu\text{m}^2$. The thickness, sheet resistance of each film are marked on the top of the AFM image and the the rms roughness is given at the bottom of the image. At 430 °C, two films were sputtered with thickness of 350 nm and 650 nm. The sheet resistance

of the thicker film decreases. The rms roughness is constant, while features size and coverage of large grains increase. At 350 $^{\circ}$ C, two films with further increased thickness of 700 nm and 800 nm were sputtered. The rms roughness of the two films are the same (52 nm). With lowest heater temperature at 250 $^{\circ}$ C, the sputtered film shows largest rms roughness of 57 nm.

The feature size of the as-grown rough ZnO:Al film can be adjusted by the deposition temperature. When the temperature is decreased, the feature size increases due to less nucleation densities of large grains. Up to now, the feature size can be improved from 500 nm to around 800 nm.

5.2.5 Different ion beam system

In the previous sections, ion beam treatments were performed only with the linear anode layer ion source. Actually, the ion beam pretreatments of glass substrates were also applied with a round anode layer ion source. The round ion source is integrated in a cluster-tool of ZnO:Al and ZnO:Ga sputtering system as a sputter-etcher. The ion source and two other ZnO targets face upwards to the substrate holder. The substrate needs to rotate if homogeneous deposition or treatment is required. Like for the linear

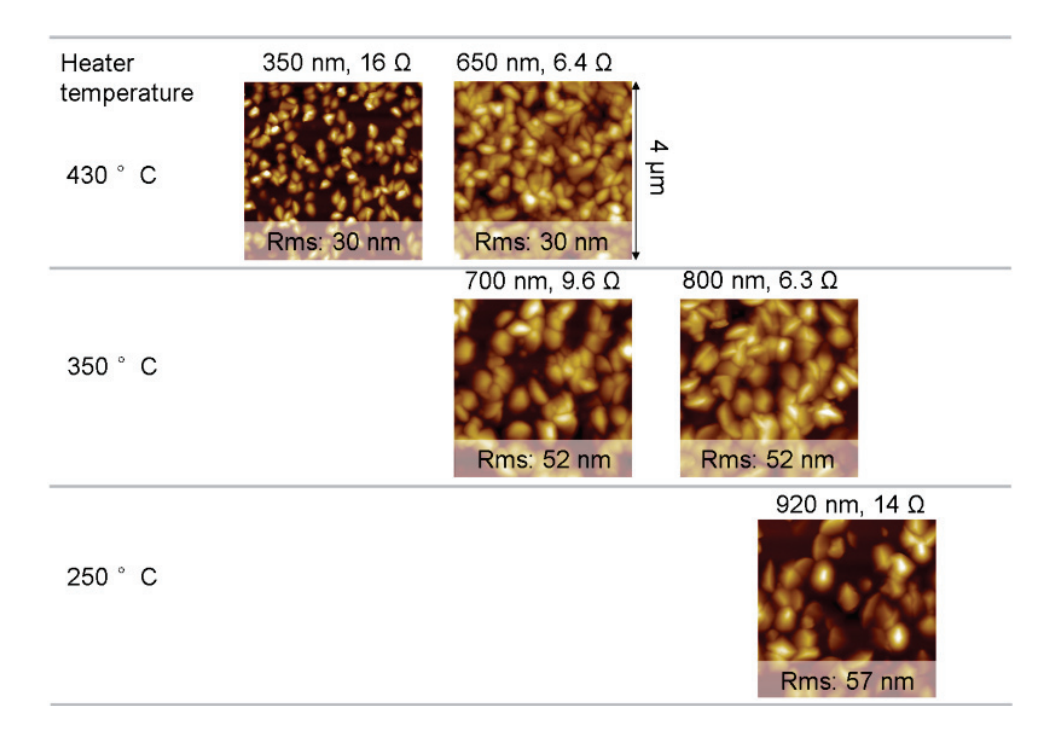


Figure 5.16: AFM images of ZnO:Al films sputtered at different temperatures. The thickness, sheet resistance and rms roughness are marked on the images.

anode layer ion source, Ar and O_2 can be used as source gas. The maximum power of this ion source is 600 W.

 $10 \, \mathrm{sccm} \, \mathrm{Ar}$ and $10 \, \mathrm{sccm} \, \mathrm{O_2}$ were utilized as source gases for the ion beam treatments. The power of the ion source was kept at 200 W. The Corning glass substrate did not rotate. Therefore, only part of the substrate was bombarded by the ion beam. After ion beam pretreatment, the glass substrate was transfered to standard ZnO:Al sputtering system and standard ZnO:Al film was rf sputtered from a ceramic target. The experimental process is shown in Fig. 5.17. As shown in the first step, area A was treated by the ion beam, while area B was not treated by the ion beam. A sharp line between area A and B can be seen by naked eye. The second step in Fig. 5.17 is magnetron sputtering on the ion beam pretreated glass substrate. The difference between area A and B becomes even more obvious. Area A is transparent while area B is milky.

The AFM measurements of area A and B are shown in Fig. 5.18. The measurement scan size for the two areas are $4\times4~\mu\text{m}^2$. The film in area A has small feature size while film in area B has large pyramids. Thickness and 4-point probe measurements were performed on the two areas. The results show that film in area B has thinner thickness and higher resistance than film in area A. The thinner thickness indicates that the film grown on the unetched area has reduced growth rate. The results are almost the same to the as-grown rough ZnO:Al films grown on Ar/O_2 treated glass by linear anode layer ion source. Therefore, ZnO:Al films grown on ion etched area A behave like the reference films, while the films on area B where the ion beam cannot reach has as-grown rough features. The reason will be analyzed in Section 5.4.3.

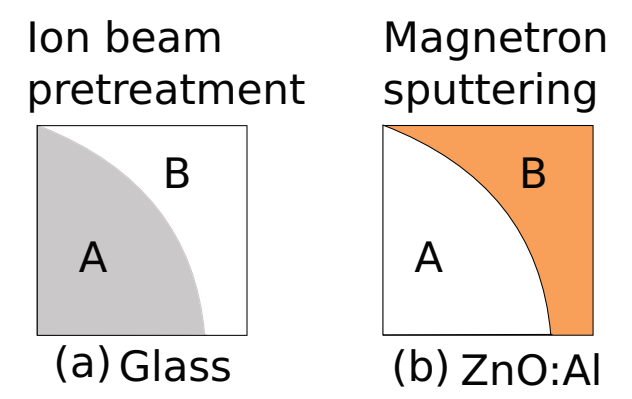
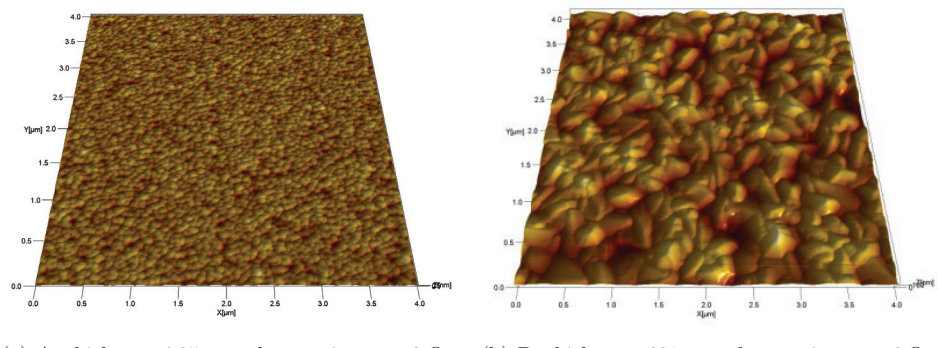


Figure 5.17: The experimental process of ion beam pretreatment in the sputter etcher system. Area A is the area where the ions were reached, area B is where the ions were not reached.



(a) A, thickness: 785 nm, sheet resistance: 3Ω

(b) B, thickness: 691 nm, sheet resistance: 6 Ω

Figure 5.18: ZnO:Al films grown on the glass substrates which were treated by ions from sputter-etcher. On different areas, the ZnO:Al films have different morphologies. (a) is on area A where the ions are reached, (b) is on area B where the ions were not reached.

5.3 Surface evolution and structural properties

The previous sections have shown that the ZnO:Al films grown on ${\rm Ar/O_2}$ treated glass substrate exhibit rough lateral features with lateral length of approximately 500 nm. Reference sputtered ZnO:Al films on untreated glass substrates are usually (0001) textured because the (0001) plane has lowest surface energy. Actually, (0001) texture dominates most sputtered ZnO:Al films [72, 138, 139]. However, in as-grown rough ZnO:Al films, two types of grains - large conical grains and small columnar grains are present. The crystal orientations of the two types of grains are unknown. This section focuses on the surface evolution and structural properties of the as-grown rough ZnO:Al films. AFM measurements of reference and as-grown rough ZnO:Al films with different thickness are given. The mechanisms in the growth process are analyzed based on the statistical values from AFM images. Next, the structural properties of as-grown rough ZnO:Al films are analyzed by TEM and XRD. The crystal orientations of the two types of grains are revealed.

5.3.1 Film evolution

In the previous sections different ion beam treatments were applied on the glass substrates. It turns out that on the ${\rm Ar/O_2}$ treated glass substrate, ZnO:Al film has largest feature size. Thus, this specific treatment will be focused and more analysis will be carried out to understand the film growth. This section examines the evolution of ZnO:Al films sputtered on untreated and ${\rm Ar/O_2}$ treated glass substrates by the theory of dynamic scaling which was introduced in Section 2.2.4.5. To do so, AFM measurements were taken on ZnO:Al films sputtered for different time. The dynamic components ob-

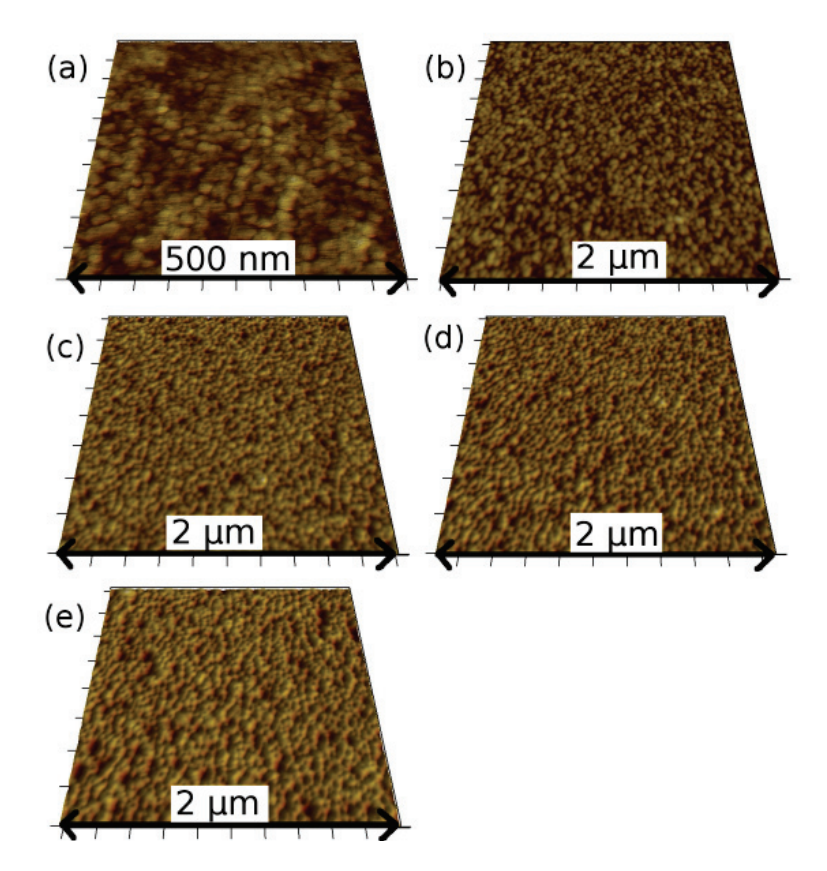


Figure 5.19: AFM measurements of reference ZnO:Al films. From (a) to (e), the films deposition time are 4 min, 19 min, 38 min, 57 min and 76 min, respectively. As depicted in the figure, the scan size of film (a) is 500×500 nm², of films (b)-(e) is 2×2 μ m².

tained from AFM measurements are compared to the theoretical values in literature. Thus, the kinetic roughening process can be related to various growth mechanisms.

In order to investigate the evolution of the ZnO:Al films grown on untreated and $\rm Ar/O_2$ ion beam treated glass, films were prepared with different thicknesses. The thickness is controlled by the deposition time. As-grown rough and reference ZnO:Al films for different deposition duration (4 min, 19 min, 38 min, 57 min, 76 min and 152 min) were sputtered at the same time. Then, AFM measurements were taken on the film surfaces. Based on the AFM measurements, various growth dynamic parameters which reflect the growth mechanism during the magnetron sputtering are investigated and compared with theoretical values.

The film topographies are shown in Fig. 5.19 and Fig. 5.20 for reference and as-

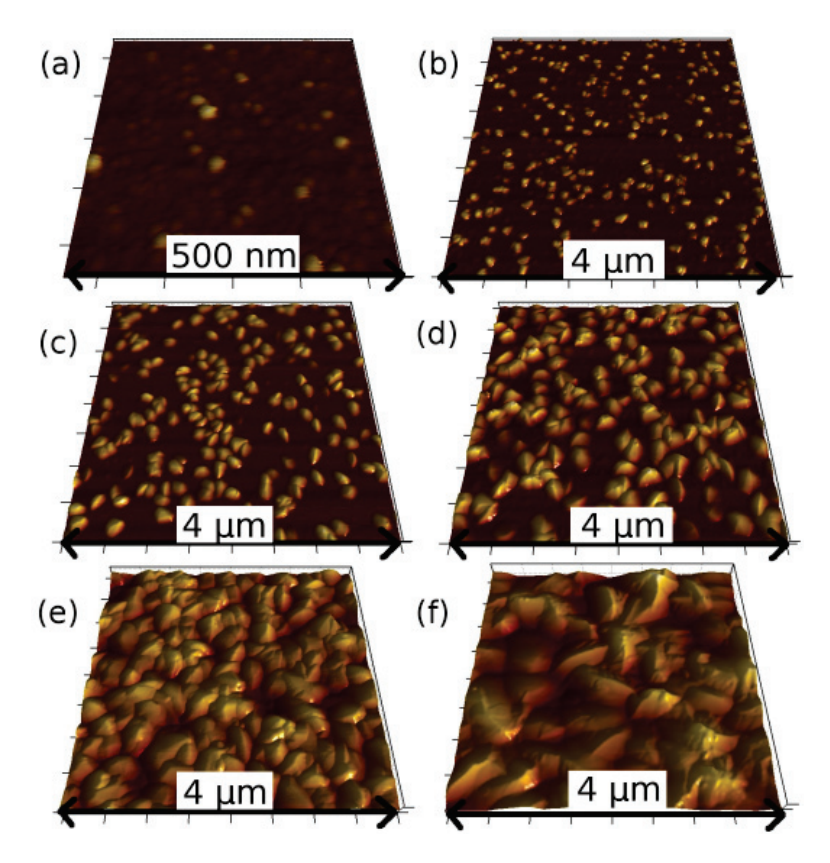


Figure 5.20: AFM measurements of as-grown textured ZnO:Al films on Ar/O₂ ion beam treated glass substrates. From (a) to (f), the films deposition time are 4 min, 19 min, 38 min, 57 min, 76 min and 152 min, respectively. As depicted in the figure, the scan size of film (a) is 500×500 nm², of film (b)-(f) are $4 \times 4 \ \mu \text{m}^2$.

grown rough ZnO:Al films, respectively. Note that the reference film at 152 min was not measured since cracks had developed on the film. The formation of cracks is related to stress in the ZnO films induced by the growth process itself or the different thermal contraction of substrate and film after deposition. This becomes usually more critical for thick films.

The reference and as-grown rough ZnO:Al films grown at 4 min have exhibited big differences. Reference film is composed of small grains with size in a range of 25-40 nm. The height of the grains is uniformly distributed. However, on the as-grown rough film, except the small grains which have similar size and height to the reference film, some bumps are developed among the small grains. The situation becomes more obvious

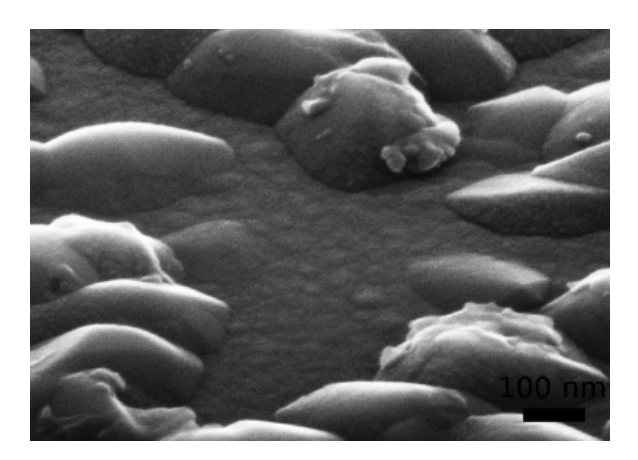


Figure 5.21: SEM micrograph of as-grown rough ZnO:Al film at 57 min. The small ZnO grains between the large grains are flat.

when the deposition time increases. For the reference films from 19 min to 76 min, the average grain size is unchanged in the range of 66-76 nm. For the as-grown rough films, at 19 min, the bumps which are distributed randomly on the surface are around 40 nm higher than the surrounding small grains. The sizes of the small grains in the flat plateaus on the as-grown rough films are not measurable from AFM measurements due to the limit of the setup. High resolution SEM micrograph of film at 57 min in Fig. 5.21 shows that the small grains are so flat that the grain boundaries are difficult to be identified.

The large grains in the AFM measurements correspond to the conical grains in SEM cross-sectional images. The large grains which start from the nucleation stage distribute on the surface randomly. Because they grow faster than the surrounding flat grains, finally they cover the whole surface of the as-grown rough ZnO:Al film. The mean diameter and coverage of the large grains for the six films were counted by advanced threshold detection method with a commercial imaging process software - scanning probe image processor (SPIP) [140]. The advanced threshold detection method first mark the area of particles and then split the grains according to the height of the grains. The results are shown in Fig. 5.22. The mean diameter and coverage of the large grains are shown by solid squares and triangles, respectively. The standard deviation of the grain size is marked by the error bars. The grain size increases with increasing film thickness, as well as the coverage of large grains on the surface. The latter reflects the fact that more and more surface areas are covered by the large grains. The dashed line indicates that the size of the large grains increases linearly with deposition time on the log-log scale. It means that the size of large grains exhibit a power law relationship to the deposition time, which is a common phenomenon for the growth of aggregates on seeds [87]

The height-height correlation function H(r,t) and power spectral density function

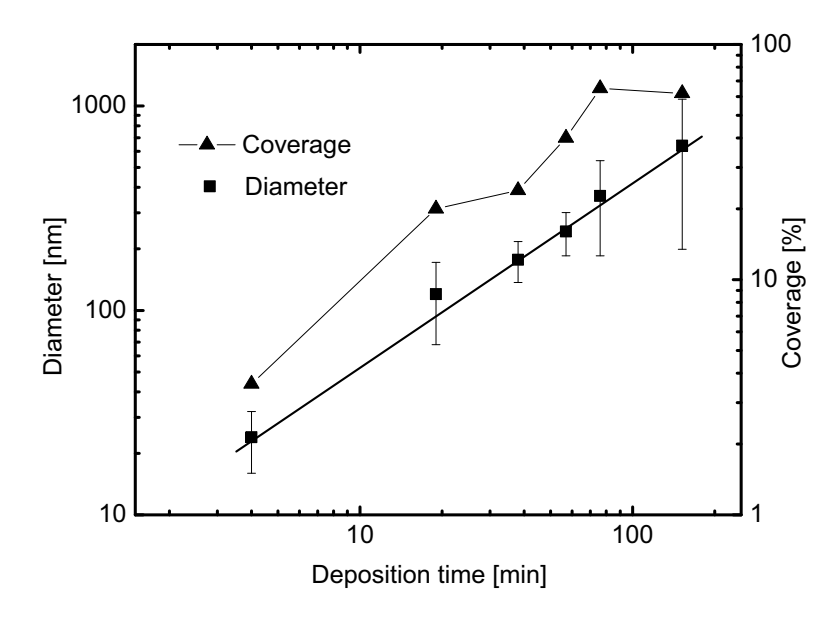


Figure 5.22: Statistics on the large conical grains of the ZnO: Al films grown on $\rm Ar/O_2$ treated glass.

PSD(k,t) of the ZnO:Al films with different deposition time can be obtained directly from AFM software. Both are displayed in Fig 5.23 in logarithmic scale. The reference ZnO:Al films are shown in black while the as-grown rough films are in blue. The deposition time is denoted in the figure.

Fig. 5.23(a) shows that H(r) increases linearly at small r and reach plateaus at large r, consistent with the asymptotic behavior predicted in Eq. 2.30. Another observation from the figure is that all H(r) curves at small r value except the as-grown rough ZnO:Al films after 57 min shift upwards gradually with increasing time. This is different to the other reports in literature of a normal scaling surface, where the local slope is time invariant [141]. The upward shift of H(r,t) at small r range indicates that the existence of anomalous scaling in the growth of ZnO:Al films. The anomalous scaling has also been found by many theoretical models [142] and experimental results [143–145].

Fig. 5.23(b) shows the PSD(k,t) functions of all the films. It is clear that all curves are composed of two regions according to equation 2.31: (a) for high k value (i.e., small length scales) there is a negative slope, indicating the existence of kinetic roughening for these length scale; (b) for small k values (i.e., saturated), indicating the absence of any lateral correlation in the surface roughness at these length scales.

From the H(r,t) curves, roughness σ , lateral correlation length ξ and roughness exponent α are obtained as introduced in Section 2.2.4.5. Firstly, the roughness exponent α for all the films are around 1 in the measurement error range. Then, roughness of

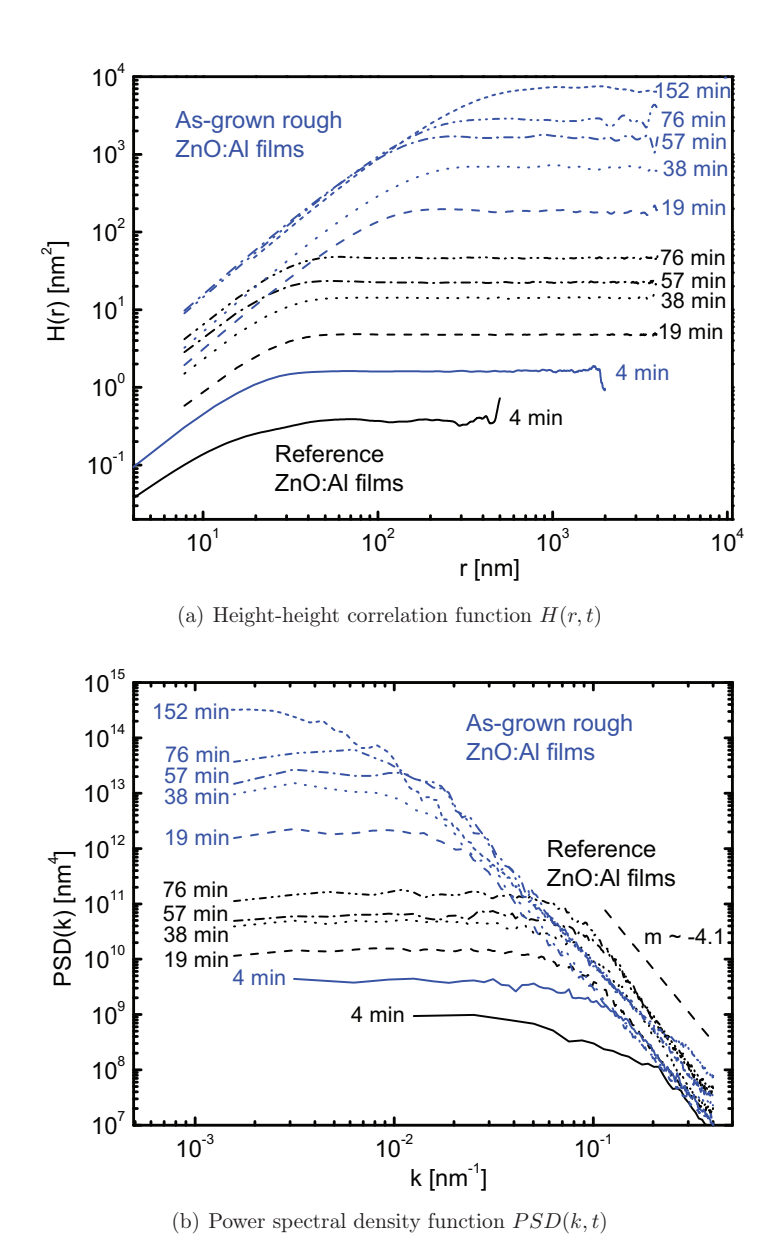


Figure 5.23: Height-height correlation function H(r,t) (a) and power spectral density function PSD(k,t) (b) of the reference (black) and as-grown rough (blue) ZnO:Al films with different deposition time (denoted near the curves).

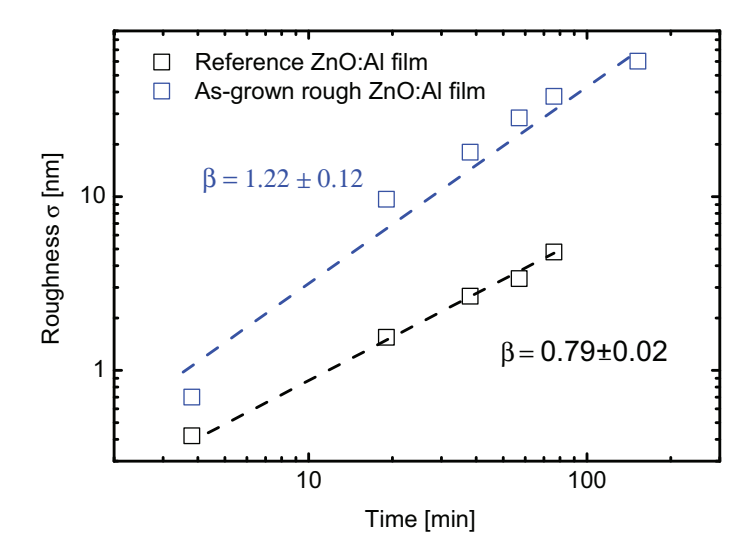


Figure 5.24: Roughness of reference and as-grown rough ZnO:Al films versus growth time. The dashed lines are the fitting lines. The slope of the dashed lines is characterized by growth exponent β .

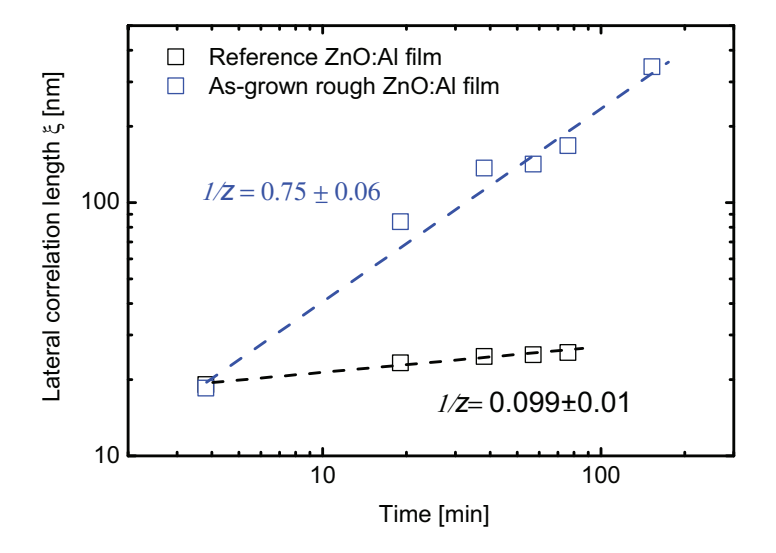


Figure 5.25: Lateral correlation length of reference and as-grown rough ZnO:Al films versus growth time. The dashed lines are the fitting lines. The slope of dashed line is characterized by coarsening exponent 1/z.

reference and as-grown rough ZnO:Al films versus growth time are drawn in Fig. 5.24 in logarithmic scale. The slope of the dashed lines is characterized by the growth exponent β . The reference ZnO:Al films have growth exponent β of 0.79 ± 0.02 and the as-grown rough ZnO:Al films have a larger value of 1.22 ± 0.12 . Therefore, $\beta/\alpha = 0.79$ and 1.22 for reference and as-grown rough films, respectively. Finally, the logarithmic plot for the evolution of lateral correlation length ξ is shown in Fig. 5.25. For the reference ZnO:Al film, coarsening exponent $1/z = 0.09 \pm 0.01$ is obtained and for the as-grown rough ZnO:Al films, $1/z = 0.75 \pm 0.06$. For both films, β/α are larger than the coarsening exponents. This indicates that the dynamic scaling relation $\beta/\alpha = 1/z$ is broken down for these two series of films. In the following, the growth mechanisms behind the breaking down behavior will be explained.

Firstly, the reference ZnO:Al films is compared with the theoretical values. The films are developed with unstable process, as indicated by $\beta=0.79\pm0.02>0.5$. Shadowing and reemission effects are dominant over the diffusion effects in determining β . The reemission effects are taken into account because the substrate is heated to 300 °C and the ZnO starts to evaporate at 380 °C. For large length scales, shadowing influences the scaling. The coarsening exponent 1/z=0.09 is close to the lower limit of the predicted value with in error. The low 1/z means that the grains grow preferably in vertical direction than lateral direction and well aligned columnar structures are developed. According to Tong et al. [88, 146], the short length scale behavior is dominated by surface diffusion effects if the PSD(k) curve has slope of -4 on a log-log plot at large k range, which is the case for ZnO:Al films (The dashed line in Fig. 5.23(b) represents line with slope of -4.1).

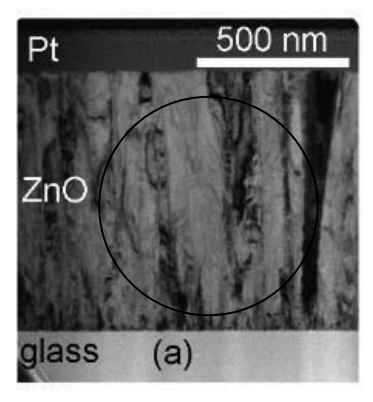
Next, for the as-grown rough films, $\beta > 1$ exceed the theoretical prediction limit. The rapidly increasing roughness indicates that the films grow under very unstable conditions. This phenomenon might be caused by enhanced shadowing effect caused by the height difference of the two types of grains. However there are no calculation to support this assumption. $\beta > 1$ was reported in the earlier growth stage of reactively sputtered AlN thin films [92]. The reason was assumed to be different sticking probabilities of impinging particles on different crystalline planes [147]. In the earlier stage of the AlN growth, wellaligned and textured grains are embedded into a randomly oriented matrix. Thus, these regions having a higher sticking probability should grow faster than the other regions. This scenario, combined with shadowing, can be used to explain the growth instability with a high β value ($\beta > 1$). The sticking difference is not limited to nitride films, but also applied to ZnO films [71]. In the bulk growth of reference ZnO:Al films, the (0002) planes are spread over the whole surface, therefore, the sticking probability is similar on the whole surface. Conversely, for the ZnO:Al films grown on ion beam treated glass substrates, the small grains might have lower sticking probability, not only because of their lower location, but also due to their crystallographic structure. The difference of sticking probability and shadowing effect lead to a high β value with $\beta = 1.22 \pm 0.12$.

As a conclusion, this section has discussed the evolution of reference and as-grown rough ZnO:Al films. The differences of growth behavior between the two types of films start from the nucleation stage. On ${\rm Ar/O_2}$ treated glass substrates, some bump grains were developed among the flat grains. The growth front surfaces for both films are not

self-affine because of the shadowing effect during the sputter deposition. The as-grown rough ZnO:Al films are characterized by very high growth exponent with $\beta > 1$. It is assumed that the reason to be that the growth instability is enhanced by different sticking probability of impinging particles on large and small grains.

5.3.2 Transmission electron microscopy measurements

This section focuses on the Transmission electron microscopy (TEM) measurements of ZnO:Al films. TEM enables us to investigate the grains in detail by transmitting a beam of electron through an ultra thin specimen and interacting with the specimen as it passes through. Not only the morphology, but also the crystallographic structures of the specimen can be abstracted from the dark-field images and diffraction patterns.



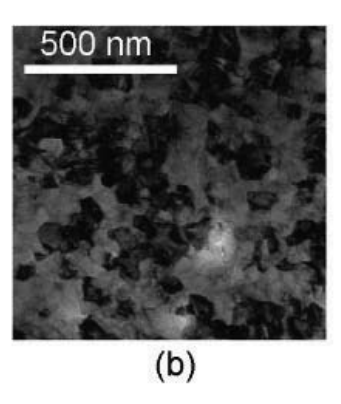


Figure 5.26: TEM bright field images of reference ZnO:Al films. (a) cross-sectional image and (b) plan-view image.

For our purpose, both reference ZnO:Al films and as-grown rough ZnO:Al films were measured by TEM. Cross-sectional and plan view specimens were prepared with different sample preparation technique as described in Section 3.3.4.2. In the following, firstly the bright field images and selected area diffraction pattern (SADP) of reference ZnO:Al films are introduced, then these of the as-grown rough ZnO:Al films are presented.

The cross-sectional and plan view TEM bright field images of the reference ZnO:Al films, i.e. grown on untreated glass, are shown in Fig. 5.26. As shown in cross-sectional TEM, the films are composed of columnar dominated grains which are directed nearly perpendicular to the glass substrate. The plan view TEM image shows that the average grain size which also corresponds to the width of the columns is measured to be approximately 50 nm. The corresponding SADP are shown in Fig. 5.27. The circle in Fig. 5.26(a) shows the aperture to obtain the diffraction pattern of the cross-section view (Fig. 5.27(a)). Two diffraction patterns of the (2-1-10) and (01-10) pole are revealed from the SADP, marked by the red and yellow circles, respectively. In addition, the

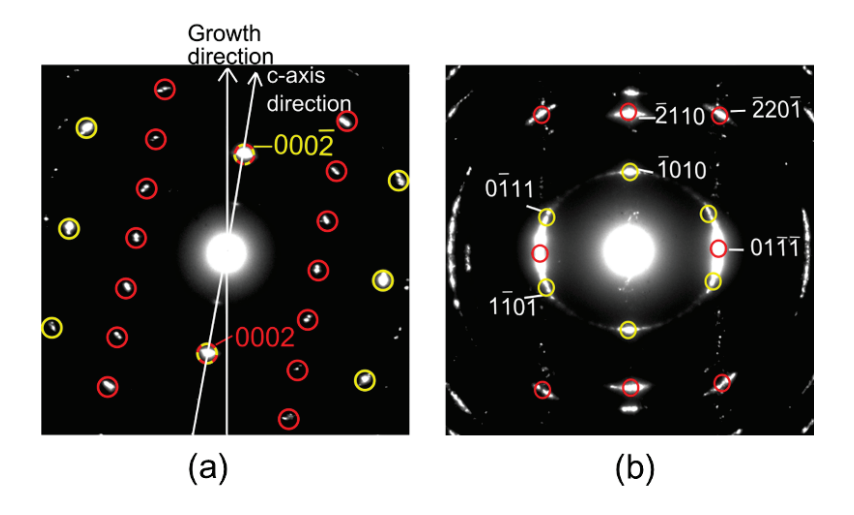


Figure 5.27: Selected area diffraction pattern (SADP) of reference ZnO:Al films. (a) is from cross-sectional specimen and (b) is from plan view specimen.

growth direction is indicated, which deviates by approximate 10° from the [0001] direction. The tilted angle of the c-axis is determined by the direction difference of the bright field image in Fig. 5.26(a) and the diffraction pattern in Fig. 5.27(a). Hence, it can be concluded, that two sets of orientation of the columnar grains prevail. The SADP of the plan view sample (Fig. 5.27(b)) is mainly composed of two diffraction patterns, too, namely the (01-12) pole (red) and the (1-21-3) pole (yellow). However, the diffraction spots are arranged in an arc-like fashion, which indicates small angular deviations of the orientation of neighboring grains.

Fig. 5.28 shows the TEM bright field image of the as-grown rough ZnO:Al films, i.e. grown on ${\rm Ar/O_2}$ treated glass. The discharge voltage of this treatment was 1 kV. Note that the voltage of the ion source doesn't have major influence on the as-grown rough features. From cross-sectional TEM (Fig. 5.28 (a)), it is seen that the film contains not only fine columnar grains, but also few large conical grains which appear at statistical, but quite regular intervals. Note that the large conical grains have been observed on the AFM image of 20 nm thick as-grown rough ZnO:Al (Fig. 5.20(a)). The bottom of cones does not appear on the glass substrate in the cross-section TEM image, because the cut is not in the center of the cones. During the film growth process, they gradually overgrow the small columnar grains and cover the whole film surface. Therefore it is concluded, that the large grains have faster growth rate than the surrounding columnar grains. For the SADP shown in Fig. 5.28(b), a small selected area aperture (marked in Fig. 5.28(a)) was applied such that only the columnar grains were included. The SADP has similar basic pattern as the reference film, together with some additional spots. The similarity between the patterns indicate that the columnar grains in the as-grown rough

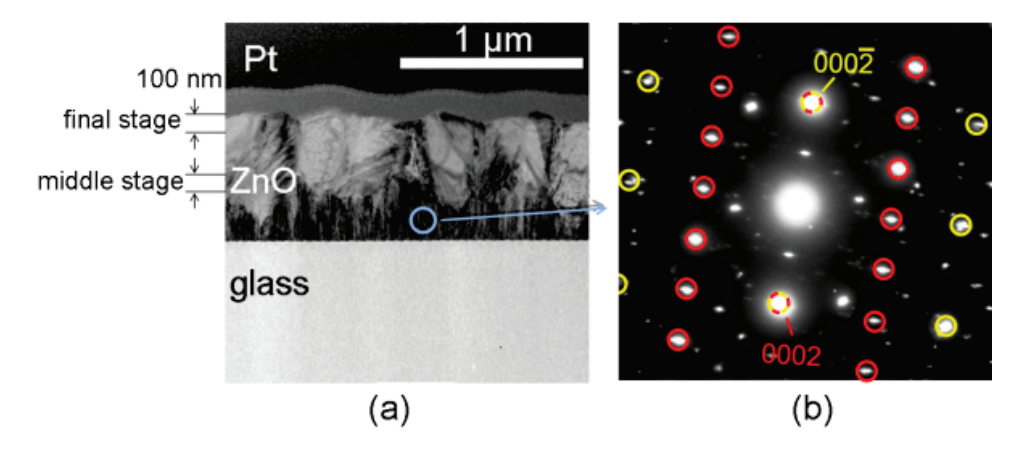


Figure 5.28: TEM of the as-grown rough ZnO:Al films. (a) is the cross-sectional bright field image and (b) is SADP of the small columnar grains. The aperture is marked by the blue circle in (a).

ZnO:Al films are similar to the reference material. The additional spots might have originated from some large grains that lay behind the columnar grains in the lamella.

In order to investigate the difference between the large and small grains, two planview TEM specimens were investigated for as-grown rough ZnO:Al films. The specimens represent a cut at thickness level of 650 nm (Fig. 5.29 (a-b)) and 350 nm (Fig. 5.29(c-f)), respectively. This implies that two different stages of the growth are seen as indicated in Fig. 5.28(a), because plan view specimens reveal only the top 100 nm of the films. Accordingly, Fig. 5.29(a) detects only the large conical grains reigning the upper part of the film which are in average 500 nm in size. Fig. 5.29(c) images roughly a cut through a layer containing both, the fine columnar grains and the large conical grains.

Interestingly, the diffraction patterns corresponding to these intermediate and final growth stages differ considerably: The diffraction pattern of the intermediate stage reproduces the features observed for the sample grown onto untreated glass (compare Fig. 5.29(d) and Fig. 5.27(b)), except for some additional spots in between the arcs. Fig. 5.29(e) and (f) show the dark field images for the diffraction spots marked by blue dashed and green solid circles, respectively (see Fig. 5.29(d)). It is confirmed that the additional spots are contributed by the large conical grains while the arcs are generated from the smaller columnar grains. In contrast to the intermediate stage, the small columnar grains are not present in the final stage. The conical grains show a ring diffraction pattern, which implies a random, azimuthal in-plane orientation of the crystallites. Note, that the selected area for the intermediate state (Fig. 5.29(d)) SADP was around 1 μ m², so the number of large conical grains and thus the number of related SADP peaks is limited and the ring is not fully developed. On the other hand, the number of large conical grains for the SADP of the final stage (Fig. 5.29(b)) is more

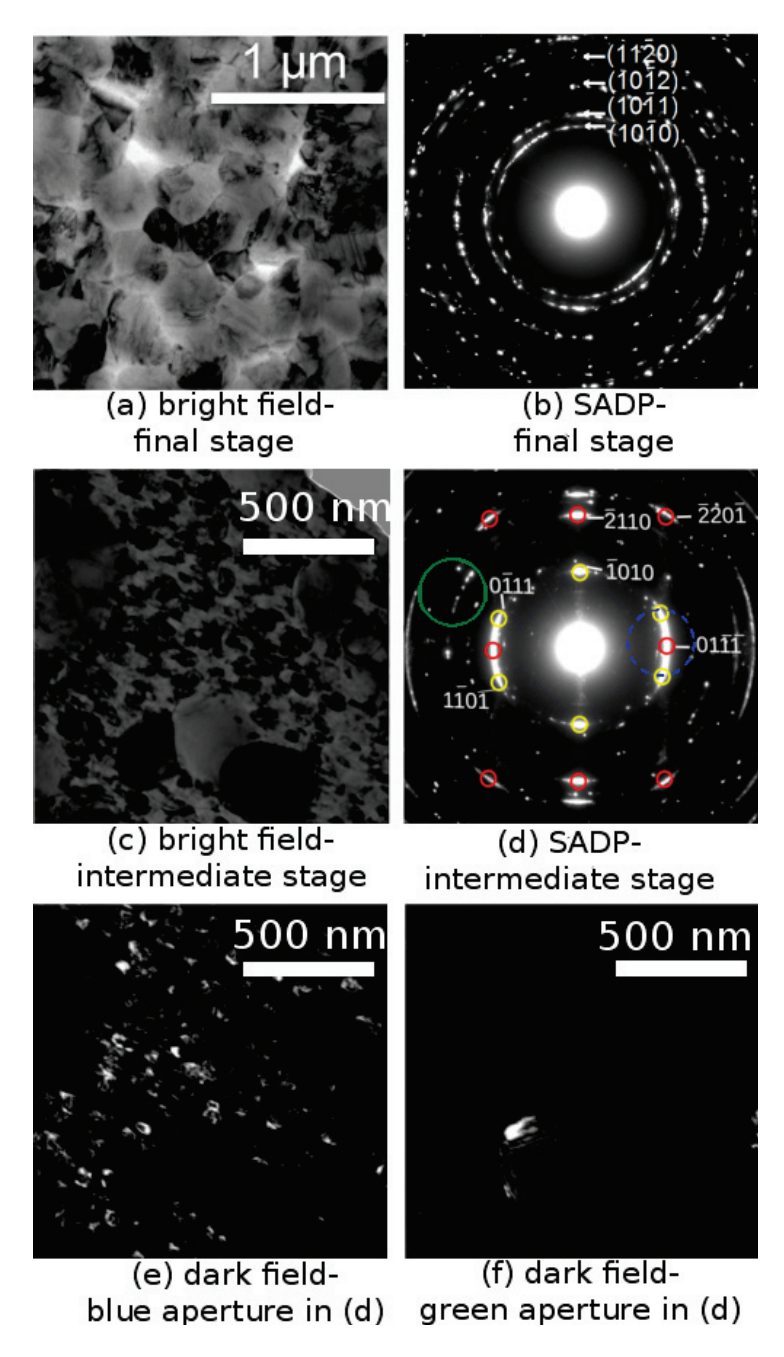


Figure 5.29: Plan view TEM bright field images of as-grown rough ZnO:Al films at final stage (a) and intermediate stage (c), and their corresponding SADP (b) and (d). (e) and (f) show the dark-field image with two different apertures as marked in (d) by blue dashed and green solid circles, respectively.

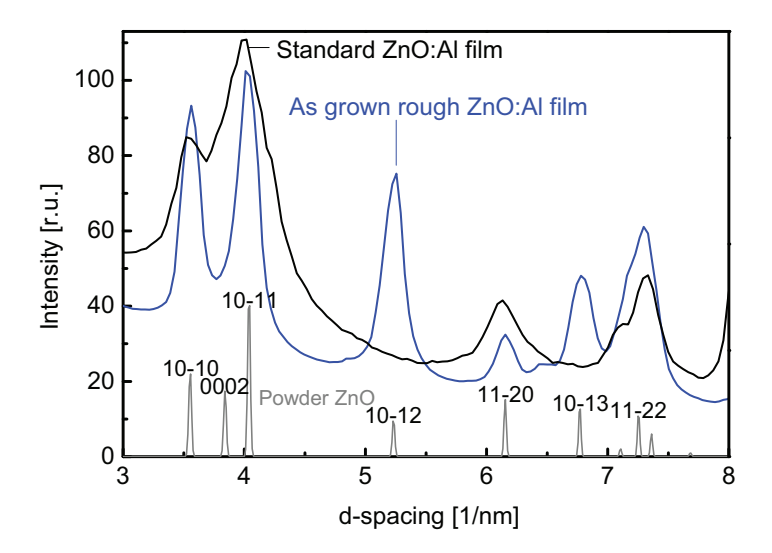


Figure 5.30: Radial profile plot of the SADP from the final stage of as-grown rough ZnO:Al films as shown in Fig. 5.29(b) (blue) and the standard ZnO:Al films as shown in Fig. 5.27(b) (black), as well as of ZnO powder (gray). All the peaks are marked by the corresponding planes.

increased, so that the ring pattern is obtained.

Fig. 5.30 shows the radial integration of the ring diffraction pattern in Fig. 5.29(b) by the blue curve. The radial integration of the diffraction pattern of standard ZnO:Al film grown on untreated glass substrate is shown by black curve. The spectra for powder ZnO is also given by thin gray curve on the bottom. Major diffracted planes are marked in the figure. For the reference ZnO:Al films, only (10-10), (11-20), (10-11) and (11-22) planes were observed. Note that only the planes parallel to the electron beam in TEM can be detected. Thus, the two planes (10-10) and (11-20) indicate the materials with c-axis orientation. The other two planes (10-11) and (11-22) indicate the materials with inclined c-axis orientation. For the large grains in as-grown rough ZnO:Al films, almost every planes are presented, except only the (0002) peak is missing, indicating that large grains exhibit quasi random out-of-plane orientation, but the c-axis of the crystallites parallel to the surface is strongly suppressed. Moreover, cross-sectional TEM measured on several conical grains give different SADP. Thus, it can be concluded that the conical grains have near random out-of-plane orientations.

The aim of this section was to determine the crystallographic structure of the two types of grains in as-grown rough ZnO:Al films by performing TEM measurements on reference and as-grown rough ZnO:Al films. It was proven that the columnar grains in reference ZnO:Al films have dominate (0002) texture, though the (0002) orientation is approximate 10° tilted to the surface normal. The grains have similar in-plane orientation in the

neighboring area, but on the large scale, the ZnO:Al grains should have random in-plane texture [139]. TEM measurements have shown that the small columnar grains and large conical grains have different orientations. The small grains have similar orientation as the columnar grains in reference ZnO:Al films, while the large grains have quasi-random out-of-plane orientation, and the grains with c-axis parallel to the surface is strongly suppressed. The in-plane orientation of the large grains are random.

5.3.3 X-ray diffraction measurements

This section examines the structural properties of as-grown rough ZnO:Al films by X-ray diffraction (XRD) technique. For this measurements, reference and as-grown rough ZnO:Al films were co-deposited with different time. The thickness of the two series of films varies from 30 nm to 1556 nm. For the reference films, due to the cracks formed in the films at thickness over 1000 nm, the maximum thickness of the analyzed films is 792 nm. As learned from the previous discussions, the conical grains already coalesce with each other when the film is 620 nm thick. The film of 1556 nm thickness contains a large fraction of conical grains.

Fig. 5.31 shows the XRD $\theta-2\theta$ measurement results of reference (a) and as-grown rough (b) ZnO:Al films at different thickness. The thickness of each film is indicated in the figure. Dominant (0002) and (0004) peaks were observed for all samples, even for very thin films. This indicates that all the films have (0002) preferential orientation. Except the dominant two peaks, some additional small peaks start to show up for the as-grown rough sample at 650 nm thick (Fig. 5.31(b)). When the as-grown rough film continues grows to 1556 nm, (0002) and (0004) peaks are still the dominate, and the additional peaks are increased slightly.

In order to investigate the additional peaks in more detail, Fig. 5.32 shows the asgrown rough and reference ZnO:Al films together. As already pointed out, (0002) and (0004) are the dominant peaks for both films, while the film on Ar/O₂ treated glass shows additional (10-10), (10-11), (10-12), (10-13) and (11-20) peaks. The peak at 30.9° is the (0002)-K_{β} peak. The one at 37.4° seems to be a parasitic peak that appears in the setup used for measurement, and it might correspond to some unknown impurity of the x-ray source.

The strong intensity of the dominant (0002) peaks of the reference as well as the asgrown rough ZnO:Al films indicate, that there is a preferential orientation of the ZnO crystallites along the c-axis. This peak is attributed to the fine columnar grains. This means, that the columnar grains on the treated substrate are similarly oriented and aligned as the reference material. The additional peaks except (0002) and (0004) are attributed to the conical grains in the as-grown rough films since they are not present in the reference material. However, some part of the conical grains might still contribute to the (0002) and (0004) peak, since the intensities of the additional peaks seem rather low considering the fact that the conical grains cover a large portion of the film volume.

In the following, the additional peaks are evaluated further, in order to find out the orientation of the conical large grains. The open triangles and circles in Fig. 5.33 show the intensity of these additional peaks of the as-grown rough ZnO:Al film with

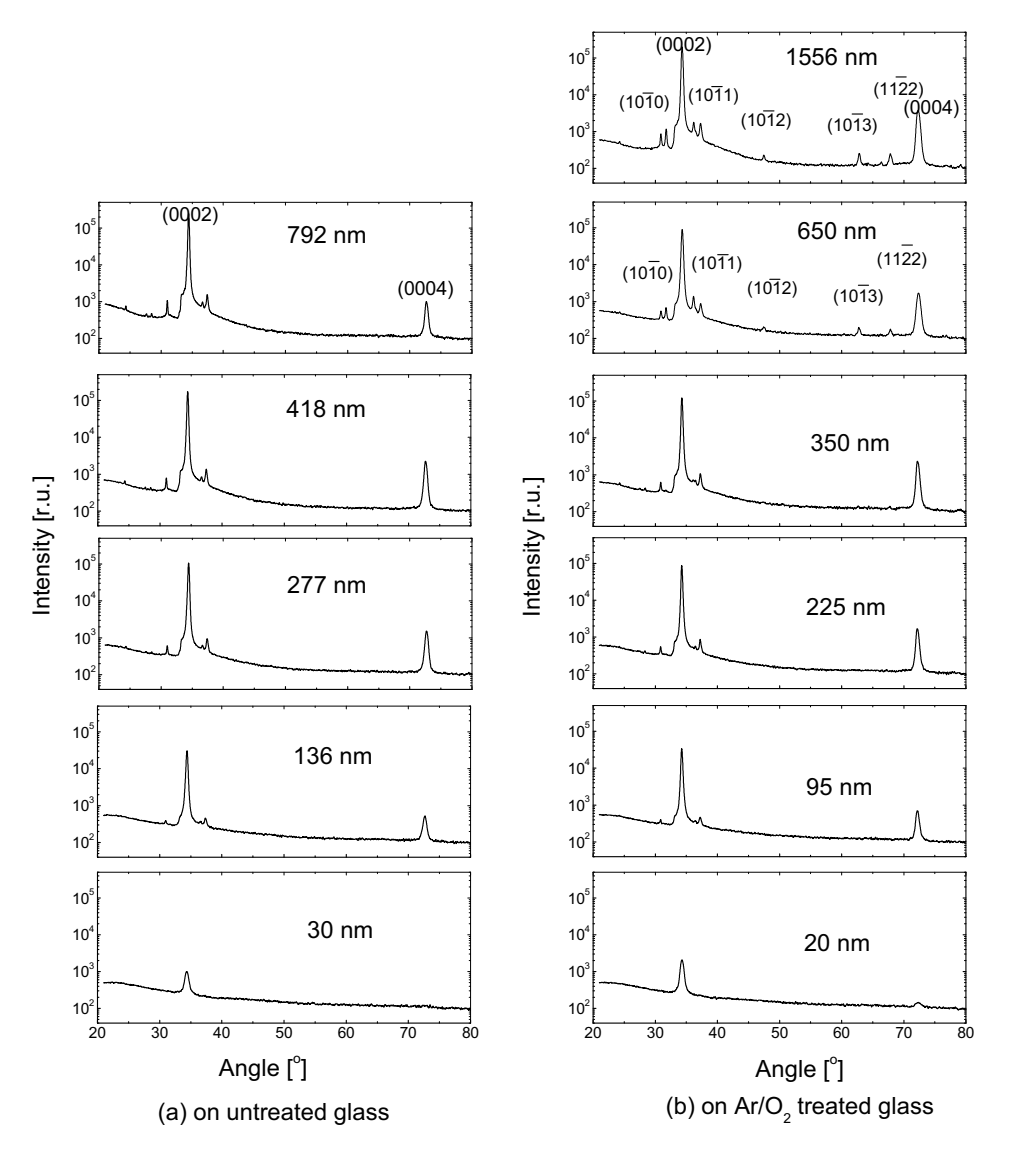


Figure 5.31: $\theta-2\theta$ XRD scans of the two ZnO:Al thickness series, in which (a) - reference ZnO:Al films, (b) - as-grown rough ZnO:Al films.

thickness of 1556 nm and 650 nm, respectively. The black solid squares represent the intensity of ZnO powder pattern. Considering the as-grown rough ZnO:Al film with 650 nm thickness, basically the intensity pattern of the additional peaks is close to the one of ZnO powder. It means that the conical grains have nearly random orientation.

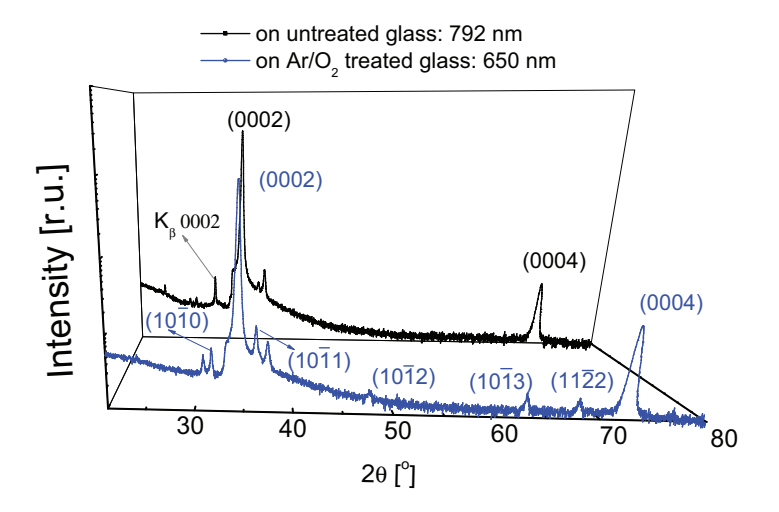


Figure 5.32: Comparison of XRD peaks for reference film (thickness: 792 nm) and asgrown rough ZnO:Al films (thickness: 650 nm).

Only the (10-11) peak is higher and (11-20) peak is lower than the corresponding peaks of the ZnO powder. The higher (10-11) peak might be related to the columnar grains, since even in the XRD signal of reference ZnO:Al films, there is a small (10-11) peak (Fig. 5.32). The not detectable (11-20) peak in as-grown rough film indicates that no crystallite has c-axis parallel to the substrate plane, which is corresponding to the suppressed (0002) peak in TEM SADP (Fig. 5.30). Comparing the additional peaks of the as-grown rough films with thickness of 1556 nm and 650 nm, the thicker film has obviously increased intensities of (10-10), (10-11) and (11-22) peaks, while the intensities of (10-12) and (10-13) peaks are only slightly increased. This might be caused by the different growth rate of various grains.

Apart from the $\theta-2\theta$ scan, the (0002) peaks were also analyzed in detail including full width at half maximum (FWHM), peak position, and peak intensity for the two thickness series, i.e. reference ZnO:Al films and as-grown rough ZnO:Al films at different thickness. The reference films are shown with solid squares in Fig.5.34 while the as-grown rough films are shown with open triangles in the figure.

FWHM of the two series have similar trends: decreases significantly at first 150 nm. This trend reflects the fact that the grains are getting larger quickly during initial stage of the grains growth. When the films are thicker than 250 nm, the vertical grain sizes for reference films evaluated from FWHM by Scherrer equation are in the range of 36-61 nm. This is much smaller than expected for the films with this thickness, since reference films have columns throughout the film thickness. This effect is well known for sputtered ZnO:Al and is attributed to strain and defects. For the as-grown rough ZnO:Al

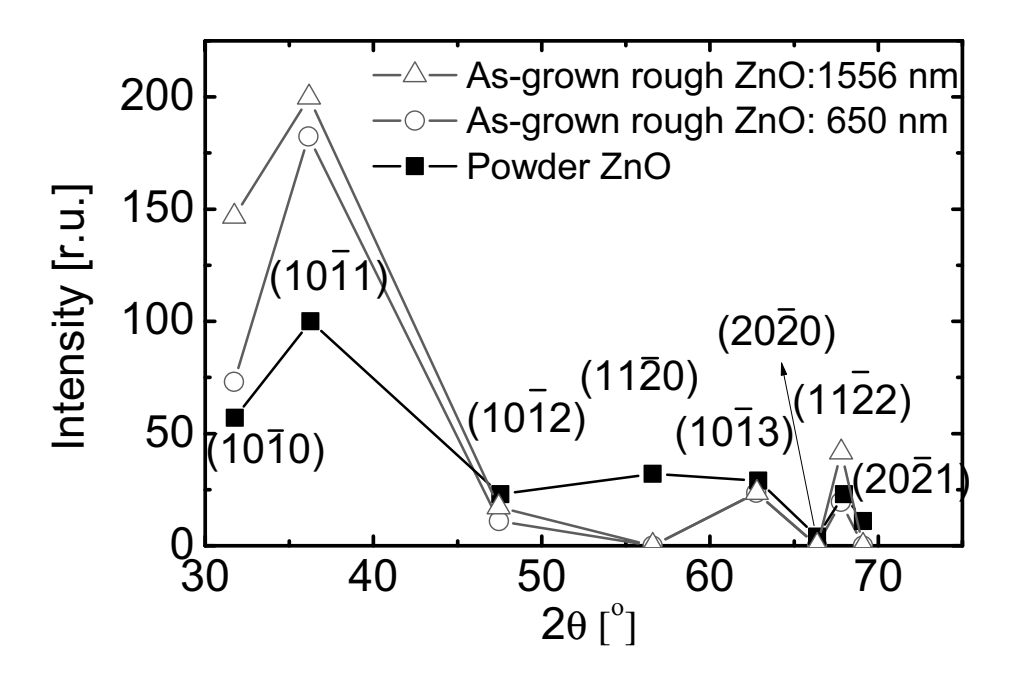


Figure 5.33: Comparison of additional XRD peaks (except (0002) and (0004)peak) of asgrown rough ZnO:Al film with thickness of 1556 nm (open triangles) and 650 nm (open circles), and the powder ZnO (solid squares).

films, the vertical grain sizes calculated from FWHM are only in between 38-48 nm, due to the high defects density in the large conical grains.

The (0002) peak positions locate at smaller angles for as-grown rough ZnO:Al films as compared with reference films, indicating more stress and defects in the films. For the two thickness series, the peak position shift to large angle when the films get thicker, indicating that the films release some stress during the growth process.

The measured peak intensity depends also on the film thickness, because some part of the X-ray is absorbed by the ZnO:Al films and not reflected back. Therefore, the intensity correction was carried out by following the typical procedure for Bragg-Brentano technique [148]:

$$I = I_d/(1 - exp(-\frac{2d\mu_{ZnO}}{sin\theta})), \tag{5.2}$$

where I_d is the measured intensity, μ_{ZnO} is the absorption coefficient for X-ray in ZnO, θ is the Bragg angle, and I is the corrected peak intensity. Unlike the measured intensity, the corrected intensity have included the part of X-ray absorbed by ZnO:Al films and therefore, larger than the measured intensity. The corrected intensities are normally used to characterize the crystal quality of polycrystalline films of films with different

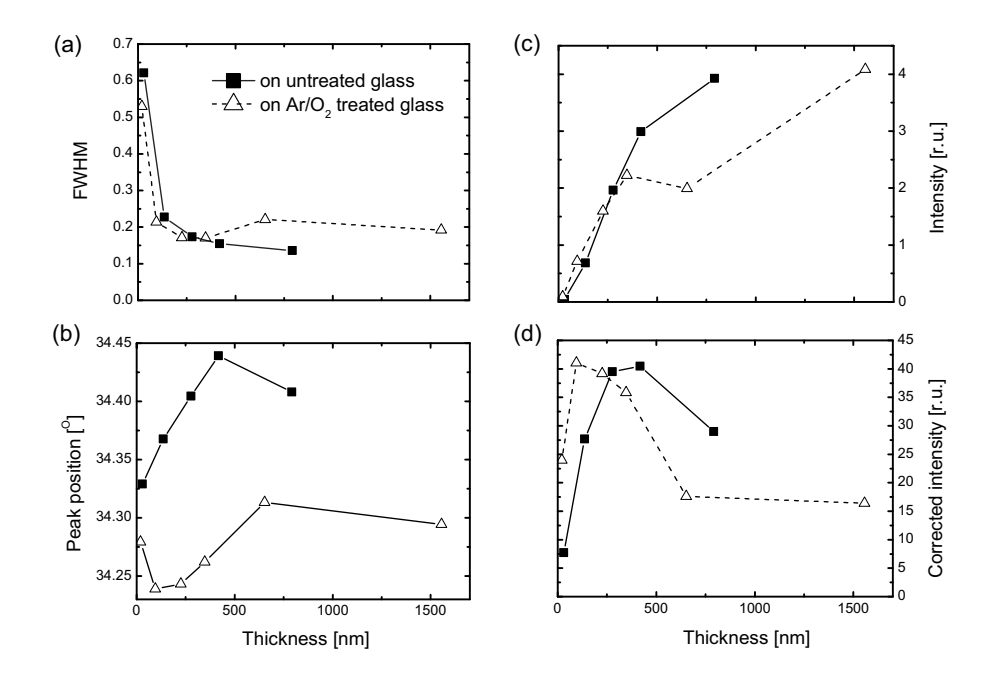


Figure 5.34: (0002) peaks analysis, including FWHM (a), peak position (b), measured intensity (c) and corrected intensity (d) of the reference and as-grown rough ZnO:Al films. The corrected intensity are calculated by Eq. 5.2.

thickness, since the factor of thickness have been excluded by this correction. Fig. 5.34(c, d) shows (0002) peak intensity before and after correction, respectively. For both films, the measured (0002) peak intensity increases with increased thickness. After correction, as the film thickness increases, the corrected intensity arises to certain value and then decreases. For the as-grown rough ZnO:Al films, similar trend is observed, but the last point is much lower, even lower than the starting point. The trend indicates that the texture of the films first increases with film thickness, and when the films are getting thick, the texture is poor. Similar results like reference ZnO:Al films were reported in [148].

This section presented the XRD measurement results of reference and as-grown rough ZnO:Al films. The reference ZnO:Al films have dominate (0002) texture, while the asgrown rough ZnO:Al films have worse (0002) preferred orientation when the films are growing thicker. The conical grains are considered to have random orientation.

5.4 X-Ray photoelectron spectroscopy of the glass substrate

This section focuses on the chemical changes of the ion beam treated glass surfaces. In the previous sections, it was concluded that the chemical changes caused by the ion beam pretreatment are responsible for the rough growth of ZnO:Al films. Surface composition changes are a common effect for ion bombardment of compound substrates. Thus, the details of the surface chemical changes are of interested. X-Ray photoelectron spectroscopy (XPS) measurements are widely used to characterize the chemical structures of sample surfaces. The introduction and sample preparation of XPS measurements can be found in Section 3.3.5. Survey and core level spectra scans were performed on ion beam treated glass surface.

5.4.1 X-Ray photoelectron spectroscopy survey scan

Survey scan can provide the chemical composition of sample surface with in a relative error range of $\pm 15\%$. In this work, the measurements were performed with two experiments, dynamic and static ion beam treatments.

5.4.1.1 Dynamic ion beam treatment

Firstly, let us look back to the Fig. 5.2 in this chapter. Four ZnO:Al films were sputtered on four different glass substrates. Apart from the untreated reference glass, the other three glass substrates were treated by Ar, O_2 and mixed Ar/O_2 ion beam, respectively. The ZnO:Al films grown on these substrates show different surface morphology and properties. On the Ar/O_2 mixed ion beam treated glass substrates, ZnO:Al films exhibit largest feature size and can be used as light scattering front contact for Si thin-film solar cells. In this section, the XPS measurement results of the four glass substrates will be shown. The difference between untreated glass and treated glass will directly show the chemical changes caused by the ion beam treatments.

Four 1×1 cm² samples were cut from the middle of the aforesaid four glass substrates and then were measured by XPS survey scan. The atomic percentage (at%) of the elements on the surface were calculated from the area of the peaks.

The compositions of the four glass surfaces used to grow ZnO:Al films in Fig. 5.2 are shown in Table 5.6. The values in the table are the atomic percentage (at%) of each element. Generally, a Corning glass surface is composed of C, Si, O, Al, and Ca. For an untreated glass substrate, the percentage of O is more than two times higher than Si, because Al-O, Ca-O, C-O, and -OH bonds are presented. C contaminations are normally not avoidable for all samples because they can be adsorbed on the surface from air, breath or gloves. On the ion beam pretreated samples, unlike to the previous reports as shown in Section 2.1.2.2, the surface chemical compositions have been changed to a large extend. Higher C contents were observed on ion beam treated glass surfaces. The contamination level of C is related to the samples storing time and place, the microroughness, and the surface activity. Therefore, it is reasonable to observe more C on

Table 5.6: XPS measurement results on a reference and three different ion beam treated Corning glass. The values in the table are the atomic percentage (at%) normalized to 100 with Rel. error of \pm 15%. The minimum measurable range was 1 at%. The four substrates were used for preparing ZnO:Al films as shown in Fig. 5.2. The rms roughness of the four ZnO:Al films are given in the last row.

Glass	Ref.	Ar treated	O_2 treated	Ar/O ₂ treated
С	19.9	33	32.3	27.8
О	56	44	46.7	49.9
Fe	-	3.8	-	5.0
Zn	-	0.1	0.5	1.2
Si	18.7	8.1	14.6	7.5
Al	3.9	5.6	3.9	3.7
Ca	0.9	2.3	0.9	2.0
N	0.7	0.6	0.9	0.3
Р	-	1.1	-	0.8
Cl	-	0.1	0.2	0.4
Ar	-	1.2	-	1.3
	rms roughness (nm)			
ZnO:Al films	4	12	34	44

the ion beam pretreated samples since the ion bombardment activated the surface. The percentage of O and Si were reduced, while Zn and Fe were added to the surface. Few Ar was implanted to the sample surface by Ar and Ar/O_2 bombardment. Additionally, slight changes were observed on Al, Ca, P, and Cl elements.

On Ar ion beam treated glass surface, Fe contamination is severe (3.8 at%), but on O_2 ion beam treated glass surface, there is almost no Fe contamination (< 0.1 at%). Zn is observed on the three ion beam treated glass surface. However, on the Ar treated glass surface, the amount of Zn contamination is very low (0.1 at%), while on the Ar/ O_2 treated glass, the Zn contamination is the highest (1.2 at%).

Lower Fe contamination from O_2 ion beam treatment is a common phenomenon for this type of ion source: Fe is sputtered from the steel cathode because of the strike of argon ions, whereas the oxygen ions lightly passivate the surface of the steel cathode, resulting in a thin oxide film on the cathode. Since the etch rate for FeO is lower than Fe, less cathode erosion is enabled by the use of O_2 gas [149]. However, with mixed Ar/O_2 ions, the sputtering rate of steel cathode might becomes larger due to additional Ar ions, leading to more Fe contaminations (5.0 at%).

The Zn contamination is supposed to be from the process chamber, since the ion source is installed in a same chamber with a rotatable $\text{ZnO:Al}_2\text{O}_3$ target (See Fig. 3.1). The difference between Ar and O_2 treatment is that Ar is physically milling off materials from glass surface while O_2 ions can also react with the substrate atoms or contaminations as well as etching off the substrate materials. More FeO, Fe₂O₃, or ZnO might be formed on

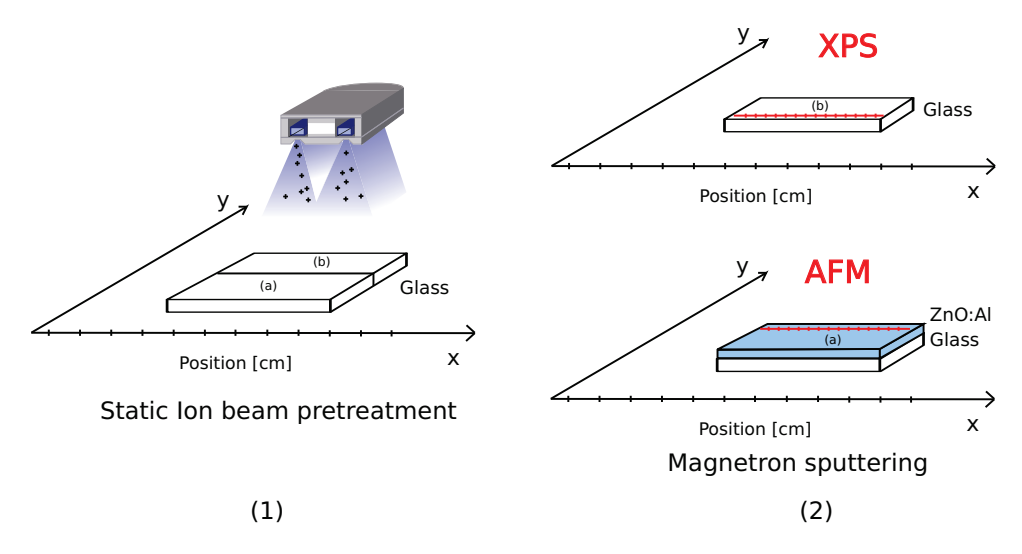


Figure 5.35: Schematic experimental process of XPS overview scans on statically ion beam pretreated glass substrates. (1): a $10 \times 10 \text{ cm}^2$ glass was treated by ion beam, (2): half of the substrate was measured by XPS, and the other half was sputtered with ZnO:Al films and then measured with AFM. The red dots indicate the points for measurement along x-direction.

the glass surface by O_2 ion beam treatment. This could be an explanation of the higher Fe and Zn concentration on the glass surface after mixed Ar/O_2 ion beam treatment.

The XPS measurements confirm that the compositions of glass substrates are changed by ion beam treatments. However, the changes are difficult to be related to the change of ZnO:Al film growth as shown in Fig. 5.2.

5.4.1.2 Static ion beam treatment

In the previous subsection, the glass substrate was dynamically moved in front of the ion source in order to get homogeneous treatment. Therefore the measurements on the treated glass substrates is supposed not to be related to the position on the sample. In this section, the substrates are treated statically by ion source. As shown in Section 4.2, the ion density is not uniform in the chamber. As a result, the ion beam has highest intensity in front of the racetrack. Therefore, in one etching experiment, a series of etching points bombarded by different intensities of ions can be obtained.

The schematic experimental process is shown in Fig. 5.35. Firstly one $30 \times 30 \text{ cm}^2$ glass substrate was treated by ion beams statically. Then the glass substrate was cut into two halves (a) and (b). Part (a) was transfered to sputtering chamber to deposit standard ZnO:Al film. AFM measurements were performed at 30 points on the ZnO:Al films. The points are depicted in Fig. 5.35 (2) by the red dots on a red straight line along x-direction. The distance between each point is 1 cm. XPS survey scans were performed

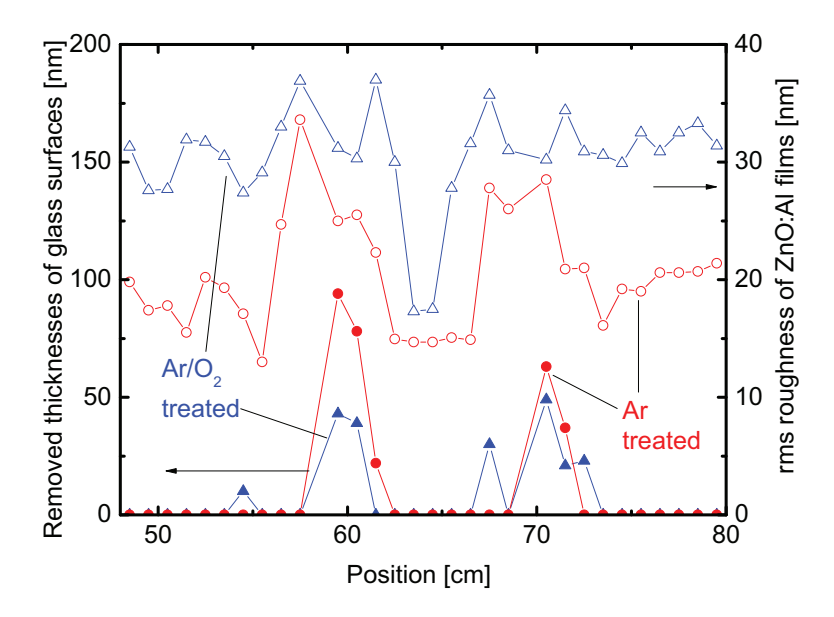


Figure 5.36: Removed thickness of statically Ar and Ar/O_2 beam treated glass substrates (left) and Rms roughness of ZnO:Al films (right) grown on the two substrates. Each position in the x-axis represents the 30 measurement points.

on the other half of glass substrate - part (b) at 30 points which have the same x values as the 30 points in part (a). The measurements points in part (b) are supposed to have the same ion beam treatments as the points in part (a). Therefore, the measurement results of same x value can be compared. 30 sccm Ar and 20/20 sccm/sccm Ar/O₂ were utilized as source gases for two ion beam pretreatments. The discharge voltage of the two ion beam treatments was 1 kV. The ion beam treatment time was 60 min.

The removed thickness of glass surfaces and the rms roughness obtained from AFM measurements of ZnO:Al films versus the positions of the 30 points are shown in Fig. 5.36. Removed thickness is the highest at racetrack positions and not detectable elsewhere. Therefore, the racetrack positions are identified at the position where highest removed thickness occurred. The Ar ion beam treatment remove more materials than the Ar/O_2 treatment because the former has higher etch rates, as discussed in Chapter 4. The figure also shows the roughness of ZnO:Al films at part (a) of the sample as shown in Fig. 5.35. Generally speaking, the films grown on Ar/O_2 treated glass show higher roughness than the films on Ar treated glass. The rms roughness of the two films is related to the position during ion beam pretreatment. The ZnO:Al films exhibit lowest rms roughness, in the middle of the two racetracks. From the center to the racetrack position, the rms roughness of ZnO:Al films increases and becomes the highest at the racetrack position. And then the rms roughness for ZnO:Al films on Ar/O_2 treated glass

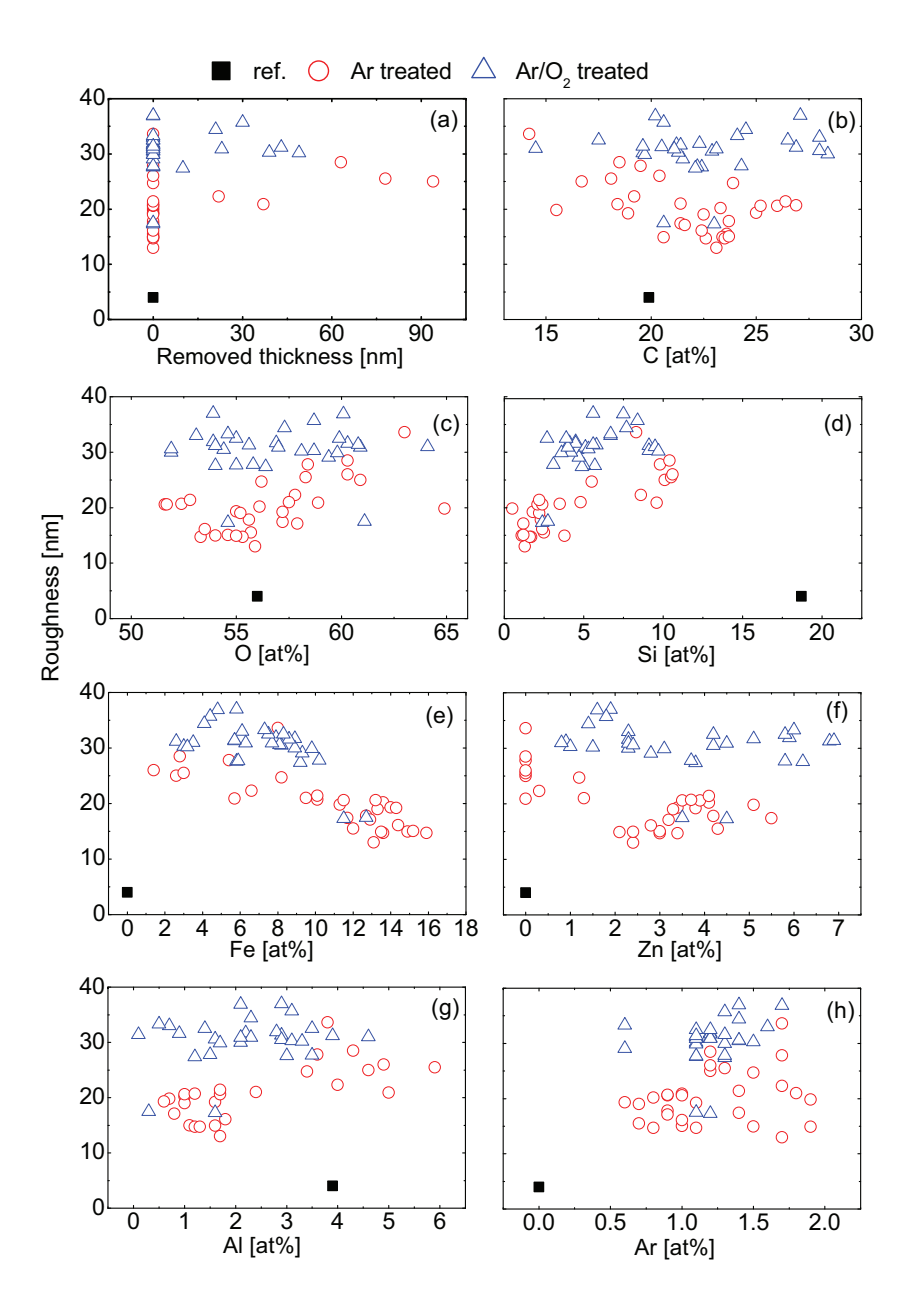


Figure 5.37: The dependence of ZnO:Al film roughnesses on the removed thicknesses (a) and surface compositions (b-h) after Ar and ${\rm Ar/O_2}$ ion beam treatments. (b)-(h) show the dependence of roughness on atomic percentage of C, O, Si, Fe, Zn, Al and Ar on glass substrates, respectively. One untreated Corning glass was added as reference.

decreases slightly, while the films grown on Ar treated glass decreased to near the lowest rms roughness.

The surface compositions of the 30 points were obtained from XPS measurements. Fig. 5.37(a) - (h) shows the dependence of rms roughness of ZnO:Al films on the removed thicknesses and atomic percentage of C, O, Si, Fe, Zn, Al, and Ar on glass substrates, respectively. The results from Ar and Ar/O₂ treatments are represented by open circles and triangles, respectively. One untreated glass is shown by solid squares as reference. Most of the 30 points on the ion treated points contain C and O in the range of 15-28 at% and 52-62 at%, respectively (figure (b) and (c)). The reference glass has a C and O concentration in the middle of above ranges. Thus, the amounts of C or O on the surface are not responsible for the change of ZnO growth. All ion beam treated points contain reduced Si as compared with untreated glass (figure (d)), indicating that Si atoms are either replaced or covered by other elements. The percentage of Si was reduced from 19 at% to 2-10 at% by ion bombardment. Fe, Zn, and Ar were added for almost all ion beam treated points, except that there was no Zn detected at some places on Ar treated surface (figure (e, f, g)). The amounts of Fe, Zn, and Ar on ion treated samples are distributed in the range of 2-16 at%, 0-7 at% and 0.5-2 at%. Al was found to be reduced on most part of ion beam treated glass surfaces (figure (g)). It is worthy to note that the aim of this experiment was to find out direct relation between rms roughness and surface compositions. However, all of the figures exhibit no direct relationships. Fig. 5.37(h) shows that rms roughness can be fitted to Ar compositions. However, it is not supported by O₂ treated surface, which contains zero Ar, still leading to rough ZnO:Al

As a conclusion of this section, the ZnO:Al films grown on ${\rm Ar/O_2}$ treated glass have higher rms roughness than films on Ar treated glass. The concentrations of Si and Al were reduced by ion bombardment, while Fe and Zn were added on the surface. The amounts of C and O on ion beam treated glass surface were randomly distributed. However, the contamination level on the treated glass surface seems not to be the control parameter for rms roughness of ZnO:Al films.

5.4.2 XPS core level spectra scan

The last section examined the XPS survey scan of dynamically and statically ion beam pretreated glass substrates. The results show that contaminations like Zn and Fe are presented after ion beam treatments. However, the bonds between the contamination and the Corning glass surface are unknown. Detailed XPS measurements provide another possibility to investigate the chemical bonds by analyzing the binding energy of the excited electrons.

Two ion beam treated glass substrates were chosen for the core level spectra scans. The first sample was treated by Ar ions for 30 min with discharge voltage of 2 kV. The second sample was treated by mixed $\rm Ar/O_2$ ions for 86 min with discharge voltage of 1 kV. The ZnO:Al films on the two films promote rough growth with roughness of 15 nm and 47 nm, respectively. Ar and $\rm Ar/O_2$ treated glass surfaces were measured by XPS in the binding energy range of $\rm 529-544~eV$ with resolution of 0.05 eV to detect O 1s

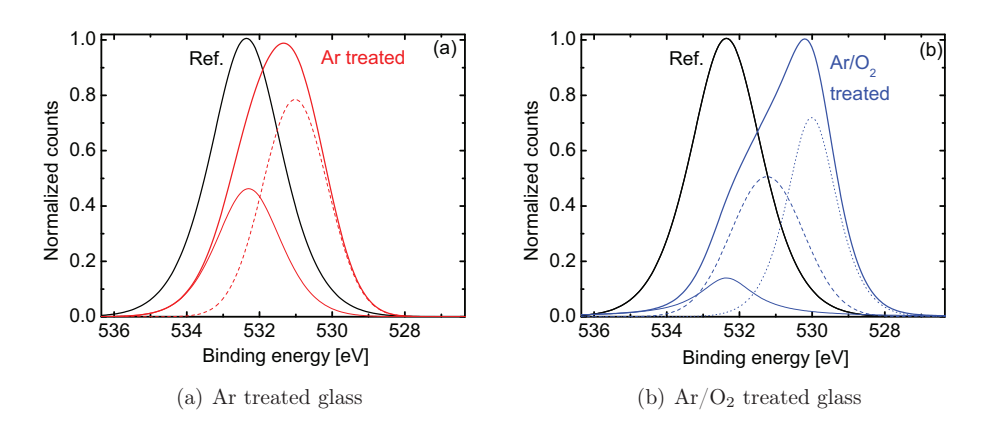


Figure 5.38: Comparison of O 1s peaks detected from Ar treated glass (a) and $\rm Ar/O_2$ treated glass (b) to reference Corning glass surfaces. The unsymmetrical peaks are decomposed into 2 or 3 Gaussian contributions.

peak.

Fig. 5.38(a) and (b) show the comparison of normalized O 1s spectra of untreated glass, the Ar treated, and Ar/O₂ treated glass substrates, respectively. The solid black curves in the two figures are the O 1s peak of reference glass. This peak is symmetric and the center locates at 532.3 eV. This peak is considered as reference O 1s peak originated from an untreated glass surface, which is composed of Si-O, OH-, C-O, and C=O. The thick red curve in figure (a) represents the O 1s peak of Ar treated glass. This peak can be decomposed to two Gaussian peaks: one is centered at 532.3 eV, the same as the reference peak and the other is centered at 531.0 eV. They are represented by thin solid and dashed curves, respectively. The contribution bonds to the left peak should be the same to the untreated glass, while the right peak shall be caused by the Ar ion treatment. The dash-dotted curve in figure (b) is the O 1s of Ar/O₂ treated glass. It is clear that this O 1s peak has a left shoulder. Three small Gaussian peaks which are located at 532.3 eV, 531.2 eV, and 530.0 eV are the deconvolution of this peak. The three small peaks are depicted by thin solid, dashed, and dotted curves, respectively. Note that the first two small peaks locates at the same position as untreated and Ar treated glass, respectively. The area under each peak represents the amounts of contributions.

Similarly, core level spectra of C 1s, Fe 2p3, Zn 2p3, and Si 2p were recorded in the binding energy region of 278-292 eV, 703-720 eV, 1016-1028 eV, and 95-109 eV, respectively. Similar as O 1s peaks, the peak is decomposed to Gaussian peaks if it is not symmetric. The quantification of the above spectra is summarized in Table 5.7. The total amount of the five elements is supposed to be 100 at%. C peaks are decomposed to three small peaks, with centers locates at about 285.0 eV, 286.3 eV, and 289.6 eV. These three peaks correspond to CH₂, C-O, and COOH, respectively.

The peaks of Fe 2p can be fitted to two small peaks, centered at about 711 eV and

I a second secon				
	glass substrates			
	Reference	Ar treated	Ar/O ₂ treated	Possible compounds
	eV/at%	eV/at%	eV/at%	
O 1s	-	-	530.0/25.61	O_2 , Si- $O_x(x<1)$
	-	531.0/33.22	531.2/24.7	ZnO, FeO, Si- $O_x(x\sim 1)$
	532.3/57.7	532.3/20.13	532.3/7.2	OH-, C+O, Si-O _x (x \sim 2)
C 1s	285.0/8.5	285.0/16.34	285.0/17.79	CH_2
	286.4/2.2	286.3/6.03	286.3/2.18	C-O
	289.6/0.3	289.2/1.57	288.9/0.99	СООН
Fe 2p	-	711.4/1.24	710.6/4.45	Fe_2O_3
	-	713.7/0.94	712.6/4.03	$Fe_2O_3(sat)$
Zn 2p	-	1022.2/1.84	1021.7/1.42	ZnO
Si 2p	103.3/31.3	102.3/18.68	102.0/11.6	$Si-O_x$

Table 5.7: XPS compound measurement results on the glass substrates.

713eV. They are corresponding to Fe^{3+} and satellite Fe^{3+} , respectively. Similarly, it means that Fe-O bonds are presented on the ion beam treated glass surfaces. The peaks of Zn 2p of the two ion beam treated samples are close to 1022 eV. This is in accordance to the reported Zn^{2+} species in ZnO films [150–152]. It means that Zn-O bonds were developed on the ion beam pretreated glass substrates. The metallic Zn seems not stable on the surface, due to its low evaporation temperature.

By ion beam treatment, the binding energy of Si 2p core level shift to small energy, indicting that the stoichiometry ratio x in SiO_x decreases [153]. It was reported that as the stoichiometry ratio x decreases from 2 to 1, the binding energy of Si 2p and O 1s peak shifts from 103.3 eV to 102 eV [153] and from 533 eV to 531.5 eV [154], respectively. Thus, the deconvolution peak of O 1s near 531 eV on Ar and $\mathrm{Ar/O_2}$ treated glass may be related to the same effect. Additionally, the lower binding energy of O 1s core level might also relate to the Zn-O and Fe-O bonds, since Zn and Fe contaminations were observed on the ion beam treated glass surface.

The deconvolution of O 1s curve of Ar/O_2 treated glass shows that even lower binding energy 530 eV is presented on the surface. This might be attributed to two aspects. First, the stoichiometry ratio x in SiO_x might decrease further more, since when x < 1, the literature suggested that the binding energy of O 1s stays almost constant at 530.1 eV [153]. Because the decrease of Si percentage on the ion beam treated glass surface, less O atoms are required in the Si-O matrix. The other cause for the low binding energy is that there might be implanted O_2 atoms on the surface. The O 1s peak at 531.6 eV and 530.5 eV have been attributed to dissociated (atomic) oxygen state and molecular peroxy species on the oxygen adsorbed Si (111) surface, respectively [155]. The rather lower binding energy of O 1s at 530.5 eV was also found for molecule O_2 on Pt (111) and Ag. It was proved that physically absorbed O = O bonds are not stable on surface at room temperature [156, 157]. The metastable peroxy species might be presented on the surface in peroxy radical atom - O - O or bridge atom - O - O - atom. Thus, the

undissociated O-O bonds might also exist on O_2 treated surface. The net effects of the above two situations would be to cause excess O dangling bonds on the ion beam treated glass surfaces. During the initial growth stage of ZnO:Al films, the metastable O-O bonds are expected to be dissociated due to the high temperature and particle sputtering, thus they behave similar as O dangling bonds.

The percentage of O dangling bonds can be estimated by subtracting metal oxides, silicon oxide and carbon oxides from the measured O 1s, as described by the following equation,

$$O_{danglingbonds} = O_{measured} - (Zn + Fe * 1.5 + Ca + Al * 1.5 + Si * x + (C - O) + (C = O) * 2)$$
(5.3)

where x is the stoichiometry ratio x in SiO_x . For reference glass, x=2 is used. For Ar treated glass, based on the decrease of Si 2p binding energy and the deconvolution of O 1s, x=1.48 is used. For the $\mathrm{Ar/O_2}$ treated glass, x=0.67 is used. The value of x is estimated from the area of deconvoluted O 1s peaks. By equation 5.3, the percentages of O dangling bonds are approximately 0.3 at%, 12 at%, and 25 at% for reference, Ar treated, and $\mathrm{Ar/O_2}$ treated glass substrates, respectively. The calculations are based on many assumptions, for example it is assumed that the metal oxides have right stoichiometry which might not be the case. Because of the many assumptions in the calculation, the obtained numbers only give relative comparisons about the number of O dangling bonds on the surface. On the reference glass substrate, a low amount of O dangling bonds is reasonable, since the glass surface is chemically stable. On the Ar and $\mathrm{Ar/O_2}$ treated glass substrates, relatively higher amount of O dangling bonds are presented.

Same parameters and methods were applied to estimate the number of O dangling bonds of statically ion beam treated glass as shown in Fig. 5.37. The obtained results are shown in Fig. 5.39, in which the x-axis is the calculated O dangling bonds and y-axis is the AFM measured roughness of ZnO:Al films grown on the 30 points. The Ar treated sample is shown in open circles and the ${\rm Ar/O_2}$ treated sample is shown in open triangles. The black square on the left bottom is the reference glass. Though a large scattering of data points, the figure shows a roughly linear relationship, that the roughness of grown ZnO:Al films is proportional to the number of O dangling bonds on the glass substrates.

The XPS core level scans have revealed the states of the elements of interest. The results showed that the stoichiometric of SiO_2 has been changed by ion bombardment, leading to O deficiency in Si-O matrix. Meanwhile additional Zn-O, Fe-O bonds are formed due to the contaminations of the ion source. By O_2 treatments, metastable O-O bonds may also be presented as indicated by the lower binding energy of O 1s spectra. The number of excess O dangling bonds were estimated and correlated to the rms roughness of ZnO:Al films. Therefore, as an important conclusion from this section, the excess O dangling bonds might be the reason for the change of ZnO growth.

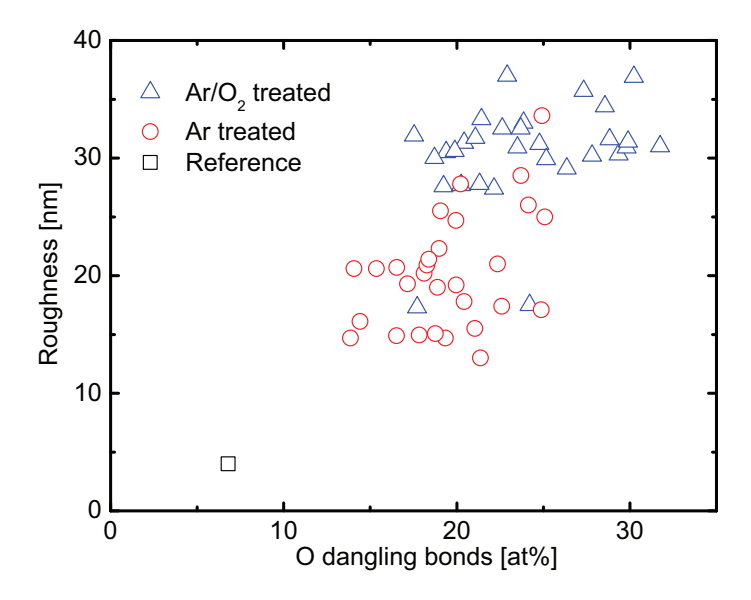


Figure 5.39: The roughness of ZnO:Al films versus the number of O dangling bonds on the static ion beam treated samples.

5.4.3 Different ion beam system

As shown in Section 5.2.5, the ion beam treatment was changed to an inverse sputter etcher. ZnO:Al films grown on etched area A seems like reference film, while the films grown on unetched area B show as-grown rough features. XPS survey and core level scans were performed for this film at area A and B. The measurement processes are the same as in last two sections.

The composition of the glass surface obtained by XPS survey scans are listed in Table 5.8. As always, one untreated Corning glass was added as reference. The percentage of Si is reduced at both areas. However, it is more strongly reduced at area B than at area A, indicating a higher contamination level at area B. This is confirmed by the observed Fe and Zn contamination at area B. At area A, there are almost no Fe contamination and few Zn concentration, while at area B, high Zn contamination and few Fe contamination were detected.

XPS core level scans of the O 1s, C 1s, Fe 2p3, Zn 2p3, and Si 2p were also performed on these samples. O 1s spectra from reference glass, area A, and area B are shown in Fig. 5.40 by solid, dashed, and dash-dotted curves, with centers located at 532.0 eV, 532.1 eV, and 531.6 eV, respectively. Similar to the analysis in Section 5.4.2, the lower binding energy might be caused by lower stoichiometry ratio x in SiO_x and additionally Zn-O and Fe-O bonds. However, lower binding energy of 530.0 eV was not observed by

Table 5.8: XPS survey scan results on the glass substrates treated by round ion source. One untreated glass was measured as reference. The values in the table are the atomic percentage (at%) normalized to 100 with Rel. error of \pm 15%. The minimum measurable range was 1 at%. The area A and B are marked in Fig. 5.17.

Element	Reference glass	Etched area A	Unetched area B
С	13.1	16.4	24.7
O	57.4	55.5	48.5
Fe	-	-	0.4
Zn	-	0.2	5.7
Si	22.2	16.8	10.8
Al	5.5	6.9	3.0
Ca	1.2	3.4	6.4
Р	-	0.8	0.3
Cl	-	-	0.3

Table 5.9: XPS core level scans on the glass substrates treated by round ion source. One untreated glass was added as reference. The values in the table are shown in binding energy [eV] / atomic percentage [at%]. The area A and B are marked in Fig. 5.17.

	9			
	glass substrates			
	Reference glass	Etched area A	Unetched Area B	Possible compounds
	eV/at%	$\mathrm{eV/at}\%$	$\mathrm{eV/at\%}$	
O 1s	-	-	531.5/37.4	ZnO, FeO, Si- $O_x(x\sim 1)$
	532.3/57.7	532.1/59.8	532.3/15.17	OH-, C+O, Si- $O_x(x\sim 2)$
C 1s	285.0/8.5	285.0/11.74	285.0/17.2	CH_2
	286.4/2.2	286.4/2.2	286.5/3.6	C-O
	289.6/0.3	289.3/1.23	289.2/1.36	СООН
Fe 2p	-	-	710.6/0.42	Fe_2O_3
	-	-	714.9/0.29	$Fe_2O_3(sat)$
Zn 2p	-	1022.5/0.17	1022.2/7.33	ZnO
Si 2p	103.3/31.3	103.1/24.85	102.7/17.35	$Si-O_x$

this experiments. One reason might be the reduced O_2 implantation under the relatively low energies ion bombardment. The core level scans of the five elements are summarized in Table 5.9.

The bonds structure of etched area A is quite similar to reference glass, except that few Zn was detected and the binding energy of O 1s and Si 2p lines decreases 0.2 eV. This is might corresponding to the slight deficiency of O in SiO₂. The bond structures of unetched area B are changed a lot. More Zn was deposited on this area. Si 2p and O 1s lines shift more to small binding energy. According to equation 5.3, the percentage of

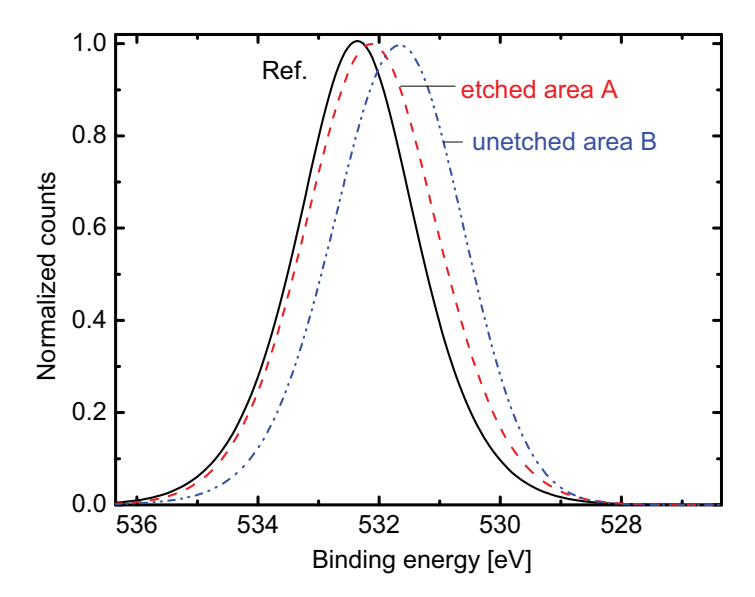


Figure 5.40: Detail scan of O 1s of the pretreated glass by sputter-etcher. Two different areas were measured, one is the etched area A, and the other is unetched area B.

O dangling bonds for reference glass, etched area A, and unetched area B are 0.3 at%, 3 at%, and 11 at%, respectively. The higher number O dangling bonds on the unetched area B explains the rough growth of ZnO:Al films in this area.

Higher contamination level on the area B lead to a fast reduction of Si-O bonds as well as an accumulation of Zn-O, Fe-O, and O-O bonds. It is assumed that when the ion source is switched on, main part of Fe contaminations sputtered from the cathode are in the ion beam, but still some parts are outside the ion beam range. Therefore, Fe contaminations are also visible on the area B where the ion beam cannot reach. The Zn ions are supposed to be distributed in the whole system chamber that the Zn contaminations are the same on the whole substrate surface. It means that area A and B have the same chance to receive contaminations. However, the contaminations deposited on area A are etched away by the ions, while the contaminations deposited on area B are not removed. Therefore, high contamination levels are formed on area B.

The XPS survey and core level scans of the treated glass surfaces in this section show that the analysis methods regarding O dangling bonds are applicable for other ion beam treatments. The unetched area B promotes excess O bondings due to the deposition of contamination layers. As a result, the growth of ZnO is changed and leading to as-grown rough surface.

5.4.4 Summary

Survey and core level scans of XPS were applied on the ion beam treated glass. They yield evidence that the glass surface chemical composition has been changed by ion beam pretreatment. On the ion beam treated glass surface, Si-O bonds are reduced, while Fe-O and Zn-O bonds are increased. On the O_2 treated glass surface, O_2 molecules might be implanted on the surface. Excess O bonds are presented on the ion beam pretreated glass surfaces. Section 5.2.2 shows that the rough growth of ZnO:Al films is not observed when the ion treated glass is etched by HCl solution or cleaned by acidic decantate. The observation is in accordance to the XPS measurements, since the excess O bonds are not stable in acidic solution.

5.5 Growth of ZnO:Al on ZnO crystal

Before the discussion of the mechanism of the rough growth of ZnO:Al film on ion beam pretreated glass substrates, this section introduces the growth of ZnO:Al films on ZnO crystal. As seen in Section 2.2.1, ZnO is a polar crystal with either Zn terminated (0001) surface or O terminated (000-1) surface along c-axis direction. In the following, the influence of the substrate polarity on the growth of sputtered ZnO:Al films are discussed, by observing and comparing ZnO:Al film growth on Zn and O-terminated ZnO crystal and Corning glass.

ZnO crystal with polished (000±1) planes were purchased from CrysTec GmbH, Berlin, Germany. The ZnO crystal polar surfaces are marked on the sample. The ZnO crystals with the two faces were glued on a Corning glass substrate by silver paste. Thus, ZnO:Al films can be sputtered on the Zn-terminated ZnO crystal, O-terminated ZnO crystal, and Corning glass at the same time.

Table 5.10: Growth parameters of polycrystalline ZnO:Al thin film deposited on a Znterminated ZnO crystal, O-terminated ZnO crystal and Corning glass [127].

Substrate	Zn-terminated ZnO		O-terminated ZnO		Corning glass	
passes	32	64	32	64	32	64
thickness[nm]	771	1434	555	977	731	1451
growth rate [nm/pass]	24	22	17	15	23	23
rms roughness [nm]	3.5	4.5	37	98	5.2	6.1

ZnO:Al films were sputtered under standard conditions as described in 3.1.1.1. Two different film thicknesses were deposited by performing the standard number of passes (32) and twice the standard number of passes (64) in front of the target. Table 5.10 lists the thickness and growth rate of the ZnO:Al films grown on different substrates. It shows that the films on Zn-polar single crystal and Corning glass have similar growth rate of around 23 nm/pass. However, the films grown on O-polar crystal have lower growth rate of around 16 nm/pass. The rms roughness determined by AFM measurements are

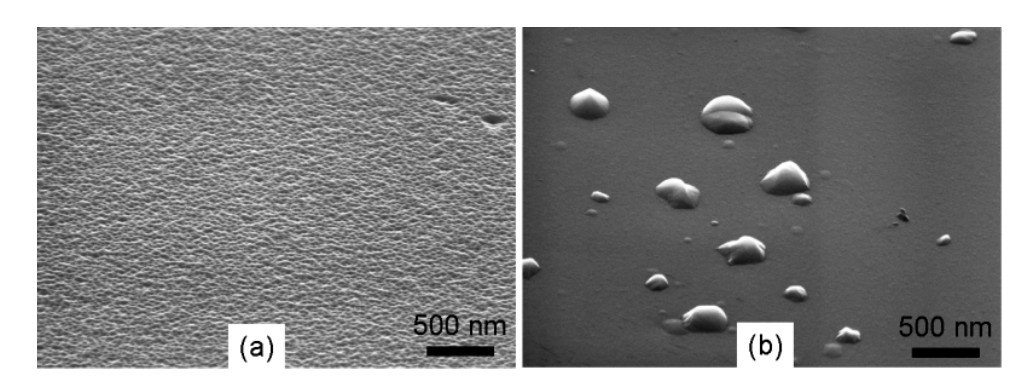


Figure 5.41: Top SEM micrographies of ZnO:Al films grown on (a) Zn-terminated ZnO crystal, (b) on O-terminated ZnO crystal. The two films were deposited with 32 passes.

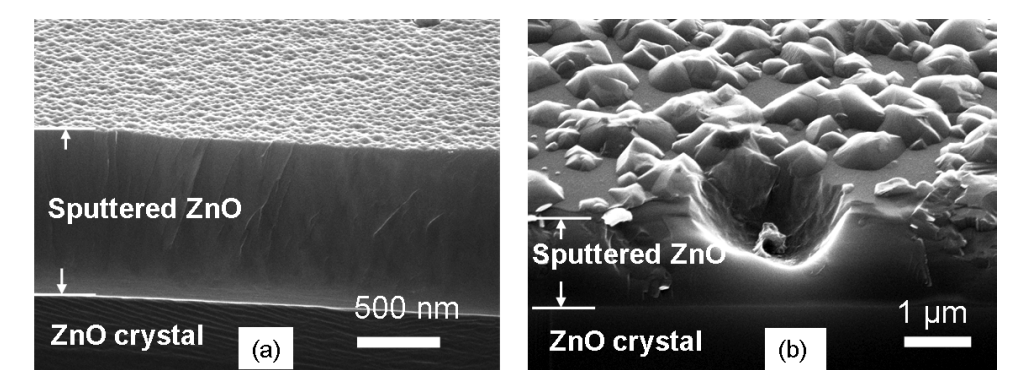


Figure 5.42: Cross-sectional SEM micrographies of ZnO:Al films grown on (a) Znterminated ZnO crystal, (b) on O-terminated ZnO crystal. The two films were deposited with 64 passes.

shown in the last row of the Table 5.10. The films grown on O-terminated ZnO crystal have significantly higher rms roughness than the other films.

The top SEM micrographs of ZnO:Al films grown on Zn-terminated and O-terminated ZnO single crystal are shown in Fig. 5.41. The two ZnO:Al films were sputtered by performing the standard number of passes (32). Film (a) was deposited on Zn-terminated crystal and composed of small crater-like features. Film (b) was sputtered on O-terminated crystal. Round hillocks with diameter in the range of 100 nm to 450 nm were observed on the otherwise flat surface.

When the films were sputtered by making twice the standard number of passes (64), cross-sectional SEM measurements were performed. The results are shown in Fig. 5.42. The interfaces between ZnO crystals and polycrystalline films are indicated in the figure.

The ZnO:Al films grown on Zn-polar crystal (Film (a)) still have small crater-like features on the surface. Moreover, columnar grains are observed on the cross section. Film (b) was developed on O-polar crystal. The bumps are growing larger with time. A hole was observed in the cross-section image, indicating that a large grain was thrown off during the break of sample. It clearly shows that the large grain start to grow during the growth of ZnO:Al films, but not from the beginning of the growth. Moreover, the large grains on the surface exhibit different lateral size, indicating that they appear at different time.

This experiment examined the growth characterization of the ZnO:Al films on various substrates. The growth rate difference of (0001) and (000-1) ZnO surfaces has also been observed for epitaxially deposited ZnO films [158, 159]. The reason for the different growth rates is due to the different dangling bond configuration of the growing surfaces. On Zn-polar surface, each O atom has three dangling bonds along c-axis, while O atom on O-polar surface only has one dangling bond. The Zn sticking coefficient on the O atom plane of Zn-polar ZnO is higher than that of the O-polar surface [160]. The growth of ZnO is easier on Zn-polar surface than on O-polar surface. Therefore, Zn-polar ZnO:Al films exhibit faster growth rate than the O-polar ZnO:Al films. The ZnO:Al films grown on Corning glass have similar growth rate as on Zn-polar ZnO crystal, indicating that the ZnO:Al films on Corning glass have Zn-polar surfaces.

Kato et al. reported homoepitaxial Zn-polar ZnO films grown on Zn-face substrates by molecular beam epitaxy (MBE). The morphologies of ZnO surfaces strongly depend on O-Zn ratio in the deposition chamber [160, 161]. Kato et al. pointed out that atomically smooth Zn-polar surface can be deposited in O-rich region. Under stoichiometric or Zn-rich conditions, the films become rough with hexagonal pits on the surface. The Zn atoms bonded to O substrates are not stable, leading to a promotion of 3D growth [160]. The crater features of the sputtered ZnO:Al films on Zn-polar crystal indicate that the growth of sputtered ZnO:Al films belongs to 3D growth.

O-polar ZnO films have been deposited by MBE or rf magnetron sputtering on Sapphire substrates [162–164] and O-face ZnO crystal [165, 166]. It was claimed by Xu et~al. that a high temperature of $1000-1050~\rm C$ together with Zn-rich condition is required to promote 2D growth of homoepitaxial O-polar ZnO film [165]. At low temperature near 600 °C, 3D island growth of O-polar surfaces were observed [165, 166]. 3D island growth was also found for heteroepitaxial O-polar ZnO on Sapphire substrates with the deposition temperature below 700 °C [159, 163, 167, 168]. Therefore, it is assumed that the sputtered O-polar ZnO:Al films in this work also has 3D growth over the whole film.

There might be many reasons to promote the as-grown rough features of ZnO:Al films on O-polar single crystal. One reason could be the flip of polarity of ZnO:Al films during the film growth process, because Zn-polar surface is more thermodynamically stable due to the low temperature. Mixed polarity is also observed for Zn-terminated surface grown on Sapphire at relatively low temperature [162]. Jo et al. observed the formation of inversion twin boundaries in sintered ZnO [169]. The flip of polarity does not start from the crystal interface due to the difficulty to form anion-anion bonds. The Zn-polar surfaces have faster growth rate and therefore overgrow other flat grains and finally dominate the surface. Additionally, due to the imperfect of the ZnO single crystal,

defect sites or edge dislocation position may be nucleation sites for differently oriented grains. In this case the different size surface textures would arise from the different growth rates associated with the particular orientation. Finally, as a combination of the two previous suggestions, the as-grown rough surface may also due to the formation of a crystal with other orientations during the growth process. It's known that sputtering is not the ideal method for epitaxial growth due to its high deposition rate. Thus, the defects in grain or at grain boundaries may provide sites for other oriented ZnO:Al films.

This experiment not only investigated the different growth on Zn-polar and O-polar surface, but also revealed the growth mechanism of reference ZnO:Al films grown on untreated and ion beam treated glass. Firstly the similarity of growth characteristics between the ZnO:Al films on Zn-terminated crystal and untreated glass suggests that the glass substrates develop primarily Zn-terminated (0001) films. This can be further confirmed by their HCl etching behavior [127]. The ZnO:Al films grown on Zn-terminated crystal have epitaxial growth and already have in-plane orientation. Therefore by HCl etching, the surfaces consist of six-fold symmetric craters. On an amorphous glass substrates, a thin random ZnO:Al layer will first grow on the surface. Then the plane (0001) which has lowest surface energy and fastest growth rate dominate the growth. Thus inplane orientation for the film does not form by this competing mechanism. SADP by TEM measurements on reference ZnO:Al films on Corning glass show that the film has local relation of in-plane orientation, but random in-plane orientation at long distance [139]. This is reflected by the round crater after HCl etching. Secondly, the reduced growth rate and rough topography of ZnO:Al films grown on O-terminated ZnO crystal is similar to the ZnO:Al films grown on ion beam treated glass. The similar conical grains on the two surfaces indicates similar growth mechanism of the ZnO:Al films. In next section, the growth model of as-grown rough ZnO:Al films grown on ion beam pretreated glass substrates will be discussed.

5.6 Growth model

In the previous sections, ZnO:Al films grown on untreated and ion beam treated glass substrates were introduced and characterized. The films grown on ion beam treated glass substrate exhibit conical grains starting from the beginning of the film growth. The conical grains grow faster than the surrounding flat grains and therefore they overgrow the flat grains and finally dominate the surface. TEM and XRD reveal that the conical grains have no favored orientation, no matter in-plane or out-of-plane. TEM also determined the orientation of the grains between the conical grains and confirmed that the small columnar grains have c-axis direction similar to the reference ZnO:Al films grown on bare glass. However, the growth rate of the columnar grains on ion treated glass is slower than the columnar grains on reference glass. Considering the slower growth rate of (000-1) grains, it is assumed that the small grains in the as-grown rough ZnO:Al films are oriented along (000-1) termination, while the reference ZnO:Al films grow in (0001) direction. Therefore, the growth rates of different grains are as follow: $G(\text{columnar grains on reference glass}) \gg G(\text{conical grains on ion beam treated})$

glass) $\gg G$ (columnar grains on ion beam treated grains), where G means the growth rate of ZnO:Al films. This relationship is in accordance to the reported

$$G(0001) \gg G(random) \gg G(000 - 1).$$
 (5.4)

Hong et al. have reported that O-terminated ZnO epitaxially deposited films were grown on O_2 plasma pre-exposed GaN/sapphire substrates by MBE, while Zn-terminated ZnO epitaxially deposited films were prepared on Zn pre-exposed sample [170, 171]. Other results considering the MBE deposited O-polar ZnO on O_2 or Ga pretreated substrates can be found in [159, 172, 173]. Specifically, Vinnichenko et al. has found that magnetron sputtered ZnO epitaxially deposited films exhibit (000-1) out-of-plane orientations on O_2 rf plasma pretreated sapphire substrates, while without O_2 rf plasma pretreatment, the epitaxially deposited films are composed with both (0001) and (000-1) oriented materials [163]. It is therefore concluded that the nucleation of ZnO films are not only strongly dependent on the deposition parameters, but also on the status of substrates. The O_2 pretreated substrates tend to promote grains oriented with (000-1) directions.

The XPS measurements revealed that additional Zn-O, Fe-O, and O dangling bonds cover the glass surface after ion bombardment. It was observed that the rms roughness of ZnO:Al films is proportional to excess O bonds on the substrates. Thus, the O bonds on the treated glass surface promote the (000-1) texture in the sputtered ZnO:Al films. At other places where no O bonds are covered, random grains are developed. Since the random grains have faster growth rate than the (000-1) grains, they overgrow the (000-1) grains and dominate the surface. The random grains start from the glass/ZnO:Al interface.

Combined with the growth characteristics of ZnO:Al films on ZnO single crystal, a model is proposed and shown in Fig. 5.43. In the figure, the (0001) and (000-1) planes are distinguished by upward and downward curved lines as well as the arrows directing towards (0001) direction. The figures (a) and (b) describe the ZnO:Al films grown on Zn-polar and O-polar ZnO crystal, respectively. The figures (c) and (d) show the ZnO:Al films sputtered on untreated and ion beam treated glass surfaces, respectively.

On Zn-polar crystal (Fig. 5.43(a)), the ZnO:Al films grow epitaxially, so that the grains show well aligned (0001) orientations. The grain sizes are uniform and the growth rates of all grains are similar. As a result, the ZnO:Al films have relatively smooth surface. Some other oriented grains might also be presented during the film growth process at defect sites, but they are overgrown by (0001) grains due to the growth rate difference.

On O-polar crystal (Fig. 5.43(b)), most of the ZnO:Al films are nucleated with (000-1) orientation due to the epitaxial growth. However, as discussed in Section 5.5, during the growth of film, many large grains overtake the small grains, resulting a rough surface. Three possible reasons for the as-grown rough growth of ZnO:Al on O terminated ZnO are depicted in the figure. From left to right, these reasons include the flipping of grain polarity from O to Zn terminated during the growth process, the growth of ZnO:Al with another orientation beginning at the underlying substrate, and the formation of a crystal with other orientations during the growth process.

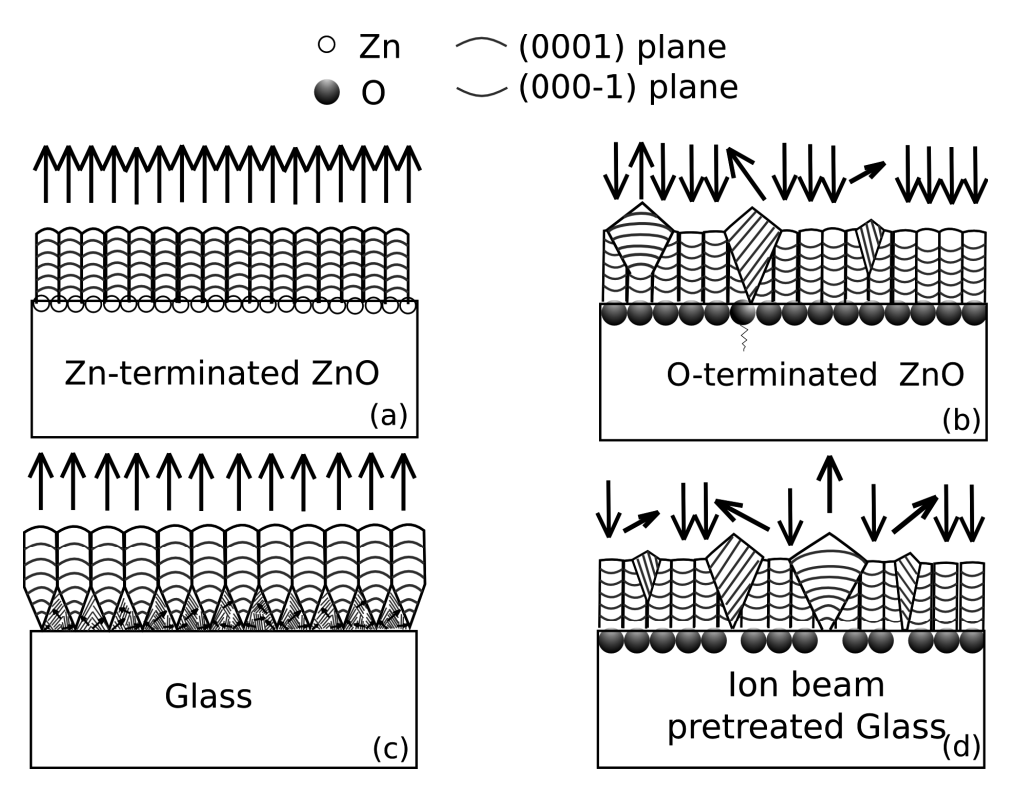


Figure 5.43: Growth model of ZnO:Al films on Zn-terminated ZnO crystal (a), Oterminated ZnO crystal (b), reference Corning glass (c), and ion beam pretreated glass substrates (d). The initial grain growth of ZnO:Al polycrystalline films on different substrates are shown. The zigzag in substrate (b) indicates defects in the imperfect single crystal.

The ZnO:Al films grown on untreated glass (Fig. 5.43(c)) start from random nucleation stage due to the amorphous substrate. This has been observed by high resolution TEM images: thin randomly oriented polycrystalline layers were developed at ZnO/glass interface [76]. During the growth of randomly oriented grains, competition of fastest growth rate exists among the grains. Finally, (0001) grains overcome others and dominate the surface.

On the ion beam treated glass surfaces (Fig. 5.43(d)), O dangling bonds and possibly other bonds exist on the surface instead of only Si-O bonds. These O dangling bonds are assumed to provide the ZnO grains higher opportunity to form (000-1) orientation instead of random orientations. Therefore, the ZnO:Al polycrystalline films have two types of grains: one is the (000-1) grains with slower growth rate, which are well aligned as columns similar to the growth on untreated glass. The other type is randomly oriented grains which overgrow the columnar grains. They are represented by the three large

grains on the right side in the figure. At around 600 nm, the random oriented grains coalesce and dominate the surface. Moreover, during the growth of the (000-1) oriented grains, some grains with other orientation may exist. This is shown by the left large grain.

This model is supported by the effects observed in Section 5.2.2. The ion beam treated glass surface is OH-terminated after cleaning in acidic solution, leading to similar growth as on untreated glass. The model is also supported by the TEM and XRD measurement results. The columnar grains on ion bombarded glass surfaces show similar SADP as the reference material grown on untreated glass despite of their inverted polarities. The large conical grains show random orientations as indicated by the ring diffraction patterns from plan-view TEM as shown in Fig. 5.29(b). Among the randomly oriented large grains, some orientations might be promoted while some are suppressed due to their growth rate difference. This is confirmed by the different increase of small XRD peaks of thicker as-grown rough ZnO:Al films as shown in Fig. 5.33.

5.7 Summary

This chapter has examined the ion beam treatment of the glass substrate in Si thin-film solar cells. Pure Ar, pure O_2 , and mixed Ar/O_2 ions were used to treat the Corning glass substrates. The morphology of the glass surface was not changed obviously by the ion beam bombardment. However, the growth of ZnO:Al films has been influenced significantly by the treatment of glass substrates. All of the three ion beam treatments lead to slower growth rate and develop pyramids on the surface of ZnO:Al films. Among them, Ar/O_2 ions develop the roughest ZnO:Al films with rms roughness of around 40 nm. The electrical and optical properties of the as-deposited rough ZnO:Al films suggested that the films could be used as front contact TCO in the Si thin-film solar cells. The wet chemical etching process used for the reference ZnO:Al films can be avoided. Amorphous, microcrystalline, and tandem Si thin-film solar cells prepared on the rough ZnO:Al films show that the front contact can provide efficient light trapping effect. The highest initial efficiencies for amorphous single junction and amorphous microcrystalline silicon tandem solar cells on as-grown rough ZnO:Al films were 9.4 % and 11.9 %, respectively.

The as-grown rough ZnO:Al films are composed of two types of grains: small columnar and large conical grains. Both types of the grains start from the glass/ZnO interface. Because of the faster growth rate of conical grains, they overgrow the columnar grains and dominate the surface. The small columnar grains have similar texture to the reference ZnO:Al materials sputtered on untreated Corning glass, while the large grains show nearly random orientations.

 ${\rm Ar/O_2}$ ion beam pretreatments were applied on other glass substrates and Si wafer instead of Corning glass and similar rough growth was observed. Alternatively, an inverse sputter etcher was used to replace the large linear ion source, and similar rough growth was only developed on the part of substrate where the ions did not impinge. The effect of rough growth of ZnO:Al films can be removed by dipping the treated glass

5 Ion beam treatment of the glass surface

into HCl solution or re-cleaning in the glass cleaning process. It was concluded that the chemical properties of the glass surface were changed by the ion beam treatment and are responsible for the rough growth of ZnO:Al films. Oxygen dangling bonds created by ion bombardment show a correlation to the rough growth.

Sputtered ZnO:Al grains on O-terminated surface tend to have (000-1) orientations which have the lowest growth rate among the other crystal orientations. Comparison to epitaxial growth on ZnO single crystals lead to the conclusion that the columnar grains grow along (000-1) direction and conical grains are randomly oriented. At the end of this chapter, a growth model was built, in order to explain the growth mechanism of as-grown rough ZnO:Al films on ion beam treated glass surface.

6 Ion beam treatment of the TCO surface

This chapter focuses on the ion beam treatment of TCO surfaces, namely the ZnO:Al films in Si thin-film solar cells. As-deposited smooth and HCl etched textured standard ZnO:Al films are treated by the ion beam. The chapter starts with the study of HCl etching, the growth of ZnO:Al and Si films on ion beam treated ZnO:Al films. Next, the changes in the morphology of the ZnO:Al films by Ar ion beam etching are given. With continuous ion beam etching, the ZnO:Al films are totally removed, resulting in the fabrication of textured glass, which is a main part of this chapter. The properties of the textured glass, the growth of ZnO:Al films on textured glass, and the application of textured glass in solar cells are presented in the following parts. At the end of this chapter, the μ c-Si:H thin-film solar cells based on various textured glass are given.

6.1 The effect of ion beam treatment on HCl etching behavior of ZnO:Al films

This section focuses on the effect of ion beam treatment on HCl etching behavior of ZnO:Al films. Firstly the etching behaviors and mechanism of reference ZnO films in HCl are briefly introduced, ending up with the motivation of ion beam treating ZnO:Al films before HCl etching. Then the AFM images of HCl etched ion beam treated ZnO:Al are presented.

The wet chemical etching of polycrystalline ZnO films is a complicated process. The grain boundaries, especially the points where three grains meet were supposed to be etching attack points as determined by TEM [127]. Starting from the attack points, the etchings spread both laterally and vertically. On the reference ZnO:Al films, etching in 0.5% diluted HCl solution for 30-40 s lead to round craters with diameter of about 1000 nm. Etching in HF solutions lead to smaller and deeper craters with higher densities [174]. The reason was attributed to that HF molecule tends to penetrate deeper before a chemical reaction [174]. The different etching behaviors of HF and HCl have been successfully used to adjust the morphology of TCO front contact by etching in HF and HCl for different duration [175]. The etching behaviors depend not only on the properties of etchant, but also on the film properties. By controlling the properties of films during the deposition process, the films have significantly different morphologies after etching in the same wet chemicals, as shown in Fig. 2.10. It has been widely discussed in Chapter 5 that the surface properties have been changed significantly by ion bombardment. Thus,

it is conceivable that the ZnO surface may also be influenced by ion beam treatment, leading to different HCl etching behavior. The size, shape, and density of craters on the ZnO:Al films for different etching time are the parameters to characterize the etching behavior. In the following, the etching properties of ion beam treated ZnO:Al films are examined.

For testing the difference of etching behavior of ion beam treated and untreated standard ZnO:Al films, the samples were dipped in HCl solution for very short time. In order to minimize the influence of the inhomogeneous deposition, one $10 \times 10~\rm cm^2$ as-deposited standard ZnO:Al film was cut into two pieces. One half was treated by ion beam and the other was not treated. Then the two halves were dipped into 0.5 % diluted HCl solution for 2 s. Then the films were measured by AFM to obtain the top morphologies. Two types of ion beam treatments with 30 sccm Ar and $20/20~\rm sccm~Ar/O_2$ as source gases were performed, respectively. The discharge voltage was kept at 2 kV during the treatments. The treatments were stopped when the removed thickness of ZnO:Al films were near 120 nm. Due to the reduced thickness, sheet resistance of the ZnO:Al films were increased from $3.2~\Omega$ to $3.9~\Omega$.

Fig. 6.1 and Fig. 6.2 give the AFM measurements of the 2 s HCl etched $\rm Ar/O_2$ and Ar ion beam treated ZnO:Al films, respectively. In both figures, the HCl etchings of untreated ZnO:Al films are shown in (a) and the etchings of treated films are shown in (b). The AFM scan size is $15 \times 15~\mu \rm m^2$. The number and size of the craters of the films

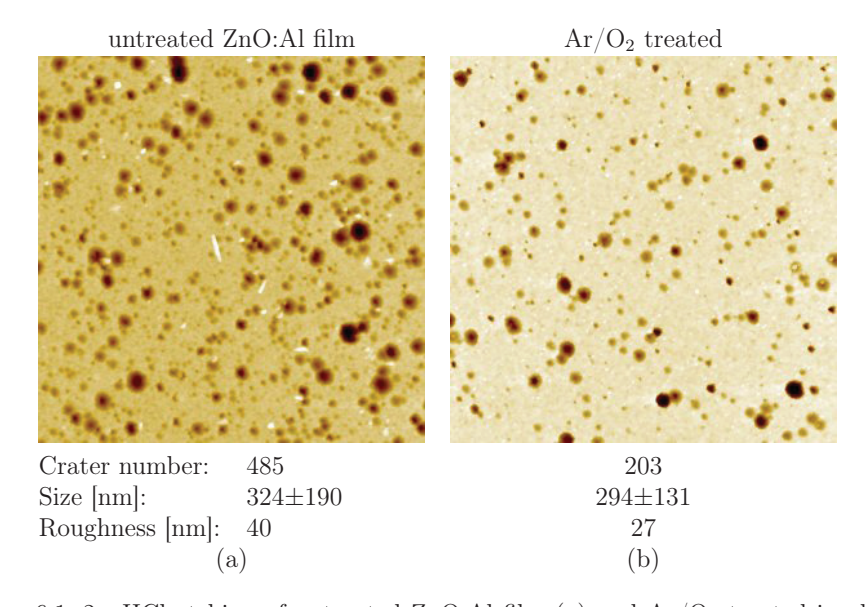


Figure 6.1: 2 s HCl etching of untreated ZnO:Al film (a) and Ar/O₂ treated ion beam treated ZnO film (b). AFM scan size is $15 \times 15~\mu\text{m}^2$. Statistical values from AFM images are listed on the bottom.

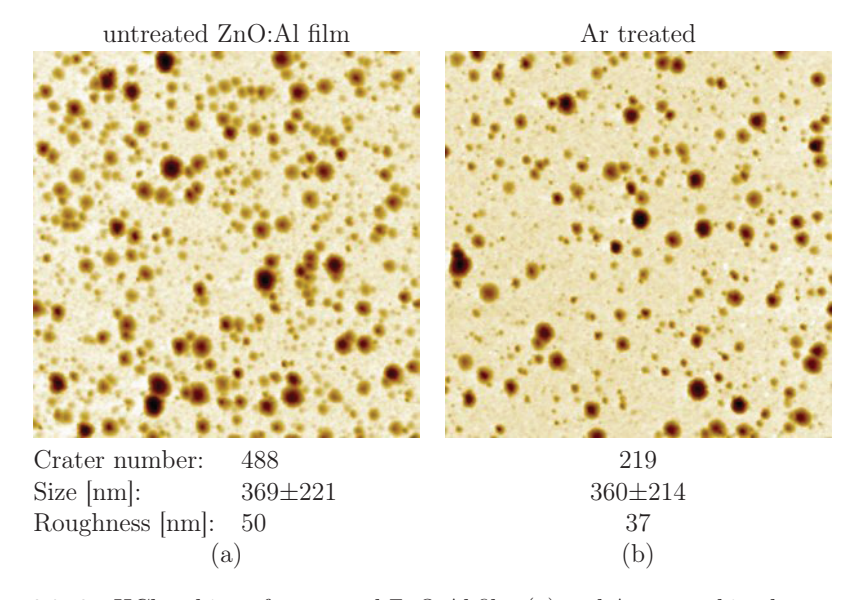


Figure 6.2: 2 s HCl etching of untreated ZnO:Al film (a) and Ar treated ion beam treated ZnO film (b). AFM scan size is $15\times15~\mu\text{m}^2$. Statistical values from AFM images are listed on the bottom.

were evaluated by the advanced threshold method in SPIP program [140]. The values are shown on the bottom of each figure, together with the rms roughness values. The crater number and rms roughness of the HCl etched film in Fig. 6.1(a) is 485 and 40 nm, while the values in Fig. 6.1(b) are 203 and 27 nm, respectively. Less and smaller craters were developed by HCl etching on ${\rm Ar/O_2}$ treated samples. Accordingly, lower rms roughness was obtained for the HCl etching ${\rm Ar/O_2}$ treated samples. Similar results were observed on Ar ion beam treated ZnO:Al films. The crater number and rms roughness of the HCl etched film in Fig. 6.2(a) is 488 and 50 nm, while the values in Fig. 6.2(b) are 219 and 37 nm, respectively. But the size of the craters does not have obviously difference, as can be seen from Fig. 6.2.

The change of etching behaviors seems to be more pronounced on ${\rm Ar/O_2}$ treated sample as compared to Ar treated sample. It has to be noted that large errors might originate from the experimental procedure due to the inaccuracy of the 2 s dip. Therefore, further experiments with longer HCl etching time were performed on ${\rm Ar/O_2}$ treated ZnO:Al samples.

The HCl etching time of ZnO:Al films was extended from 2 s to 10 s and 40 s. Mixed $\rm Ar/O_2$ gas were used as source gas. The ion beam was generated with soft and strong intensities by fixing the discharge voltage at 1 kV and 2 kV, respectively. The soft ion beam treatment removed 45 nm ZnO:Al films, while the strong ion beam treatment removed ZnO:Al films approximately 115 nm.

The AFM measurements of the 2 s, 10 s, and 40 s HCl etched films are shown in Fig.

	untreated ZnO:Al film	Soft Ar/O ₂ treated	Strong Ar/O ₂ treated		
2 s					
	Crater number: 285	260	97		
	Size [nm]: 404±148	479±160	465±205		
	Roughness [nm]: 39	48	32		
10 s					
	Crater number: 403	409	381		
	Size [nm]: 671±312 Roughness [nm]: 100	652±312 102	632±339 100		
40 s					
	Crater number: 243	249	244		
	Size [nm]: 897±472 Roughness [nm]: 137	917 ± 426 125	891±495 118		
	1tougimess [iiii]. 157	120	110		

Figure 6.3: 2 s, 10 s and 40 s HCl etching of untreated ZnO:Al film, soft Ar/O₂ ion beam treated ZnO film and strong Ar/O₂ ion beam treated ZnO film. AFM scan size is 15 \times 15 $\mu m^2.$

6.3. The AFM scan size was $15 \times 15 \ \mu m^2$. In the figure, AFM images of HCl etching of untreated samples, soft ion beam treated samples, and strong ion beam treated sample are shown from left to right column. The statistical values from AFM images including crater number, size, and rms roughness are listed on the bottom of each image. AFM measurements of 2 s HCl etched ZnO:Al films show that the strong ion beam treated ZnO:Al film has obviously less craters than the reference film, while the soft ion beam treated ZnO:Al has similar number of craters as the reference film. When the HCl etching time was increased to 10 s, AFM images (see second row) show that the reference and soft ion beam treated ZnO:Al films have similar shape while the strong ion beam treated ZnO:Al film has slightly less craters. As the HCl etching time is further increased to 40 s, the three films have similar number and size of craters. However the strong ion beam treated ZnO:Al film has smallest rms roughness (118 nm) as compared with the reference film (137 nm). The smaller rms roughness shall be caused by lower crater depth, because the number and size of the craters of this film are similar to other two films. Further calculations of the three AFM images reveal that the crater depth of the reference, soft ion beam treated and strong ion beam treated ZnO:Al films are 589 nm, 550 nm, and 487 nm, respectively.

The two experiments in this section indicate that ion beam treatments of ZnO:Al films have changed their etching behavior. Ion beam treated ZnO:Al films have less attack points as compared with the reference film. With longer etching time, the distribution of the craters are similar, but the depth of the craters are shallower. The exact reason is unclear. As mentioned, it is believed that the grain boundaries of standard polycrystalline ZnO:Al films are attacked by the HCl etchant. Thus, less HCl attack points might be caused by less grain boundaries or more compact material on the ion beam treated ZnO:Al surfaces. Owen et al. has observed that the density of craters have similar trends as the density of grains during the growth of standard ZnO:Al films [127]. Densities of grain boundaries should be approximately constant for a standard ZnO:Al film with thickness around 800 nm and another standard film which is 120 nm thinner. Therefore, it is assumed some grain boundaries on the surface are filled by redeposited ZnO films. Thus, less attack points were observed at the initial stage of HCl etching on ion beam treated ZnO films. When the etching time is increased, the change of HCl etching is less pronounced, because the influence of ion beam treatment lies mainly in the surface region. From this fact, it is suggested to perform ion beam treatment after HCl-etching rather than before.

6.2 ZnO:Al films grown on ion beam treated ZnO:Al films

This section examines the effect of ion beam treatment of ZnO:Al films on the growth of ZnO:Al films. In this work, the influences of ion beam treatment of glass substrate on the growth of ZnO:Al films, and the influence of ion beam treatment of ZnO:Al films on their HCl etching behavior have been investigated in Chapter 5 and 6.1, respectively.

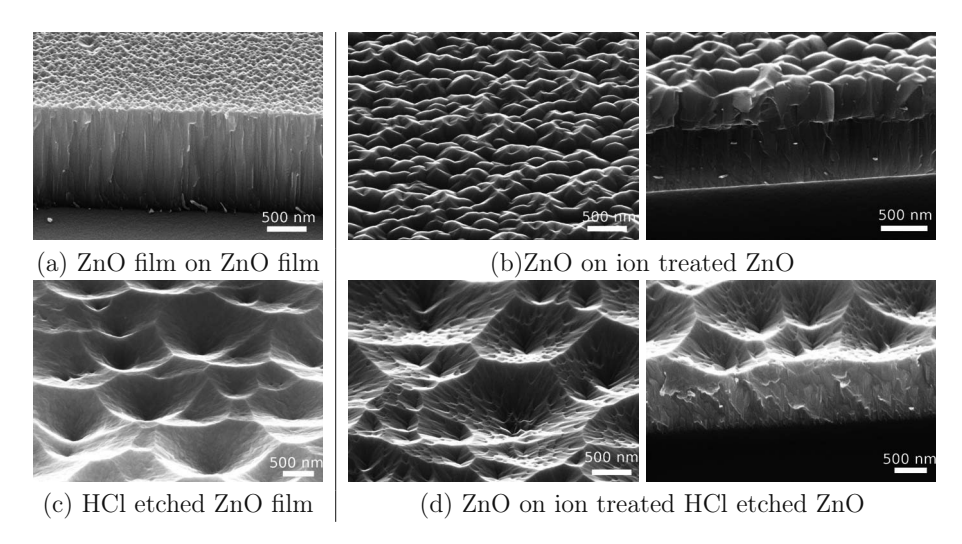


Figure 6.4: SEM micrographs of ZnO:Al film grown on reference ZnO:Al film (a), HCl etched reference ZnO:Al film (c), ZnO:Al film grown on Ar/O₂ treated asdeposited (b) and HCl textured ZnO:Al (d). Both top and cross-section view images are shown for film (b) and (d).

The ion beam treatments have significant effects on the treated surface. The changes of the growth or etching properties have been attributed to the alteration of the ion beam treated surface. It has also been investigated that the ZnO:Al films have epitaxial growth on etched ZnO:Al films if there is no buffer layer at the interface [127]. However if a SiO_x buffer layer is prepared on the ZnO:Al substrate, the c-axis of new deposited ZnO:Al films is perpendicular to the substrate surface [127]. In the following, ZnO:Al films grown on ion beam treated ZnO:Al films are presented.

Standard as-deposited and HCl etched ZnO:Al films were treated by Ar/O_2 ion beam. The discharge voltage was 1 kV. Afterwards, standard ZnO:Al films were deposited on the Ar/O_2 ion beam treated ZnO:Al films. SEM were taken on the ZnO:Al films.

Fig. 6.4 shows the top and cross-sectional SEM micrographs of ZnO:Al films grown on Ar/O_2 ion beam treated as-deposited (b) and HCl etched (d) ZnO:Al films. For comparison, the reference ZnO:Al film sputtered on untreated ZnO:Al film is shown by Fig. 6.4(a), and HCl etched reference ZnO:Al film is shown by Fig. 6.4(c). As mentioned, the sputtered ZnO:Al on ZnO:Al film show epitaxial growth. The interface between the two layers is hardly observed. The morphology of the film exhibits small crater feature. On the ion beam treated ZnO:Al films, the new ZnO:Al films show granular grains with larger size. The interface between the new deposited ZnO:Al films and the substrate is clear in the cross-sectional SEM image. The ZnO:Al substrate has small columnar grains while the new deposited ZnO:Al films have much larger grains. The new nucleation is easily observed in the cross-sectional image. The newly deposited ZnO:Al films are much thinner than the underlying ZnO:Al substrate although the deposition condition

and duration are the same. Therefore, it is concluded that the ZnO:Al films on ion beam treated ZnO:Al films have reduced growth rate. On the HCl etched ZnO:Al films, the new ZnO:Al film maintains the crater shape. However, small flower structures are formed on the crater walls as seen by comparison of Fig. 6.4(c) and (d). Cross-sectional SEM image shows no clear new nucleation of the newly deposited ZnO:Al film.

From the top SEM image, it seems that the large grains of the ZnO:Al films grown on Ar/O₂ treated ZnO:Al are similar to the films grown on Ar/O₂ treated Corning glass. However, the cross-sectional SEM reveals that all of the nucleated crystallites on the Ar/O₂ treated ZnO:Al are the larger grains, while only few large conical grains are nucleated on the Ar/O₂ treated glass. The lower growth rate of the large grains suggests that they might also have opposite c-axis polarity. The flip of polarity might be caused by the O_2 exposure similarly to the (000-1) ZnO epitaxially deposited films grown on O_2 pretreated sapphire substrates [163, 170]. XPS survey scans on Ar/O₂ treated ZnO:Al films revealed that the fraction of Zn and O were changed from 44 at% and 56 at% to 26at% and 71 at%, respectively. It supports that more O and less Zn were terminated on the surface. Thus, new nucleations with preferred (000-1) orientation might dominate. It is not clear why the flower structures were developed on the ZnO:Al films grown on Ar/O₂ treated craters. Nevertheless, the different morphologies of the ZnO:Al films on Ar/O₂ treated ZnO:Al show that the ZnO:Al surface has been changed by the ion beam treatment. It is possible to modify the growth of ZnO:Al films by applying ion beam treatment on the glass or ZnO:Al films.

6.3 Modification of the TCO surface by ion beam etching

It was reported that ion beam treatment on LPCVD deposited ZnO:B films can modify the morphology of TCO front contact, in a way that the V shape structures change into U shape. The former V shape structures might lead to bad crystalline quality in the μ c-Si layer, resulting in relatively lower FF and V_{oc} [136, 137]. Through the modification of the ZnO:B films by ion beam treatment, the FF and V_{oc} of solar cells can be improved [7, 176]. Moreover, it was reported that there is potential to further enhance the absorption in solar cells if the craters are partly filled or cut [177]. The ion beam etching may be employed to cut the top of craters. Therefore, the influence of ion beam treatment of sputtered ZnO:Al films on the performance of solar cells is interesting. In this section, firstly the morphology change of HCl etched sputtered ZnO:Al films is investigated, and then in next section, the growth of Si on ion beam treated TCO front contact is studied.

Reference ZnO:Al films were etched in 0.5~% HCl solution for $40~\rm s$. Then Ar ion beam was applied on the ZnO:Al films for different duration. During the ion beam treatment, the ion source was tilted 40° to the substrate normal. The discharge voltage was kept at $2~\rm kV$. The treatment time was varied by different passes the carrier moves through the ion beam. The ZnO:Al films were treated by Ar ion beam by 2, 4, 6, 8, and $10~\rm passes$,

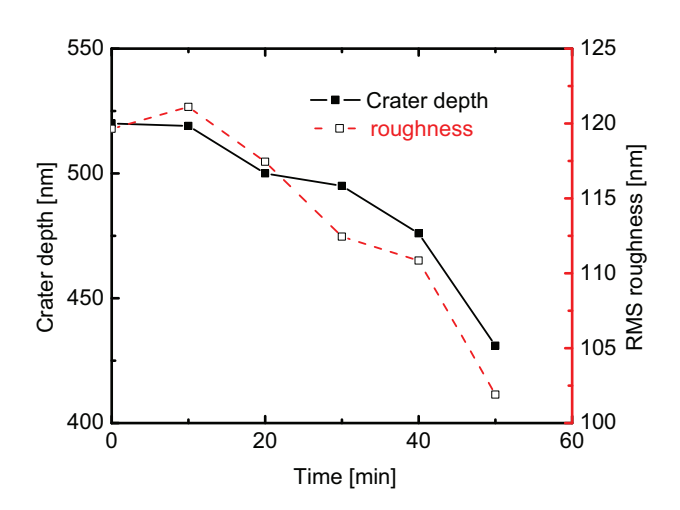


Figure 6.5: rms roughness and crater depth of the Ar etching series of the ZnO films

with the treatment time approximately of 10, 20, 30, 40, and 50 min, respectively. After each treatment, the ZnO:Al films were taken to measure the removed thickness and surface morphology by AFM.

Fig. 6.5 shows the crater depth (solid squares) and rms roughness (open squares) of Ar ion beam etched ZnO:Al films versus the ion beam etching time. The crater depth is calculated from the AFM measurements, representing the average depth of the craters. The crater depth and rms roughness of the ZnO:Al films decreases with the etching time, indicating that the ion beam treatment has smoothing effect on the ZnO:Al films. The surface morphology of ZnO:Al films measured by AFM are shown in Fig. 6.6, in which Fig. 6.6(a) is the ZnO:Al film before ion beam etching, and Fig. 6.6(b)-6.6(f) show the morphology of ZnO:Al films after ion beam treatments. The sharp edge between the craters get smoother with increased etching time. The shape of the craters are changed from symmetric to asymmetric by the tilted ion beam etching. Shadowing effect and the angle dependent sputtering yield are the main reason for the asymmetric craters when the ion source is tilted. The shape of the craters show that the ions are shot from left side. For Ar etching, the smoothening effect might be caused by the difference between the collision cascade at crater top and valley. For normal bombardment, where no shadow exists, more surface atoms are involved in collision cascade for crater top as compared with crater valley. Therefore, the top of craters is etched faster than the valley, leading to a smoothening effect. For ion bombardment with tilted incident angle, the shadowing effect enhance the smoothening process because the valleys receives less ions. O₂ and mixed Ar/O₂ ion etching were also performed and similar smoothening effects were obtained.

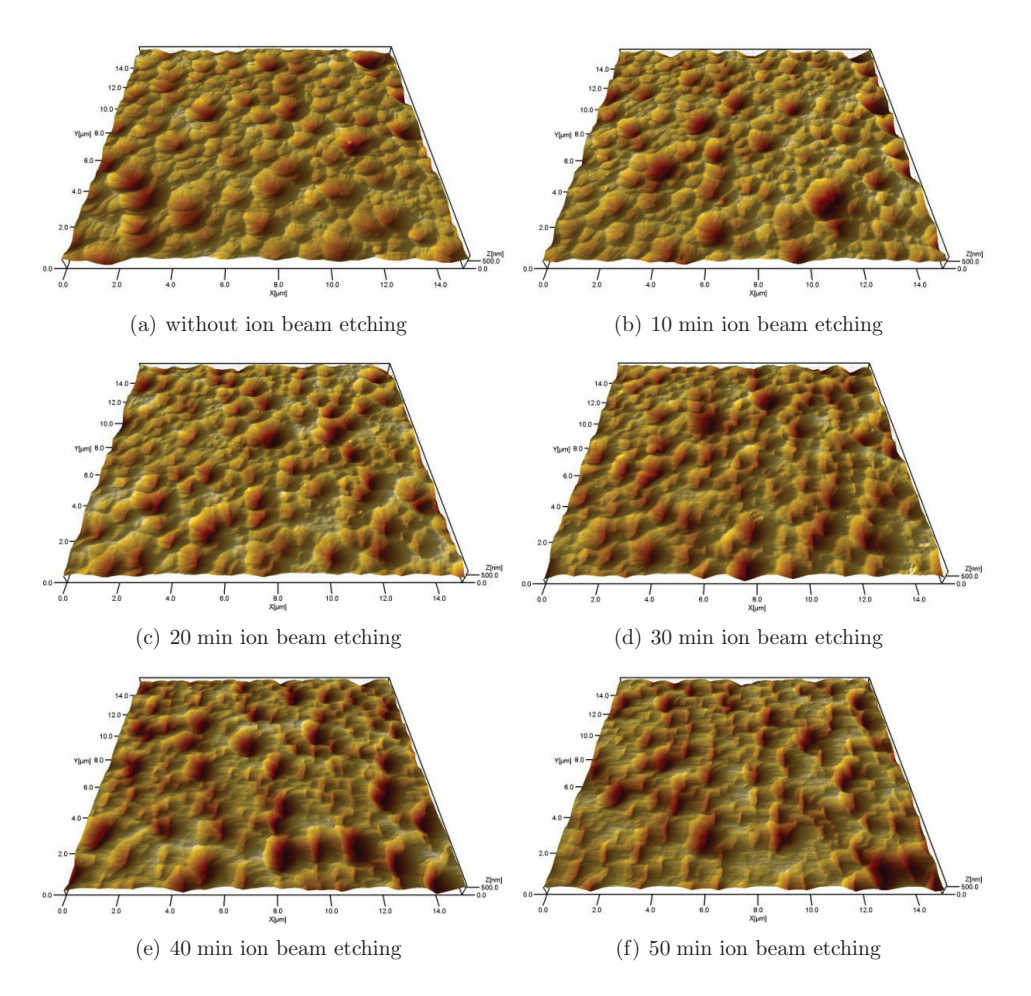


Figure 6.6: The topographies of Ar ion beam etched HCl textured ZnO:Al films. The ion source was tilted 40° to surface normal. Ar etching time: (a):0 min, (b): 10 min, (c): 20 min, (d):30 min, (e): 40 min and (f): 50 min. The scan size is $15\times15~\mu\mathrm{m}^2$.

However, it is common to observe roughening effect when CF_4 or SF_6 plasma are utilized to etch Si surface [178, 179]. It was also reported that $CH_4/H_2/Ar$, Cl_2/Ar , $Cl_2/H_2/Ar$, and CHF_3 plasma can roughen ZnO films [180, 181]. The roughening effect indicates that the valley of crater is removed faster than the top of crater. The etchant particle from gas phases hits the surface at one point. The incident reactive particle either sticks to the surface and removes the substrate materials or it is reemitted from the surface and reach another point on the surface. If the sticking coefficient is low,

most of the incident particles are reemitted from the surface, the valley of the craters have more chance to receive incident ions, then ion beam etching has roughening effect [95]. Thus, the chemical etching tends to end up with a rougher surface.

This section has examined the morphology change of ion beam treated ZnO:Al films. The craters of the HCl textured films become less deep and the films are smoothened after ion beam etching. Thus, the ion beam etching can be used to cut the top of crater top as mentioned in the beginning of this section. However, before the solar cells are deposited on the smoothed ZnO:Al films, the growth of Si on the ion beam treated ZnO has to be investigated.

6.4 Silicon grown on ion beam treated ZnO:Al films

It was shown that ion beam etching can smoothen the HCl textured ZnO surface. This section investigates the performance of solar cells and the growth of Si p-layers on ion beam treated ZnO:Al films.

Three 10×10 cm² ZnO:Al films were etched in 0.5 % diluted HCl solution for 30 s, and then two of them were treated by Ar ion beam for 1 min and 30 min, with strong and soft intensity, respectively. The removed thicknesses for the two films were expected to be approximately 12 nm. Finally, standard microcrystalline Si p-i-n solar cells were prepared on the three substrates in a same run. AFM measurements of the untreated, 1 min, and 30 min treated ZnO:Al films show that the rms roughness are all around 135 nm. The roughness exponent α obtained from height-height correlation function is only slightly increased after ion beam treatments. It indicates the change of the surface morphology is so little that it is hardly to be observed by AFM. 18.1×1 cm² small cells were defined by Ag back contacts on each substrate. J-V measurement results of the three solar cells under standard condition are shown in Table 6.1 and the external quantum efficiency (EQE) is shown in Fig. 6.7. Note that the J-V results were the average value of three best small cells while the QE was measured on one best cell.

The J-V measurement results show that the V_{oc} is slightly increased while the J_{sc} is slightly decreased on the ion beam treated ZnO substrates as compared with reference. As a result, the η of the solar cells on ion treated ZnO:Al films is approximately 0.1% reduced. Spectral response in Fig. 6.7 show that the light scattering effect in long wavelength region is not influenced by the ion beam treatment, because the removed

Table 6.1: J-V measurement results of the μ c-Si solar cells prepared on untreated ZnO:Al films, 1 min and 30 min Ar treated ZnO:Al films.

Substrates	η	FF	V_{oc}	J_{sc}
	%	%	mV	mA
Reference	7.45	72.7	499	20.5
1 min treated	7.33	72.6	503	20.1
30 min treated	7.35	72.7	503	20.1

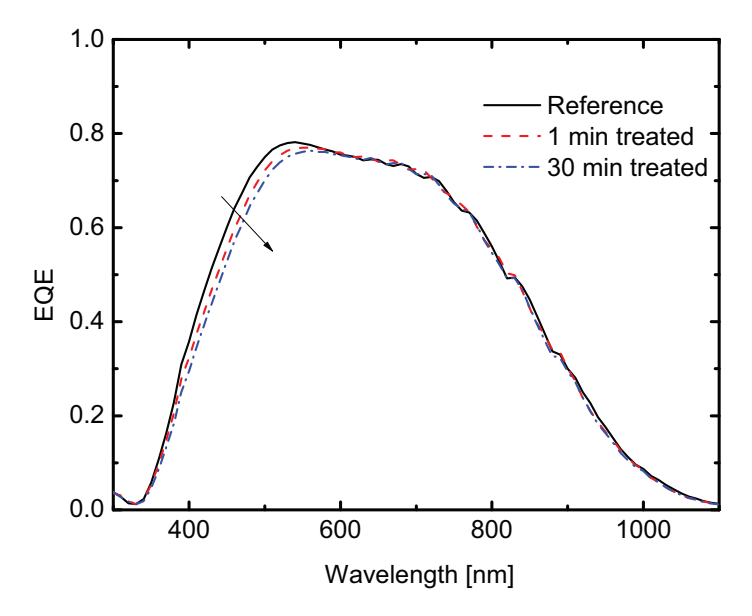


Figure 6.7: External quantum efficiency (EQE) of the μ c-Si solar cells prepared on untreated ZnO:Al films (solid curve), 1 min (dashed curve) and 30 min (dashed curve) Ar treated ZnO:Al films.

thickness of the ZnO film is very thin. The reduction of current locates mainly in the short wavelength region, indicating that the p-layer is altered on ion treated ZnO films. Further experiments to investigate the influence of ion beam treatment on the crystallinity of Si p-layer were conducted.

The first experiment deals with the influences of Ar ion beam treatment on the crystallinity of μ c-Si. The Ar treatments were performed with a tilted ion source (40° to substrate normal). Discharge voltage was fixed at 3 kV. As-deposited and HCl etched ZnO:Al films were utilized in this experiment. The Ar ion beam treatment time was varied from 5 to 25 min by moving the substrates through the ion beam from 1 to 5 passes. After the Ar treatment, 20 nm p-type μ c-Si was deposited on the ZnO:Al films with standard parameters by PECVD. Then, Raman measurements were performed on the thin Si p-layers to determine the crystallinity.

Fig. 6.8 gives the crystallinity of μ c-Si p-layers deposited on different ZnO:Al films. The as-deposited ZnO:Al films are shown with full squares while the HCl etched samples are given with open squares. On untreated ZnO:Al film, the crystallinities of μ c-Si are in the range of 40-60 %. The HCl etching of ZnO:Al films does not have obviously effects on the crystallinity. On Ar ion beam treated ZnO:Al film, the crystallinities of μ c-Si are significantly reduced to less than 20%, no matter how long is the treatment. The reduction of crystallinity in μ c-Si p-layers shall be the reason for the reduced J_{sc} of the

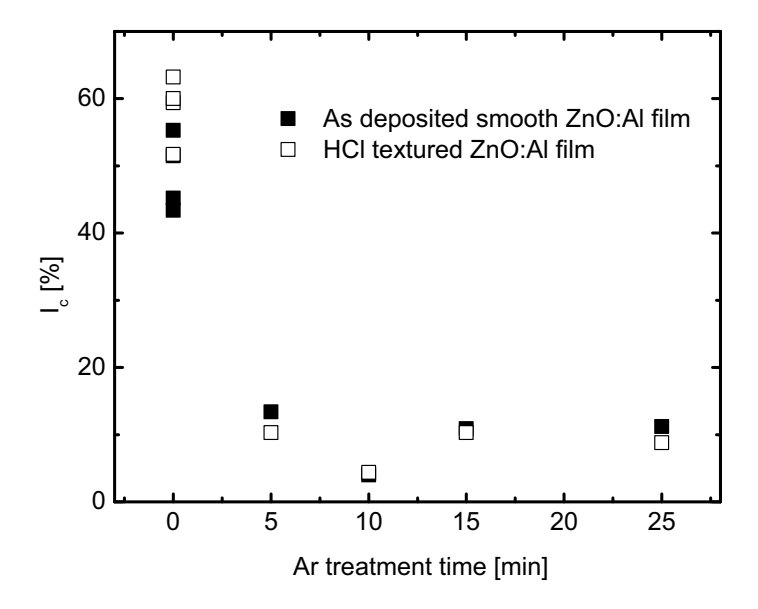


Figure 6.8: Crystallinities (I_c) of μ c-Si p-layer deposited on Ar ion beam treated asdeposited (full squares) and HCl etched ZnO films (open squares) versus the time of Ar ion beam treatments.

cells in short wavelength region.

The next experiment changes the source gas from only Ar to O_2 , Ar+ O_2 , and mixed Ar/ O_2 . In this treatment, only as-deposited ZnO:Al films were used and the ion source was not tilted. The discharge voltage was kept at 2 kV. The ZnO:Al films were treated for 33 min by moving the substrates through the ion beam for 10 passes. Ar+ O_2 ion beam treatments indicates the film was treated by first 8 passes of Ar and then 2 passes of O_2 . 20 nm μ c-Si p-layers were developed on the ZnO:Al films with standard parameters by PECVD. Finally, Raman measurements were performed on the thin Si layers to determine the crystallinity.

The results are shown in Fig. 6.9. The μ c-Si grown on reference film has crystallinity around 30%. On Ar, O₂, Ar+O₂, and mixed Ar/O₂ ion beam treated ZnO films, the crystallinity of Si films are around 29%, 14%, 12%, and 5%, respectively. The Ar treatment in this experiment does not lead to significant decrease of crystallinity, while the other three treatments reduce the crystallinity of Si layers obviously.

The reason of the low crystallinity of Si layers on ion beam treated ZnO:Al films is not clear. It might be related to the modification of the ZnO:Al films by ion bombardment in a similar way to the different growth and HCl etching behavior on ion beam treated ZnO:Al films. XPS measurements performed on Ar, O_2 , $Ar+O_2$, and mixed Ar/O_2 ion beam treated ZnO films show that the percentage of Zn was reduced, while Fe, C, and O

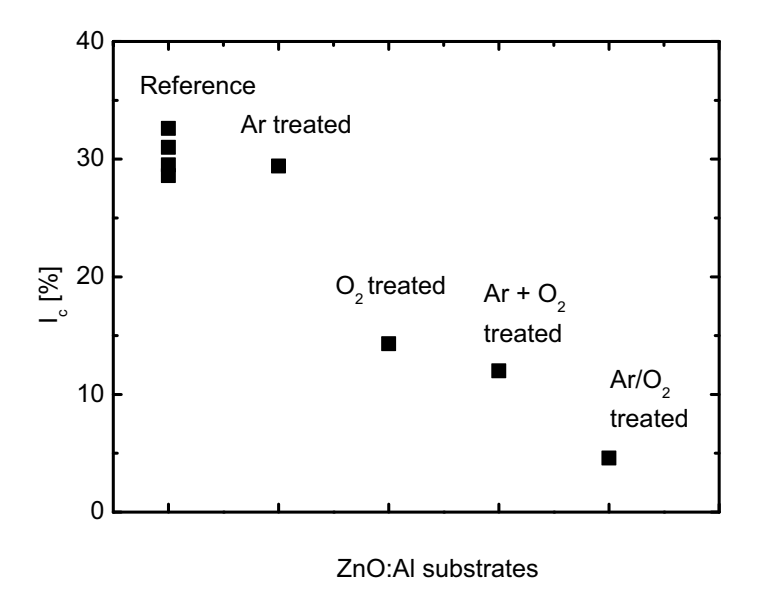


Figure 6.9: Crystallinities (I_c) of μ c-Si deposited on reference, Ar, O₂, Ar+O₂ and mixed Ar/O₂ ion beam treated ZnO films. Ar+O₂ indicates first 8 passes of Ar treatment and then 2 passes of O₂ treatment.

were increased as compared with reference ZnO:Al films. Thus, the ZnO/Si interface was changed by ion beam treatment, resulting in that the crystallization of Si layer becomes difficult. The direct relation between the change of the interface and the growth behavior of Si is not further investigated in this work. The focus of this work moves to textured glass which seems more promising.

6.5 Textured glass

Apart from the textured TCO surface, textured glass is an alternative way to increase the light scattering in Si thin-film solar cells. Textured glass has attracted much interest in recent years, for example 1-D or 2-D patterned glass distinguished by mark preparation, and self-organized patterning, sandblasting glass, or HF etched glass have been applied in Si thin-films solar cells [15–17]. Basically, the principle of using textured glass in thin-film solar cells is feasible. In this work, another promising method to create textured glass is proposed: with features similar to the sputtered and wet-chemically etched ZnO films, compatible with the present sputtering technology. Possible benefits of using textured glass are illustrated by a simple geometric optical model. This section begins with the introduction of the concept and the motivation of using textured glass in Si

thin-film solar cells. Then the method of producing textured glass is introduced, followed by some examples of textured glass and different ZnO:Al films grown on the textured glass. Finally, Si thin-film solar cells on textured glass are presented.

6.5.1 Motivation

In Fig. 6.10 the schematic diagrams of the solar cells based on the traditional wetchemically etched ZnO (a) and the textured glass (b) are compared. Conformal growth of ZnO:Al films on the glass substrates are assumed. The incident light enters the devices perpendicular to the glass surface. Then it is refracted at the first textured interface before it reaches the silicon absorber layer. Therefore, for the traditional structure, the light starts to scatter from the TCO/Si interface, while for the second structure, the light starts to be scattered at the glass/TCO interface and it has to pass two rough interfaces until the light beam reaches the absorber layer.

The light scattering angles in absorber layer of the two structures is calculated by geometrical optics. The local tilt angle of the rough interface is denoted as α , and the angle of the scattered light in silicon is denoted as θ . Applying Snell's law on each layer interface, θ is calculated at different surface tilt angle α for the two structures. For structure (a) flat glass + HCl textured ZnO, θ is calculated as a function of α by

$$\theta = |\arcsin(\frac{n_{ZnO}\sin(\alpha)}{n_{Si}}) - \alpha|, \tag{6.1}$$

where the refractive indexes of ZnO and Si n_{ZnO} and n_{Si} are 1.9 and 3.5, respectively.

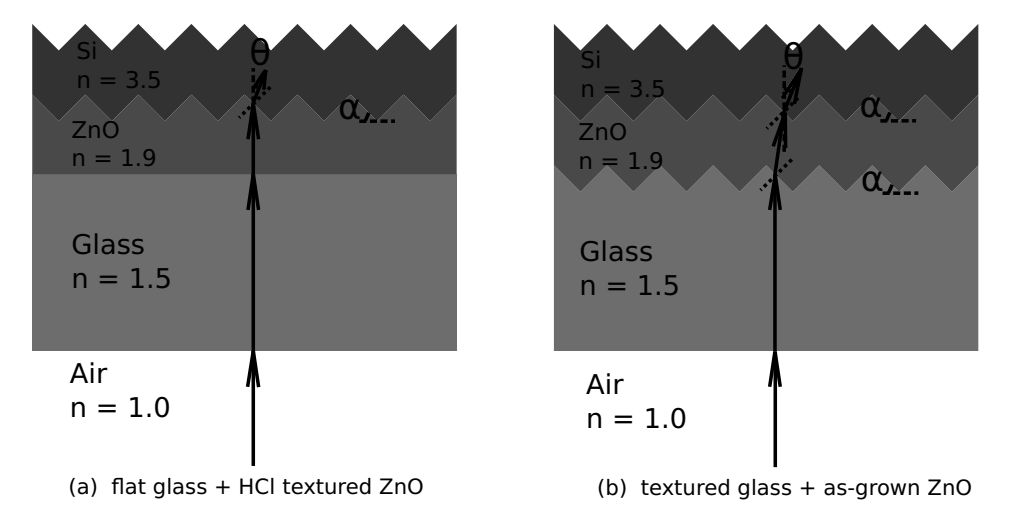


Figure 6.10: The schematic diagram of the solar cells based on traditional flat glass (a) and textured glass (b).

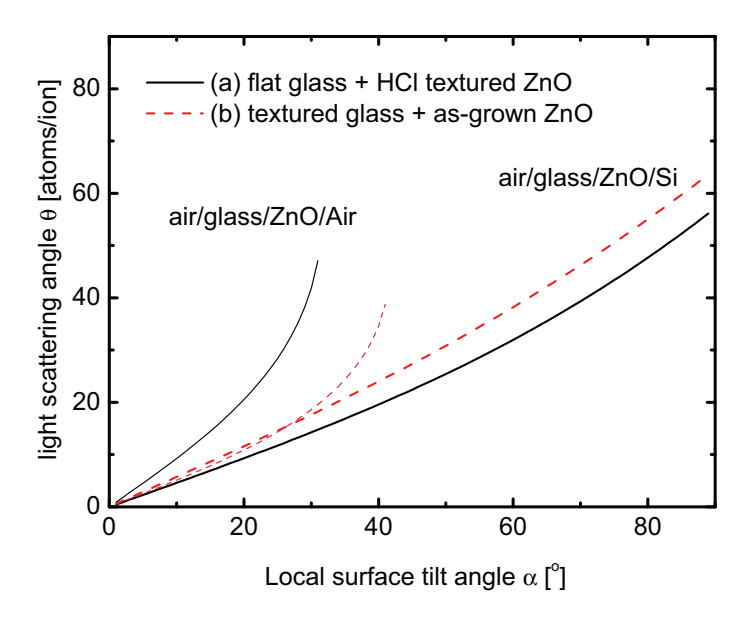


Figure 6.11: Light scattering angle θ versus α which is the tilt angle of local textured interface for the two structures. The θ and α are denoted in Fig. 6.10.

For structure (b) textured glass + as-grown ZnO, θ is calculated by

$$\theta = |\arcsin(\frac{n_{glass}\sin(\alpha)}{n_{Si}}) - \alpha|, \tag{6.2}$$

where the refractive index of glass n_{glass} is 1.5. The results are shown by the thick solid and dashed curves in Fig. 6.11. Here only the scattering at the front contact interfaces rather than all scattering events in the device are considered. Small ZnO:Al thickness as compared to the lateral surface feature size is also assumed.

Note that during a optical measurement of the ZnO:Al films on glass substrates, the light is scattered into air. Therefore, for the 'air/glass/ZnO/air' configuration, the scattered angle θ is calculated by the following equation

$$\theta = |\arcsin(\frac{n_{ZnO}\sin(\alpha)}{n_{air}}) - \alpha| \tag{6.3}$$

for structure (a), and the equation

$$\theta = |\arcsin(\frac{n_{ZnO}\sin(\alpha)}{n_{air}}) - \alpha| \tag{6.4}$$

for structure (b). The results are shown by thin solid and dashed curves. The two curves do not reach 90° due to the internal reflection.

With increasing surface tilt angle α , the scattered angle θ and the discrepancy between cases (a) and (b) also increases. Since a larger angle θ leads to an increase of the optical path length, in principle steeper surface textures might be favorable for light-trapping in solar cells. Note that multiple scattering events at the interfaces which might occur especially for high α are not taken into account. Since the scattered angles θ for the textured glass structure are larger than θ for traditional structure, there is potential to improve the light scattering behavior of solar cells based on the textured glass structure. However, this benefit can not be measured in air, since in air the textured glass configuration tend to scatter light into smaller angle.

6.5.2 Preparation of textured glass

In the following, the preparation process of textured glass is given. The technique is based on the physical ion beam etching with 3D etching mask, which was also use to prepare optical micro-devices [182, 183]. The shape of the etching mask is transfered on the glass substrate, since glass can also be etched by ion beam. Due to the different etch rate of glass substrate and etching mask, as well as the smoothening effect of the ion beam etching, the morphology of the textured glass is modified during transfer. In this work, HCl etched ZnO:Al films are used as etching mask.

The schematic preparation process is shown in Fig. 6.12. A randomly HCl etched ZnO:Al film on glass substrate was etched by the ion beam (a). The ZnO:Al films were removed by the incident ion beam, and some part of the glass substrate was exposed to

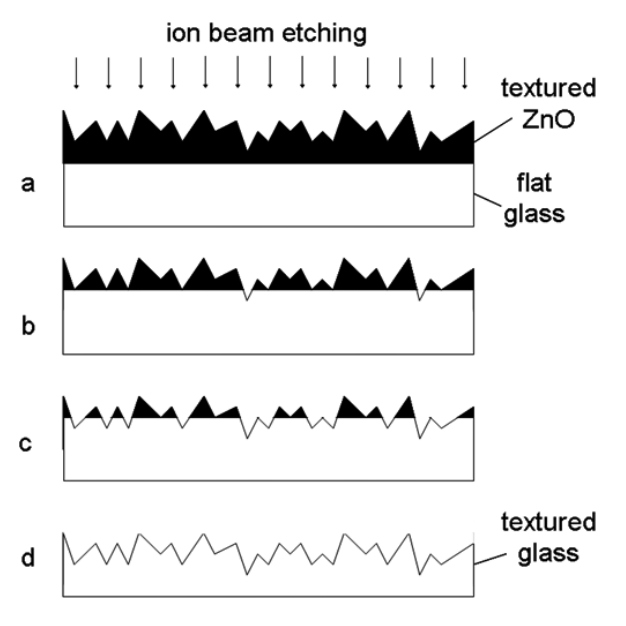


Figure 6.12: Preparation process of textured glass.

and etched by the ion beam (b, c). Finally, the ZnO:Al film is totally removed, the glass revealed the crater morphology similar to the ZnO:Al films (d).

The preparation of textured glass by ion beam etching of ZnO:Al films might not be economically feasible for industry process. However, it provides textured glass with similar crater morphology, which is interesting for studying light trapping effect. Textured ZnO:Al films can also be replaced by cheap materials, such as ZnO nano-particles or micro-particles. Some examples are shown in Section 6.5.3.

The topography of textured glass is shown in Fig. 6.13, in which Fig. 6.13(a) shows the textured ZnO:Al film which was etched in HCl for 60 s, and Fig. 6.13(b) shows the resulting textured glass after ion beam etching. The ion source was not tilted for this experiment. Therefore, the textured glass has symmetric craters. The lateral size of the large craters is similar for the two samples, but the small craters have disappeared on the textured glass. The craters on the textured glass become shallower, because of the smoothening effect.

The topography of textured glass can be adjusted by the ZnO:Al films. Fig. 6.14 shows surface analysis data of a series of textured glass obtained by ion beam etching of different ZnO:Al films. The as-grown ZnO:Al films have thickness around 800 nm. They were etched in 0.5 % HCl solution for different time, from 60 s to 150 s. The crater depth, rms roughness, and lateral correlation length of the ZnO:Al films are shown by solid squares in the figure. Ion beam etching with different time were applied on the ZnO:Al films, till the ZnO:Al material were totally removed. The ion source was not tilted in these experiments. The corresponding parameters obtained by AFM measurements of the resulting textured glass are shown as open squares. The figure shows that the crater depth and roughness have similar trends for the ZnO:Al films and textured glass. With increasing etching time, they first increase and then decrease. The largest crater depth and roughness are observed when the HCl etching time is 100 s. When the etching time is less than 120 s, the correlation length of ZnO:Al surface is slightly increased, while for very long time etching 150 s, the correlation length of ZnO:Al surface increases significantly. The crater depth and roughness decreases by 240 nm and 50 nm for the textured glass as compared with the ZnO:Al films. Maximum

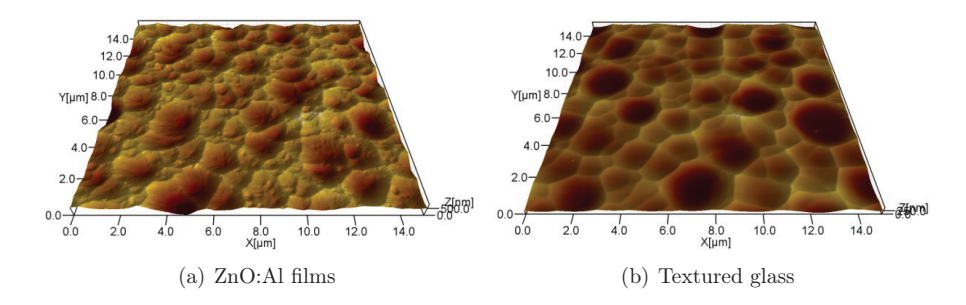


Figure 6.13: AFM images of textured glass (b) prepared by ion beam etching of 60s HCl etched ZnO films (a). The scan sizes are $15 \times 15 \ \mu m^2$.

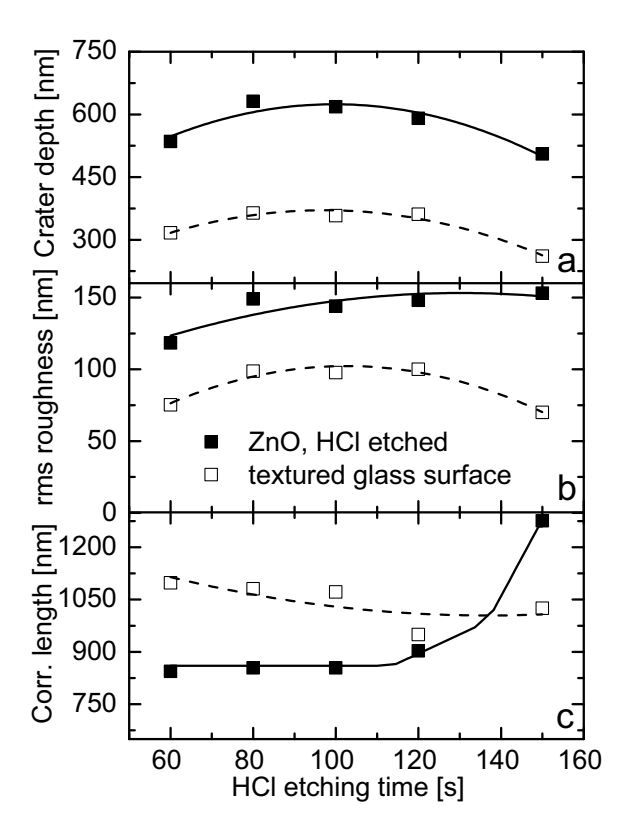


Figure 6.14: (a) Crater depth, (b) rms roughness, and (c) lateral correlation length of 800 nm thick wet chemically etched ZnO:Al films (Solid squares) and the values for the corresponding textured glass (open squares). All lines are guide for the eyes. The ion source was not tilted during this process.

crater depth and rms roughness for textured glass of 360 nm and 100 nm were obtained. The lateral correlation length of textured glass is larger than the ZnO:Al films when the etching time is less than 120 s and smaller than the ZnO:Al film when the etching time is 150 s. The increase of lateral correlation length might be caused by the elimination of small craters. The decrease of crater depth and roughness of ZnO:Al films after 100 s is because the glass has been reached by HCl etching. Since glass is not etched by HCl solution, the surface becomes smoother for further etching. The textured glass is smoother than the corresponding ZnO:Al films, which confirms again that the ion beam etching has smoothening effect.

Fig. 6.15 gives the haze results of the above ZnO:Al films and corresponding textured glass. The samples with different HCl etching time are shown in the legends. ZnO:Al films and textured glass are denoted in the figure. Clearly, textured glass have lower

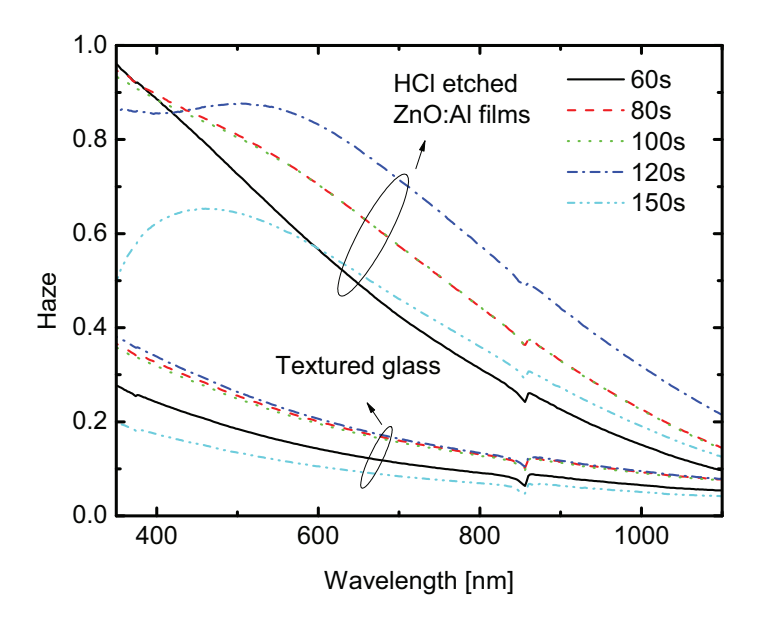


Figure 6.15: Haze of 800 nm thick wet chemically etched ZnO:Al films (upper curves) and the values for the corresponding textured glass (bottom curves) as shown in Fig. 6.14.

haze than the ZnO:Al films. Note that the haze of 80 s and 100 s HCl etched sample is very close to each other, which can also be identified by the very similar crater depth and rms roughness values as shown in Fig. 6.14. It indicates many uncertainties during the etching process, such as the time accuracy of different people, the difference of samples in various deposition series and the ambient temperature.

The size and depth of the craters on the glass substrate can be further adjusted by changing the thickness of the ZnO:Al etching mask. A series of 800 nm and 1500 nm ZnO:Al films were etched in HCl for 30-330 s. Then, ion beam etching was applied on the ZnO:Al films. The ion source was tilted by 40° to the substrate normal in order to get faster etch rate. AFM was measured on the ZnO:Al films and resulting textured glass surfaces. The crater depth, rms roughness, and lateral correlation length of the ZnO:Al film and textured glass surfaces are shown in Fig. 6.16. For the ZnO:Al films with initial thickness of 800 nm and 1500 nm, the maximum crater depth of 700 nm and 900 nm were achieved after 75 and ~ 300 s etching, respectively. Thus, the use of thicker films allows for creating deeper craters in the ZnO:Al etching masks. As compared to the corresponding ZnO:Al etching masks with initial thickness of 800 nm and 1500 nm, the crater depth of textured glass was reduced by 90-230 nm and 100-300 nm, respectively. Accordingly, maximum crater depth of 600 nm and 800 nm were achieved for textured glass. The trend of rms roughness was again similar to the crater depth. The

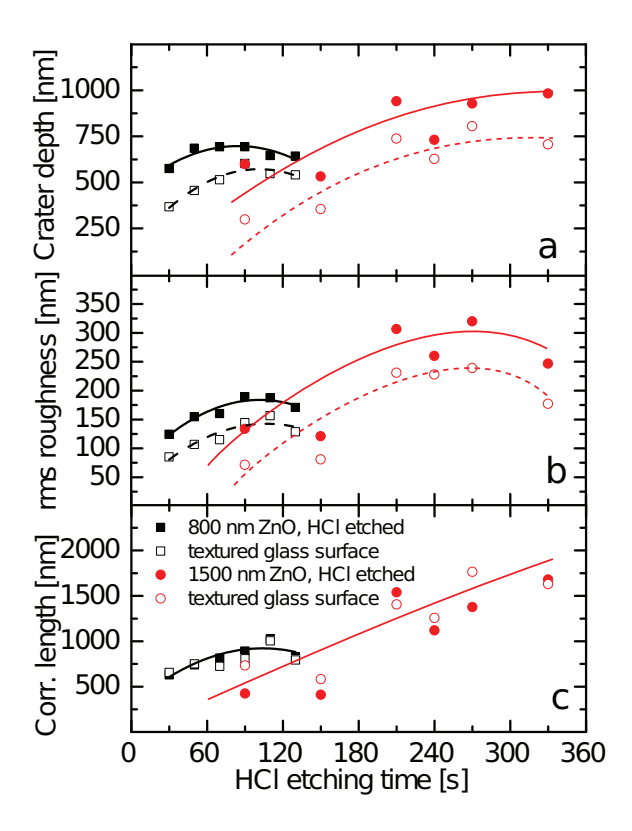


Figure 6.16: (a) Crater depth, (b) rms roughness, and (c) lateral correlation lengths of 800 nm (full squares) and 1500 nm (full circles) thick wet-etched ZnO films and the values for the corresponding glass surfaces (open symbols). All lines are guide for the eyes. The ion source was tilted 40° to the substrate normal.

maximum rms roughnesses for HCl etched ZnO:Al films were 190 nm and 320 nm for 800 nm and 1500 nm initial film thicknesses, respectively. The rms roughness of glass was about 30-80 nm smaller than for the corresponding ZnO:Al surface. Accordingly, maximum rms roughness of textured glass was 157 nm and 320 nm. The correlation length of the longer HCl etched ZnO:Al films increased to around 1500 nm, indicating large size of the craters. The lateral correlation length of textured ZnO and glass are comparable for these samples. This might be due to unsymmetrical craters caused by the tilt of ion source. As compared to the textured glass prepared by normal ion incidence, tilted ion beam etching leads to rougher textured glass.

This section examined the textured glass prepared by ion beam treatment of HCl etched ZnO:Al film, in which the ZnO:Al film was used as 3D etching mask. The

morphology of textured glass can be adjusted in a large range, by changing the initial thickness and morphology of etching mask. The textured glass exhibit shallower craters topographies as compared with ZnO:Al films.

6.5.3 Different etching mask

As discussed in the last section, other materials than ZnO:Al films can also be used as etching masks. This section introduces the textured glass made by ion beam etching of AsahiU SnO_2 :F films and ZnO micro-particles.

AsahiU SnO₂:F films were etched by ion beam, until the SnO₂:F material was totally removed. The ion source was tilted 40° to the substrate normal. As a result, the glass has textured morphology. Fig. 6.17 shows the AFM images of the SnO₂:F film and the resulting textured glass. The scan size is $4 \times 4 \ \mu m^2$. SnO₂:F film exhibit pyramid features with rms roughness of around 42 nm. After the ion beam etching, the roughness was decreased to 12 nm. The small roughness of textured glass is due to small roughness of the etching mask. The shape of the pyramids changed to shallow craters. Because of the tilted ion source, unsymmetrical craters were obtained.

ZnO micro-particles with size range of $1-3~\mu m$ were coated on clean glass substrates by spin coating. The ZnO micro-particles was mixed in mixed solution of glycerol and ethanol. After spin coating, the liquid residues were evaporated during annealing on a hot plate with temperature of 120° . Then, the samples were treated by ion beam for certain time. If the micro-particles was not fully removed by ion beam, the samples were etched and cleaned in HCl solution. Many parameters can be adjusted such as the concentration of the micro-particles in the liquid, the speed of the spin coating, the type of the micro-particless and the ion beam etching time and so on. Fig. 6.18 gives some examples of textured glass with varying parameters. The scan size of the AFM measurements was $4 \times 4~\mu m^2$. The textured glass of Fig. 6.18(a) exhibit hillock shapes with lateral feature size around 500 nm and vertical height around 200 nm. The one of Fig. 6.18(b) show deep craters with flat plateau. For this film, the micro-particless were not totally removed by ion beam, but etched by HCl solution. Thus, large plateaus were left on the glass surface. The last one (Fig. 6.18(c)) is characterized by shallow craters

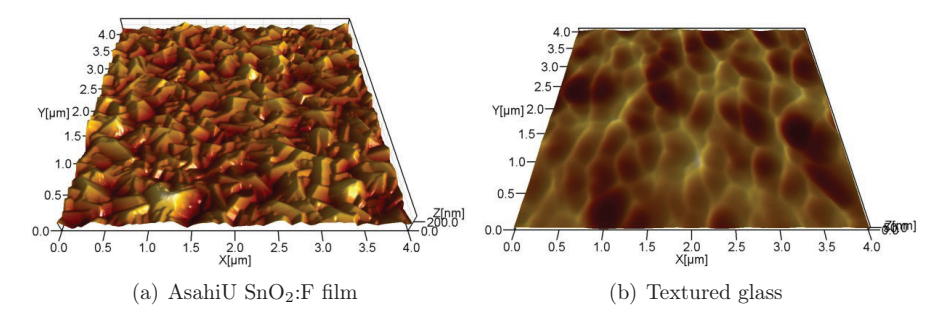


Figure 6.17: Textured glass (b) prepared by ion beam etching of AsahiU SnO₂:F film(a).

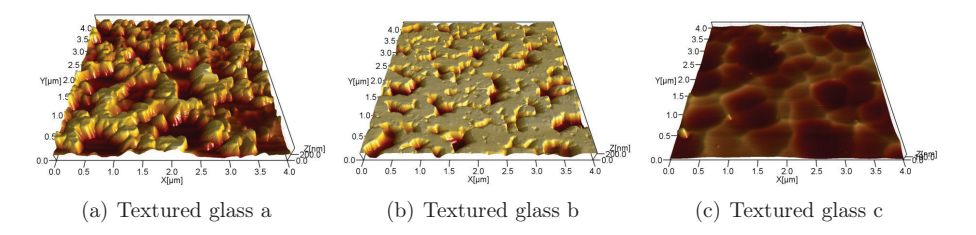


Figure 6.18: Textured glass prepared by ion beam etching of ZnO micro-particles. The differences between (a), (b) and (c) are adjusted by the concentration, spin speed of the spin coating and the time of the ion beam etching. For detail information, see [184].

with lateral size around 500 nm. More details can be found in [184].

This section presented a variety of textured glass prepared by ion beam etching. Depending on the type of etching masks, the morphology of the textured glass can be varied in a large range. This technique provides a large potential for creating differently textured interfaces in Si thin-film solar cells.

6.5.4 ZnO:Al films on textured glass

This section examines the growth of ZnO:Al films on textured glass. As one of the advantages of textured glass, the ZnO:Al films must not be etched in wet chemicals in order to achieve textured surface. Therefore, the requirements for the sputter depositions of ZnO:Al films are relaxed. The textured glass samples were always prepared by Ar ion beam etching of HCl etched ZnO:Al films, due to the fast etch rate of Ar ions. Afterwards, the textured glass were directly used, or treated by Ar/O_2 ion beam, or cleaned by standard cleaning process. Thus, the ZnO:Al films directly grown on the textured glass are the so called ZnO:Al on Ar treated textured glass, while films grown on the other two types of glass are called as ZnO:Al films on Ar/O_2 treated and cleaned textured glass, respectively. In the following, the standard sputtered ZnO:Al films on Ar treated, Ar/O_2 treated, and cleaned textured glass are investigated. The benefit of double textures are presented by AFM and optical measurements in this section and solar cells in next section.

6.5.4.1 ZnO:Al films on Ar treated textured glass

A standard ZnO:Al film was etched in 0.5% diluted HCl solution for 80 s, then the textured ZnO:Al film was dry etched by Ar ion beam to remove all ZnO:Al material. Finally standard ZnO:Al film was deposited on the textured glass. AFM measurements, optical Haze and ARS measurements were performed on one textured glass and as-grown ZnO:Al film on the textured glass. AFM scan size was $15 \times 15 \ \mu m^2$.

Fig. 6.19 shows the AFM images of Ar treated textured glass (a) and the ZnO:Al films on the textured glass (b). Apart from the background of the textured glass, the ZnO:Al

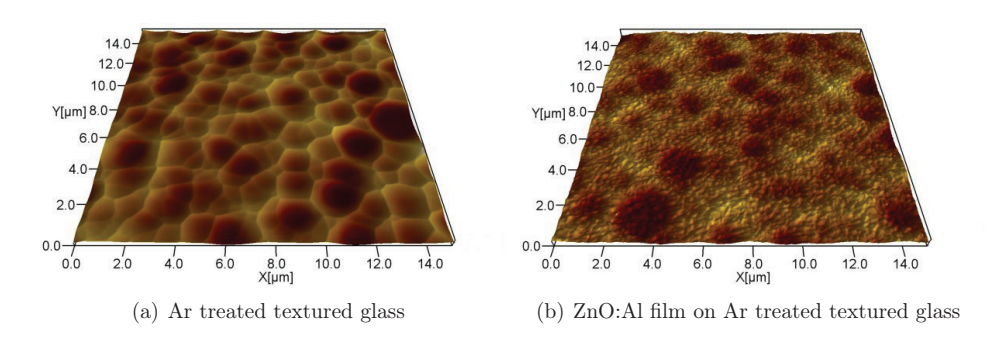


Figure 6.19: AFM measurements of ZnO:Al films (b) grown on Ar treated textured glass (a). The scan size was $15 \times 15 \ \mu m^2$.

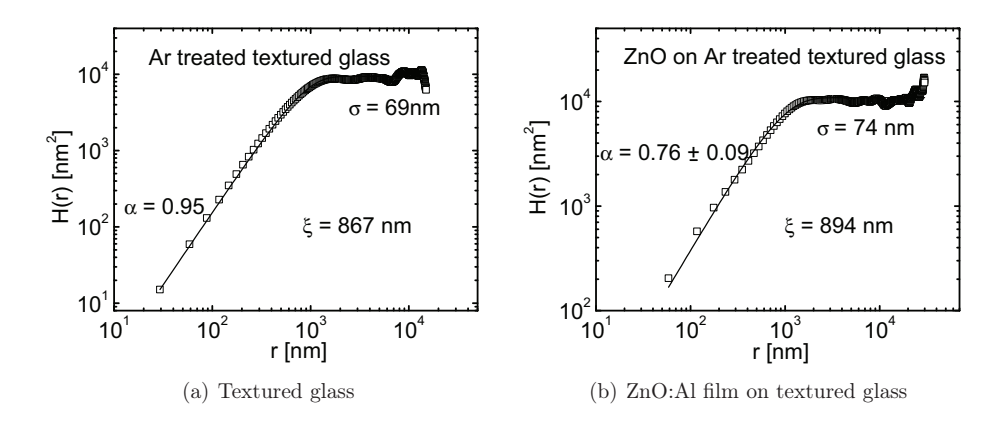


Figure 6.20: Height-height correlation function of Ar treated textured glass (a) and ZnO:Al film grown on the textured glass (b) as shown in Fig. 6.19. Lateral correlation length ξ , roughness exponent α , and rms roughness σ are denoted in the figure.

film has small granular features. Fig. 6.20 shows the height-height correlation functions of the textured glass (a) and ZnO:Al film (b) calculated from the AFM measurements. Lateral correlation length ξ , roughness exponent α , and rms roughness σ are denoted in the figure. The meaning of the three parameters can be found in Section 2.2.4.5. After the deposition of ZnO:Al film, the rms roughness and lateral correlation length ξ are slightly increased from 69 nm to 74 nm and from 867 nm to 894 nm, respectively. The roughness exponent α is decreased from 0.95 to 0.76. The slightly increase of σ and ξ indicate that the average size of craters in lateral and vertical direction become slightly larger, while the decrease of α suggest that small rough features are added to the crater morphology. The small rough features shall be corresponding to the as-grown rough

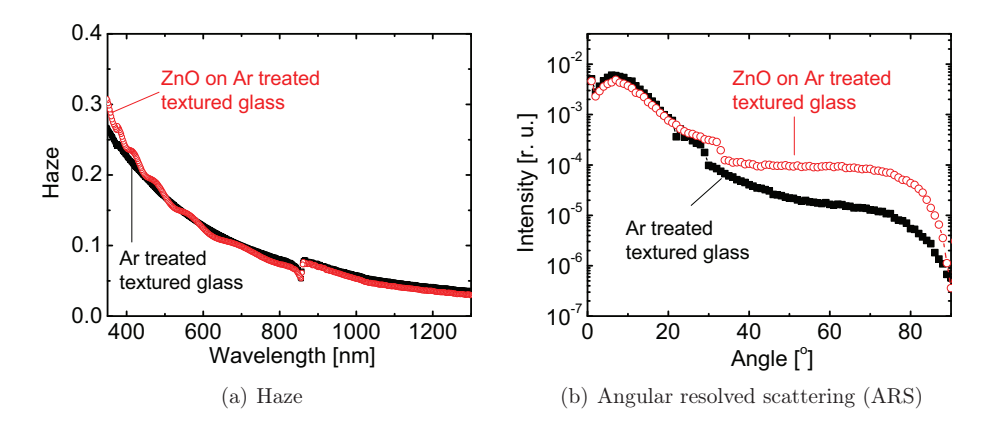


Figure 6.21: Haze (a) and ARS (b) of the Ar treated textured glass (solid squares) and the ZnO:Al films grown on Ar treated textured glass (open circles).

polycrystalline ZnO:Al films.

Fig. 6.21 gives the haze and ARS measurements of the two samples, in which the textured glass is shown in full squares and the ZnO:Al film grown on the textured glass is shown in open circles. Haze of the two samples are almost the same, except the ZnO:Al film has slightly higher haze at wavelength region of 350-500 nm. It is consistent to the slightly increase of rms roughness. The intensity of scattered light versus scattering angle is shown by log-scale in Fig. 6.21(b). For both samples, the scattering intensity increases with the scattering angle till 7°, then decreases sharply till 20°. As mentioned in Section 6.5.1, the light tends to be scattered to larger angle in Si layer on textured glass. However, the benefit can not be measured here, because the ARS measurement was performed in air. When the scattering angle is less than 20°, the scattering light of ZnO:Al film is slightly lower than that of textured glass, which might be due to enhanced absorption and reflection by the ZnO:Al layer. In the angle range of $20-90^\circ$, the intensity of scattered light decreases further with increasing angle, but the scattered light of ZnO:Al film is higher than of textured glass. Higher scattered light at large angle is supposed due to the small rough features of ZnO:Al films.

6.5.4.2 ZnO:Al films on Ar/O₂ treated textured glass

This section examines the growth of ZnO:Al film on Ar/O_2 treated textured glass. A standard ZnO:Al film was etched in 0.5% diluted HCl solution for 90 s, then the textured ZnO:Al film was dry etched by Ar ion beam to remove all ZnO:Al material. Afterwards, the textured glass was treated by Ar/O_2 ion beam with low intensity. The removed thickness by the Ar/O_2 treatment can be neglected. Finally standard ZnO:Al film was deposited on the textured glass. Similarly characterizations - AFM, haze, and ARS measurements were performed on the textured glass and ZnO:Al film on the glass.

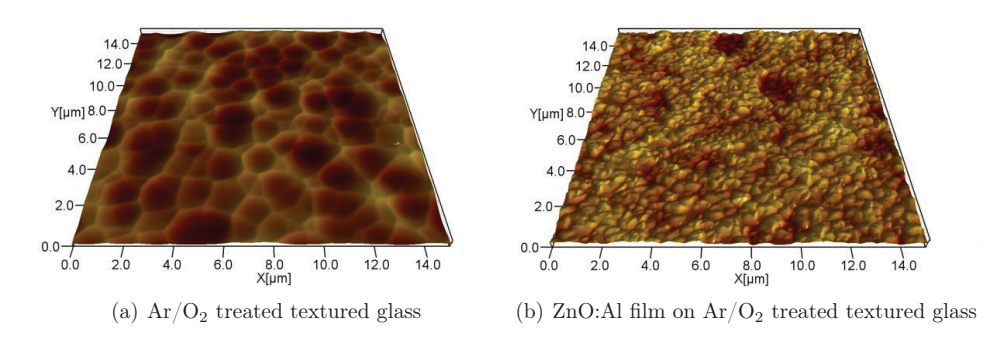


Figure 6.22: AFM measurements of ZnO:Al films (b) grown on Ar/O_2 treated textured glass (a). The scan size was $15 \times 15 \ \mu m^2$.

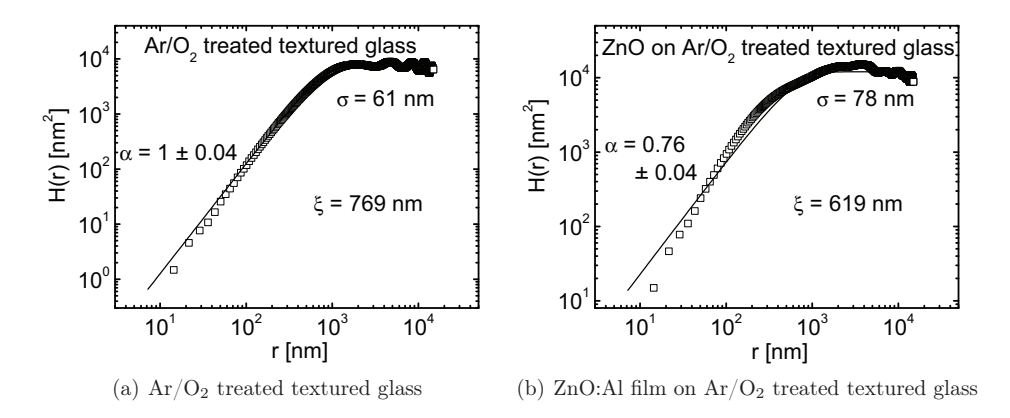


Figure 6.23: Height-height correlation function of Ar/O_2 treated textured glass (a) and ZnO:Al film grown on the textured glass (b). Lateral correlation length ξ , roughness exponent α , and rms roughness σ are denoted in the figure.

Fig. 6.22 shows the AFM images of Ar/O₂ treated textured glass (a) and the ZnO:Al films on the glass (b). Compared with the ZnO:Al film on Ar treated textured glass, the ZnO:Al film on Ar/O₂ treated textured glass has large granular features, and the background of the textured glass is difficult to be observed. The second texture added by the ZnO:Al films are caused by the Ar/O₂ treatment of glass substrate which has been widely discussed in Chapter 5. Fig. 6.23 shows the height-height correlation functions of the textured glass (a) and ZnO:Al film (b) calculated from the AFM measurements. Lateral correlation length ξ , roughness exponent α , and rms roughness σ are also denoted in the figure. After the deposition of ZnO:Al film, the rms roughness is increased from 61 nm to 78 nm. Lateral correlation length is decreased from 769 nm to 619 nm. The roughness exponent α is decreased from 1 to 0.76. The increase of σ and decrease of

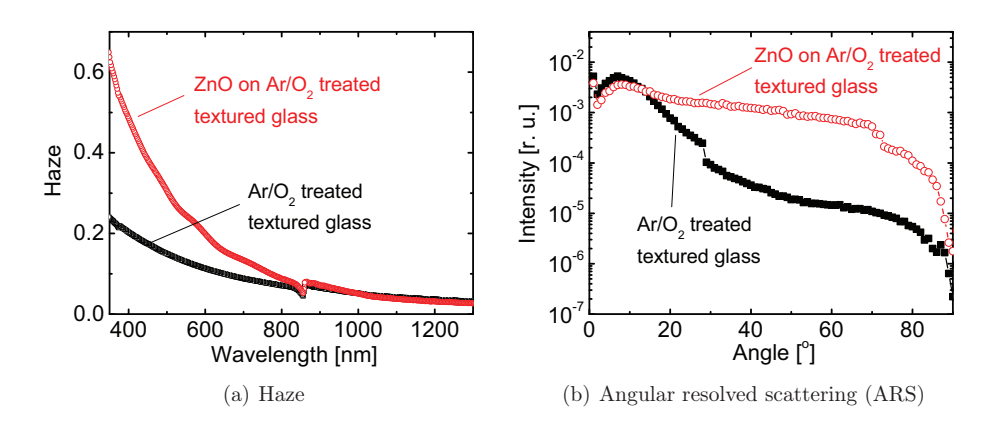


Figure 6.24: Haze (a) and ARS (b) of the Ar/O_2 treated textured glass (solid squares) and the ZnO:Al films grown on Ar/O_2 treated textured glass (open circles).

 α indicate that both the ZnO:Al film becomes rougher than the textured glass both in large and small scale.

Fig. 6.24 gives the haze and ARS measurements of the two samples, in which the textured glass is shown in full squares and the ZnO:Al film grown on the textured glass is shown in open circles. The ZnO:Al film has nearly two times higher haze at wavelength range 350-800 nm. The significantly increase of haze at short wavelength region is contributed by the small texture of ZnO:Al film. At the rest of the wavelength range, the haze of the two samples are similar. The ARS curves also have difference at the angle range of $18-90^{\circ}$. ZnO:Al film scatter more light to the large angle region. It can be concluded that for the ZnO:Al films, the peak at 7° is contributed by the textured glass substrate, while the high light scattering in the angle range of $30-90^{\circ}$ is contributed by the as-grown textured ZnO:Al films. Therefore, with the double texture features, more light can be scattered to large angles.

6.5.4.3 ZnO:Al films on cleaned textured glass

This section examines the growth of ZnO:Al film on cleaned textured glass. Similar to the previous sections, a standard ZnO:Al film was etched in 0.5% diluted HCl solution for 90 s, then the textured ZnO:Al film was dry etched by Ar ion beam to remove all ZnO:Al material. Afterwards, the textured glass was re-cleaned by the standard cleaning process. Finally standard ZnO:Al film was deposited on the textured glass. The growth of ZnO:Al film shall be different to the Ar or Ar/O₂ treated textured glass as expected from the experiments on flat glass investigated in Section 5.2.2. In the following, the AFM images and the optical properties of textured glass and ZnO:Al film are studied.

Fig. 6.25 shows the AFM images of cleaned textured glass (a) and the ZnO:Al films on the glass (b). The textured glass exhibit a large fraction of flat bottom due to the long

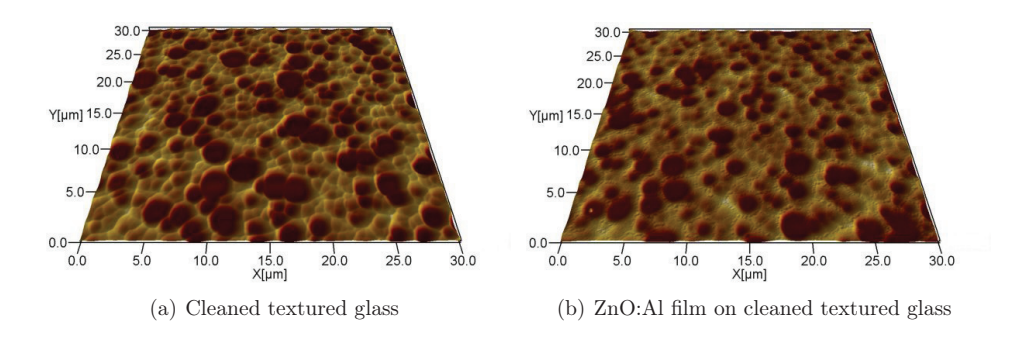


Figure 6.25: AFM measurements of ZnO:Al films (b) grown on cleaned textured glass (a). The scan size was $30 \times 30 \ \mu m^2$.

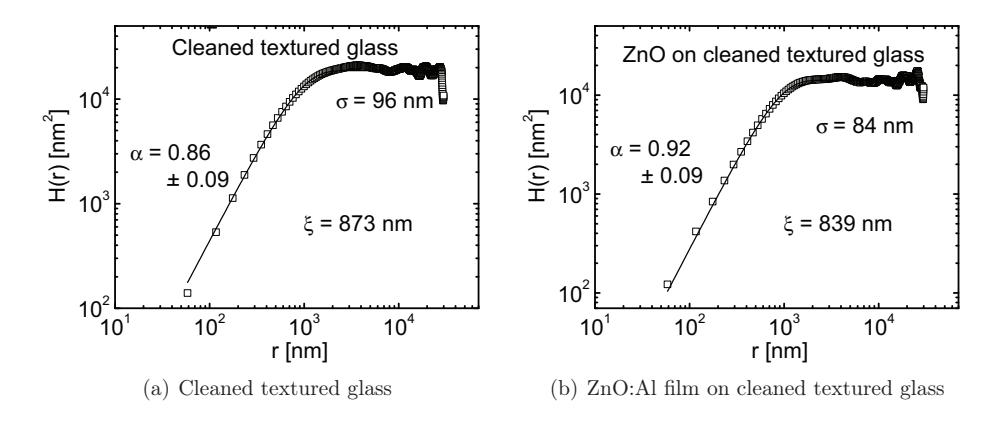


Figure 6.26: Height-height correlation function of cleaned textured glass (a) and ZnO:Al film grown on the textured glass (b). Lateral correlation length ξ , roughness exponent α , and rms roughness σ are denoted in the figure.

HCl etching time in the preparation process. Compared with the ZnO:Al film on Ar or Ar/O₂ treated textured glass, the ZnO:Al film on cleaned glass has conformal growth. The background of the textured glass is maintained to a large extend in the ZnO:Al film. The small holes on the rim of the craters which can also be observed from SEM images might originate from the defects produced in growth process. The nucleation of ZnO:Al films shall be perpendicular to the underlying substrate, thus less materials are sputtered on the rim of craters. Fig. 6.26 shows the height-height correlation functions of the textured glass (a) and ZnO:Al film (b) surfaces. Lateral correlation length ξ , roughness exponent α , and rms roughness σ are also denoted in the figure. After the deposition of ZnO:Al film, the rms roughness is decreased from 96 nm to 84 nm. Lateral correlation length is slightly decreased from 873 nm to 839 nm. The roughness exponent

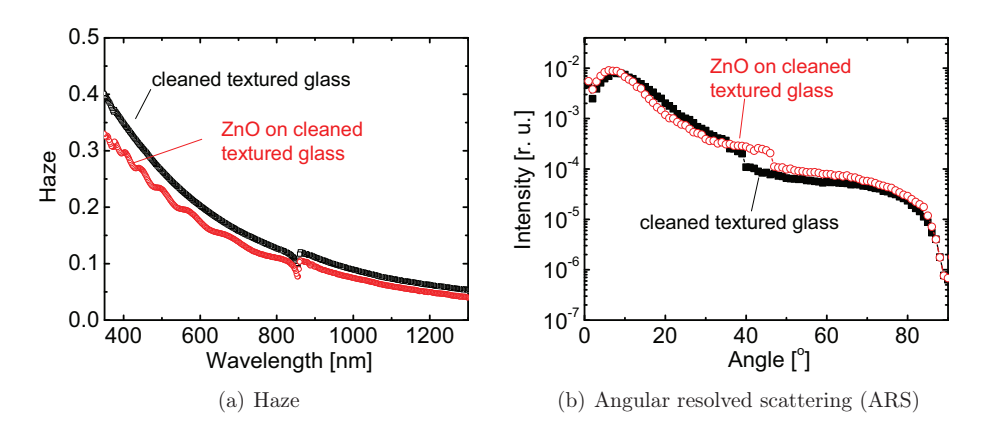


Figure 6.27: Haze (a) and ARS (b) of the Ar/O_2 treated textured glass (solid squares) and the ZnO:Al films grown on Ar/O_2 treated textured glass (open circles).

 α is slightly increased from 0.86 to 0.92. The change of above parameters indicate that the small features on the textured glass are smoothened after sputtering of ZnO:Al films.

Fig. 6.27 gives the haze and ARS measurements of the two samples, in which the textured glass is shown in full squares and the ZnO:Al film grown on the textured glass is shown in open circles. The ZnO:Al film has even slightly lower haze than the textured glass, which is expected from reduced rms roughness value. The ARS curves are almost the same. The scattered light has highest intensity around 7° and reduced intensity at large angle. The Haze and ARS measurements confirmed that the sputtered ZnO:Al films grown on textured glass show conformal growth. As a result, the ZnO:Al film might even be slightly smoother than textured glass.

6.5.4.4 Summary

The previous three sections presented the morphologies of ZnO:Al films sputtered on cleaned, Ar and Ar/O_2 treated textured glass. On a cleaned textured glass, the polycrystalline ZnO columns grow perpendicular to the substrate. The lateral feature size of ZnO:Al film is similar to the reference ZnO:Al on flat glass which is around 50 nm. As a result of the conformal growth, the ZnO:Al film exhibit similar morphology to the textured glass, thus similar rms roughness, lateral correlation length, and roughness exponent are observed. At the rim of the craters, due to the competing growth of grains with different directions, holes are present. On Ar or Ar/O_2 treated textured glass, the lateral feature size of ZnO:Al film is larger. Especially on Ar/O_2 treated textured glass, the lateral feature size of the ZnO:Al film is as large as 500 nm. Therefore, the ZnO:Al surfaces are composed of double textures: one is from the textured glass and the other is from their large grains. The double textures provide the ZnO:Al film at the short

wavelength range and more light is scattered into large angles. Therefore, the double textured ZnO:Al films might be favorable TCO layers in Si thin-film solar cells.

6.5.5 Solar cells

This section gives the solar cell results based on textured glass. Two series of solar cells were prepared to analyze the feasibility of incorporating textured glass in solar cells. In the first series, ZnO:Al films were prepared on differently treated textured glass, including cleaned textured glass, Ar and Ar/O_2 treated textured glass. The second series compares the textured glass prepared by ion beam etching of HCl etched ZnO:Al films with different HCl etching time.

6.5.5.1 Influence of the treatment on textured glass

This section examines the influence of different treatment on textured glass. Firstly the surface morphology and optical properties of three ZnO:Al films on differently treated textured glass are presented. The three textured glass were prepared with the same parameters, only the post treatments were different. Then the μ c-Si:H cells grown on the three substrates are investigated.

Three textured glass samples were co-prepared by Ar ion beam etching of 40 s HCl etched ZnO:Al film. Afterwards, one textured glass was treated by ${\rm Ar/O_2}$ ions and another one was cleaned. Standard ZnO:Al films were sputtered on the three textured glass. Therefore, the differences of the three ZnO:Al films were mainly caused by the different growth of ZnO:Al films. 1.1 μ m thick μ c-Si single junction solar cells were co-deposited by PECVD on the three ZnO:Al substrates. A 50 s HCl etched standard ZnO:Al film was added as reference. Back contacts of 700 nm Ag were deposited by thermal evaporation. The performance of the cells were characterized by J-V and QE measurements.

Fig. 6.28 shows the SEM micrographs of three different ZnO:Al substrates. From (a) to (c), they were grown on cleaned textured glass, Ar treated, and Ar/O_2 treated textured glass, respectively. The ZnO:Al film grown on cleaned textured glass still have

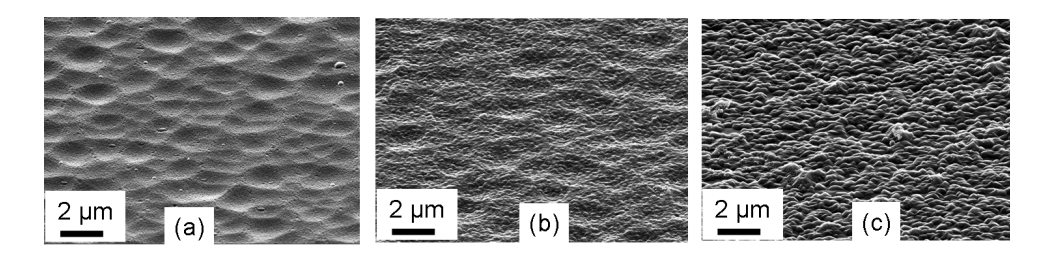


Figure 6.28: SEM micrographs of substrates for μ c-Si single junction solar cells: (a) ZnO:Al on cleaned textured glass, (b) ZnO:Al on Ar treated textured glass and (c) ZnO:Al on Ar/O₂ treated glass.

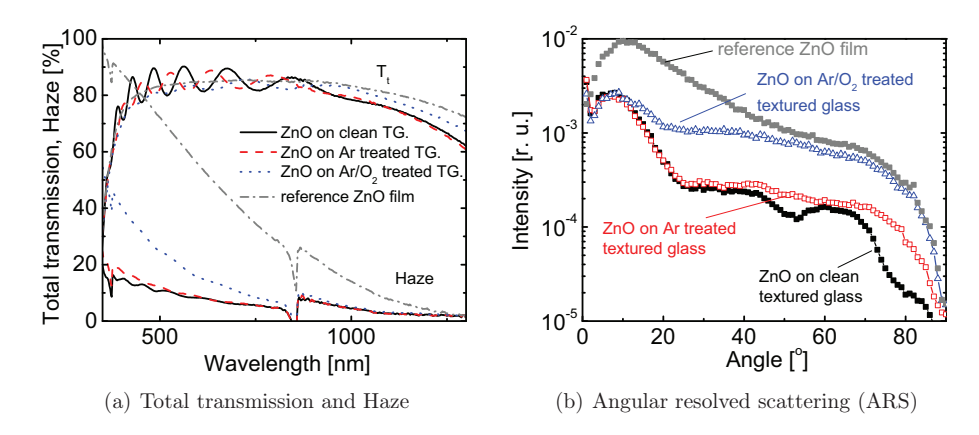


Figure 6.29: Total transmission, Haze (a) and ARS (b) of the ZnO:Al substrates grown on cleaned, Ar treated, Ar/O₂ treated textured glass and reference ZnO:Al substrate.

similar morphology to textured glass. The other two films exhibit obviously larger lateral feature size as compared with the first one, due to the textured growth of ZnO:Al films.

Fig. 6.29(a) presents total transmission (T_t) and haze of the four ZnO:Al substrates. T_t and haze of ZnO:Al films grown on cleaned, Ar and Ar/O₂ treated textured glass are shown with solid, dashed, and dotted curves, respectively. The HCl etched reference ZnO:Al film is shown by dash-dotted curve. It has the highest haze and T_t among these samples at the whole wavelength range. For the rest three samples, the film on Ar treated glass has slightly higher haze than the film on cleaned textured glass, while the film on Ar/O₂ treated glass has much higher haze at wavelength range of 350 – 800 nm. Therefore, it is concluded that due to the differences of feature size, the textured glass contribute more to light scattering at long wavelength, while the as-grown textured ZnO:Al film contribute more at short wavelength. T_t of the film grown on Ar/O₂ treated glass has higher value than the other two films, because it has lowest growth rate and accordingly lower thickness. The pronounced interference in the T_t of ZnO:Al films on cleaned and Ar treated textured glass suggest that the two films are quite smooth.

Fig. 6.29(b) shows the ARS curves of the ZnO:Al substrates. The films grown on cleaned, Ar treated, and Ar/O₂ treated textured glass are shown in full, open squares, and open triangles, respectively. The first two films have similar light scattering behavior. The ARS of the ZnO:Al film grown on Ar/O₂ treated textured glass represents the combination of textured glass and as-grown textured ZnO:Al film. Therefore, it has one scattering peak at 7°, and still preserve higher scattering intensities at $17-90^{\circ}$ as compared with the other two substrates. The reference ZnO:Al film is shown by gray squares, it has highest scattering light at all angles, but larger fractions of scattered light locates in small angle.

Table 6.2 and Fig. 6.30 give J-V and QE measurement results of $\mu c\text{-Si:H}$ cells

Table 6.2: The J-V results of μ c-Si single junction solar cells based on cleaned, Ar treated, Ar/O₂ treated textured glass, and reference ZnO:Al film.

ZnO:Al films	η	FF	V_{oc}	J_{sc}
	%	%	mV	$\mathrm{mA/cm^2}$
on cleaned textured glass	5.58	73	495	15.45
on Ar treated textured glass	5.65	72	489	16.05
on Ar/O ₂ treated textured glass	6.34	70	494	18.29
reference ZnO:Al film	6.73	72	505	18.38

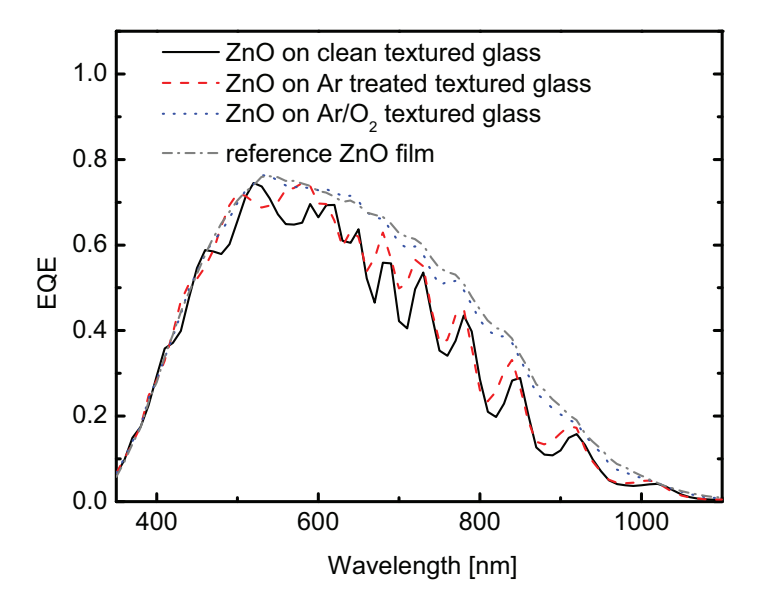


Figure 6.30: Quantum efficiency (QE) of μ c-Si single junction solar cells based on cleaned (solid curve), Ar treated (dashed curve), Ar/O₂ treated (dotted curve) textured glass and reference ZnO:Al film (dash-dotted curve).

grown on these substrates. In Fig. 6.30, the cells grown on cleaned, Ar treated, Ar/O₂ treated glass, and reference ZnO:Al film are shown by solid, dashed, dotted, and dash-dotted curves, respectively. Si solar cells grown on cleaned textured glass has lowest J_{sc} of 15.45 mA/cm². Its QE curve shows that the low current is due to poor light scattering at long wavelength range. The roughness of the textured glass is only around 52 nm which is quite low as compared to the HCl etched ZnO:Al film. The J_{sc} of the cell on ZnO:Al film grown on Ar treated textured glass is increased slightly to 16.05 mA/cm². From QE it is observed that the improvements can be attributed to the better light scattering at long wavelength region and better light incoupling at short wavelength region. However,

the interference at long wavelength range is large, due to the low roughness of 55 nm. The J_{sc} of the cell on ${\rm Ar/O_2}$ treated textured glass is the highest $18.29~{\rm mA/cm^2}$. The QE reflects that the light scattering and incoupling at whole wavelength range is much improved. The spectra response of cell grown on ${\rm Ar/O_2}$ treated textured glass is quite similar to reference cell at short wavelength region, while at long wavelength region the values are slightly reduced. As a result, the J_{sc} is $0.1~{\rm mA/cm^2}$ less than reference cell. Considering the lower haze of the ZnO:Al film on ${\rm Ar/O_2}$ treated textured glass, the good light scattering performance shall be provided by the improved angular resolved scattering.

FF and V_{oc} of the three cells are less influenced by the substrates. It seems that the FF decreases slightly when the ZnO:Al films are grown with self-texture. It might be caused by the slightly deteriorated electrical properties of as-grown textured ZnO:Al films or due to worse growth of μ c-Si on the textured ZnO:Al. Nevertheless, the cell grown on Ar/O_2 treated textured glass has much higher η , due to the improved light scattering properties. The cell grown on cleaned textured glass can not provide efficient light trapping effect to the solar cells, because of the lower roughness. If rough enough textured glass substrates were used for cells, together with the self-texture of ZnO:Al films on Ar/O_2 treated surface, the potential of further increasing of J_{sc} is high. Additionally, the double texture might be even better for tandem cells.

6.5.5.2 Influence of HCl etching time on textured glass

Last section has shown that the ZnO:Al films grown on Ar/O_2 treated textured glass exhibit double textures, which can provide enhanced light trapping for thin-film solar cells. In this section, μ c-Si single junction solar cells are deposited on Ar/O_2 treated different textured glass. As discussed in Section 6.5.2, the textured glass are prepared by ion beam etching of HCl etched ZnO:Al films. Depending on the initial thickness and HCl etching time of the ZnO:Al films, textured glass with different lateral size and roughness can be fabricated.

800 nm thick ZnO:Al films were etched in 0.5 % HCl solution for 50 s, 70 s, 90 s, 110 s, and 130 s. Ar ion beam etching was applied on the ZnO:Al films till the ZnO:Al material was totally removed. Ar/O₂ mixed ion beam treatments were performed on the five textured glass at the same time. Then standard ZnO:Al films were sputtered on the textured glass surfaces. Afterwards, 1.1 μ m thick μ c-Si single junction solar cells were co-deposited by PECVD on these substrates. Finally, back contacts of 700 nm Ag were deposited by thermal evaporation. The performance of the cells were characterized by J-V and QE measurements.

Fig. 6.31 shows the haze of the textured glass. The HCl etching time is denoted by the legends in the figure. It is shown that the haze first increases with the etching time till 110 s, and then decreases with further etching. This observation is in accordance to the trend of rms roughness versus HCl etching time in Fig. 6.14. The decrease of haze and roughness after long time HCl etching is related to the flat plateau at bottom. A ZnO:Al film grown on textured glass prepared from 130 s HCl etching is given in the figure, in order to show that the haze of ZnO:Al film is improved.

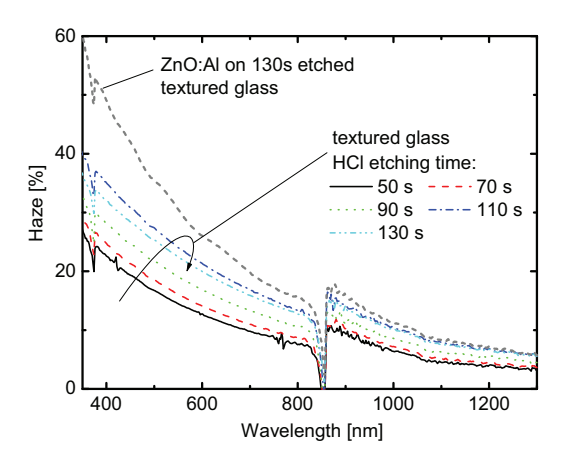


Figure 6.31: Haze of a series of textured glass which were prepared from different HCl etched ZnO:Al films. The HCl etching time are marked in the figure.

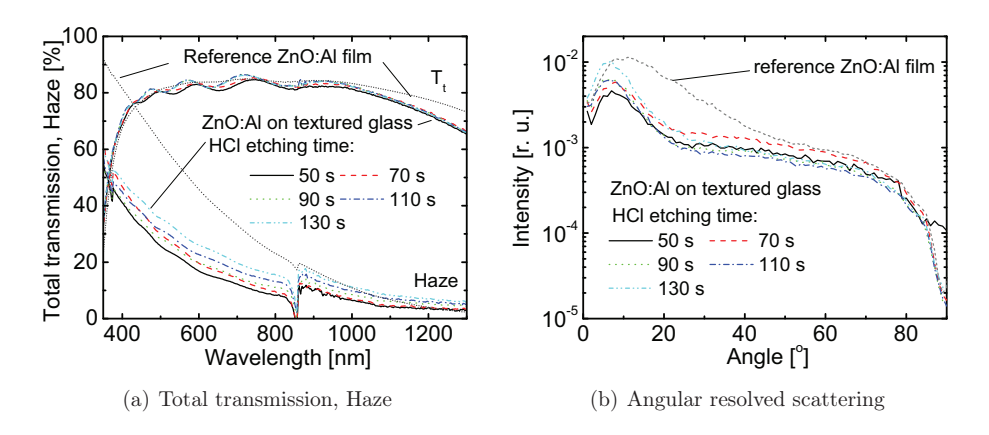


Figure 6.32: Haze (a) and ARS (b) of ZnO:Al films grown on the series of textured glass. The textured glass were prepared from different HCl etched ZnO:Al films. The HCl etching time are marked in the figure. A HCl etched standard ZnO:Al film is added as reference (small dot dark gray curve).

The total transmission, haze and ARS were measured on the ZnO:Al films and the results are given in Fig. 6.32. One 40 s HCl etched ZnO:Al film is added as reference and is shown in small gray dots. The other curves represent the ZnO:Al films grown on textured glass. The HCl etching time during the preparation of textured glass are denoted in the legend. Fig. 6.32(a) shows the haze of the ZnO:Al films. It is clearly visible that the reference ZnO:Al film has the highest haze and total transmission. Haze of the

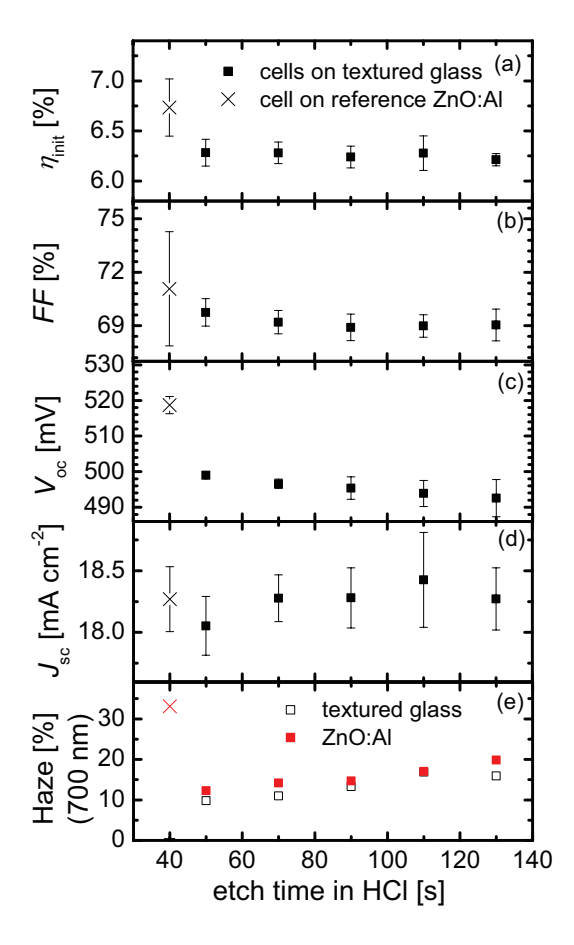


Figure 6.33: The results of μ c-Si single junction solar cells deposited on textured glass prepared from different HCl etching time of ZnO:Al films (full squares). Solar cell prepared on HCl textured standard ZnO:Al film is shown as reference (cross).

ZnO:Al films on textured glass vary in a small range and have higher values for films grown on textured glass made of ZnO:Al films with long time HCl etching. Compared with the textured glass, the ZnO:Al films have higher haze at whole wavelength range. However, the enhancement of Haze is more pronounced in short wavelength range than in long wavelength range, because the as-grown rough ZnO:Al film exhibit lateral feature size of 500 nm. ARS curves in Fig. 6.32(b) show that the intensity of total scattered light of ZnO:Al films on textured glass is not as high as reference ZnO:Al film. However, the fraction of light scattered into large angle is higher than that of reference ZnO:Al film.

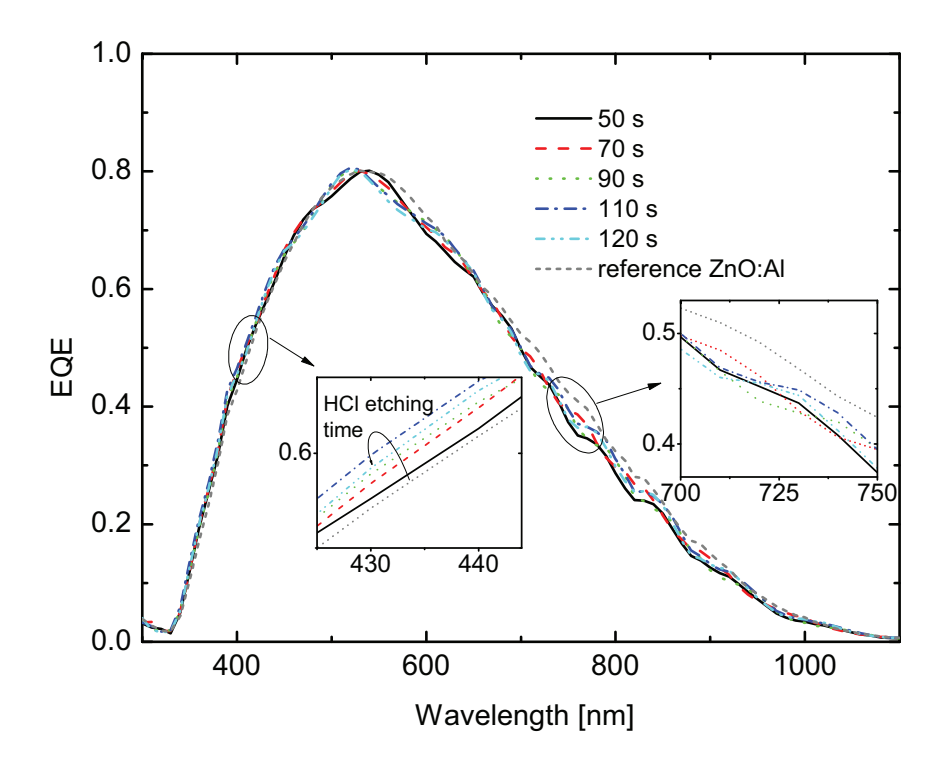


Figure 6.34: Quantum efficiency (QE) of μ c-Si single junction solar cells deposited on textured glass prepared from different HCl etching time of ZnO:Al films. Solar cell prepared on HCl textured standard ZnO:Al film is shown as reference (small dotted dark gray curve).

The J-V and QE measurement results of the solar cells are shown in Fig. 6.33(a-d) and Fig. 6.34, respectively. The cell results give as average value of 12 test cells on a $5 \times 10 \text{ cm}^2$ sample, while the QE was measured on the best cell. In Fig. 6.33, the reference cell grown on HCl etched reference ZnO:Al film is shown with the cross, and the other cells prepared on different textured glass are shown with full squares. The x-axis refers the HCl etching time of ZnO:Al films. In Fig. 6.34, the reference cells is given by dotted gray curve and the HCl etching time of other cells are denoted in the legend. V_{oc} and FF of the cells grown on textured glass are lower than the reference cell, while The differences in J_{sc} are not so obvious. The two insets in QE reveal that the cells on Ar/O₂ treated textured glass produce more current at short wavelength region, while the reference cell lead to more current at long wavelength range. At short wavelength region, the QE of cells on textured glass increases with increasing HCl etching time till 110 s, and then decrease with 130 s HCl etching. At long wavelength region, the spectra

response of cells on textured glass shows to trend with HCl etching time. The cell grown on textured glass which was prepared from a 110 s HCl etched ZnO:Al film has highest J_{sc} of 18.4 mA/cm². Lower V_{oc} and FF of the solar cells grown on textured glass were already discussed in section 5.1.4.2 and are related to the worse growth of Si on the pyramid structures.

In order to further analyze the J_{sc} , the haze of textured glass and ZnO:Al films at 700 nm are shown in Fig. 6.33(e) by open and solid squares, respectively. As discussed, the haze of textured glass increases with HCl etching time and reaches maximum at 110 s HCl etching. The trend of J_{sc} versus HCl etching time is very similar to the haze of textured glass. All ZnO:Al films exhibit higher haze than the corresponding textured glass, but the increment is different for each sample. The samples with 90 s and 110 s HCl etching present relatively less increase. As a result, the trend between J_{sc} and haze of ZnO:Al film is not the same. The haze of reference ZnO:Al film is also shown by cross. The reference ZnO:Al film give highest haze, but not highest J_{sc} . The different trends of haze with HCl etching time between textured glass and ZnO:Al films might be caused by measurement error or different growth of ZnO:Al films on the samples. The relation between J_{sc} and HCl etching time was also reported in [185]. A series of standard ZnO:Al films with different HCl etching time were used as back contact in n-i-p μ c-Si:H cells and the results showed that highest current density was obtained when the HCl etching time was 90 s. It indicates that the morphology of craters of standard ZnO:Al films can be further optimized by changing the HCl etching time. The morphology of textured glass can be adjusted with more possibility than front contact ZnO:Al films in p-i-n solar cells, since the thickness and electrical properties of TCO layers do not need to be considered. Furthermore, the as-grown rough ZnO:Al films are promising to provide more favorable angular resolved scattering behavior for solar cells.

6.6 Summary

This chapter has focused on the ion beam treatment of ZnO:Al films in the Si thin-film solar cells. Ion beam treatments of ZnO:Al films also have influence on the etching behavior, the growth of ZnO:Al films and Si films. Less HCl attack points were observed on ion beam treated ZnO:Al films. The reason was attributed to that the grain boundaries at the surface area become more compact by the redeposited ZnO material. ZnO:Al films develop larger grains on flat Ar/O_2 treated ZnO:Al films and additional flower structures on the crater walls on Ar/O_2 treated HCl textured ZnO:Al films. Si films exhibit lower crystallinity on ion beam treated ZnO:Al films, indicating that it is difficult for Si atoms to form crystallites on ion treated ZnO:Al films. These are probably related to the chemical modification of the ZnO:Al surfaces by the ion beam treatments. However, more measurements or experiments are required to identify the exact reasons.

The Ar ion beam treatments have a smoothening effect on HCl textured ZnO:Al films, since the top of craters are etched faster than the bottom of craters. If the HCl textured ZnO:Al films are considered as etching mask, dry etching leads to the production of textured glass. The motivation of textured glass in Si thin-film solar cells

was introduced by a simple optical calculation. The morphologies of textured glass can be adjusted by the etching masks. Therefore, by adjusting the initial thickness and HCl etching time, textured glass with a large variety of topographies were prepared. The application of textured glass in Si thin-film solar cells were presented with μc -Si solar cells. ZnO:Al films with double texture were realized by combining textured glass and as-grown textured ZnO:Al films on Ar/O₂ treated glass. The double texture has potential to provide better light scattering in solar cells.

7 Summary and Outlook

Ion beam treatment is typically used for dry etching, surface and growth modification in thin-film devices. The task of this work was to evaluate how ion beam treatment can be utilized in photovoltaics to improve silicon thin-film solar cells. This work proposed two novel techniques to produce as-sputtered rough ZnO:Al films and textured glass, which are used to provide light trapping effects in silicon layer. With the as-grown rough ZnO:Al films or textured glass, traditionally wet chemical etching of ZnO:Al films can be avoided, as well as the vacuum break. It means that the cooling and heating cycles and the vacuum equipment usage can be reduced, which are attractive for industry process. The as-grown rough ZnO:Al films are sputtered on ion beam pretreated glass surface, and the textured glass is prepared from ion beam etching of three dimensional etching mask.

As a foundation for further experimental works, the ion beam etching was characterized by etch rates in the first results chapter (Chapter 4). The etch rates of Ar and O_2 ions on glass substrates and ZnO:Al films were experimentally investigated and compared with theoretical values, estimated from ion source characteristics and TRIM simulations. Next, the ion beam treatments were applied to glass substrates and ZnO:Al films.

The growth of ZnO:Al films was significantly influenced by ion beam pretreatment of glass substrates. On ${\rm Ar/O_2}$ pretreated glass, ZnO:Al films develop pyramids at the surface with rms roughness of approximately 40 nm and lateral feature size of 500 nm. The as-grown rough features of ZnO:Al films on ${\rm Ar/O_2}$ treated glass substrates are caused by the additional conical grains in addition to the columnar grains grown on reference glass. Both types of grains start from the glass/ZnO interface. The conical grains grow faster than the columnar grains, leading to a rough surface dominated by pyramid structures. Amorphous, microcrystalline, and tandem silicon thin-film solar cells prepared on the rough ZnO:Al films show that this front contact can provide excellent light trapping effect. The highest initial efficiencies for amorphous single junction and amorphous microcrystalline silicon tandem solar cells on as-grown rough ZnO:Al films were 9.4 % and 11.9 %, respectively. Moreover, there might still be potential for improvement of light trapping by optimization of ZnO:Al growth by deposition conditions in combination with pretreated glass.

In order to understand the modified growth of as-grown rough ZnO:Al films, ion beam treatments were applied on other types of glass substrates and Si wafer, in an inverse sputter etcher, or the ZnO:Al films were deposited under different conditions. Similar conical growth of ZnO:Al grains with rough surfaces were observed. However, by cleaning of the ion beam treated glass substrates in acidic solutions for sufficient duration, the growth of ZnO:Al films returned to the usual case of columnar grains. It

was observed that the large conical grains exhibited quasi random orientation, while the c-axis of the small columnar grains was perpendicular to the substrates. Analysis of surface composition and bond structures of ion beam treated glass substrates revealed oxygen dangling bonds as source of modified growth and roughness of the ZnO:Al films. Additionally, epitaxial growth of polycrystalline ZnO:Al films on Zn- and O- polar ZnO single crystals were investigated. The ZnO:Al films grown on O-polar crystal show a slower growth rate and rougher surface than the films on Zn-polar crystal.

Based on these experimental studies, a growth model was proposed to explain the relationships among substrate surface, orientation of the ZnO:Al grains, and film surface structures. The c-axis aligned columnar grains in as-grown rough ZnO:Al films were supposed to exhibit (000-1) orientation, which might be caused by the excess O bonds on the ion beam treated glass surface. Random nucleation occurs at the sites where not terminated by O bonds. Thus, the randomly oriented conical grains overgrow the o-terminated columnar grains, since the (000-1) oriented grains have the lowest growth rate.

The next part of this work examined the ion beam treatments of ZnO:Al films. The initial points of attack by HCl etching decreased in ion beam treated ZnO:Al films. The reason was attributed to the compact grain boundaries at the surface area after ion beam treatment. It is conceivable that the effect lies only in the surface region. With long duration HCl etching, the etching behavior returned to usual case. The growth of ZnO:Al films on ion beam treated ZnO:Al films started with new nucleation center. Concerning the growth of Si films on ion beam treated ZnO:Al films, the crystalline fraction of the p-doped μ c-Si:H was reduced.

By prolonged ion beam treatment of HCl etched ZnO:Al films, the optimized ZnO:Al surface structure can be transferred to the textured glass. Cheaper materials, for example spin or spray coated nano-powders, can also be used as three-dimensional etching masks. The morphologies of textured glass can be adjusted in a large range by changing the thickness and shape of the etching mask.

More interestingly, textured glass provides the possibility of "double textures" by combining with as-grown rough ZnO:Al films. The μ c-Si:H solar cells prepared on Ar/O₂ treated textured glass have proved that the "double textures" can provide improved light trapping than textured glass. Moreover, the as-grown rough ZnO:Al films, textured glass, and double structures possess further potential for optimization, for example regarding the reproducibility, module incorporation, quality and cost aspects.

This work revealed new insights in the growth mechanisms of sputter deposited ZnO:Al films. The morphologies of sputtered ZnO:Al films can be controlled not only by the sputtering parameters, but also the substrate conditions. The new surface features of the textured glass and as-grown rough ZnO:Al films provide more opportunities to study the light trapping in solar cells.

Bibliography

- [1] J. Zhao, A. Wang, M. Green, and F. Ferrazza, "19.8% efficient honeycomb textured multicrystalline and 24.4% monocrystalline silicon solar cells," *Applied Physics Letters*, vol. 73, p. 1991, 1998.
- [2] M. Green, "Recent developments in photovoltaics," Solar energy, vol. 76, p. 3, 2004.
- [3] J. Yang, A. Banerjee, and S. Guha, "Triple-junction amorphous silicon alloy solar cell with 14.6% initial and 13.0% stable conversion efficiencies," *Applied Physics Letters*, vol. 70, p. 2975, 1997.
- [4] C. Wronski, B. Von Roedern, and A. Kolodziej, "Thin-film Si: H-based solar cells," Vacuum, vol. 82, p. 1145, 2008.
- [5] J. Hüpkes, B. Rech, S. Calnan, O. Kluth, U. Zastrow, H. Siekmann, and M. Wuttig, "Material study on reactively sputtered zinc oxide for thin film silicon solar cells," *Thin Solid Films*, vol. 502, p. 286, 2006.
- [6] H. Zhu, J. Hüpkes, E. Bunte, and S. Huang, "High rate reactive magnetron sputtering of ZnO:Al films from rotating metallic targets," Surface and Coatings Technology, vol. 205, p. 773, 2010.
- [7] D. Dominé, P. Buehlmann, J. Bailat, A. Feltrin, and C. Ballif, "High-efficiencz micromorph silicon solar cells with in-situ intermediate reflector deposited on various rough LPCVD ZnO," in 23rd Europen Photovoltaic Solar Energy Conference, Valencia, Spain, 2008.
- [8] I. Volintiru, M. Creatore, B. J. Kniknie, C. I. M. a. Spee, and M. C. M. van de Sanden, "Evolution of the electrical and structural properties during the growth of Al doped ZnO films by remote plasma-enhanced metalorganic chemical vapor deposition," *Journal of Applied Physics*, vol. 102, p. 043709, 2007.
- [9] T. Minami, H. Sato, S. Takata, N. Ogawa, and T. Mouri, "Large-area milky transparent conducting Al-doped ZnO films prepared by magnetron sputtering," *Japanese Journal of Applied Physics*, vol. 31, p. 1106, 1992.
- [10] T. Nakada, Y. Ohkubo, and A. Kunioka, "Effect of water vapor on the growth of textured ZnO-based films for solar cells by DC-magnetron sputtering," *Japanese Journal of Applied Physics*, vol. 30, p. 3344, 1991.

- [11] H. Sato, T. Minami, S. Takata, T. Mouri, and N. Ogawa, "Highly conductive and transparent ZnO:Al thin films prepared on high-temperature substrates by d.c. magnetron sputtering," *Thin Solid Films*, vol. 220, p. 327, 1992.
- [12] H. Sato, T. Minami, Y. Tamura, S. Takata, T. Mouri, and N. Ogawa, "Aluminium content dependence of milky transparent conducting ZnO:Al films with textured surface prepared by d.c. magnetron sputtering," *Thin Solid Films*, vol. 246, p. 86, 1994.
- [13] J. Selvan, H. Keppner, and A. Shah, "The Growth of Surface Textured Aluminum Doped ZnO Films for a-Si Solar Cells by RF Magnetron Sputtering at Low Temperature," *Materials research society symposium*, vol. 426, p. 497, 1996.
- [14] O. Kluth, Präparation und Charakterisierung von texturierten Metalloxid-Schichten für Dünnschichtsolarzellen. Diplomarbeit, Rheinisch-Westfälische Technische Hochschule Aachen, 1996.
- [15] U. Blieske, T. Doege, P. Gayout, M. Neander, D. Neumann, and A. Prat, "Light-trapping in solar modules using extra-white textured glass," in *Proceedings of 3rd World Conference on Photovoltaic Energy Conversion*, vol. 1, p. 188, IEEE, 2003.
- [16] P. I. Widenborg and A. G. Aberle, "Polycrystalline Silicon Thin-Film Solar Cells on AIT-Textured Glass Superstrates," Advances in OptoElectronics, vol. 2007, p. 1, 2007.
- [17] O. Isabella, F. Moll, J. Krč, and M. Zeman, "Modulated surface textures using zinc-oxide films for solar cells applications," *physica status solidi* (a), vol. 207, p. 642, 2010.
- [18] J. J. Cuomo, S. M. Rossnagel, and H. R. Kaufman, eds., *Handbook of Ion Beam Processing Technology: Principles, Deposition, Film Modification, and Synthesis*, vol. 112. William Andrew Publishing, 1989.
- [19] R. Reuschling and E. Schultheiss, "Ion Sources for Vacuum Thin Film Technology," *Vakuum in Forschung und Praxis*, vol. 18, p. 46, 2006.
- [20] V. V. Zhurin, H. R. Kaufman, and R. S. Robinson, "Physics of closed drift thrusters," *Plasma Sources Science and Technology*, vol. 8, p. R1, 1999.
- [21] A. Shabalin, M. Amann, M. Kishinevsky, K. Nauman, and C. Quinn, "Industrial ion sources and their application for dlc coating," in SVC 42nd Annual Technical Conference, 1999.
- [22] F. Chen and J. Chang, Lecture notes on principles of plasma processing. Springer, 2003.

- [23] E. Krishnakumar and S. Srivastava, "Cross-sections for electron impact ionization of O2," *International journal of mass spectrometry and ion processes*, vol. 113, p. 1, 1992.
- [24] N. R. Daly and R. E. Powell, "Electron collisions in oxygen," Proceedings of the Physical Society, vol. 90, p. 629, 1967.
- [25] J. Pavlik and R. Hrach, "Study of argon/oxygen plasma used for creation of aluminium oxide thin films," Superficies y Vacio, vol. 9, p. 131, 1999.
- [26] Y.-K. Kim and J.-P. Desclaux, "Ionization of carbon, nitrogen, and oxygen by electron impact," *Physical Review A*, vol. 66, 2002.
- [27] W. Hwang, Y.-K. Kim, and M. E. Rudd, "New model for electron-impact ionization cross sections of molecules," *The Journal of Chemical Physics*, vol. 104, p. 2956, 1996.
- [28] H. Straub, P. Renault, B. Lindsay, K. Smith, and R. Stebbings, "Absolute partial cross sections for electron-impact ionization of H2, N2, and O2 from threshold to 1000 eV.," *Physical Review. A*, vol. 54, p. 2146, 1996.
- [29] I. Toth, R. I. Campeanu, V. Chis, and L. Nagy, "Electron impact ionization of diatomic molecules," The European Physical Journal D, vol. 48, p. 351, 2008.
- [30] "Betriebsanleitung Ionenquelle LION 420," tech. rep., VON ARDENNE Anlagentechnik GmbH, 2007.
- [31] A. Anders, "Plasma and ion sources in large area coating: A review," Surface and Coatings Technology, vol. 200, p. 1893, 2005.
- [32] A. Shabalin, M. Amann, M. Kishinevsky, C. Quinn, and N. Capps, "Characterization of the Low-Voltage, High-Current Single-Cell Ion Source," *Most*, p. 283, 2000.
- [33] "Round and Linear Ion Beam Sources brochure," tech. rep., Advanced Energy.
- [34] H. Gnaser, Low Energy Ion Irradiation of soild surfaces. Springer, 1999.
- [35] P. Sigmund, Stopping of Heavy Ions. Springer, 2004.
- [36] R. M. Bradley, "Theory of ripple topography induced by ion bombardment," 1988.
- [37] A. Keller, S. Facsko, and W. Möller, "Evolution of ion-induced ripple patterns on SiO2 surfaces," *Nuclear Instruments and Methods in Physics Research Section B: Beam Interactions with Materials and Atoms*, vol. 267, p. 656, 2009.
- [38] W. Mickelson, S. Aloni, W.-Q. Han, J. Cumings, and A. Zettl, "Packing C60 in boron nitride nanotubes," *Science*, vol. 300, p. 467, 2003.

- [39] P. Sigmund, "Theory of Sputtering. I. Sputtering Yield of Amorphous and Polycrystalline Targets," *Physical Review*, vol. 184, p. 383, 1969.
- [40] P. Sigmund, "Theory of sputtering. I. Sputtering yield of amorphous and polycrystalline targets. Erratum," *Physical Review*, vol. 187, p. 768, 1969.
- [41] P. C. Zalm, "Quantitative sputtering," Surface and Interface Analysis, vol. 11, p. 1, 1988.
- [42] W. Wilson, L. Haggmark, and J. Biersack, "Calculations of nuclear stopping, ranges, and straggling in the low-energy region," *Physical Review B*, vol. 15, p. 2458, 1977.
- [43] P. Zalm, "Some useful yield estimates for ion beam sputtering and ion plating at low bombarding energies," J. Vac. Sci. Technol. B, vol. 2, p. 151, 1984.
- [44] H. Bay and J. Bohdansky, "Sputtering yields for light ions as a function of angle of incidence," *Applied Physics A: Materials Science & Processing*, vol. 19, p. 421, 1979.
- [45] H. Oechsner, "Untersuchungen zur Festkörperzerstäubung bei schiefwinkligem Ionenbeschußpolykristalliner Metalloberflächen im Energiebereich um 1 keV," Zeitschrift für Physik A: Hadrons and Nuclei, vol. 261, p. 37, 1973.
- [46] H. Oechsner, "Applied Physics sputtermg a Review of Some Recent Experimental and Theoretical Aspects," Applied Physics A: Materials Science & Processing, vol. 8, p. 185, 1975.
- [47] S. Johar and D. Thompson, "Spike effects in heavy-ion sputtering of Ag, Au and Pt thin films," *Surface Science*, vol. 90, p. 319, 1979.
- [48] D. Thompson and S. Johar, "Sputtering of silver by heavy atomic and molecular ion bombardment," *Nuclear Instruments and Methods*, vol. 170, p. 281, 1980.
- [49] K. Kim, W. Baitinger, J. Amy, and N. Winograd, "ESCA studies of metal-oxygen surfaces using argon and oxygen ion-bombardment," *Journal of Electron Spec*troscopy and Related Phenomena, vol. 5, p. 351, 1974.
- [50] J. Malherbe, S. Hofmann, and J. Sanz, "Preferential sputtering of oxides: A comparison of model predictions with experimental data," *Applied surface science*, vol. 27, p. 355, 1986.
- [51] D. F. Mitchell, G. I. Sproule, and M. J. Graham, "Sputter reduction of oxides by ion bombardment during Auger depth profile analysis," *Surface and Interface Analysis*, vol. 15, p. 487, 1990.
- [52] I. Bertóti, R. Kelly, M. Mohai, and A. Tóth, "A possible solution to the problem of compositional change with ion-bombarded oxides," *Surface and interface analysis*, vol. 19, p. 291, 1992.

- [53] I. Bertóti, R. Kelly, M. Mohai, and A. Tóth, "Response of oxides to ion bombard-ment: the difference between inert and reactive ions," Nuclear Instruments and Methods in Physics Research Section B: Beam Interactions with Materials and Atoms, vol. 80-81, p. 1219, 1993.
- [54] A. Sulyok, M. Menyhard, and J. Malherbe, "Stability of ZnO{0001} against low energy ion bombardment," Surface Science, vol. 601, p. 1857, 2007.
- [55] U. Özgür, Y. Alivov, C. Liu, A. Teke, M. Reshchikov, S. Dogan, V. Avrutin, S.-J. Cho, and H. Morkoc, "A comprehensive review of ZnO materials and devices," Journal of Applied Physics, vol. 98, 2005.
- [56] F. Decremps, J. Zhang, and R. Liebermann, "New phase boundary and high-pressure thermoelasticity of ZnO," *Europhysics Letters*, vol. 51, p. 268, 2000.
- [57] K. Ellmer, A. Klein, and B. Rech, eds., Transparent Conductive Zinc Oxide Basics and Applications in Thin Film Solar Cells. Springer, 2008.
- [58] K. Ellmer, "Resistivity of polycrystalline zinc oxide films: current status and physical limit," *Journal of Physics D: Applied Physics*, vol. 34, p. 3097, 2001.
- [59] D. Look, J. Hemsky, and J. Sizelove, "Residual native shallow donor in ZnO," Physical Review Letters, vol. 82, p. 2552, 1999.
- [60] G. Tomlins, J. Routbort, and T. Mason, "Zinc self-diffusion, electrical properties, and defect structure of undoped, single crystal zinc oxide," *Journal of Applied Physics*, vol. 87, p. 117, 2000.
- [61] W. Baer, "Faraday rotation in ZnO: Determination of the electron effective mass," Physical Review, vol. 154, p. 785, 1967.
- [62] B. Utsch and A. Hausmann, "Hall-effect and conductivity measurements of Zinc-Oxide single-crystals with oxygen vacancies as donors," *Zeitschrift für Physik B Condensed Matter*, vol. 21, p. 27, 1975.
- [63] D. Look, D. Reynolds, J. Sizelove, R. Jones, C. Litton, G. Cantwell, and W. Harsch, "Electrical properties of bulk ZnO," Solid state communications, vol. 105, p. 399, 1998.
- [64] E. Ziegler, A. Heinrich, H. Oppermann, and G. Stöver, "Electrical properties and non-stoichiometry in ZnO single crystals," physica status solidi (a), vol. 66, p. 635, 1981.
- [65] I. Kobiakov, "Elastic, piezoelectric and dielectric properties of ZnO and CdS single crystals in a wide range of temperatures," Solid State Communications, vol. 35, p. 305, 1980.

- [66] F. Blom, F. Van de Pol, G. Bauhuis, and T. Popma, "RF planar magnetron sputtered ZnO films II: Electrical properties," *Thin Solid Films*, vol. 204, p. 365, 1991.
- [67] H. Rupprecht, "Über Konzentration und Electronen in Zinkoxydeinkristallen mit Definierten Zusatzen," Journal of Physics and Chemistry of Solids, vol. 6, p. 144, 1958.
- [68] J. Hüpkes, Untersuchung des reaktiven Sputterprozesses zur Herstellung von aluminiumdotierten Zinkoxid- Schichten für Silizium-Dünnschichtsolarzellen. Dissertation, Rheinisch-Westfälische Technische Hochschule Aachen, 2005.
- [69] S. Mahieu, Biaxial alignment in sputter deposited thin films. Dissertation, Universiteit Gent, 2006.
- [70] D. Köhl, The influence of energetic bombardment on the structure formation of sputtered zinc oxide films - Development of an atomistic growth model and its application to tailor thin film properties. Dissertation, Rheinisch-Westfälische Technische Hochschule Aachen, 2011.
- [71] Y. Kajikawa, "Texture development of non-epitaxial polycrystalline ZnO films," Journal of Crystal Growth, vol. 289, p. 387, 2006.
- [72] N. Fujimura, "Control of preferred orientation for ZnOx films: control of self-texture," *Journal of Crystal Growth*, vol. 130, p. 269, 1993.
- [73] A. Wander and A. Harrison, "An ab-initio study of ZnO(11-20)," Surface Science, vol. 468, p. L851, 2000.
- [74] A. Wander, F. Schedin, P. Steadman, A. Norris, R. McGrath, T. Turner, G. Thornton, and N. Harrison, "Stability of Polar Oxide Surfaces," *Physical Review Letters*, vol. 86, p. 3811, 2001.
- [75] Y. Yoshino, S. Iwasa, Y. DeGuchi, Y. Yamamoto, and K. Ohwada, "Transmission electron microscopy study of interface microstructure in ZnO thin films grown on various substrates.pdf," Mat. Res. Soc. Symp. Proc., vol. 441, p. 241, 1997.
- [76] Y. Yoshino, "Effect of substrate surface morphology and interface microstructure in ZnO thin films formed on various substrates," *Vacuum*, vol. 59, p. 403, 2000.
- [77] J. Venables, G. Spiller, and M. Hanbucken, "Nucleation and growth of thin films," Reports on Progress in Physics, vol. 47, p. 399, 1984.
- [78] J. Thornton, "Influence of apparatus geometry and deposition conditions on the structure and topography of thick sputtered coatings," *Journal of vacuum Science* and *Technology*, vol. 11, p. 666, 1974.

- [79] J. Thornton, "High Rate Thick Film Growth," Annual Review of Materials Science, vol. 7, p. 239, 1977.
- [80] O. Kluth, "Modified Thornton model for magnetron sputtered zinc oxide: film structure and etching behaviour," *Thin Solid Films*, vol. 442, p. 80, 2003.
- [81] J. A. Thornton, "The microstructure of sputter-deposited coatings," Journal of Vacuum Science & Technology A: Vacuum, Surfaces, and Films, vol. 4, p. 3059, 1986.
- [82] G. Jost, E. Bunte, J. Worbs, H. Siekmann, and J. Hüpkes, "Surface Characterization of sputtered ZnO:Al for silicon thin-film solar cells," in 25th European Photovoltaic Solar Energy Conference and Exhibition, 2010.
- [83] S. Nicolay, S. Faÿ, and C. Ballif, "Growth Model of MOCVD Polycrystalline ZnO," Crystal Growth & Design, vol. 9, p. 4957, 2009.
- [84] S. Faÿ, J. Steinhauser, N. Oliveira, E. Vallatsauvain, and C. Ballif, "Opto-electronic properties of rough LP-CVD ZnO:B for use as TCO in thin-film silicon solar cells," *Thin Solid Films*, vol. 515, p. 8558, 2007.
- [85] R. Groenen, J. Löffler, P. Sommeling, J. Linden, E. Hamers, R. Schropp, and M. Van DE Sanden, "Surface textured ZnO films for thin film solar cell applications by expanding thermal plasma CVD," *Thin Solid Films*, vol. 392, p. 226, 2001.
- [86] S. Krantz, Einfluss von Stickstoff auf die reaktive Sputterdeposition von aluminiumdotierten Zinkoxidschichten. Diplomarbeit, Rheinisch-Westfälische Technische Hochschule Aachen, 2007.
- [87] M. Pelliccione and T.-M. Lu, Evolution of Thin Film Morphology, modeling and simulations. Springer, 2008.
- [88] A.-L. Barabasi and H. Stanley, Fractal concepts in surface growth, vol. 83. Cambridge University Press, 1995.
- [89] B. C. Mohanty, H.-R. Choi, and Y. S. Cho, "Scaling of surface roughness in sputter-deposited ZnO:Al thin films," *Journal of Applied Physics*, vol. 106, p. 1, 2009.
- [90] B. C. Mohanty, H.-R. Choi, and Y. S. Cho, "Fluctuations in global surface scaling behavior in sputter-deposited ZnO thin films," *Europhysics Letters*, vol. 93, p. 26003, 2011.
- [91] M. A. Auger, L. Vázquez, R. Cuerno, M. Castro, M. Jergel, and O. Sánchez, "Intrinsic anomalous surface roughening of TiN films deposited by reactive sputtering," *Physical Review B*, vol. 73, p. 1, 2006.
- [92] M. A. Auger, L. Vázquez, O. Sánchez, M. Jergel, R. Cuerno, and M. Castro, "Growth dynamics of reactive-sputtering-deposited AlN films," *Journal of Applied Physics*, vol. 97, p. 123528, 2005.

- [93] M. Pelliccione, T. Karabacak, and T.-M. Lu, "Breakdown of Dynamic Scaling in Surface Growth under Shadowing," *Physical Review Letters*, vol. 96, p. 1, 2006.
- [94] J. Yao and H. Guo, "Shadowing instability in three dimensions," *Physical Review E*, vol. 47, p. 1007, 1993.
- [95] T. Lu, Y. Zhao, J. Drotar, T. Karabacak, and G. Wang, "Novel Mechanisms on the Growth Morphology of Films," *Materials Research Society Symposium Proceedings*, vol. 749, p. 3, 2003.
- [96] H. Yang, Y. Zhao, G. Wang, and T. Lu, "Noise-induced roughening evolution of amorphous Si films grown by thermal evaporation.," *Physical Review Letters*, vol. 76, p. 3774, 1996.
- [97] J. Jeffries, J. Zuo, and M. Craig, "Instability of Kinetic Roughening in Sputter-Deposition Growth of Pt on Glass.," *Physical Review Letters*, vol. 76, p. 4931, 1996.
- [98] H. Huang, C. H. Woo, H. L. Wei, and X. X. Zhang, "Kinetics-limited surface structures at the nanoscale," *Applied Physics Letters*, vol. 82, p. 1272, 2003.
- [99] E. Vasco, C. Zaldo, and L. Vázquez, "Growth evolution of ZnO films deposited by pulsed laser ablation," *Journal of Physics: Condensed Matter*, vol. 13, p. L663, 2001.
- [100] F. Ruske, V. Sittinger, W. Werner, B. Szyszka, and R. Wiese, "Flux of Positive Ions and Film Growth in Reactive Sputtering of Al-Doped ZnO Thin Films," *Plasma Processes and Polymers*, vol. 4, p. S336, 2007.
- [101] D. Staebler and C. Wronski, "Reversible conductivity changes in discharge-produced amorphous Si," Applied Physics Letters, vol. 31, p. 292, 1977.
- [102] R. A. Street, Hydrogenated Amorphous Silicon. Cambridge University Press, 1991.
- [103] K. Jun, R. Carius, and H. Stiebig, "Optical characteristics of intrinsic microcrystalline silicon," *Physical Review B*, vol. 66, p. 115301, 2002.
- [104] R. E. I. Schropp and M. Zeman, Amorphous and microcrystalline silicon solar cells: modelling, material and device technology. Springer, 1998.
- [105] H. Zhu, E. Bunte, J. Hüpkes, H. Siekmann, and S. Huang, "Aluminium doped zinc oxide sputtered from rotatable dual magnetrons for thin film silicon solar cells," *Thin Solid Films*, vol. 517, p. 3161, 2009.
- [106] H. Zhu, J. Hüpkes, E. Bunte, and S. Huang, "Oxygen influence on sputtered high rate ZnO:Al films from dual rotatable ceramic targets," *Applied Surface Science*, vol. 256, p. 4601, 2010.

- [107] O. Kluth, Texturierte Zinkoxidschichten Für Silizium-Dünnschichtsolarzellen. Dissertation, Rheinisch-Westfälische Technische Hochschule Aachen, 2001.
- [108] T. Repmann, Stapelsolarzellen Aus Amorphem Und Mikrokristallinem Silizium. Dissertation, Rheinisch-Westfälische Technische Hochschule Aachen, 2003.
- [109] W. Zhang, Ion beam treatment of ZnO films for silicon thin film solar cells. Master thesis, Carl von Ossietzky University Oldenburg, 2008.
- [110] Surface Imaging Systems, "Ultra Objective SIScan panel user guide." 2008.
- [111] D. B. Williams and C. B. Carter, Transmission electron microscopy A Textbook for Materials Science, vol. 2. 2008.
- [112] D. A. Shirley, "High-resolution x-ray photoemission spectrum of the valence bands of gold," *Physical Review B*, vol. 5, p. 4709, 1972.
- [113] J. H. Scofield, "Hartree-slater subshell photoionization cross-sections at 1254 and 1487 ev," *Journal of Electron Spectroscopy and Related Phenomena*, vol. 8, p. 129, 1976.
- [114] W. M. Haynes, ed., CRC Handbook of Chemistry and Physics. CRC Press, 91st editi ed., 1993.
- [115] H. Naguib and R. Kelly, "Criteria for bombardment-induced structureal changes in non-metallic solids," *Radiation Effects and Defects in Solids*, vol. 25, p. 1, 1975.
- [116] W. Möller and M. Posseöt, "TRIDYN FZR User Manual, FZR Report No 317," tech. rep., Forschungszentrum Rossendorf, Dresden, 2001.
- [117] P. W. May, G. Pineau des Forêts, D. R. Flower, D. Field, N. L. Allan, and J. a. Purton, "Sputtering of grains in C-type shocks," Monthly Notices of the Royal Astronomical Society, vol. 318, p. 809, 2000.
- [118] G. Aylward and T. Findly, SI chemical data. John Wiley & Sons Australasia Ltd., 1974.
- [119] M. Chase, C. Davies, J. Downey, D. Frurip, R. McDonald, and A. Syverud, "NIST JANAF THERMOCHEMICAL TABLES," 1985.
- [120] J. Ziegler, The Stopping and Range of Ions in Matter. 2009.
- [121] J. Krč, M. Zeman, F. Smole, and M. Topič, "Optical modeling of a-Si:H solar cells deposited on textured glass/SnO[sub 2] substrates," *Journal of Applied Physics*, vol. 92, p. 749, 2002.
- [122] J. Krc, M. Zeman, O. Kluth, and F. Smole, "Light scattering properties of SnO2 and ZnO surface-textured substrates," in *Photovoltaic Energy Conversion*, 2003. Proceedings of 3rd World Conference on, vol. 2, p. 1823, IEEE, 2003.

- [123] H. Stiebig, T. Brammer, O. Kluth, N. Senoussaoui, A. Lamberty, and H. Wagner, "Light scattering in Micro crystalline silicon thin film solar cells," in 16th Europen Photovoltaic Solar Energy Conference, Glasgow, 2000.
- [124] H. Stiebig, M. Schulte, C. Zahren, C. Haase, B. Rech, and P. Lechner, "Light trapping in thin-film silicon solar cells by nano-textured interfaces," in *Proceedings* of SPIE, vol. 6197, p. 619701, 2006.
- [125] F. Ruske, M. Roczen, K. Lee, M. Wimmer, S. Gall, J. Hüpkes, D. Hrunski, and B. Rech, "Improved electrical transport in Al-doped zinc oxide by thermal treatment," *Journal of Applied Physics*, vol. 107, p. 013708, 2010.
- [126] M. Berginski, Lichtstreuende Oberflächen, Schichten und Schichtsysteme zur Verbesserung der Lichteinkopplung in Silizium - Dünnschichtsolarzellen. Dissertation, Rheinisch-Westfälische Technische Hochschule Aachen, 2008.
- [127] J. I. Owen, Growth, Etching, and Stability of Sputtered ZnO:Al for Thin-Film Silicon Solar Cells. Dissertation, Rheinisch-Westfälische Technische Hochschule Aachen, 2011.
- [128] M. Wimmer, F. Ruske, S. Scherf, and B. Rech, "Improving the electrical properties of DC-sputtered ZnO:Al by thermal post deposition treatment," in 8th international conference on coating on glass and plastics, Braunschweig, Germany, p. 445, 2010.
- [129] M. Wimmer, F. Ruske, S. Scherf, and B. Rech, "Improving the electrical and optical properties of DC-sputtered ZnO: Al by thermal post deposition treatments," Thin Solid Films, 2011.
- [130] M. Schulte, S. Jorke, C. Zahren, J. Hüpkes, and H. Stiebig, "Analysis of the Scattering Properties of Textured TCO Structures for Thin Film Silicon Solar Cells," in 22nd Europen Photovoltaic Solar Energy Conference, Milan, Italy, p. 2190, 2007.
- [131] P. Lechner, R. Geyer, H. Schade, B. Rech, O. Kluth, and H. Stiebig, "Optical TCO properties and Quantum Efficiencies in thin-film silicon solar cells," 19th Europen Photovoltaic Solar Energy Conference, p. 1591, 2004.
- [132] W. Dewald, V. Sittinger, B. Szyszka, A. Gordijn, J. Hüpkes, F. Hamelmann, H. Stiebig, and F. Säuberlich, "Angular resolved light scattering of structured TCOs for the application in a-Si:H/uc-Si:H solar cells," in 8th international conference on coating on glass and plastics, Braunschweig, Germany, p. 415, 2010.
- [133] J. T. Wätjen, Zinc Oxide Silver Back Reflectors in Microcrystalline Silicon Thin Film Solar Cells. mastersthesis, der Rheinisch-Westfälischen Technischen Hochschule Aachen, 2008.

- [134] H. Sai, H. Fujiwara, M. Kondo, and Y. Kanamori, "Enhancement of light trapping in thin-film hydrogenated microcrystalline Si solar cells using back reflectors with self-ordered dimple pattern," Applied Physics Letters, vol. 93, p. 143501, 2008.
- [135] Y. Nasuno, M. Kondo, and A. Matsuda, "Microcrystalline silicon thin-film solar cells prepared at low temperature using PECVD," Solar Energy Materials and Solar Cells, vol. 74, p. 497, 2002.
- [136] L. Feitknecht, J. Steinhauser, R. Schlüchter, S. Faÿ, D. Dominé, E. Vallat-sauvain, F. Meillaud, C. Ballif, and A. Shah, "Investigations on fill-factor drop of microcrystalline silicon PIN solar cells deposited onto highly surface-textured ZnO substrates," in 15th International Photovoltaic Science and Engineering Conference, Shanghai, China, p. 473, 2005.
- [137] M. Python, E. Vallatsauvain, J. Bailat, D. Domine, L. Fesquet, a. Shah, and C. Ballif, "Relation between substrate surface morphology and microcrystalline silicon solar cell performance," *Journal of Non-Crystalline Solids*, vol. 354, p. 2258, 2008.
- [138] O. Kappertz, R. Drese, and M. Wuttig, "Correlation between structure, stress and deposition parameters in direct current sputtered zinc oxide films," *Journal of Vacuum Science & Technology A: Vacuum, Surfaces, and Films*, vol. 20, p. 2084, 2002.
- [139] D. Köhl, M. Luysberg, and M. Wuttig, "Highly textured zinc oxide films by room temperature ion beam assisted deposition," physica status solidi (RRL) Rapid Research Letters, vol. 3, p. 236, 2009.
- [140] Image Metrology, "Particle & Pore Analysis, Tutorials of the Scanning Probe Image Processor."
- [141] G. Palasantzas and J. Krim, "Scanning tunneling microscopy study of the thick film limit of kinetic roughening," *Physical Review Letters*, vol. 73, p. 3564, 1994.
- [142] F. Family and T. Vicsek, "Scaling of the active zone in the Eden process on percolation networks and the ballistic deposition model," *Journal of Physics A: Mathematical and General*, vol. 18, p. L75, 1985.
- [143] R. Cuerno and L. Vázquez, "Universality issues in surface kinetic roughtening of thin solid films," in *Advance in Condensed Matter and Statistical Physics* (E. Korutcheva and L. Vázquez, eds.), p. 237, NY: Nova Science, 2004.
- [144] J. Ramasco, J. López, and M. Rodríguez, "Generic Dynamic Scaling in Kinetic Roughening," *Physical Review Letters*, vol. 84, p. 2199, 2000.
- [145] J. López, M. Rodríguez, and R. Cuerno, "Superroughening versus intrinsic anomalous scaling of surfaces," *Physical Review E*, vol. 56, p. 3993, 1997.

- [146] W. Tong, E. Snyder, R. Williams, A. Yanase, Y. Segawa, and M. Anderson, "Atomic force microscope studies of CuCl island formation on CaF2 (111) substrates," Surface Science, vol. 277, p. L63, 1992.
- [147] Y. Kajikawa, S. Noda, and H. Komiyama, "Comprehensive perspective on the mechanism of preferred orientation in reactive-sputter-deposited nitrides," *Journal of Vacuum Science & Technology A: Vacuum, Surfaces, and Films*, vol. 21, p. 1943, 2003.
- [148] I. Petrov, V. Orlinov, and A. Misiuk, "Highly oriented ZnO films obtained by dc reactive sputtering of a zinc target," Thin Solid Films, vol. 120, p. 55, 1984.
- [149] S. V. Thomsen, R. H. Petrmichl, V. S. Veerasamy, A. V. Longobardo, H. A. Luten, and D. R. Hall, "US Patent: Method of manufacturing window using ion beam milling of glass substrate.," 2004.
- [150] M. N. Islam, T. Ghosh, K. Chopra, and H. Acharya, "XPS and X-ray diffraction studies of aluminum-doped zinc oxide transparent conducting films," *Thin Solid Films*, vol. 280, p. 20, 1996.
- [151] M. Chen, "Surface characterization of transparent conductive oxide Al-doped ZnO films," Journal of Crystal Growth, vol. 220, p. 254, 2000.
- [152] B. Choi, I. Kim, D. Kim, K. Lee, T. Lee, B. Cheong, Y. Baik, and W. Kim, "Electrical, optical and structural properties of transparent and conducting ZnO thin films doped with Al and F by rf magnetron sputter," *Journal of the European Ceramic Society*, vol. 25, p. 2161, 2005.
- [153] Y. Sun, A. Feldman, and E. Farabaugh, "X-ray photoelectron spectroscopy of O 1s and Si 2p lines in films of SiOx formed by electron beam evaporation," *Thin Solid Films*, vol. 157, p. 351, 1988.
- [154] G. Hollinger, J. Tousset, and T. M. Duc, "X-Ray Photoelectron Study of SiO," in AIP Conf. Proc., p. 102, 1974.
- [155] U. Höfer, P. Morgen, W. Wurth, and E. Umbach, "Metastable molecular precursor for the dissociative adsorption of oxygen on Si (111)," *Physical Review Letters*, vol. 55, p. 2979, 1985.
- [156] F. Matsui, H. Yeom, K. Amemiya, K. Tono, and T. Ohta, "Reinterpretation of the Molecular O2 Chemisorbate in the Initial Oxidation of the Si (111) 7x7 Surface," *Physical Review Letters*, vol. 85, p. 630, 2000.
- [157] H. Yeom, "Comment on 'Molecular oxygen on the Si(111)-7x7 surface'," Physical Review B, vol. 66, p. 2001, 2002.

- [158] H. Kato, K. Miyamoto, M. Sano, and T. Yao, "Polarity control of ZnO on sapphire by varying the MgO buffer layer thickness," *Applied Physics Letters*, vol. 84, p. 4562, 2004.
- [159] X. Wang, Y. Tomita, O.-H. Roh, M. Ohsugi, S.-B. Che, Y. Ishitani, and A. Yoshikawa, "Polarity control of ZnO films grown on nitrided c-sapphire by molecular-beam epitaxy," *Applied Physics Letters*, vol. 86, p. 011921, 2005.
- [160] H. Kato, M. Sano, K. Miyamoto, and T. Yao, "High-quality ZnO epilayers grown on Zn-face ZnO substrates by plasma-assisted molecular beam epitaxy," *Journal* of Crystal Growth, vol. 265, p. 375, 2004.
- [161] H. Kato, M. Sano, K. Miyamoto, and T. Yao, "Homoepitaxial Growth of High-Quality Zn-Polar ZnO Films by Plasma-Assisted Molecular Beam Epitaxy," Japanese Journal of Applied Physics, vol. 42, p. L1002, 2003.
- [162] I. Ohkubo, A. Ohtomo, T. Ohnishi, Y. Mastumoto, H. Koinuma, and M. Kawasaki, "In-plane and polar orientations of ZnO thin films grown on atomically flat sapphire," *Surface Science*, vol. 443, p. L1043, 1999.
- [163] M. Vinnichenko, N. Shevchenko, A. Rogozin, R. Grötzschel, A. Mücklich, A. Kolitsch, and W. Möller, "Structure and dielectric function of two- and singledomain ZnO epitaxial films," *Journal of Applied Physics*, vol. 102, p. 113505, 2007.
- [164] H. Xu, K. Ohtani, M. Yamao, and H. Ohno, "Control of ZnO (000-1)/Al2O3 (11-20) surface morphologies using plasma-assisted molecular beam epitaxy," *Physica Status Solidi (B)*, vol. 243, p. 773, 2006.
- [165] H. Xu, K. Ohtani, M. Yamao, and H. Ohno, "Surface morphologies of homoepitaxial ZnO on Zn- and O-polar substrates by plasma assisted molecular beam epitaxy," Applied Physics Letters, vol. 89, p. 071918, 2006.
- [166] H. Matsui, H. Saeki, T. Kawai, A. Sasaki, M. Yoshimoto, M. Tsubaki, and H. Tabata, "Characteristics of polarity-controlled ZnO films fabricated using the homoepitaxy technique," *Journal of Vacuum Science & Technology B: Microelec*tronics and Nanometer Structures, vol. 22, p. 2454, 2004.
- [167] Y. Chen, H.-J. Ko, S.-K. Hong, T. Yao, and Y. Segawa, "Morphology evolution of ZnO(000-1) surface during plasma-assisted molecular-beam epitaxy," *Applied Physics Letters*, vol. 80, p. 1358, 2002.
- [168] H. Kato, M. Sano, K. Miyamoto, and T. Yao, "Effect of O/Zn Flux Ratio on Crystalline Quality of ZnO Films Grown by Plasma-Assisted Molecular Beam Epitaxy," *Japanese Journal of Applied Physics*, vol. 42, p. 2241, 2003.
- [169] W. Jo, S. Kim, and D. Kim, "Analysis of the etching behavior of zno ceramics," Acta Materialia, vol. 53, p. 4185, 2005.

- [170] S. K. Hong, Y. Chen, H. J. Ko, H. Wenisch, T. Hanada, and T. Yao, "ZnO and related materials: Plasma-Assisted molecular beam epitaxial growth, characterization and application," *Journal of Electronic Materials*, vol. 30, p. 647, 2001.
- [171] S.-K. Hong, T. Hanada, H. Makino, H.-J. Ko, Y. Chen, T. Yao, A. Tanaka, H. Sasaki, S. Sato, D. Imai, K. Araki, and M. Shinohara, "ZnO epilayers on GaN templates: Polarity control and valence-band offset," *Journal of Vacuum Science & Technology B: Microelectronics and Nanometer Structures*, vol. 19, p. 1429, 2001.
- [172] Z. X. Mei, Y. Wang, X. L. Du, M. J. Ying, Z. Q. Zeng, H. Zheng, J. F. Jia, Q. K. Xue, and Z. Zhang, "Controlled growth of O-polar ZnO epitaxial film by oxygen radical preconditioning of sapphire substrate," *Journal of Applied Physics*, vol. 96, p. 7108, 2004.
- [173] X. Du, M. Murakami, H. Iwaki, Y. Ishitani, and A. Yoshikawa, "Effects of Sapphire (0001) Surface Modification by Gallium Pre-Exposure on the Growth of High-Quality Epitaxial ZnO Film," *Japanese Journal of Applied Physics*, vol. 41, p. L1043, 2002.
- [174] J. I. Owen, J. Hüpkes, H. Zhu, E. Bunte, and S. E. Pust, "Novel etch process to tune crater size on magnetron sputtered ZnO:Al," *Physica Status Solidi* (a), vol. 208, p. 109, 2011.
- [175] H. Zhu, J. Hüpkes, E. Bunte, J. Owen, and S. Huang, "Novel etching method on high rate ZnO:Al thin films reactively sputtered from dual tube metallic targets for silicon-based solar cells," *Solar Energy Materials and Solar Cells*, vol. 95, p. 964, 2011.
- [176] M. L. Addonizio, R. Manoj, and I. Usatii, "Optimisation of low pressure-chemical vapour deposited ZnO thin films as front electrode of thin film silicon based solar cells," in 22nd Europen Photovoltaic Solar Energy Conference, Milan, Italy, 2007.
- [177] C. Rockstuhl, S. Fahr, F. Lederer, K. Bittkau, T. Beckers, and R. Carius, "Local versus global absorption in thin-film solar cells with randomly textured surfaces," Applied Physics Letters, vol. 93, p. 061105, 2008.
- [178] Y. Zhao, J. Drotar, G. Wang, and T. Lu, "Roughening in plasma etch fronts of Si (100)," Physical Review Letters, vol. 82, p. 4882, 1999.
- [179] P. Brault, P. Dumas, and F. Salvan, "Roughness scaling of plasma-etched silicon surfaces," *Journal of Physics: Condensed Matter*, vol. 10, p. L27, 1998.
- [180] J. S. Park, H. J. Park, Y. B. Hahn, G.-C. Yi, and a. Yoshikawa, "Dry etching of ZnO films and plasma-induced damage to optical properties," *Journal of Vacuum Science & Technology B: Microelectronics and Nanometer Structures*, vol. 21, p. 800, 2003.

- [181] L. P. Schuler, M. M. Alkaisi, P. Miller, R. J. Reeves, and A. Markwitz, "Comparison of DC and RF Sputtered Zinc Oxide Films with Post-Annealing and Dry Etching and Effect on Crystal Composition," *Japanese Journal of Applied Physics*, vol. 44, p. 7555, 2005.
- [182] D. Flamm, A. Schindler, T. Harzendorf, and E. Kley, "Fabrication of microlens arrays in CaF by ion milling," in *Proceedings of SPIE*, vol. 4179, p. 108, 2000.
- [183] Y. Kamihara, H. Ohashi, and A. Imamura, "De Patent: Verfahren zur Herstellung eines optischen Elements.," 1994.
- [184] T. Guo, Textured Glass as Substrate for Silicon Thin Film Solar Cells. Master thesis, Aachen University of Applied Sciences, 2009.
- [185] W. Böttler, V. Smirnov, S. Jorke, J. Hüpkes, and F. Finger, "Optimisation of ZnO based back reflector morphologies and light trapping effects in n-i-p microcrtsalline thin film solar cells," in *Photovoltaic technique conference*, 2011.

Acknowledgement

I would like to thank all those who helped make this work possible. Specific thanks are due to the following people for their contribution:

- Dr. Eerke Bunte, for being an excellent supervisor and for his guidance, encouragement, and support throughout the work for this thesis;
- Dr. Jürgen Hüpkes, for many interesting and fruitful discussions, for being supervisor for the last half year, and for the perusal of this thesis;
- Prof. Dr. Uwe Rau, for providing this opportunity to work at such a worldrenowned institution, and for the suggestions in many projects;
- Prof. Dr. Reinhard Carius, and Dr. Aad Gordijn, for insightful discussions on the surface characterization and solar cells;
- Hilde Siekmann, Janie Worbs, Joachim Kirchhoff and Andreas Mück, for many technological supports and the preparation of ZnO:Al films and solar cells;
- Alain Doumit and Brigitte Zwaygardt, for many characterizations of ZnO:Al films;
- Dr. Astrid Besmehn and Dr. Uwe Breuer, for providing me the opportunity to measure XPS and SIMS in ZCH, and for many interesting discussions on the results;
- Dr. Florian Ruske, Mark Wimmer and Dr. Dominik Köhl, for the help and discussions on XRD measurements, and for performing of capping-annealing;
- Philipp Spiekermann and Dr. Martina Luysberg, for the measurement of TEM in IFF, and for many interesting discussions on the results;
- Silvia Jorke and Dr. Melanie Schulte, for the instructions on the AFM measurements, and many helps on the analysis;
- Wilfried Reetz, Chirstoph Zahren, Dr. Etienne Moulin, Janis Kroll, Jonas Noll, and Rebecca Van Aubel for the measurement of solar cells;
- Hans Peter Bochum and Elke Brauweiler-Reuters for the performing of SEM measurements;
- Dr. Matthias Meier and Thomas Zimmermann, for the kind help on the OES measurement of ion beams;
- Jorj Owen and Dr. Sascha E. Pust, for the proofreading of this work;

- Marek Warzecha, Hongbing Zhu, Jost Gabrielle, David Wippler, and Ting Guo, for the nice cooperation and discussions in many projects;
- Dr. Christian Sellmer, for the help on the small but efficient skills about Latex.
- Andrea Mülheims, Roswitha Bley, and Dirk Schramm, for the organization works on the contracts, taxes, visas, etc.;
- Finally, special thanks are to my husband and parents, who give me unfailing emotional support and encouragement.

Band / Volume 156

Self-consistent modeling of plasma response to impurity spreading from intense localized source

M. Koltunov (2012), V, 113 pp. ISBN: 978-3-89336-828-0

Band / Volume 157

Phosphorsäureverteilung in Membran-Elektroden-Einheiten dynamisch betriebener Hochtemperatur-Polymerelektrolyt-Brennstoffzellen

W. Maier (2012), VI, 105 pp. ISBN: 978-3-89336-830-3

Band / Volume 158

Modellierung und Simulation von Hochtemperatur-Polymerelektrolyt-Brennstoffzellen

M. Kvesic (2012), ix, 156 pp. ISBN: 978-3-89336-835-8

Band / Volume 159

Oxidation Mechanisms of Materials for Heat Exchanging Components in $\text{CO}_2/\text{H}_2\text{O}$ -containing Gases Relevant to Oxy-fuel Environments

T. Olszewski (2012), 200 pp. ISBN: 978-3-89336-837-2

Band / Volume 160

Ice Crystal Measurements with the New Particle Spectrometer NIXE-CAPS

J. Meyer (2013), ii, 132 pp. ISBN: 978-3-89336-840-2

Band / Volume 161

Thermal Shock Behaviour of Different Tungsten Grades under Varying Conditions

O. M. Wirtz (2013), XIV, 130 pp.

ISBN: 978-3-89336-842-6

Band / Volume 162

Effects of ¹³⁷Cs and ⁹⁰Sr on structure and functional aspects of the microflora in agricultural used soils

B. Niedrée (2013), XII, 92 pp. ISBN: 978-3-89336-843-3

Band / Volume 163

Lidar observations of natural and volcanic-ash-induced cirrus clouds

C. Rolf (2013), IX, 124 pp. ISBN: 978-3-89336-847-1

Schriften des Forschungszentrums Jülich Reihe Energie & Umwelt / Energy & Environment

Band / Volume 164

CO2-Abscheidung, -Speicherung und -Nutzung:

Technische, wirtschaftliche, umweltseitige und gesellschaftliche Perspektive Advances in Systems Analysis 2

W. Kuckshinrichs; J.-F. Hake (Eds.) (2012), iv, 354 pp.

ISBN: 978-3-89336-850-1

Band / Volume 165

Interest Mediation and Policy Formulation in the European Union Influence of Transnational Technology-Oriented Agreements on European Policy in the Field of Carbon Capture and Storage

Advances in Systems Analysis 3

O. Schenk (2013), XIII, 253 pp. ISBN: 978-3-89336-852-5

Band / Volume 166

Versagensverhalten plasmagespritzter Mg-Al-Spinell-Schichten unter Thermozyklierung

S. M. Ebert (2013), X, 173 pp. ISBN: 978-3-89336-853-2

Band / Volume 167

Coupled modeling of water, vapor and heat in unsaturated soils - Field applications and numerical studies

C. Steenpaß (2013), X, 123 pp. ISBN: 978-3-89336-854-9

Band / Volume 168

An analysis of the global atmospheric methane budget under different climates

A. Basu (2013), v, 110 pp. ISBN: 978-3-89336-859-4

Band / Volume 169

Experimental determination of the partitioning coefficient of nopinone as a marker substance in organic aerosol

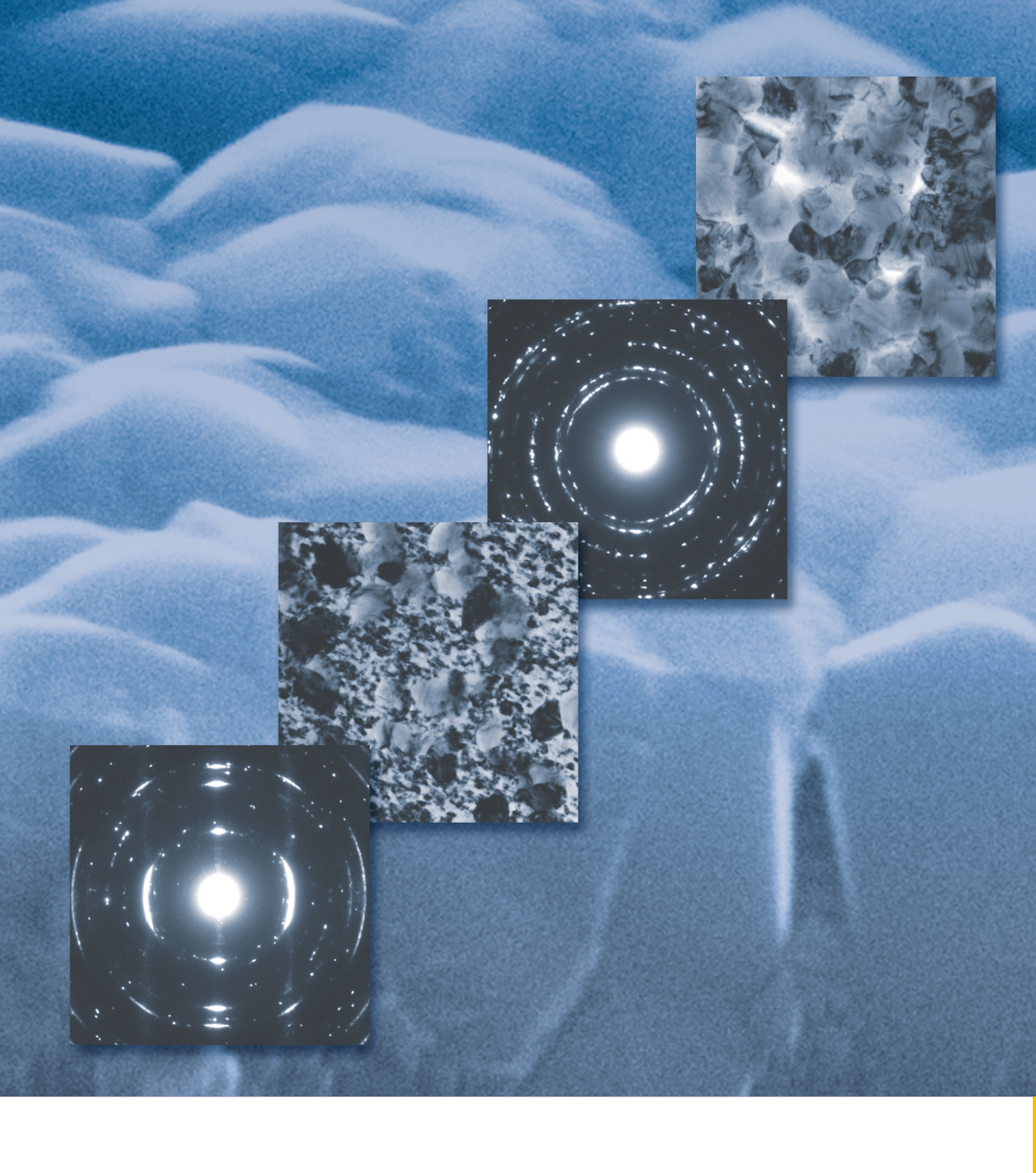
B. Steitz (2013), 132 pp. ISBN: 978-3-89336-862-4

Band / Volume 170

Ion Beam Treatment of Functional Layers in Thin-Film Silicon Solar Cells

W. Zhang (2013), xi, 191 pp. ISBN: 978-3-89336-864-8

Weitere Schriften des Verlags im Forschungszentrum Jülich unter http://www.zb1.fz-juelich.de/verlagextern1/index.asp



Energie & Umwelt / Energy & Environment Band / Volume 170 ISBN 978-3-89336-864-8

